APPLIED COMPUTATIONAL ELECTROMAGNETICS SOCIETY JOURNAL

Special Issue on ACES-China 2017

Guest Editors:

Xiu Yin Zhang, South China University of Technology, P. R. China
Wei E. I. Sha, Zhejiang University, P. R. China
Sheng Sun, University of Electronic Science and Technology of China, P. R. China

May 2018
Vol. 33 No. 5
ISSN 1054-4887

The ACES Journal is abstracted in INSPEC, in Engineering Index, DTIC, Science Citation Index Expanded, the Research Alert, and to Current Contents/Engineering, Computing & Technology.

The illustrations on the front cover have been obtained from the research groups at the Department of Electrical Engineering, The University of Mississippi.

EMERITUS ASSOCIATE EDITORS-IN-CHIEF

EMERITUS EDITORIAL ASSISTANTS

MAY 2018 REVIEWERS: REGULAR PAPERS

Hongcai Chen
John Daniel
Li Gao
Alfredo Gomes Neto
Bernhard Hoenders
Zhixiang Huang
Ian Jeffrey
Jie Li
Ping Li
Chun Lu
Cengiz Ozzaim
Andrew Peterson
Shishir Punjala
Shi-Wei Qu
Luis Ramirez
Wei E. I. Sha
Ali Shahi
Sheng Sun
Mehmet Tabakcioglu
Junwu Tao
Ren Xingang
Xiu Yin Zhang
Weijiang Zhao

THE APPLIED COMPUTATIONAL ELECTROMAGNETICS SOCIETY JOURNAL

Vol. 33 No. 5 May 2018

TABLE OF CONTENTS – REGULAR PAPERS

Design of Wideband Filtering Power Dividers with Harmonic Suppression Based on the Parallel-Coupled Line Structures

Xi Yu, Sheng Sun, and Yun Liu

School of Electronic Science and Engineering
University of Electronic Science and Technology of China, Chengdu, 611731, China
sunsheng@ieee.org

Abstract ─ This paper presents a wideband filtering power divider with harmonic suppression. By embedding two coupled-line sections to each way of the conventional Wilkinson structure, four resonant modes excited by two coupled lines and one original mode of the Wilkinson structure are incorporated to improve the in-band filtering responses. In order to enhance the frequency selectivity, a pair of long open stubs are inserted between these coupled-line sections to produce a pair of transmission zeros on both sides of the passband. Meanwhile, two additional transmission zeros at the upper stopband can be introduced to broaden the bandwidth of the stopband. Moreover, a short open stub is installed at the input port, which can also introduce one transmission zero to enhance upper stopband rejection. Finally, a prototype of the wideband filtering power divider operating at the center frequency of 3 GHz is designed and fabricated. The measured results show a 15-dB bandwidth of 56%, an isolation better than 18-dB and a 35-dB wide stopband from 4.44 to 7.73 GHz.

Index Terms ─ Coupled line, filtering power divider, harmonic suppression, wideband.

I. INTRODUCTION

In the modern wireless communication system, power dividers and filters as indispensable components have been widely used in the RF front ends of both receivers and transmitters. In order to meet the demands of high integration and multiple function, the filtering power dividers which combine both characteristics of filters and power dividers have attracted much attention in recent years.

To realize the filtering function, the techniques of coupling matrix and J/K inverter for the filter design can be applied to the filtering power divider design [1, 2]. Based on the coupling coefficients, a compact power divider with Chebyshev filtering response was implemented by using folded net-type resonators [1]. Although a good in-band isolation can be achieved, the frequency selectivity is poor. In order to achieve a high selectivity, the *K*-inverters implemented by dual-path coupling structure were proposed to produce two transmission zeros on both sides of the passband and provide arbitrary power ratios at the same time [2]. In addition, E-shaped dual-mode resonators [3] and quarter-mode substrate integrated waveguide (SIW) circular cavities [4] were utilized to further reduce the circuit size. Nevertheless, the existing harmonic at upper stopband could degrade the out-of-band performance of the system. Therefore, the mixed electric and magnetic couplings as well as the cross coupling could be used to generate transmission zeros near the passband and the second harmonic [5]. Additionally, the discriminating coupling structure [6], short-circuited half-wavelength resonators [7] and open stubs [8] were also applied to achieve a wide upper stopband of the filtering power divider.

For the wideband applications, the hybrid slotline to microstrip line transition was proposed to be integrated with the Wilkinson power divider [9]. Although the response is ultra-wideband [9, 10], the out of band rejection level is not enough. By utilizing the first few resonant modes, the multi-mode resonator [11, 12] and ring resonator [13, 14] can be embedded to the power divider for a wide bandwidth and a filtering response. Since the coupled line provides not only a suitable coupling but also a filtering performance, it was often used to form the main structures of a wideband filtering power divider [15-18]. They can be installed at each port as matching networks to achieve a wideband response [15]. In [16], a pair of coupled lines terminated with open stubs were applied to replace the quarter-wavelength transmission lines in the conventional Wilkinson power dividers. A 70% fractional bandwidth can be achieved, whereas the out-of-band rejection level needs to be improved. Although the bandwidth and stopband suppression are acceptable by using the multi-sections quasi-coupled lines and short/open stubs [17], the in-band return loss was unsatisfactory. By utilizing two-sections coupled lines with center-loaded open stubs and two shorted stubs, the stopband can be extended [18]. On the other hand, the filtering power divider can be also designed to meet other special demands such as dual-

Submitted On: September 30, 2017
Accepted On: April 10, 2018

band [19, 20], balanced-to-balanced/unbalanced [21, 22], and multi-output [23-25].

In this paper, a wideband filtering power divider with wide stopband rejection is proposed. Conventionally, quarter-wavelength transmission lines are used in the design of Wilkinson power divider. By installing a short open stub at the input port, the required length of transmission lines can be shortened and a transmission zero would be produced at the upper stopband. Two coupled-line sections are embedded to each way of the power divider, which can excite four resonate modes. Together with the original mode of the Wilkinson structure, totally five transmission poles can be produced to construct a wideband filtering response. By choosing different even-odd mode impedances of embedded coupled lines, these resonate modes can be controlled to adjust the bandwidth of the filtering power divider. In addition, a long open stub is inserted between these two coupled lines, which not only considered provides the couplings between two coupled lines as a *K*-inverter [24], but also produces two transmission zeros on both sides of the passband to enhance the roll-off skirt. Meanwhile, two additional transmission zeros could also be produced at the upper stopband to broaden the bandwidth of upper stopband. These transmission zeros with the one produced by the short open stub can well suppress the harmonic and thus improve the upper stopband rejection. The theoretical analysis and design procedures are presented in the following sections in detail. To verify our proposal, a prototype of the wideband filtering power divider operating at center frequency of 3 GHz is finally designed, fabricated and measured. The measured results have good agreement with the simulated ones.

II. ANALYSIS AND DESIGN

Figure 1 shows the configuration of the two-way wideband filtering power divider. It consists of a transmission line, two section coupled lines and a long open stub in each way. A short open stub is loaded at the input port and a resistor R is connected between the two output ports. Z_i and Z_{ei}, Z_{oi} (i = 1, 2) are the characteristic impedances of the microstrip lines and the even-odd mode impedances of the coupled lines, while θ and θ_S are the electrical length of the corresponding transmission lines, respectively. In this work, θ is chosen to be $\theta_0 = \pi/2$, which is quarter-wavelength at the center operating frequency f_0. For simplicity, the phase velocities of the even and odd modes are assumed to be the same so that the coupled line structures have the same even/odd-mode electrical length. Due to the fully symmetric structure, the proposed filtering power divider can be decomposed into two half equivalent circuits under the even and odd excitations, as shown in Figs. 2 (a) and (b). When the even mode is excited, the *ABCD*-matrix of the half circuit model can be derived as:

$$[A]_e = \begin{bmatrix} A_e & B_e \\ C_e & D_e \end{bmatrix}. \tag{1}$$

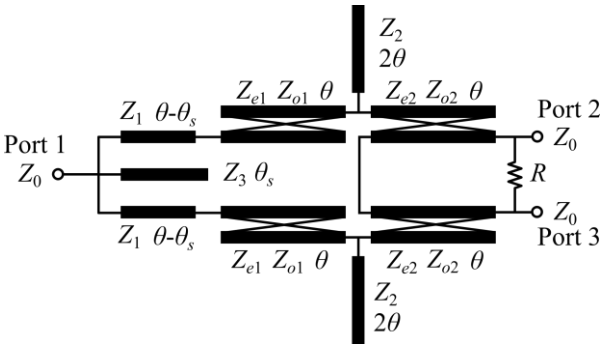

Fig. 1. The schematic of the proposed wideband filtering power divider.

Then, the *S*-parameters [S^e] of the even-mode circuit with two different port impedances can be obtained by using the following relationships:

$$S_{11}^e = \frac{A_e Z_0 + B_e - 2C_e Z_0^2 - 2D_e Z_0}{A_e Z_0 + B_e + 2C_e Z_0^2 + 2D_e Z_0}, \tag{2}$$

$$S_{21}^e = \frac{2\sqrt{2}\left(A_e D_e - B_e C_e\right) Z_0}{A_e Z_0 + B_e + 2C_e Z_0^2 + 2D_e Z_0}, \tag{3}$$

$$S_{22}^e = \frac{-A_e Z_0 + B_e - 2C_e Z_0^2 + 2D_e Z_0}{A_e Z_0 + B_e + 2C_e Z_0^2 + 2D_e Z_0}. \tag{4}$$

On the other hand, when the odd mode is excited, the second coupled line is loaded with a short-circuited and an open-circuited terminations. The equivalent circuit of this coupled line is also shown in Fig. 2 (b). It can be found that the frequency response of this coupled line is all-stop. Therefore, the S-parameters [S^o] of the single-port odd-mode circuit can be expressed as:

$$S_{22}^o = \frac{Z_{in} - Z_0}{Z_{in} + Z_0}, \tag{5}$$

where

$$Z_{in} = \frac{j2R\left(Z_{e2} + Z_{o2}\right)\tan\theta}{4R + j\left(Z_{e2} + Z_{o2}\right)\tan\theta}. \tag{6}$$

Based on the even-odd mode analysis, the S-parameters [*S*] of the filtering power divider can be given as:

$$S_{11}(\theta) = S_{11}^e(\theta), \tag{7}$$

$$S_{12}(\theta) = S_{21}(\theta) = S_{13}(\theta) = S_{31}(\theta) = \frac{S_{21}^e(\theta)}{\sqrt{2}}, \tag{8}$$

$$S_{22}(\theta) = S_{33}(\theta) = \frac{S_{22}^e(\theta) + S_{22}^o(\theta)}{2}, \tag{9}$$

$$S_{23}(\theta) = S_{32}(\theta) = \frac{S_{22}^e(\theta) - S_{22}^o(\theta)}{2}, \tag{10}$$

and the S_{11} can be further written as:

$$S_{11} = -\frac{k_1 \cos\theta_S + k_2 \sin\theta_S \tan\theta_S + jk_3 \sin\theta_S}{k_1 \cos\theta_S + k_2 \sin\theta_S \tan\theta_S + jk_4 \sin\theta_S}, \quad (11)$$

where

$$k_1 = Z_3\left[2Z_0^2\left(Z_{e1}-Z_{o1}\right)^2 - Z_1^2\left(Z_{e2}-Z_{o2}\right)^2\right],$$

$$k_2 = Z_0^2 Z_1\left(Z_{e1}-Z_{o1}\right)^2,$$

$$k_3 = Z_0 Z_1[(Z_1-2Z_3)\left(Z_{e2}-Z_{o2}\right)^2 + Z_3\left(Z_{e1}-Z_{o1}\right)^2],$$

$$k_4 = Z_0 Z_1[(Z_1-2Z_3)\left(Z_{e2}-Z_{o2}\right)^2 - Z_3\left(Z_{e1}-Z_{o1}\right)^2].$$

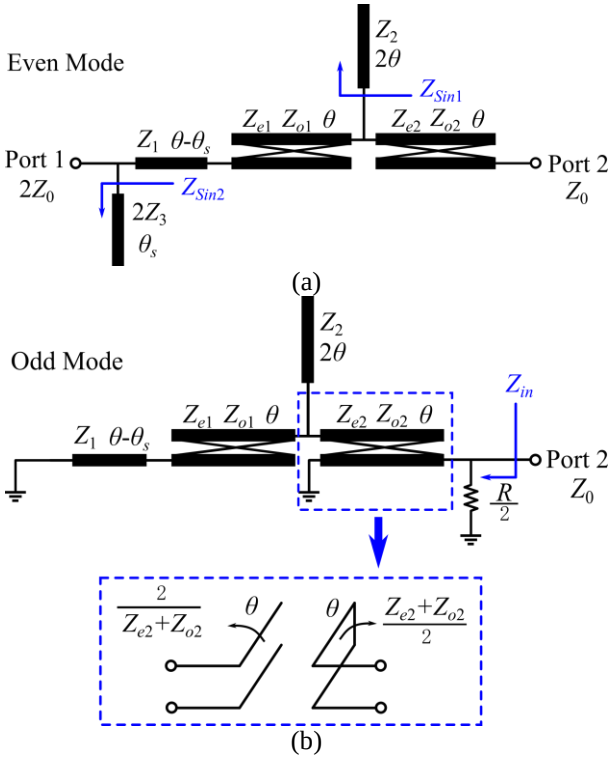

Fig. 2. The decomposed equivalent circuits of the filtering power divider. (a) Even-mode circuit model. (b) Odd-mode circuit model.

In order to achieve a good in-band return loss, we can solve the equation of $S_{11}(\theta) = 0$ at the center frequency. Then, Z_1 and Z_3 can be deduced as:

$$Z_1 = \frac{Z_0\sqrt{2\left(Z_{e1}-Z_{o1}\right)^2 + \left[2-\left(\frac{Z_{e1}-Z_{o1}}{Z_{e2}-Z_{o2}}\right)^2\right]\tan^2\theta_S}}{Z_{e2}-Z_{o2}}, \quad (12)$$

$$Z_3 = \frac{Z_1\left(Z_{e2}-Z_{o2}\right)^2}{2\left(Z_{e2}-Z_{o2}\right)^2 - \left(Z_{e1}-Z_{o1}\right)^2}. \quad (13)$$

From (12) and (13), it can be noticed that once the even-odd mode impedances of the coupled lines are determined, Z_1 and Z_3 can be evaluated by choosing a proper value of θ_S. According to (12) and (13), Z_1 and Z_3 increase as θ_S increases. When $\theta_S = 0$, Z_1 can be calculated as:

$$Z_1 = \sqrt{2}Z_0\frac{Z_{e1}-Z_{o1}}{Z_{e2}-Z_{o2}}. \quad (14)$$

In this work, $(Z_{e1} - Z_{o1})$ is larger than $(Z_{e2} - Z_{o2})$. Therefore, compared with the conventional Wilkinson power divider, the value of Z_1 is larger than $\sqrt{2}Z_0$ due to the influence of the embedded coupled lines.

Figure 3 shows the *S*-parameters of the filtering power divider with different θ_S. The corresponding realizable characteristic impedances of each curve plotted in Fig. 3 are summarized in Table 1. As θ_S, increases, the frequency response has little influence, as shown in Fig. 3. However, when θ_S increases to 60°, Z_3 becomes very large and exceeds the maximal realizable characteristic impedance of the microstrip line. Thus, the in-band response is deteriorated extremely. Considering that the maximal characteristic impedance of the realizable microstrip line on the substrate of RO4350B with a thickness of 0.508 mm and a dielectric constant of 3.66 is 134 Ohm, and $(Z_{e1} - Z_{o1})$ is about 100~107 Ohm, and $(Z_{e2} - Z_{o2})$ is 90~95 Ohm, the maximal θ_S is about 52° when the performance is acceptable and the impedance is realizable.

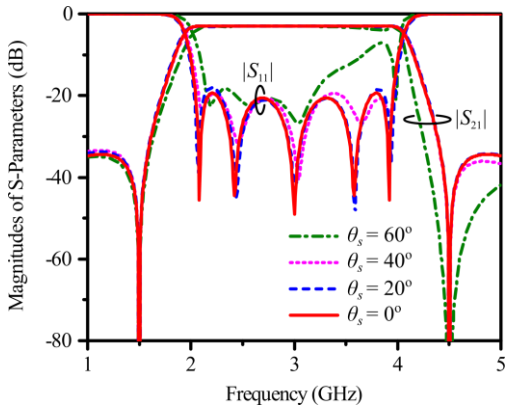

Fig. 3. The S-parameters of the wideband filtering power divider with different θ_S.

Table 1: The corresponding realizable characteristic impedances of the filtering power divider with different θ_S

θ_S	Z_1	Z_2	Z_3	Z_{e1}	Z_{o1}	Z_{e2}	Z_{o2}
0°	80	36	-	156	51	154	61
20°	82	36	120	157	51	155	61
40°	87	34	126	148	48	147	56
60°	105	26	134	134	45	136	53

As shown in Fig. 3, when θ_S equals to 0°, 20°, and 40° respectively, there are five transmission poles in the passband and two transmission zeros on two sides of the

passband. In comparison with the conventional Wilkinson power divider, the two embedded coupled lines can provide four in-band poles and the length of the conventional quarter-wavelength transmission line can be reduced to be $\pi/2 - \theta_S$. The two transmission zeros near the passband are introduced by loading the long open stubs between coupled lines. When the impedance of the long open stub equals to zero, the current of the circuit would be directly shorted to the ground, which can produce a transmission zero. Therefore, the location of these two transmission zeros can be found by solving the following equation:

$$Z_{Sin1} = -jZ_2 \cot 2\theta = 0, \quad (15)$$

the positions are finally obtained as:

$$f_{S1n} = \frac{(2n-1)\cdot 90^0}{2\theta} f_0 = \frac{2n-1}{2} f_0 \quad (\text{n=1, 2…}). \quad (16)$$

As it can be found in (15), the impedance of the open stub is a pure reactance or susceptance within the passband, which can be equivalent to a *K*-inverter [24]. Therefore, the two long open stubs can not only produce the out-of-band transmission zeros, but also can provide the in-band coupling between the two coupled lines as a *K*-inverter. Similar to the long open stub, the short open stub at the input port can also provide transmission zeros at higher frequency band. By solving the equation:

$$Z_{Sin2} = -j2Z_3 \cot \theta_S = 0, \quad (17)$$

the locations of the transmission zeros can be obtained as:

$$f_{S2n} = \frac{(2n-1)\cdot 90^0}{\theta_S} f_0 \quad (n = 1, 2\ldots). \quad (18)$$

In order to improve the in-band isolation between two output ports, the resistor can be loaded and determined as $R = 2Z_0$ by letting $S_{23} = 0$.

Figure 4 illustrates the influence of Z_2 on the in-band response. As Z_2 increases, the reflection at port 2/3 is almost unchanged and in-band $|S_{22(33)}|$ is below -20 dB. However, the in-band performance of $|S_{11}|$ and $|S_{23}|$ are deteriorated near the edge frequency of the passband. Therefore, a proper value of Z_2 needs to be determined in order to achieve a good in-band return loss and isolation.

Figure 5 shows the influence of impedances on the bandwidth. Once the operating center frequency f_0 is chosen, the transmission zeros introduced by the long open stub are determined according to (16), and the passband of each way is limited between the first two transmission zeros. However, these transmission zeros cannot be independently controlled by only one open stub, so that the bandwidth cannot be adjusted by only changing the length of the long open stub. If the length is changed, these two transmission zeros can move at the same time and the operating center frequency of the passband f_0 is also shifted. Therefore, in order to maintain f_0 unchanged, the lengths of all the transmission lines are fixed and the impedances is utilized to control the bandwidth of the filtering power divider. Three cases with θ_S = 0 are given to demonstrate the bandwidth control with the different characteristic impedances of transmission lines, and the detail specifications and results are shown in Table 2. As illustrated in Fig. 5 and Table 2, Case III has a wider bandwidth than other two cases. Although the out-of-band rejection level and the in-band isolation is unsatisfactory compared with the others, a sharp roll-off skirt can be achieved. For the Case I, the bandwidth is narrower than Case II and III with very high even-odd mode impedances and low characteristic impedance of the long open stub (Z_3). It can be also found that as the increase of the bandwidth, Z_2 increases gradually while the other impedances decrease. Therefore, according to Table 2, different bandwidths can be achieved by choosing proper characteristic impedances with fixed electric length of the transmission lines.

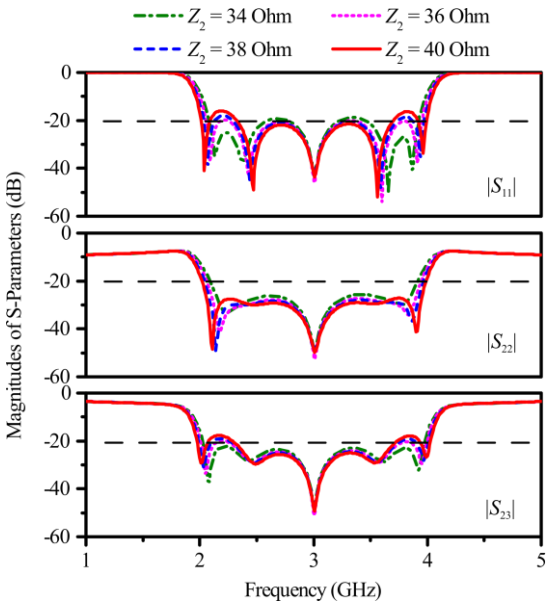

Fig. 4. The S-parameters of the wideband filtering power divider with different Z_2 when $\theta_S = 20^o$.

Finally, the design procedure of the proposed wideband filtering power divider can be summarized as follows:

1) Determine the operating center frequency f_0 and the positions of the two transmission zeros near the passband can be calculated by (16);
2) Choose the positions of the transmission zeros at the higher frequency band according to (18) and determine the θ_S;
3) Based on Tables 1, 2, Fig. 4 and Fig. 5, choose the proper Z_2 and even-odd mode impedance of the coupled lines. According to (12) and (13), Z_1 and Z_3 can be determined;
4) Determine the isolation resistor R=2Z_0.

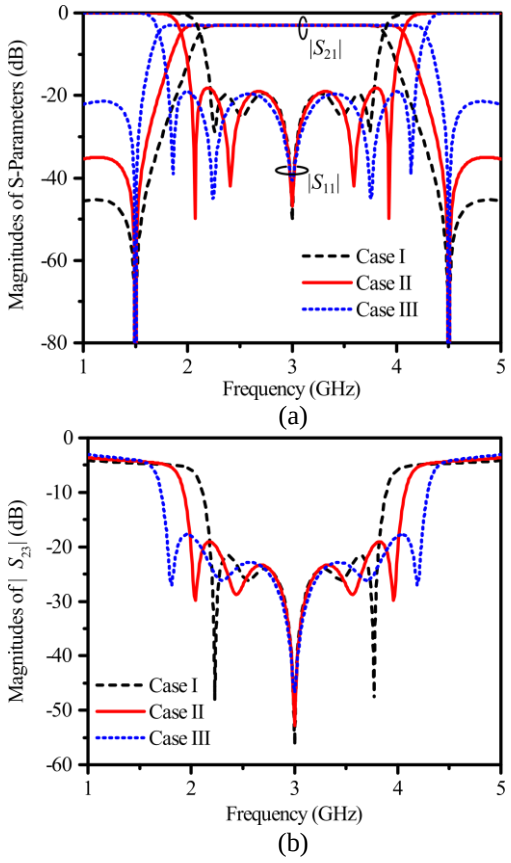

Fig. 5. The magnitudes of S-parameters for the Case I, II, and III. (a) The magnitudes of $|S_{11}|$ and $|S_{21}|$. (b) The magnitudes of $|S_{23}|$.

Table 2: The corresponding characteristic impedances and simulated results for Case I, II, and III

Case	Z_1	Z_2	Ze_1	Zo_1	Ze_2	Zo_2	FBW/ RL[1]	R[2]/ I[3]
I	83	25	192	81	180	86	51.7%/ 19.6 dB	45 dB/ 21 dB
II	80	36	156	51	154	61	65.0%/ 18.0 dB	35 dB/ 19 dB
III	79	76	142	30	143	42	78.6%/ 19.5 dB	21 dB/ 17 dB

RL[1]: return loss; R[2]: out-of-band rejection level; I[3]: in-band isolation

III. IMPLEMENT AND RESULTS

A prototype of the wideband filtering power divider is designed and fabricated on the substrate of RO4350B with a thickness of 0.508 mm and a dielectric constant of 3.66 at the operating center frequency of 3 GHz. In order to suppress the second harmonic around 6 GHz, θ_S is chosen as 45°, while the circuit size becomes smaller accordingly. The circuit layout and the photograph of the fabricated wideband filtering power divider are depicted in Fig. 6 and Fig. 7, respectively. In order to realize the high even-odd mode impedance and provide strong couplings, two apertures are etched on the ground plane. vAs shown in Fig. 6, the main dimensions of the proposed wideband filtering power divider are finally optimized to be: $w_0 = 0.95$, $w_1 = 0.1$, $w_2 = 0.23$, $w_3 = 1.36$, $l_1 = 6.37$, $l_2 = 7.57$, $l_3 = 14.7$, $l_4 = 29.28$, $l_5 = 15.7$, $s_1 = 0.12$, and $s_2 = 0.11$ (units: mm). The isolation resistor is calculated as 100 Ohm. Figure 8 shows the circuit simulated frequency responses when θ_S is 0° and 45° respectively. It can be found that when there is no short open stub, the second harmonic is generated at 6 GHz. When θ_S is 45°, the harmonic at 6 GHz is suppressed by the transmission zero. However, the harmonic mode still exists and is pushed up to a higher frequency, so that there is a peak on S_{11} at 6.5 GHz. Although the harmonic mode still exists, the magnitude of S_{21} is pulled down below -20 dB due to the introduced transmission zero. Figure 9 shows the EM simulated surface current at 6.5 GHz. There is very strong current distribution on the short open stub and the first coupled-line section. Since the width of coupled lines is small and two apertures are just etched behind them on the ground plane to provide strong in-band couplings, some radiation from the apertures could happen at 6.5 GHz.

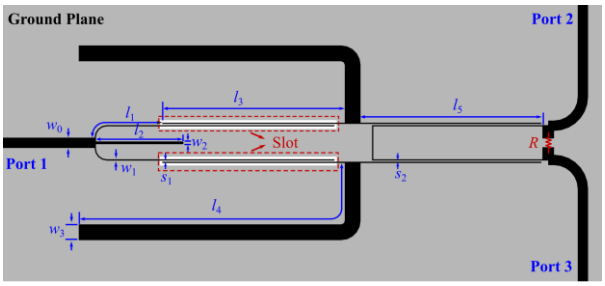

Fig. 6. The layout of the wideband filtering power divider.

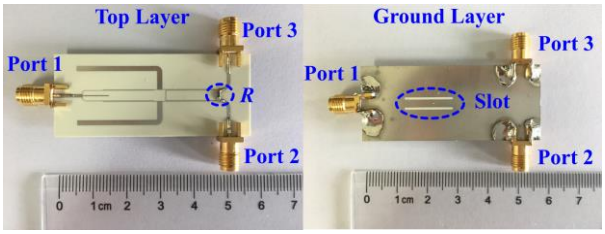

Fig. 7. The photograph of the fabricated wideband filtering power divider.

The full-wave simulated results and measured results are plotted in Fig. 10. The in-band return loss is better than 15 dB and the minimum insertion loss is -3-0.7 dB. The measured fractional bandwidth of 15-dB in-band return loss is about 56% over the frequency range from 2.30 to 3.98 GHz. The in-band isolation is better than

18 dB. In addition, a 35-dB harmonic suppression can be achieved at the stopband from 4.44 to 7.73 GHz, although the leakage from the apertures seems more obvious at 6.5 GHz. As shown in Fig. 10 (a), it can be noticed that there are six transmission zeros over the concerned frequency band. The first two transmission zeros (f_{tz1}, f_{tz2}) and the last one (f_{tz6}) are located at 1.5 GHz, 4.5 GHz and 7.5 GHz, which is introduced by the long open stub. f_{tz3} introduced by the short open stub is allocated at 6.18 GHz to suppress the second harmonic of the center frequency. Because of the existing of coupled lines, two more transmission zeros f_{tz4} and f_{tz5} are introduced at 6.73 GHz and 7.05 GHz. Owing to the four transmission zeros (f_{tz3}, f_{tz4}, f_{tz5}, and f_{tz6}) at the upper stopband, the spurious harmonic frequencies can be well suppressed and a wide stopband can be obtained. The magnitude and phase imbalance between two output ports are less than ±0.2 dB and ±1.3°, respectively, as depicted in Fig. 11 (a). Figure 11 (b) shows the in-band group delay of the filtering power divider. Comparison with the other design in previous work is tabulated in Table 3. It can be found that the proposed filtering power divider has achieved a wide bandwidth of 56%, a well harmonic suppression of 35 dB and six transmission zeros in total.

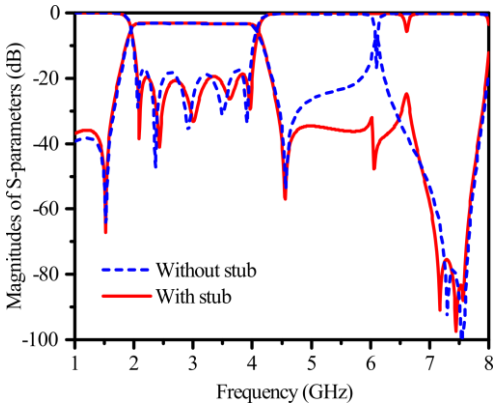

Fig. 8. The circuit simulated frequency responses of the filtering power divider with and without short open stub.

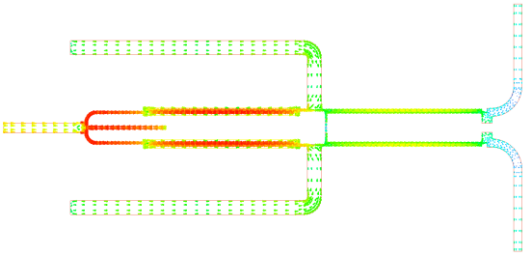

Fig. 9. The surface current of the filtering power divider at 6.5 GHz.

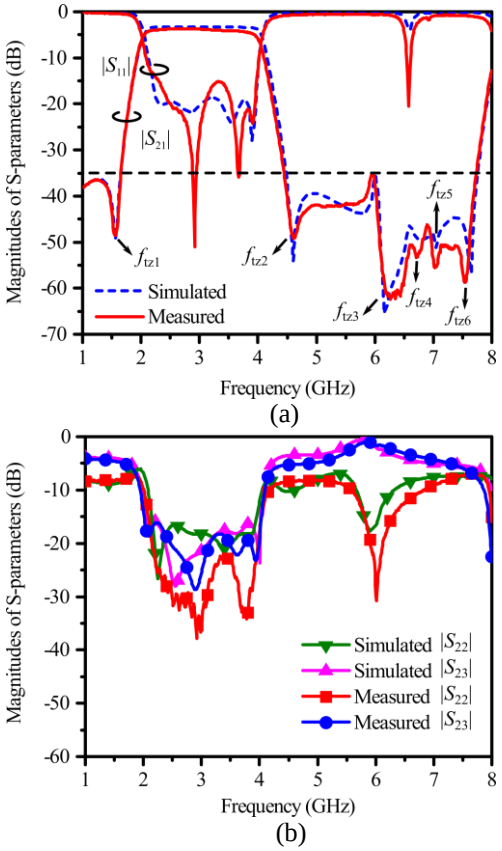

Fig. 10. The EM simulated and measured results of the wideband filtering power divider. (a) The magnitudes of S_{11} and S_{21}. (b) The magnitudes of S_{22} and S_{23}.

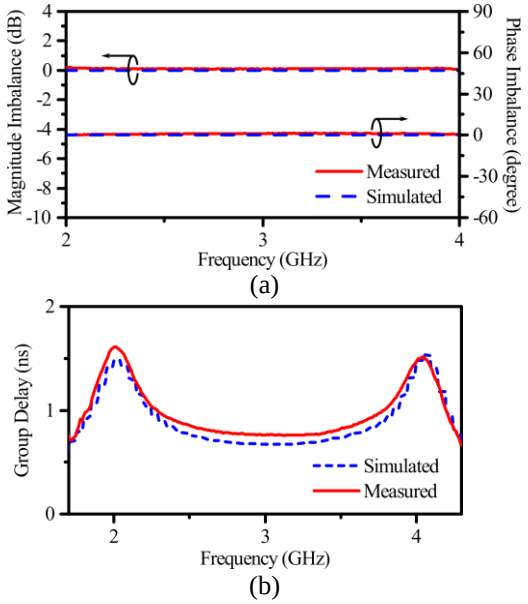

Fig. 11. (a) The in-band magnitude and phase imbalance. (b) The group delay of the filtering power divider.

Table 3: Comparison with the wideband filtering power divider in the literature

Ref.	f_0 (GHz)	FBW/RL[1] (In-band)	BW/IL[2] (Stopband)	Isolation	TZs[3]
[8]	6.80	85.3% 15 dB	-	15.0dB	-
[9]	2.15	31.0% 17 dB	4.2 f_0 20 dB	17.0 dB	2
[10]	2.05	62.0% 10.14 dB	0.95 f_0 15.8 dB	10.0 dB	5
[11]	1.50	60% 14 dB	-	20 dB	2
[12]	2.00	62.0% 15 dB	-	20.0 dB	-
[13]	3.00	70.0% 20 dB	2.6 f_0 13 dB	16.7 dB	4
[14]	3.00	104.5% 15 dB	3.4 f_0 15 dB	15.0 dB	3
[15]	1.00	43.0 % 20 dB	3.9 f_0 20 dB	20.0 dB	5
This work	**3.00**	**56.0 % 15 dB**	**1.1 f_0 35 dB**	**18.0 dB**	**6**

[1]RL: Return Loss; [2]IL: Insertion Loss; [3]TZs: Transmission zeros

IV. CONCLUSION

In this paper, a wideband filtering power divider with wide stopband has been proposed. Based on the two embedded coupled lines and long open stubs, the wideband filtering response has been achieved with a sharp roll-of skirt. The introduced short open stub at the input port not only reduced the length of the conventional quarter-wavelength in Wilkinson structure, but also provided a transmission zero at upper stopband to improve the out-of-band rejection level. With the help of total five resonances and six transmission zeros, a 56% bandwidth, a high 35-dB stopband rejection and an isolation better than 18 dB have been achieved.

ACKNOWLEDGMENT

This work was supported by the National Natural Science Foundation of China No. 61622106 and No. 61721001.

REFERENCES

[1] C. F. Chen and C. Y. Lin, "Compact microstrip filtering power dividers with good in-band isolation performance," *IEEE Microw. Wireless Compon. Lett.*, vol. 24, no. 1, pp. 17-19, Jan. 2014.

[2] K. X. Wang, X. Y. Zhang, and B. J. Hu, "Gysel power divider with arbitrary power ratios and filtering responses using coupling structure," *IEEE Trans. Microw. Theory Techn.*, vol. 62, no. 3, pp. 431-440, Mar. 2014.

[3] G. Zhang, J. Wang, L. Zhu, and W. Wu, "Dual-mode filtering power divider with high passband selectivity and wide upper stopband," *IEEE Microw. Wireless Compon. Lett.*, vol. 27, no. 7, pp. 642-644, July 2017.

[4] X. Wang and X. W. Zhu, "Quarter-mode circular cavity substrate integrated waveguide filtering power divider with via-holes perturbation," *Electron. Lett.*, vol. 53, no. 12, pp. 791-793, June 8, 2017.

[5] X. Y. Zhang, K. X. Wang, and B. J. Hu, "Compact filtering power divider with enhanced second-harmonic suppression," *IEEE Microw. Wireless Compon. Lett.*, vol. 23, no. 9, pp. 483-485, Sept. 2013.

[6] X. L. Zhao, L. Gao, X. Y. Zhang, and J. X. Xu, "Novel filtering power divider with wide stopband using discriminating coupling," *IEEE Microw. Wireless Compon. Lett.*, vol. 26, no. 8, pp. 580-582, Aug. 2016.

[7] W. M. Chau, K. W. Hsu, and W. H. Tu, "Wide-stopband Wilkinson power divider with bandpass response," *Electron. Lett.*, vol. 50, no. 1, pp. 39-40, Jan. 2, 2014.

[8] M. Hayati and S. Roshani, "A novel Wilkinson power divider using open stubs for the suppression of harmonics," *ACES J.*, vol. 28, no. 6, pp. 501-506, June 2013.

[9] K. Song, Y. Zhu, Q. Duan, M. Fan, and Y. Fan, "Extremely compact ultra-wideband power divider using hybrid slotline/microstrip-line transition," *Electron. Lett.*, vol. 51, no. 24, pp. 2014-2015, Nov. 19, 2015.

[10] A. Piroutiniya and P. Mohammadi, "The substrate integrated waveguide T-junction power divider with arbitrary power dividing ratio," *ACES J.*, vol. 31, no. 4, pp. 428-433, Apr. 2016.

[11] Y. Deng, J. Wang, and J.-l. Li, "Design of compact wideband filtering power divider with extended isolation and rejection bandwidth," *Electron. Lett.*, vol. 52, no. 16, pp. 1387-1389, Aug. 4, 2016.

[12] Y. Deng, Y. He, and J. Wang. "Design of a compact wideband filtering power divider with improved isolation," *ACES J.*, vol. 31, no. 9, pp. 1079-1083, Sept. 2016.

[13] S. S. Gao, S. Sun, and S. Xiao, "A novel wideband bandpass power divider with harmonic-suppressed ring resonator," *IEEE Microw. Wireless Compon. Lett.*, vol. 23, no. 3, pp. 119-121, Mar. 2013.

[14] Y. Liu, S. Sun, and X. Yu, "Design of a wideband filtering power divider with stub-loaded ring resonator," in *Int. Applied Computational Electromagnetics Society Symp.* (ACES-2017), Suzhou, China, Aug. 2017.

[15] M. A. Maktoomi, M. S. Hashmi, and F. M. Ghannouchi, "Theory and design of a novel wideband DC isolated Wilkinson power divider," *IEEE Microw. Wireless Compon. Lett.*, vol. 26, no. 8, pp. 586-588, Aug. 2016.

[16] B. Zhang and Y. Liu, "Wideband filtering power

divider with high selectivity," *Electron. Lett.*, vol. 51, no. 23, pp. 1950-1952, Nov. 5, 2015.
[17] C. W. Tang and J. T. Chen, "A design of 3-dB wideband microstrip power divider with an ultra-wide isolated frequency band," *IEEE Trans. Microw. Theory Techn.*, vol. 64, no. 6, pp. 1806-1811, June 2016.
[18] Y. Wu, Z. Zhuang, Y. Liu, L. Deng, and Z. Ghassemlooy, "Wideband filtering power divider with ultra-wideband harmonic suppression and isolation," *IEEE Access*, vol. 4, pp. 6876-6882, 2016.
[19] G. Zhang, J. Wang, L. Zhu, and W. Wu, "Dual-band filtering power divider with high selectivity and good isolation," *IEEE Microw. Wireless Compon. Lett.*, vol. 26, no. 10, pp. 774-776, Oct. 2016.
[20] C. Shao, Y. Li, and J. X. Chen, "Compact dual-band microstrip filtering power divider using T-junction structure and quarter-wavelength SIR," *Electron. Lett.*, vol. 53, no. 6, pp. 434-436, Mar. 16, 2017.
[21] K. Xu, J. Shi, L. Lin, and J. X. Chen, "A balanced-to-unbalanced microstrip power divider with filtering function," *IEEE Trans. Microw. Theory Techn.*, vol. 63, no. 8, pp. 2561-2569, Aug. 2015.
[22] X. Gao, W. Feng, W. Che, and Q. Xue, "Wideband balanced-to-unbalanced filtering power dividers based on coupled lines," *IEEE Trans. Microw. Theory Techn.*, vol. 65, no. 1, pp. 86-95, Jan. 2017.
[23] P. H. Deng and Y. T. Chen, "New Wilkinson power dividers and their integration applications to four-way and filtering dividers," *IEEE Trans. Compon., Packag. Manuf. Technol.*, vol. 4, no. 11, pp. 1828-1837, Nov. 2014.
[24] F. J. Chen, L. S. Wu, L. F. Qiu, and J. F. Mao, "A four-way microstrip filtering power divider with frequency-dependent couplings," *IEEE Trans. Microw. Theory Techn.*, vol. 63, no. 10, pp. 3494-3504, Oct. 2015.
[25] H. Zhu, A. M. Abbosh, and L. Guo, "Wideband four-way filtering power divider with sharp selectivity and wide stopband using looped coupled-line structures," *IEEE Microw. Wireless Compon. Lett.*, vol. 26, no. 6, pp. 413-415, June 2016.

Xi Yu received the B.Eng. degree in Electronic Engineering from The University of Electronic Science and Technology of China (UESTC), Chengdu, China in 2013, and he is currently working towards the Ph.D. degree in UESTC. His research interests include the synthesis and design of microwave filters and antennas, multi-functional integrated devices, as well as the wireless power transfer system.

Sheng Sun received the B.Eng. degree in Information Engineering from the Xi'an Jiaotong University, China, in 2001, and the Ph.D. degree in Electrical and Electronic Engineering from the Nanyang Technological University (NTU), Singapore, in 2006.

Sun was with the Institute of Microelectronics in Singapore (2005-2006), and with the NTU (2006-2008) as a Postdoc Research Fellow. He was also a Humboldt Research Fellow with the Institute of Microwave Techniques at the University of Ulm in Germany (2008-2010), and a Research Assistant Professor at The University of Hong Kong (2010-2015). Since 2015, he has been the Young Thousand Talents Plan Professor at The University of Electronic Science and Technology of China (UESTC). His research interests include electromagnetic theory and computational mathematics, multi-physics, numerical modeling of planar circuits and antennas, microwave passive and active devices, as well as the microwave and millimeter-wave communication systems. He has coauthored one book and two book chapters, over 140 journal and conference publications. He was a co-recipient of the several Best Paper Awards at international conferences. He received the Outstanding Reviewer Award from IEEE Microwave and Wireless Components Letters in 2010. He was the recipient of the General Assembly Young Scientists Award from the International Union of Radio Science (URSI) in 2014. He also received the Hildegard Maier Research Fellowship of the Alexander Von Humboldt Foundation (Germany), in 2008, and the recipient of the ISAP Young Scientist Travel Grant (Japan), in 2004. Sun was an Associate Editor of the IEICE Transactions on Electronics (2010-2014), a Guest Associate Editor of the ACES Journal (2017). He is currently a Member of Editor Board of International Journal of RFMiCAE and Journal of Communications and Information Networks, as well as an Associate Editor of IEEE Microwave and Wireless Components Letters.

Yun Liu received the B.Eng. degree in Electronic Engineering from The University of Electronic Science and Technology of China (UESTC), Chengdu, China in 2015, and she is currently pursuing the Ph.D. degree in UESTC. Her research interests include microwave power dividers, planar multifunctional microwave passive components, as well as patch antennas.

Study of Passive Chipless IR-UWB Indoor Positioning Based on Time-of-Arrival and Band-Notch

Jian Liu

School of Communication and Information Engineering
Xi'an University of Science and Technology, Xi'an, 710054, China
Liujian02@xust.edu.cn

Abstract ─ In the paper, a passive and chipless IR-UWB indoor positioning system is proposed that follows the criteria of spectral and temporal joint identification. In the scenario of a 2D positioning, the system is coordinated by three anchors; a node can then be positioned by recognizing the pulse's time-of-arrival (TOA) and the pulse's band-notch in its backscattered spectrum. The model of the positioning system is established and the numerical analysis is committed in terms of a conceived positioning example. Results validate the system that the positioning is accurate, and the accuracy can be further improved by calibrating the value of TOA through the time offset made by the pulses backscattered by the anchor with and without band-notch, respectively.

Index Terms ─ Band-notch, indoor positioning, IR-UWB, TOA.

I. INTRODUCTION

Indoor positioning is quite necessary in many fields such as the healthcare where tracking human body and limbs movement is required [1]. Compared with outdoor, the indoor positioning is very difficult because the channel is more easily influenced by the phenomenon of reflection or dispersion. In the recent years, people began to seek solution in the field of transient electromagnetism, considering of the transient field can render radio signal be more constraint in time domain. Research has demonstrated that short pulses can be really effective in avoiding channel deterioration and system noise, so as to make positioning be accurate at least for the system where positioning is mainly depending on the value of time-of-arrival (TOA).

One specification for the application of transient electromagnetic field is the ultra-wideband (UWB) that was released in 2002 by the Federal Communications Commission (FCC) for the unlicensed frequency band (from 3.1 GHz to 10.6 GHz) used for the short range communication. Nowadays, the UWB has increasingly become a substitution for the traditional narrow band circumstance in the area of radio frequency identification (RFID). The UWB enabled RFID (UWB-RFID) is recognized as a more advanced architecture used for the identification or the localization of an object in a very short range area [2-4].

In theory, the ultra-wideband (UWB) refers to the radio with a bandwidth exceeding the lesser of 500 MHz or 20% of the arithmetic center frequency. The UWB signal in time domain is therefore a very constraint pulse shortened in nanosecond, usually known as the Impulse Radio Ultra-Wideband (IR-UWB) [5]. It is the shortness of the pulse that can readily render IR-UWB positioning be accurate, and the accuracy can be improved further by employing shorter, more precise pulse with higher level of integrity. It's sure a good solution in this regards, but it also brings about a lot of critical technical problems, for example, the shorter pulses have to make the realization of clock jitter or the retrieving of critical parameters from pulse's figure become quite difficult [6].

Nevertheless, there are still some efforts had been dedicated to this area [7-10]. For example in [11], a uni-planar monopole antenna is proposed that is made by a passive and chipless IR-UWB tag, committing to positioning based on the parameters contained in the antenna modem and controlled by the length of meandrous coplanar waveguide plane (CWP) loaded, respectively, by impedance match circuit, open circuit and short circuit. The location and the polarity of the late-time pulse correlated by the pulse received by the object for positioning (node) in early time become the rule governing the whole procedure of positioning.

Although the example comes forth a very simple and easy implementation for positioning in accordance with the modem of antenna mode (In the theory of transient field, the wave backscattered by antenna is composed of two modes, one is called the structural mode, another is called the antenna mode), it has no way to offer clues to make anchor be clearly identified, although in some circumstance, this parameter or value are indispensable [12]. So, in this paper, we design and develop a positioning system based on the IR-UWB architecture that is novel enough in the aspect of the recognition of pulse and the corresponding anchor solely depending on the feature of anchor's band-notch. We

Submitted On: September 18, 2017
Accepted On: April 21, 2018

focus on the 2D positioning; therefore the positioning system is coordinated by three anchors that are the sort of passive and chipless IR-UWB tag decorated with different band-notches. A node can be positioned and scaled on account of them through retrieving and analyzing the feature of pulse both in the temporal (TOA) and in the spectral domain (band-notch).

The reminders of the paper are: the IR-UWB positioning system for the 2D application is firstly introduced in Section II with interpretation of the exact algorithm and criteria of positioning. Secondly, the topology of anchor and node are illustrated with the details of the geometric dimensions shown in Section III. Thirdly, the procedure, analyzing, calibrating are described by a complete analysis of each result in Section IV. Finally, the conclusions are made in Section V.

II. THE ARCHITECTURE OF PASSIVE AND CHIPLESS IR-UWB POSITIONING SYSTEM

The coordinate of the proposed positioning system in terms of the 2D scenario is the Cartesian where a node can be scaled and benchmarked by three anchors that are distributed orthogonally each other, as shown in Fig. 1. According to the theory of IR-UWB, all the anchors are the sort of passive and chipless tags, functioning to make impinging pulse backscatter to node. The node is, however, an object for positioning that is an active and chip-have UWB-RFID tag for instead. In a specific positioning, the node works to transmitting a UWB pulse to anchors, and then receives the backscattered copy of them. As a result, the exact position of the node can be determined by retrieving and analyzing the TOA and the band-notch feature borne in the backscattered structural mode.

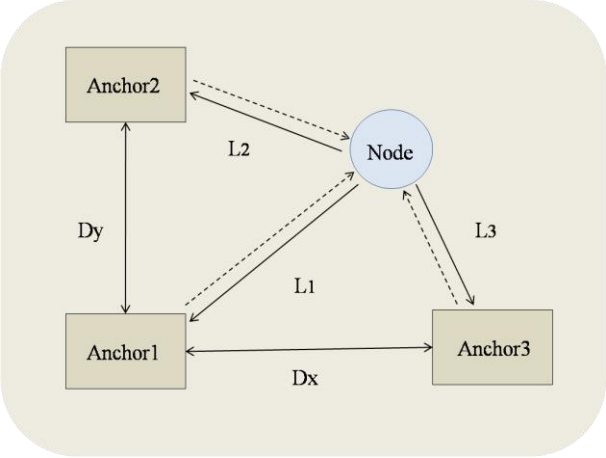

Fig. 1. The model of the passive and chipless IR-UWB positioning system.

A. Positioning model

The Cartesian is coordinated by three anchors known as anchor1, anchor2 and anchor3, as shown in Fig. 1. The horizontal line linking the anchor1 and the anchor3 forms the *x* axial scaled by *Dx*, denoting the distance between the anchor1 and the anchor3. The vertical line linking the anchor1 and the anchor2 forms the *y* axial scaled by *Dy* that denotes the distance between the anchor1 and the anchor2. If one node is assumed to be placed at (*x*, *y*), L_1, L_2 and L_3 are used to represent the distances from the node to the anchor1, the anchor2 and the anchor3, respectively.

B. Positioning algorithm

The positioning algorithm is configured in terms of the system that is based on the temporal and spectral joint identification. Referring to the model illustrated in Fig. 1, the coordinate (*x*, *y*) of a node can be determined by:

$$\begin{cases} x = \left[D_x^2 - \left(L_3^2 - L_1^2 \right) \right] \Big/ 2D_x \\ y = \left[D_y^2 - \left(L_2^2 - L_1^2 \right) \right] \Big/ 2D_y \end{cases}, \tag{1}$$

in which, $L_1=t_1/2c$, $L_2=t_2/2c$, $L_3=t_3/2c$; t_1, t_2 , t_3 are the TOA at node after being backscattered by the anchor1, the anchor2 and the anchor3, respectively; *c* is the velocity of pulse travelling in free space.

It is evidence that TOA in the algorithm isn't sufficient to issue a positioning alone. On the contrary, it is quite necessary to know the pulse and the corresponding anchor that the pulse is backscattered. So, there shall be an assumption hindered in the algorithm that anchor can be virtually identified by the band-notch of the pulse in the backscattered spectrum. The algorithm plus the hindered assumption will determine the configurations of both the node and the anchor simultaneously.

III. THE CONFIGURATION OF ANCHOR AND NODE

A. Node topology

Node is the object-for-positioning. Under the architecture of IR-UWB, the node shall be facilitate to transmitting and receiving UWB signals, and then give them an analysis. So, the topology of the node shall be constructed by two parts: one is the antenna covering UWB band, another is the digital processing unit (IC chipset) used for launching the algorithm of positioning. To make the node simple in structure, the UWB antenna is configured specifically by a planar metallic patch decorated by symmetric double concaved angles, as shown in Fig. 2 (a). The positioning unit is connected to the antenna through a microstrip line. The dimension of the topology of the node are listed in Table1 that make the node satisfy for the specifications of UWB with frequency range from 3.1 GHz to 10.6 GHz [13].

Table 1: Dimension of anchor and node (Unit:mm)

Symbol	Value	Definition
Wp	18.6	Width of rectangular patch
Hp	15.5	Height of rectangular patch
Hc	1.5	Height of staircase 1
Hd	1.5	Height of staircase 2
Wc	1.5	Width of staircase 1
Wd	1.5	Width of staircase 2
Hg	10.4	Height of grounding plane
Hf	11.0	Height of microstrip line

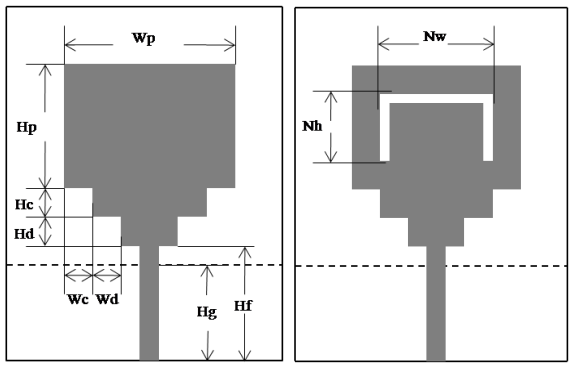

Fig. 2. The topology of node (a) and anchor (b).

B. Anchor topology

Anchors fabricate the coordinate of the positioning system. Under the architecture of IR-UWB, the anchors function to make positioning pulse be backscattered while leaves only the structural mode there. So, the topology of the anchor shall be constructed by a passive and chipless UWB tag equipped with an UWB antenna and an impedance match load (usually 50 Ohm resistance). In addition, a U-slot is etched on the facet of the antenna on each anchor [14], as shown in Fig. 2 (b). Study has shown that the U-slot can give anchor a band-notch in the spectrum of the backscattered structural mode [15-17]. In terms of 2D positioning, three anchors are need, each is borne with different band-notch. The lengths of U-slot attached to each anchor are listed in Table 2.

Table 2: Length of U-slot on anchor (Unit:mm)

Symbol	Anchor1	Anchor2	Anchor3
Nw	12.0	10.0	9.0
Nh	8.0	7.0	6.5

IV. POSITIONING PROCEDURE, ANAYZING AND CALIBRATION

The positioning signal is set by a Gaussian pulse as shown in Fig. 3. Since the anchors are all impedance match, the pulses backscattered by anchors are only the structural modes, as shown in Fig. 4.

Figure 5 (b) shows the spectrum of the structural modes backscattered by anchors with different U-slots. Compared with the pulse that is presumed to be backscattered by the anchor with the same size, without band-notch as shown in Fig. 5 (a), the anchor1 can be determined to have a band-notch at 5.26 GHz, the anchor2 has band-notch at 5.94 GHz, and the anchor3 has a band-notch at 6.49 GHz.

A. Positioning procedure

The positioning procedure is illustrated, assuming a node is placed at (60, 80) mm. When the pulse shown in Fig. 3 is transmitted by the node, it will impinge to the anchor1 and be backscattered. The pulse reaching at the node is the pulse as shown in Fig. 6. According to the algorithm, the TOA of the pulse can be determined by the time of the peak of the pulse with correspondence to the time interval. The peak of the pulse from the anchor1 is at the time of 0.8452ns. Compared with the peak of the pulse transmitted by the node at the time of 0.4405ns, the time interval in between is 0.4047ns, representing that the distance between the anchor1 and the node is 101.41mm (L_1). Likewise, Fig. 7 shows the pulse backscattered by the anchor2 and arrived at the node. The peak of the pulse from the anchor2 is at the time of 0.7214ns. Compared with the peak of the pulse transmitted by the node at the time of 0.4405ns, the time interval is 0.2809ns, indicating that the distance between the anchor2 and the node is 64.27mm (L_2). Similarly, Fig. 8 shows the pulse backscattered by the anchor3 and arrived at the node. The peak of the pulse from anchor3 is at the time of 0.8066ns. Compared with the peak of the pulse transmitted by the node at the time of 0.4405ns, the time interval is 0.3661ns, denoting the distance between the anchor3 and the node is 89.93mm (L_3).

Using the Equation (1), the position of the node can be determined by the coordinate of (60.94, 80.79) mm. The result shows that the deviation of the positioning in the horizontal direction is about 0.94mm; but in the vertical direction, the deviation is 0.79mm.

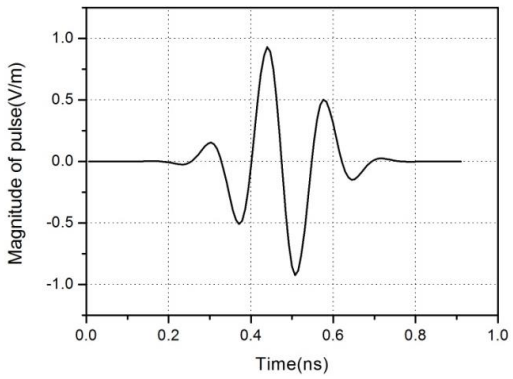

Fig. 3. Ultra-wideband Gaussian pulse used for positioning.

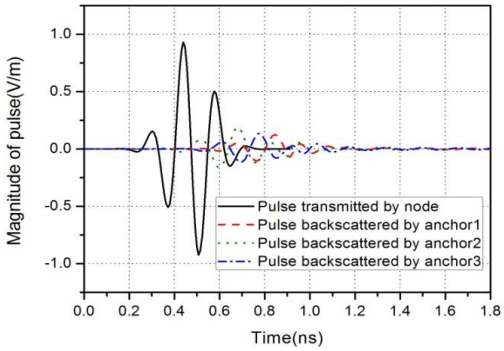

Fig. 4. Pulses (structural mode) backscattered by anchors and arrived at node.

B. Positioning calibration

Since the introduction of U-slot into anchor's facet, it is certainty that the pulse backscattered there will be distorted somewhat compared with that from the anchor not be equipped with U-slot. Through numerical analysis, we can show that the distortion of the pulse backscattered by the anchor1 is as illustrated in Fig. 9. The time offset at the peak of the pulse is 0.00349ns. This offset can be used to calibrate the exactness of the TOA in terms of the pulse backscattered by the anchor1. The TOA after being calibrated is turned to 0.8417ns; and accordingly, the distance (L_1) is revised to 100.36mm [18].

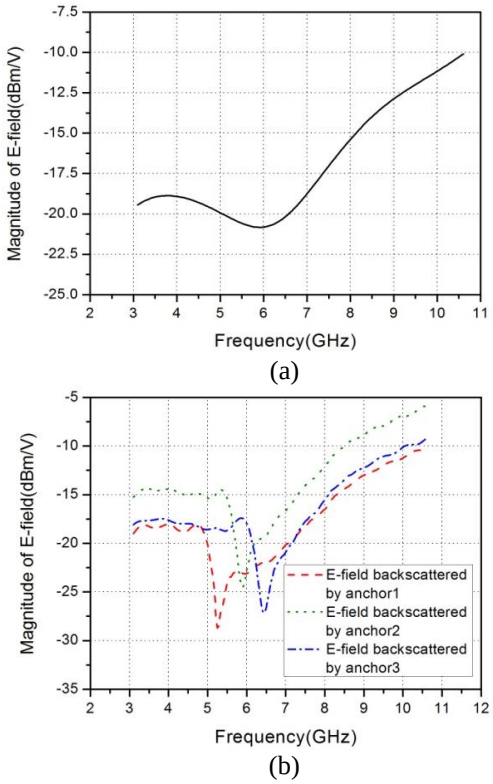

Fig. 5. Spectrum of pulses: (a) for anchor without band-notch; (b) for three anchors with different band notches.

In Fig. 10, the time offset caused by the anchor2 is 0.00247ns. The TOA after being calibrated is changed to 0.7189ns; and accordingly, the distance (L_2) is revised to 63.53mm.

Similarly, in Fig. 11, the time offset caused by the anchor3 is 0.00002ns, the TOA after being calibrated is to be 0.80662ns; and accordingly, the distance (L_3) can be revised to 89.84mm.

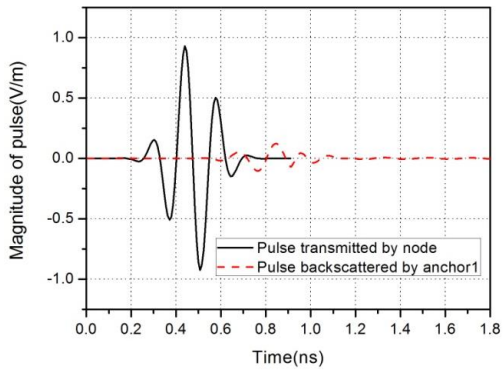

Fig. 6. Pulse backscattered by anchor1 compared with that transmitted by node.

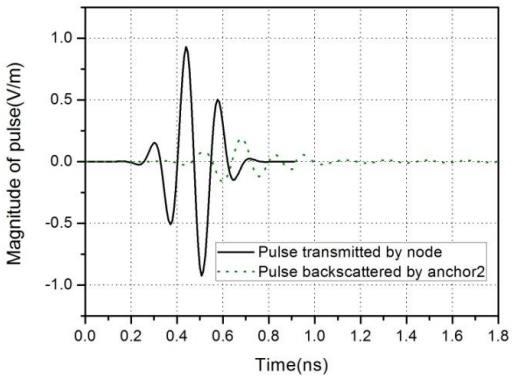

Fig. 7. Pulse backscattered by anchor2 compared with that transmitted by node.

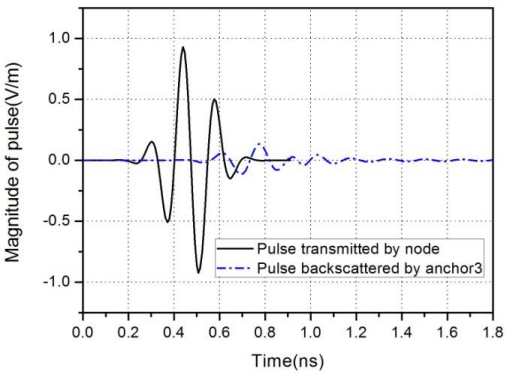

Fig. 8. Pulse backscattered by anchor3 compared with that transmitted by node.

Using the Equation (1) again, the coordinate of the node after calibration by time offset can be revised to (60.00542, 80.18034) mm. It is obviousness that, through the calibration, the deviation of the node in the horizontal direction is reduced to 0.00542mm, and the deviation in the vertical direction can be reduced to 0.18034mm simultaneously.

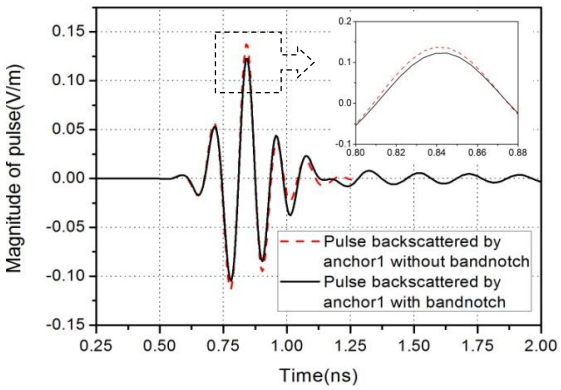

Fig. 9. Pulse backscattered by anchor1compared with that without band notch.

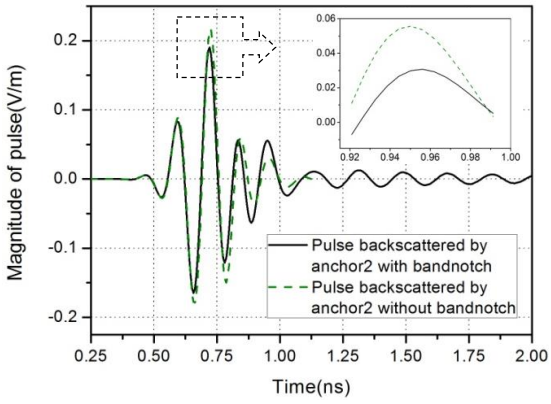

Fig. 10. Pulse backscattered by anchor2 compared with that without band notch.

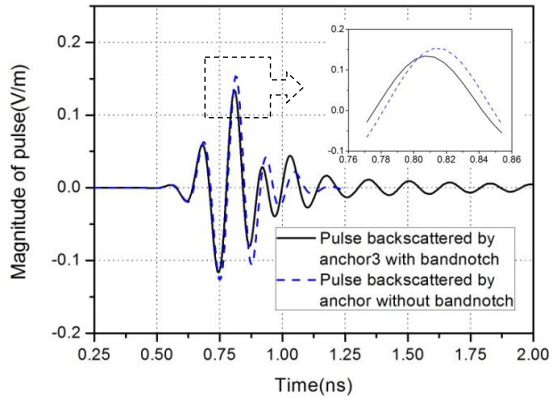

Fig. 11. Pulse backscattered by anchor3 compared with that without band notch.

V. CONCLUSION

According to the study in the paper, it can be concluded that compared with the narrow band circumstance, the IR-UWB is more effective in giving an accurate positioning, and the accuracy can be further improved by employing shorter, more precise pulses with higher level integrity. It is also concluded that the passive and chipless IR-UWB positioning is a simple and cost-efficient system. The positioning under this architecture can be implemented by recognizing not only the TOA of pulse but also the band-notch for anchor scrutinizing. Moreover, it can be concluded that the positioning deviation can be compensated by calibrating TOA with the time offset made by the pulses backscattered by the anchor with and without band-notch, respectively.

REFERENCES

[1] R. Bharadwaj, S. Swaisaenyakorn, C. G. Parini, et al., "Impulse radio-ultra wideband communications for localization and tracking of human body and limbs movement for healthcare applications," *IEEE Transactions on Antennas & Propagation*, vol. 65, no. 12, pp. 7298-7309, Dec. 2017.

[2] A. Alarifi, A. Al-Salman, M. Alsaleh, et al., "Ultra wideband indoor positioning technologies: Analysis and recent advances," *Sensors*, vol. 16, no. 5, article 707, 2016.

[3] S. Gezici, Z. Tian, G. B. Giannakis, H. Kobayashi, A. F. Molisch, H. V. Poor, and Z. Sahinoglu, "Positioning via ultra-wideband radios: a look at positioning aspects for future sensor networks," *IEEE Signal Process. Mag.*, vol. 22, no. 4, pp. 70-84, July 2005.

[4] D. Dardari, et al., "Ultrawide bandwidth RFID: The next generation?," *Proc. IEEE*, vol. 98, no. 9, pp. 1570-1582, Sep. 2010.

[5] R. J. Fontana, "Recent system applications of short-pulse ultra-wideband (UWB) technology," *IEEE Trans. Microw. Theory Tech.*, vol. 52, no. 9, pp. 2087-2104, Sep. 2004.

[6] M. S. Svalastog, "Indoor Positioning-Technologies, Services and Architectures," Cand. Scient. Thesis, University of Oslo, Oslo, Norway, 2007.

[7] C. C. Cruz, J. R. Costa, and C. A. Fernandes, "Hybrid UHF/UWB antenna for passive indoor identification and positioning systems," *IEEE Trans. Antennas Propag.*, vol. 61, no. 1, pp. 354-361, Sep. 2013.

[8] A. Chehri, P. Fortier, and P. M. Tardif, "UWB-based sensor networks for positioning in mining environments," *Ad Hoc Networks*., vol. 7, no. 5, pp. 987-1000, 2009.

[9] N. Decarli, F. Guidi, and D. Dardari, "Passive UWB RFID for tag positioning: architectures and design," *IEEE Sensors J.*, vol. 16, no. 5, pp. 1385-1397, Mar. 2016.

[10] L. Taponecco, A. A. D'Amico, and U. Mengali, "Joint TOA and AOA estimation for UWB positioning applications," *IEEE Trans. Wireless Commun.*, vol. 10, no. 7, pp. 2207-2217, July 2011.
[11] S. Hu, Y. Zhou, C. L. Law, and W. Dou, "Study of a uniplanar monopole antenna for passive chipless UWB-RFID positioning system," *IEEE Trans. Antennas Propag.*, vol. 58, no. 2, pp. 271-278, Feb. 2010.
[12] C. A. Balanis, *Antenna Theory: Analysis and Design*. 3rd edition, Wiley–Interscience, Hoboken, NJ, 2005.
[13] J. Liu and B. P. Li, "Palladium decorated SWCNTs sensor for detecting methane at room temperature based on UWB-RFID," *Applied Computational Electromagnetics Society Journal*, vol. 31, no. 8, pp. 989-996, Aug. 2016.
[14] A. Ramos, A. Lazaro, D. Girbau, et al., "Time-domain measurement of time-coded UWB chipless RFID tags," *Progress in Electromagnetics Research*, vol. 116, no. 8, pp. 313-331, 2011.
[15] Y. J. Cho, K. H. Kim, D. H. Choi, S. S. Lee, and S.-O. Park, "A miniature UWB planar monopole antenna with 5-GHz band-rejection filter and the time-domain characteristics," *IEEE Trans. Antennas Propag.*, vol. 54, no. 5, pp. 1453-1460, May 2006.
[16] K. Chung, J. Kim, and J. Choi, "Wideband microstrip-fed monopole antenna having frequency band-notch function," *IEEE Microw. Wireless Comp. Lett.*, vol. 15, no. 11, pp. 766-768, Nov. 2005.
[17] B. Tong, X. Wu, L. Xiao, et al., "Dual band-notched ultra-wideband antenna based on U-shaped slit and split ring slot," *Asia-Pacific Microwave Conference, IEEE*, pp. 1-3, 2015.
[18] CST Microwave Studio, ver. 2009, Computer Simulation Technology, Framingham, MA, 2009.

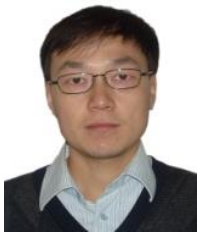

Jian Liu was born in Xi'an, Shaanxi, in 1967. He received the B.S. and M.S. degrees in the Electromagnetic Field Engineering from Xidian University, Xi'an, in 1990 and 1996. From 1990 to 1996, he was an Assistant Professor with the Communication Engineering Department, Xi'an Mining Institute. From 1997 to 1998, he was an Electrical Engineer with RF & Wireless Laboratory, ZTE. From 1998 to 2000, he was a Lecturer with the Communication Engineering Department, Xi'an Science and Technology College. From 2000 to 2003, he was the Senior Scientist and Project Leader with Philips Research Laboratory. From 2004 to 2010, he was Department head of PTCC, Panasonic Research and Development Cooperation Limited. Since 2010, he has been a Lecturer with the School of Communication and Information Engineering, Xi'an University of Science and Technology. He is the author of 1 text book, more than 10 articles, and holds 7 patents. His research interests include Computational Electromagnetism, Antenna, RF & Microwave Communication and Sensors.

A Broadband CPW Fractal Antenna for RF Energy Harvesting

Xue Bai, Jia-wei Zhang, Lei-jun Xu*, and Bu-hui Zhao

School of Electrical and Information Engineering
Jiangsu University, Zhenjiang, 212013, China
*xlking@ujs.edu.cn

Abstract ─ A novel broadband CPW-fed 2-iteration fractal antenna based on the circular patch and the equilateral triangle slot is designed for RF energy harvesting. The simulated and measured results show that the proposed antenna offers an impedance bandwidth of 162% from 0.88 to 8.45 GHz and a peak gain of 8.7 dBi. Afterwards, the single-stage voltage multiplier rectifier with a T shape LC matching network to reduce the reflection losses is used to realize RF-to-DC conversion in energy harvesting; here, it is also integrated with the fractal antenna to form the rectenna. Accumulating RF power from 2G (GSM), 3G (the third generation), 4G-LTE and WLAN frequency-bands, the measured results across an optimized load resistor of 4.7-kΩ show that the maximum rectenna efficiency is 51.8%, 46.1% and 45.08% at the center frequency of 2.4 GHz, 2.1 GHz and 1.9 GHz, respectively. Additionally, the measured peak conversion efficiency of the system is 24.03% at 2.4 GHz.

Index Terms ─ Broadband, energy harvesting, fractal antenna, rectenna.

I. INTRODUCTION

Recently, the ambient RF power density is growing since there is an increasingly frequency bands are being occupied such as WLAN, GSM, DCS, 3G and 4G LTE. The idea of using RF energy harvesting technique to convert these ambient RF energy into usable electrical energy to power low-power electronic devices has become an upsurge of research [1-3]. In general, the system of this technique is mainly composed of the rectifying antenna (rectenna). For weak ambient RF power density, the designed rectenna requires high gain to improve the input power and also need wide impedance bandwidth to accumulate more RF power from different frequency bands, such as Yagi antenna array [4] and six-band dual circular polarization (CP) log-periodic rectenna [5], respectively. However, the mentioned antennas cannot be satisfied because of their large dimension and complex structure. On the other hand, other various designs have been investigated, such as the anti-spiral slot resonator [6], differential structure [7], circularly polarized [8, 9] and so on. Analogously, most of these proposed antennas only accumulate RF power within narrow frequency-bands, which greatly restricts the efficiency of energy harvesting. For this, antennas with multiband, high gain and compact structure are greatly preferred.

Since the self-similarity and spatial filling can be converted into multi-frequency characteristics and dimension reduction in antenna design, the fractal technique can be proposed to be one of the potential candidate for increasing antenna bandwidth. Numerous fractal techniques have been investigated, for instance, elliptical fractal shapes [10] and Sierpinski [11] have been discussed for bandwidth enhancement. In [10], a novel printed elliptical nested fractal antenna operates at 910 MHz, 2.4 GHz, 3.2 GHz, 3.8 GHz and additional 5 GHz band, the ground plane located on both sides of the antenna feeding line adopts Hilbert fractal structure, which greatly increases the impedance bandwidth. In [12], a broadband bent triangular omnidirectional antenna with a bandwidth from 850 MHz to 1.94 GHz is presented. Due to the advantage of receiving both horizontal and vertical polarized waves, a peak rectenna efficiency of 60% and 17% is obtained over a resistor of 500 Ω at 980 MHz and 1800 MHz, respectively. Whereas, the input power is higher than the low-power density ambient too much during its measurement process.

In this paper, a novel CPW-fed broadband fractal antenna is presented for RF energy harvesting. By using the novel fractal technique with a 2-iteration circular-based triangle slot, the antenna designed for receiving 2G (GSM), 3G (the third generation), 4G-LTE and WLAN RF signals can offer a relative bandwidth of 162% (0.88-8.45 GHz). Afterwards, the rectifier with a T shape LC matching network is proposed for making up a rectenna. By actual manufacturing and debugging, the measurement for rectenna efficiency and system efficiency are performed. The results have verified that our proposed rectenna not only has advantages over the bandwidth and dimension, but also the RF-to-DC conversion efficiency, which make it suitable for multiband RF energy harvesting application.

Submitted On: September 23, 2017
Accepted On: March 31, 2018

II. FRACTAL ANTENNA DESIGN

The structure of the proposed fractal antenna with a 2-iteration circular-based triangle slot is depicted in Fig. 1 (a). It can be seen that top of the antenna substrate covers radiation metal patch, while the bottom does not. The ground plane located on both sides of the feeder forms the structure of coplanar waveguide (CPW) feed, which decreases the losses of signal transmission. According to [13], antennas with CPW-fed are easy to be fabricated and integrated with circuits, especially the impendence bandwidth can be extended.

The 0-iteration fractal antenna based on the CPW-fed planar circular patch is depicted in Fig. 1 (b), which can motivate a variety of resonant modes. R_1 is the radius of circular patch and can be explained by the equation:

$$R_1 = \frac{1.841c}{2\pi f\sqrt{\varepsilon_r}}, \tag{1}$$

where ε_r is the relative permittivity of the substrate, f represents the center frequency of the designed antenna and c is the speed of light in vacuum. Meanwhile, Fig. 1 (c) shows the 1-iteration fractal antenna, it can be seen that an equilateral triangle is slotted on the circular patch. The 2-iteration fractal antenna is based on the 1-iteration structure, as described in Fig. 1 (a), an inner circle inserts the slotted equilateral triangle, simultaneously, a smaller equilateral triangle horizontally symmetrical to the previous is slotted on the inner circle. At last, it is worth noting that both of the triangles and the circles have the same center point.

Here, the scaling factor K (K>1) is introduced to describe the mathematical relationship of the proposed fractal structure. In general, the size of slotted equilateral triangles and inner circle are directly determined by the scaling factor K, the larger the value of K, the smaller the fractal slot is. Assuming the radius of the inner circle is R_i, the distance from the apex to the center of slotted triangle and the side length of slotted triangle is L_i and S_i, respectively. These mentioned parameters are summarized in the following equations: (i is the iteration of the fractal antenna):

$$R_i = \frac{R_1}{2^{i-1}\times K} + 2 \quad (i>1), \tag{2}$$

$$L_i = \frac{R_1}{2^{i-1}\times K} \quad (i>1), \tag{3}$$

$$S_i = \sqrt{3}\times L_i \quad (i>1). \tag{4}$$

The designed 2-iteration fractal antenna is fabricated on a substrate with a relative permittivity of 4.4 and a thickness of 1.6 mm. The antenna has a total size of 100×100 mm^2. The width and length of the feeder is W_k and L_k, respectively. The length and width of the coplanar waveguide is M and B, respectively. Here, an optimized scaling factor K is 1.5 and the optimized antenna parameters are illustrated in Fig. 1 (a).

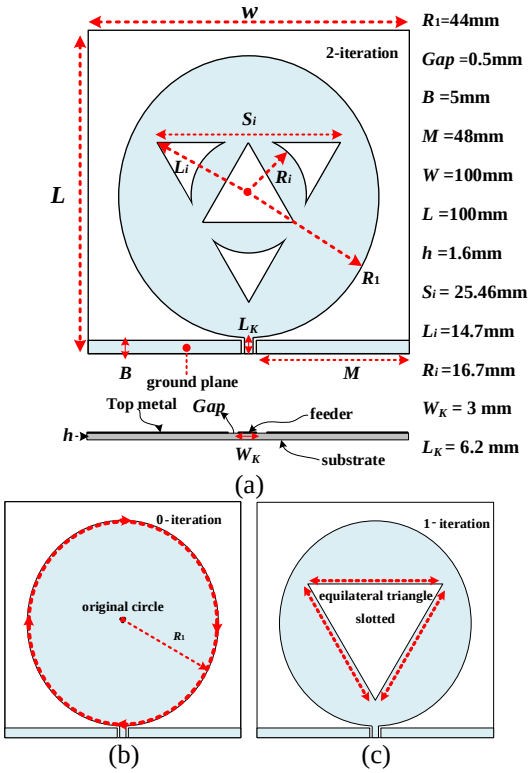

Fig. 1. Geometric structure and size of the antenna: (a) 2-iteration, (b) 0-iteration, and (c) 1-iteration.

III. PERFORMANCE ANALYSIS

For the designed antenna, the novel fractal technique is used to expand the impedance bandwidth. Then, the antenna is modeled and optimized by means of the HFSS software. To sufficiently investigate the impedance matching performance of the proposed fractal antenna with 2-iteration structure, here, the key parameters are selected and investigated as followings: the iteration of the fractal, the length of *Gap*, and the substrate thickness h. All these parameter simulations are based on the premise that the substrate thickness h is 0.6 mm and the value of scaling factor K is 1.5.

The return loss of the fractal antenna with variation of iterations is depicted in Fig. 2. It can be seen that the impedance matching performance of the 2-iteration fractal structure is better than the 1-iteration fractal structure with the frequency-bands roughly from 0.8 to 1.4 GHz and 1.85 to 6 GHz. Also, the same relationship that the 1-iteration fractal structure is better than the 0-iteration fractal structure. This is because employing the fractal technique, the current path on radiation metal patch is increased, which greatly expands the antenna impedance bandwidth. Thus, the 2-iteration fractal antenna is more suitable for RF energy harvesting.

Then, the length of *Gap* is varied and the effect on the impedance matching is investigated as depicted in Fig. 3. It is found that the 2-iteration fractal antenna

with good impedance matching can be implemented when *Gap* is greater than 0.3 mm. When the frequency is below 3 GHz, the antenna impedance matching becomes better along with the increase of the length of *Gap*, which can be accounted for the reason that antenna input impedance is affected by the variation of waveguide parameters. On the other hand, to reduce the reflection losses and parasitic effects caused by electromagnetic waves when propagating in coplanar waveguide, the length of *Gap* should not be too large. Parasitic effects also arouse high order harmonics to interfere with the antenna radiation performance. Hence, the length of *Gap* is more suitable for 0.5 mm.

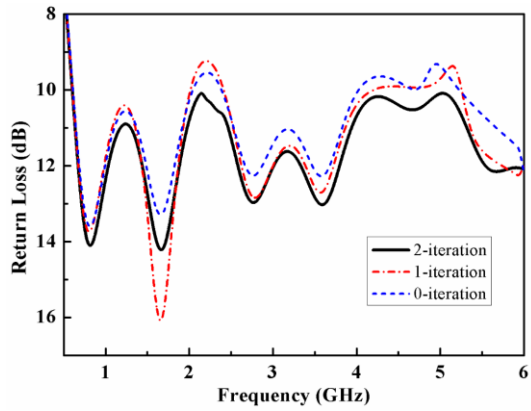

Fig. 2. Effects of fractal iterations on the return loss.

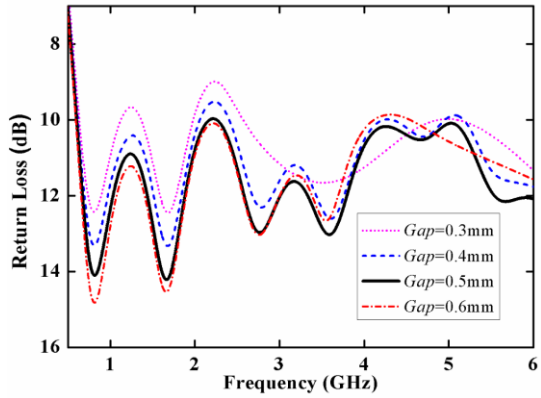

Fig. 3. Effects of the length of *Gap* on the return loss.

Figure 4 depicts the parameter effects on the impedance matching of the proposed fractal antenna with variation of the substrate thickness *h*. When *h* is selected 0.6 mm, the proposed fractal antenna has achieved a broad impedance bandwidth, while, keep on increasing the value of *h*, the impedance matching performance becomes better. This can be explained by some reasons, one is related to the empirical formula:

$$VSWR < 2 : BW(MHz) = 5.04 f^2(GHz) h(mm), \quad (5)$$

where it demonstrates the relationship between the thickness of substrate and the antenna bandwidth. In addition, the other reason can be explicated by the antenna cavity model calculation that antenna input impedance is determined by the thickness of substrate. Meanwhile, to restrain surface wave and improve the antenna radiation efficiency, the substrate thickness *h* should not too large. Thus, the parameter *h* = 1.6 mm is more suitable for antenna fabrication.

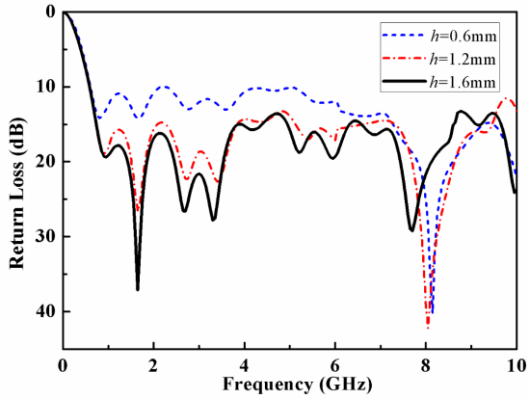

Fig. 4. Effects of substrate thickness *h* on the return loss.

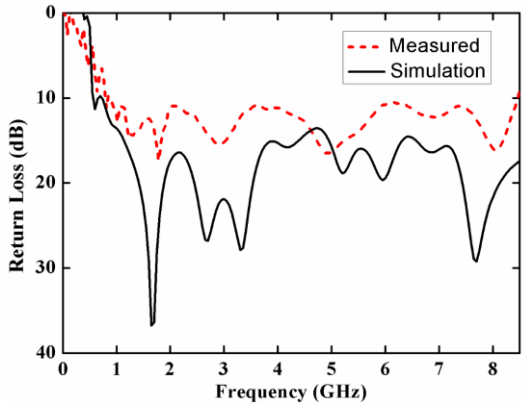

Fig. 5. The simulated and measured return loss.

Figure 5 depicts the simulated and measured impedance bandwidth of the designed fractal antenna. It can be seen that the measured return loss is more than 10 dB within the bandwidth from 0.88 to 8.45 GHz (the relative bandwidth is 162%), which shows a good impedance matching. Different from the ideal metal conductor in simulation, there may exist certain error partially due to the connector welding in actual fabrication, which directly degrades the performance of antenna impedance bandwidth. In general, the fabricated antenna meets the requirement for multiband RF energy harvesting. Figure 6 shows the gain of the proposed antenna varied with the frequency. We can find that the

maximum gain of the antenna is 8.7 dBi.

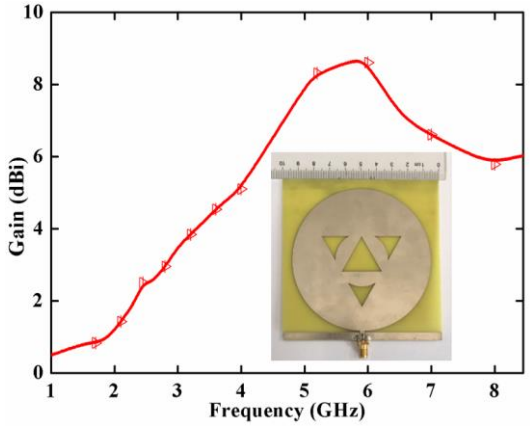

Fig. 6. The gain of the proposed fractal antenna.

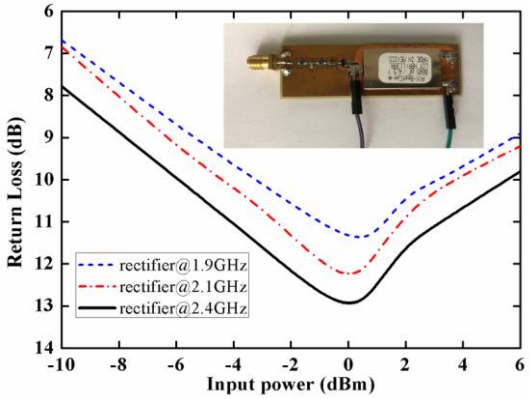

Fig. 7. Measured return loss versus input power of the rectifier at different frequency bands.

IV. ANTENNA APPLICATION IN RF ENERGY HARVESTING

The rectifying circuit performs the function of RF-to-DC power conversion, to reduce the power loss, the designed rectifying circuit should only consist of few components, as proposed in [14] the rectifier is directly integrated with the antenna. In this paper, a single-stage voltage multiplier rectifier is proposed and the Schottky HSMS-2852 diode is adopted as the core rectifying component due to its low threshold voltage, high switching frequency and low power consumption. It has been demonstrated in [15] that the number of rectifying diodes is sensitive to the RF-to-DC efficiency. For the low input power, the more voltage multiplier stages, the lower RF-to-DC efficiency can be gained. Whereas, it is the opposite for the high input power. Hence, in case of weak ambient sources, the designed single-stage voltage multiplier rectifier is more suitable for RF energy harvesting. Since the nonlinearity of rectifying diodes, the input impedance of the rectifier varies as a function of frequency and input power level, thus, the broadband matching between the rectifier and the fractal antenna is a huge challenge. By using harmonic-balance and large signal analysis of ADS software, here, an optimized T shape LC matching network is employed to decrease the power reflection. Final topology of the rectifier is shown in Fig. 7 with a fabricated example. The substrate is FR4, with a relative permittivity of 4.4 and a thickness of 1.6 mm. To convert the accumulated RF power from 2G (GSM), 3G (the third generation), 4G-LTE and WLAN bands, the main center frequency for measurement is selected as 1.9 GHz, 2.1 GHz and 2.4 GHz, respectively. Figure 7 depicts the return loss of the proposed rectifier versus input power levels at three main frequency bands. It is found that the rectifier is well matched for input power levels between -6 dBm and 5 dBm at 2.4 GHz.

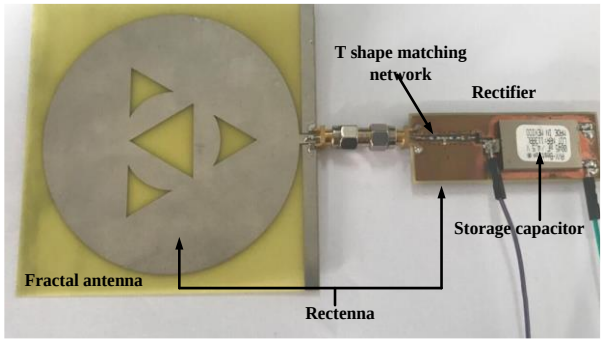

Fig. 8. The structure of the fabricated rectenna.

The rectenna combined by the fabricated rectifier and the fractal antenna is shown in Fig. 8, which is used as the receiver for energy harvesting. Meanwhile, the another identical fractal antenna is connected with the AV1442 signal generator to form the transmitting antenna. In actual measurement, the distance between transceiver antennas is 15 cm. The received RF power P_{RF} is measured by connecting the fractal antenna with the spectrum analyzer. Subsequently, the spectrum analyzer will be removed and rectenna is placed at the same position, then the DC voltage V_{out} is measured across an optimized load resistor R_{load} of 4.7-kΩ. The output DC power P_{out} of the rectenna and the rectenna efficiency η_1 can be calculated according to the following equations:

$$P_{out} = \frac{V_{out}^2}{R_{load}}, \tag{6}$$

$$\eta_1 = \frac{P_{out}}{P_{RF}}. \tag{7}$$

The measured rectenna efficiency η_1 is depicted in Fig. 9. It can be seen that the maximum efficiency is 51.8%, 46.1% and 45.08% at 2.4 GHz, 2.1 GHz and 1.9 GHz, respectively, in case of the input power is 0 dBm.

The measured efficiency η_2 of the whole system is also depicted in Fig. 9. The system efficiency η_2 including air loss can be calculated by the equation:

$$\eta_2 = \frac{P_{out}}{P_{in}}, \tag{8}$$

where the input power P_{in} is generated by the AV1442 signal generator. It can be seen that the maximum system efficiency η_2 is 24.03% at 2.4 GHz with the input power of 0 dBm. Table 1 shows the comparison between our designed rectenna and other designs reported previously. It can be seen that our design not only has advantages over the antenna impedance bandwidth and dimension, but also the satisfied conversion efficiency in low input power level.

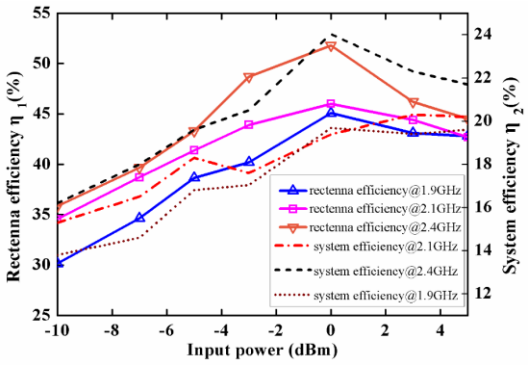

Fig. 9. The measured rectenna efficiency η_1 and system conversion efficiency η_2.

Table 1: Comparison of the proposed rectenna and the related designs reported previously

Ref.	Frequency (GHz)	Antenna Dimension (mm^3)	Maximum Gain (dBi)	Input Power Level for Peak Efficiency (dBm)	Conversion Efficiency (%)
[4]	Dual-band 1.8, 2.2	300×380×1.6	10.9, 13.3	3 to 5	50
[12]	0.85-1.94	94×82×1.6	2	>0	60
[16]	0.9-1.1, 1.8-2.5	NS	3.3	0-23	75
[17]	Dual-band 0.915, 2.45	60×60×60	1.87, 4.18	-10 to 0	50
This work	0.88-8.45	100×100×1.6	8.7	-5 to 0	51.8

V. CONCLUSION

In this paper, a novel broadband CPW-fed fractal antenna is proposed. The simulation and measurement have demonstrated that the designed antenna offers a bandwidth of 162% (0.88–8.45 GHz) and a peak gain of 8.7 dBi. Then, the rectifier with a T shape LC matching network is fabricated and integrated with the fractal antenna to form a rectenna. The measured results show that the maximum rectenna efficiency is 51.8%, 46.1% and 45.08% at 2.4 GHz, 2.1 GHz and 1.9 GHz, respectively. The peak energy conversion efficiency of the whole system is 24.03% at 2.4 GHz. At last, the designed rectenna is suitable for RF energy harvesting.

ACKNOWLEDGMENT

This work is sponsored by National Natural Science Foundation of China (Grant No. 51741704), the Natural Science Foundation of Jiangsu Province, China (BK20161352), Six talent peaks project in Jiangsu Province (DZXX-018), Independent Innovation in Agricultural Science and Technology Foundation of Jiangsu Province (CX(17)3001), the Priority Academic Program Development of Jiangsu Higher Education Institutions (PAPD).

REFERENCES

[1] A. Collado and A. Georgiadis, "Conformal hybrid solar and electromagnetic (EM) energy harvesting rectenna," in *IEEE Transactions on Circuits and Systems I: Regular Papers*, vol. 60, no. 8, pp. 2225-2234, Aug. 2013.

[2] X. Lu, P. Wang, D. Niyato, D. I. Kim, and Z. Han, "Wireless networks with RF energy harvesting: A contemporary survey," in *IEEE Communications Surveys & Tutorials*, vol. 17, no. 2, pp. 757-789, May 2015.

[3] H. J. Visser and R. J. M. Vullers, "RF energy harvesting and transport for wireless sensor network applications: Principles and requirements," in *Proceedings of the IEEE*, vol. 101, no. 6, pp. 1410-1423, June 2013.

[4] H. Sun, Y. X. Guo, M. He, and Z. Zhong, "A dual-band rectenna using broadband Yagi antenna array for ambient RF power harvesting," in *IEEE Antennas and Wireless Propagation Letters*, vol. 12, pp. 918-921, July 2013.

[5] C. Song, *et al*., "A novel six-band dual CP rectenna using improved impedance matching technique for ambient RF energy harvesting," in *IEEE Transactions on Antennas and Propagation*, vol. 64, no. 7, pp. 3160-3171, July 2016.

[6] M. Palandöken, "Microstrip antenna with compact anti-spiral slot resonator for 2.4 GHz energy harvesting applications," in *Microwave & Optical Technology Letters*, vol. 58, no. 6, pp. 1404-1408, June 2016.

[7] M. Arrawatia, M. S. Baghini, and G. Kumar, "Differential microstrip antenna for RF energy harvesting," in *IEEE Transactions on Antennas and Propagation*, vol. 63, no. 4, pp. 1581-1588, Apr. 2015.

[8] C. C. Kang, *et al*., "Corporate feed with dual segment circular polarized array rectenna for low power RF energy harvesting," in *Journal of Engineering Science & Technology*, vol. 11, no. 6, pp. 796-805, June 2016.

[9] S. B. Vignesh, Nasimuddin, and A. Alphones, "Circularly polarized strips integrated microstrip antenna for energy harvesting applications," in *Microwave & Optical Technology Letters*, vol. 58, no. 5, pp. 1044-1049, Mar. 2016.

[10] M. Taghadosi, L. Albasha, N. Qaddoumi, and M. Ali, "Miniaturised printed elliptical nested fractal multiband antenna for energy harvesting applications," in *IET Microwaves, Antennas & Propagation*, vol. 9, no. 10, pp. 1045-1053, July 2015.

[11] C. A. Figueroa-Torre, J. L. Medina-Monroy, and H. Lobato-Morales, "A novel fractal antenna based on the Sierpinski structure for super wide-band applications," in *Microwave & Optical Technology Letters*, vol. 59, no. 5, pp. 1148-1153, Mar. 2017.

[12] M. Arrawatia, M. S. Baghini, and G. Kumar, "Broadband bent triangular omnidirectional antenna for RF energy harvesting," in *IEEE Antennas and Wireless Propagation Letters*, vol. 15, pp. 36-39, Apr. 2016.

[13] H.-D. Chen and H.-T. Chen, "A CPW-fed dual-frequency monopole antenna," in *IEEE Transactions on Antennas and Propagation*, vol. 52, no. 4, pp. 978-982, Apr. 2004.

[14] Y.-J. Ren and K. Chang, "5.8-GHz circularly polarized dual-diode rectenna and rectenna array for microwave power transmission," in *IEEE Transactions on Microwave Theory and Techniques*, vol. 54, no. 4, pp. 1495-1502, June 2006.

[15] P. Nintanavongsa, U. Muncuk, D. R. Lewis, and K. R. Chowdhury, "Design optimization and implementation for RF energy harvesting circuits," in *IEEE Journal on Emerging and Selected Topics in Circuits and Systems*, vol. 2, no. 1, pp. 24-33, Mar. 2012.

[16] C. Song, *et al*., "Matching network elimination in broadband rectennas for high-efficiency wireless power transfer and energy harvesting," in *IEEE Transactions on Industrial Electronics*, vol. 64, no. 5, pp. 3950-3961, May 2017.

[17] K. Niotaki, S. Kim, S. Jeong, A. Collado, A. Georgiadis, and M. M. Tentzeris, "A compact dual-band rectenna using slot-loaded dual band folded dipole antenna," in *IEEE Antennas and Wireless Propagation Letters*, vol. 12, pp. 1634-1637, Dec. 2013.

Xue Bai was born in 1975. She received her Ph.D. degree in the field of Agricultural Information Technology from Jiangsu University in 2011. She is now an Associate Professor in School of Electrical and Information Engineering, Jiangsu University, China. Her current research area is Agricultural IoT and self-power technology for sensors.

Jiawei Zhang was born in 1994. He received the B.S. degree from Jingjiang College of Jiangsu University, Zhenjiang, China, in 2016. He is currently pursuing the M.S. degree at the Jiangsu University, Zhenjiang, China. His research interests include rectennas for energy harvesting and the design of RF WPT system.

Leijun Xu was born in 1976. He received his Ph.D. degree in the field of RF & Millimeter-Wave Integrated Circuit from Southeast University in 2010. He is now a Professor in School of Electrical and Information Engineering, Jiangsu University, China. His current research area is RF & THz integrated circuit for agricultural application. He is Member of IEEE Solid-State Circuits Society.

Buhui Zhao was born in 1957. He received his B.S. degree in Automatic Control Engineering in 1982 and M.S. degrees in Mechanical Design Engineering from Jiangsu University in 1996. He is now a Professor in School of Electrical and Information Engineering, Jiangsu University, China. His current research work includes hybrid control system, Petri-net theory and power saving technology for agricultural IoT.

Microstrip Reflectarray for Generation of Electromagnetic Waves with Beam Vorticity

Hai-Tao Chen [1], Rui Pan [2], Wei-Zhong Sun [1], and Si-Yuan He [3]

[1] Department of Antennas Research
Wuhan Maritime Communication Research Institute, Wuhan, 430079, China
hbcht@163.com, swizon@163.com

[2] Department of Technology Develpment
Wuhan Maritime Communication Research Institute, Wuhan, 430079, China
451995901@qq.com

[3] Electronic Information School
Wuhan University, Wuhan, 430072, China
siyuanhe@whu.edu.cn

Abstract ─ One type of orbital angular momentum (OAM) reflectarray antenna is presented to radiate the electromagnetic wave with beam vorticity. Microstrip double square loops are adopted as the element for the proposed reflectarray. Reflect phase of the elements with various sizes are analyzed by HFSS software with periodic boundary condition and Floquet mode. Then massive elements with different sizes are arranged helically to form the reflectarray, transforming the incident spherical wave into a vortex phase front. Several OAM reflectarray examples with different OAM mode and different feed mode are designed and fabricated. The phase patterns of far-zone field are simulated by FEKO software and measured by near-field scanning system, which demonstrates the phase singularity and vortex.

Index Terms ─ Orbital angular momentum, reflectarray antenna, vortex electromagnetic wave.

I. INTRODUCTION

Recently, much attention has been focused on vortex electromagnetic waves. Vortex electromagnetic waves have helical phase wavefronts and can carry orbital angular momentum (OAM) [1], [2]. The OAM is related to beam vorticity and phase singularity, which contains infinity eigenstates theoretically. The eigenstates of OAM are mutually orthogonal to each other, so the OAM can be used to add communication channels without increasing the frequency bandwidth.

For vortex electromagnetic waves application, various antennas have been presented in literatures, such as the twisted parabolic antenna [2], circular antenna array [3], [4], open cylinder resonant cavity [5], planar-spiral phase plate (planar-SPP) [6], and so on. The planar-SPP proposed in [6] can be seen as transmit array to transform the incoming phase front into a desired outputting phase front, in which air holes in substrate are adopted as the unit cell to provide the phase shift.

Different from the planar-SPP presented in [6], another quasi-periodic planar structure based on the reflectarray theory can also be used to generate vortex electromagnetic wave. The reflectarray antenna can be seen as a hybrid of reflectors and arrays, which have been widely discussed and in-depth [7-9]. Recently, a reconfigurable graphene reflectarray has been proposed in [10] for the generation of vortex waves in THz band, in which graphene reflect units are adopted.

In this paper, the design of an OAM microstrip reflectarray is presented. The proposed reflectarray antennas adopt double square loops printed on the grounded substrate as the element and the linear polarization horn is adopted to provide an incident spherical wave as a primary source. Massive elements with different sizes are arranged quasi-periodically to transform the spherical wave to waves with OAM in different states.

For the OAM reflectarray, the key parameter are the phase response provided by the elements arranged in array lattice, which are specifically designed to compensate for the differential spatial phase delays from the feed and form a helical phase front on the reflectarray aperture. Double square loops are adopted as the element and analyzed in Section II. Several OAM reflectarray examples are presented and simulated in Section III, including with prime focus feed and offset feed. Some experimental results are shown in Section IV, and Section V is the conclusion.

Submitted On: August 11, 2017
Accepted On: December 31, 2017

II. ELEMENT DESIGN

The OAM reflectarray antenna, presented in this paper is a quasi-periodic array illuminated by a horn. Double square loops, as shown in Fig. 1, are adopted as the element in view of its wide scope of phase response. The double square loops include an outer loop with edge length L_1 and an inner loop with edge length L_2. Different reflect phase response can be obtained by changing the edge length of the outer loop and inner loop. In order to create the anticipation aperture phase distribution to generate OAM, the scale of the element shall be varied according to its position.

Reflect phase of the element is analyzed by HFSS software with periodic boundary condition and Floquet mode, as shown in Fig. 1 (b). The simulated results are shown in Fig. 2, in which different ratio of the edge length between L_1 and L_2 are chosen. Other parameters of the double square loop are chosen as follows: width of the outer loop and inner loop are both 0.5mm, the substrate Rogers RT5880 and height 2mm, plus the periodic size 8mm and the frequency being 12.5GHz. It can be seen from the results shown in Fig. 2 that the wider scope of phase shift can be obtained if L_2 is more closed to L_1, and the slope of the curve will become steeper at the same time. According to the results, L_2 is chosen as L_2=0.7L_1 in this paper and then a phase shift range approach to 360 degrees is obtained by adjusting the edge-length of the outer square loop L_1 from 5.0mm to 7.5mm, which is enough to realize the arbitrary required phase distribution on the reflectarray.

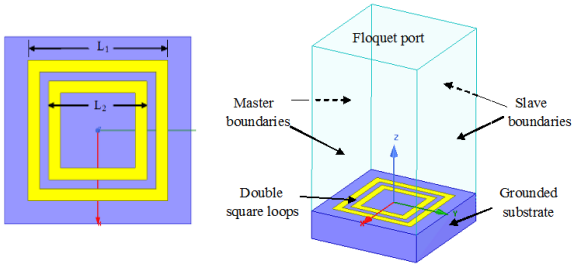

(a) (b)

Fig. 1. Double square loops on a grounded substrate and its HFSS model: (a) double square loops, and (b) HFSS model with periodic boundary condition and Floquet mode excitation.

For designing the reflectarray, we shall seek the size of the elements according to the requested phase shift. So the curve of the reflect phase shift against the element size is fitted piecewise by the 2-order polynomial, as shown in Fig. 3. It's convenient for building the geometry model of the massive quasi-periodic array, and the edge length of the outer loop L_1 of the n^{th} element can be calculated directly as:

$$L_1 = \begin{cases} -0.000015\beta_n^2 - 0.00093\beta_n + 7.5 & 0 \le \beta_n < 180 \\ 0.000062\beta_n^2 - 0.043\beta_n + 12.7 & 180 \le \beta_n < 360 \end{cases}, \quad (1)$$

where β_n is the requested phase shift (deg.) of the n^{th} element.

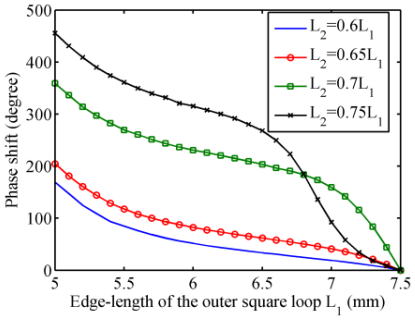

Fig. 2. Reflect phase shift of the double square loops element with different ratio between the outer loop edge length L_1 and the inner loop edge length L_2. The results are simulated by HFSS.

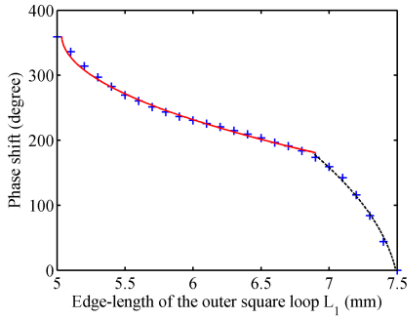

Fig. 3. Reflect phase shift of the elements with various sizes. The cross line is obtained from HFSS, while the red solid line and black dash line are fitting results.

III. THE ARRAY LAYOUT AND SIMULATED RESULTS

As shown in Fig. 4, a reflectarray is placed on the xy-plane. The reflectarray is illuminated by a y-polarization horn located at (x_f, y_f, F), where F is the distance between the aperture of the horn and the surface of the reflectarray elements.

The electromagnetic wave excited by the feed horn can be approximated as a spherical wave which originates from the center of the horn aperture. When the feed horn is adopted to illuminate the reflectarray, there are some non-uniform phase distributions for the incident wave on the aperture of the reflectarray. Then the phase shift of each element is designed to compensate for the spatial delay of the incident wave, and provide a vortex phase distribution on the aperture that generates a wave with beam vorticity at the specific direction

Assume the beam direction is perpendicular to the aperture of the proposed reflectarray. In order to create vortex phase front, the requested phase shift for the element located at (x_n, y_n) can be written as:

$$\beta_n = l\varphi_n + k_0\left(\sqrt{(x_n - x_f)^2 + (y_n - y_f)^2 + F^2} - \sqrt{x_f^2 + y_f^2 + F^2}\right), \quad (2)$$

where l is the OAM mode number, φ_n is the azimuthal angle of the element position. In the right of Equation (2), the second part represent compensating for the differential spatial phase delays from the feed, and the first part is used to form the request vortex phase front.

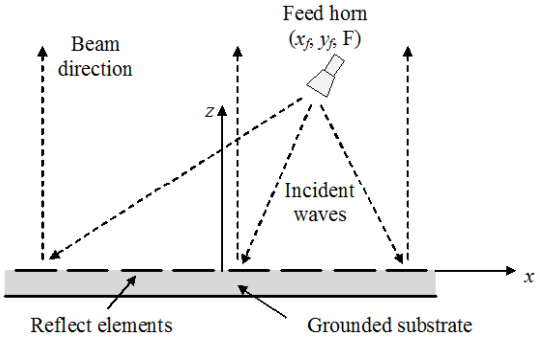

Fig. 4. Configuration of the reflectarray illuminated by a horn located at (x_f, y_f, F). The beam direction is perpendicular to the reflect elements surface.

A. Prime focus feed OAM reflectarray

The design examples of prime focus feed OAM reflectarray are presented firstly. The mode number of the OAM is chosen as "1" and "2" respectively. The scale of the reflectarray D×D is 160mm×160mm and the number of the elements is 20×20. The feed horn is located at (0, 0, F), and F is chosen as 80mm, which means F/D=0.5. By using Equation (2), size of each element can be calculated

Because of electrically large size, combined with massive elements and thin dielectric layer, the full-wave simulation is a challenging task for the reflectarray. The surface meshing approach will be more appropriate than the volume meshing method for this problem [11]. As such, the multi-level fast multipole method (MLFMM) based on integral equation and method of moment (MoM) technique is more effective than other numerical techniques such as finite element method or finite difference method. Then the commercial MLFMM software FEKO v.7.1 is adopted here for full-wave simulation of the reflectarray. The reflectarray modeled in FEKO with OAM mode l=1 is shown in Fig. 5. The simulated gain pattern and phase pattern is shown in Fig. 6, in which the phase pattern is obtained on a plane $50\lambda_0$ away from the reflectarray. The observation distance $50\lambda_0$ is only an example, and arbitrary distance which is much large than wavelength can be chosen.

For the simulation of this example, FEKO uses 1348 metallic triangles in free space, 56,486 metallic triangles that coincide with the surface of a dielectric, and 28,552 triangles for the surface of a dielectric to mesh the model. 232,916 unknown basis functions need to be calculated by the FEKO MLFMM solver. The peak memory usage during the whole solution is 13.31GB and the CPU time is 1854 seconds on a 4 core 2.80GHz Intel(R) Xeon(R) Dell Precision 7710 computer.

It can be seen in Fig. 6 that there is a radiation null at the beam direction and the phase varied from 0° to 360° around the center singularity point, which conforms to the vortex wave with "1" order OAM.

The FEKO model of the reflectarray with OAM mode l=2 is shown in Fig. 7, and the simulated results are shown in Fig. 8. The phase pattern is also obtained on a plane $50\lambda_0$ away from the reflectarray. It can be seen that the phase varied from 0° to 720° around the center singularity point, which conforms to the vortex wave with "2" order OAM.

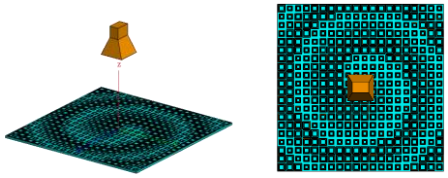

Fig. 5. FEKO model of the reflectarray with OAM mode l=1: (a) perspective view and (b) top view.

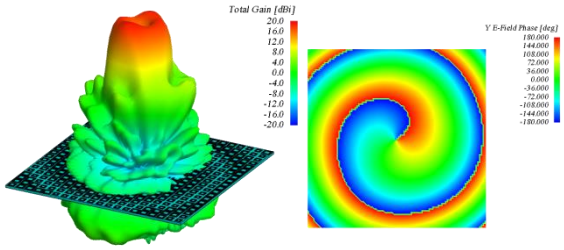

Fig. 6. Simulated results for the 1 order OAM reflectarray: (a) gain pattern and (b) phase pattern.

B. Offset feed OAM reflectarray

The OAM reflectarray can also be designed as offset feed configuration. Assuming the feed horn is located at (0, -D/2, F), substitute the y_f in Equation (2) with -D/2 and build the layout of the reflect elements for the vortex beam with OAM mode l=1, as shown in Fig. 9. The beam direction is assumed perpendicular to the reflectarray surface. It can be seen that the layout of elements for offset feed is much different to the case of prime focus feed. The elements are not arranged helically but more complicated.

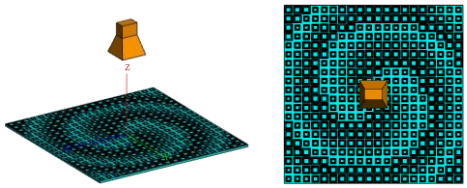

(a) (b)

Fig. 7. FEKO model of the reflectarray with OAM mode l=2: (a) perspective view and (b) top view.

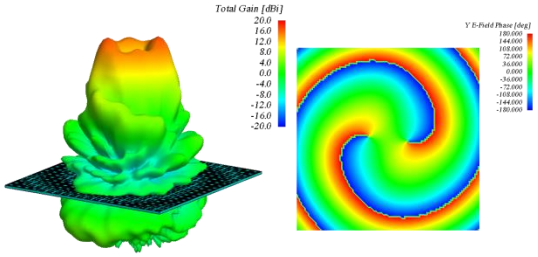

(a) (b)

Fig. 8. Simulated results for the 2 order OAM reflectarray: (a) gain pattern and (b) phase pattern.

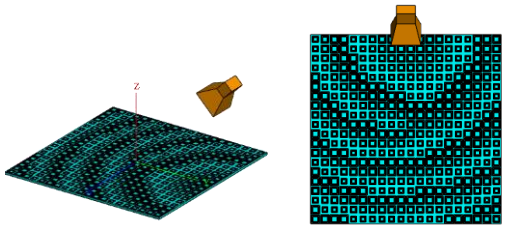

(a) (b)

Fig. 9. FEKO model of the 1 order OAM with offset feed: (a) perspective view and (b) top view.

The radiation pattern and phase pattern of the offset feed OAM reflectarray are shown in Fig. 10, which is obtained on a plane $50\lambda_0$ away from the reflectarray and demonstrate the helical phase front and field singularity along the beam direction, which is in line with the radio vorticity well.

C. Discussion of the aperture efficiency

Because of the radiation null at the beam direction, it's ambiguous for evaluating the gain or efficiency of the OAM antenna as conventional antenna. A conversion efficiency for the OAM metasurface was considered in [12] as the ratio of the energy carried by the OAM wave to the total energy of the transmitted wave. This conversion efficiency can be seen as an OAM mode efficiency. In order to evaluate the gain of the OAM reflectarray, we introduce a relative efficiency here which is defined as the aperture efficiency relative to the twisted parabolic antenna [2] with same area and same feed source.

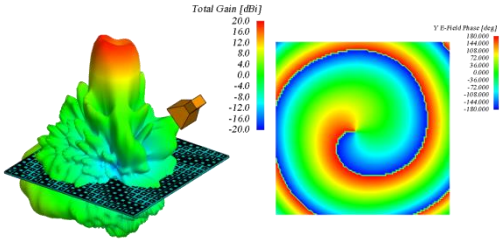

(a) (b)

Fig. 10. Simulated results for the 1 order OAM reflectarray with offset feed: (a) gain pattern and (b) phase pattern.

As example, the relative efficiency of the 1 order OAM reflectarray proposed in Part A is invetsgated. A twisted parabolic antenna with radius 90mm is established and modeled in FEKO. The twisted parabolic antenna has same aperture area and is fed by the same horn as that of the OAM reflectarray.

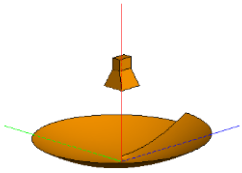

Fig. 11. FEKO model of the twisted parabolic antenna which is used as a referenced antenna to evaluate the aperture efficiency of the proposed reflectarray.

The FEKO model of the twisted parabolic antenna is shown in Fig. 11, and the simulated results of gain pattern are shown in Fig. 12, in which simulated results of the OAM reflectarray are also given. It can be seen that the gain patterns of the OAM reflectarray are approached to that of the twisted parabolic antenna and have about 1.8dB descrease than the latter in E-plane when θ is near to the beam direction. It means that the relative aperture effciency of the OAM reflectarray is about 66% relative to the twisted parabolic antenna. The decrease of the aperture efficiency can be attributed to the aperture shape and phase distortion.

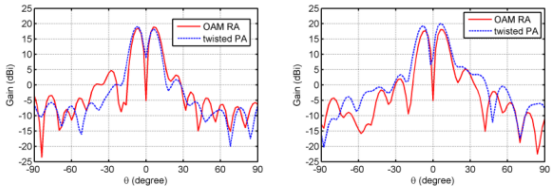

(a) (b)

Fig. 12. Gain pattern of the proposed OAM reflectarray and the twisted parabolic antenna: (a) H-plane (xoz-plane), and (b) E-plane (yoz-plane). In the label, OAM RA represents OAM reflectarry and twisted PA represents twisted parabolic antenna.

IV. PROTOTYPE AND EXPERIMENTAL RESULTS

The designed prototypes are fabricated using printed circuit board (PCB) technology and shown in Fig. 13, in which (a) is the 1-order OAM reflectarray with prime focus feed, (b) is the 2-order OAM reflectarray with prime focus feed and (c) is the 1-order reflectarray with offset feed.

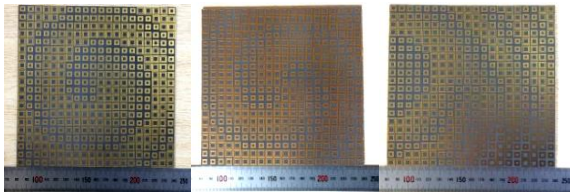

(a) (b) (c)

Fig. 13. Photographs of the fabricated OAM reflectarrays: (a) OAM l=1 with prime focus feed, (b) OAM l=2 with prime focus feed, and (c) OAM l=1 with offset feed.

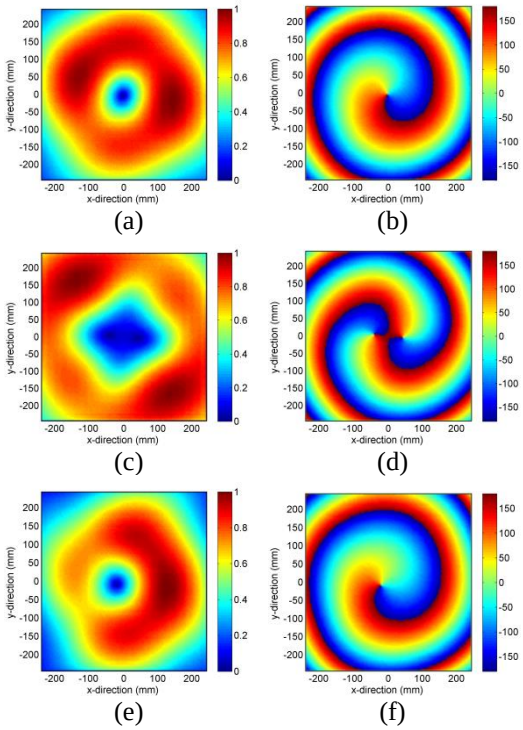

(a) (b) (c) (d) (e) (f)

Fig. 14. The intensity patterns and the phase patterns of the OAM reflectarray propotypes. Those results are calculated from the measurement near-field data and plotted using Matlab code. The left-side figure (a), (c), (e) are the intensity patterns for the three prototypes shown in Fig. 13 respectively, and the right-side figure (b), (d), (f) are the phase patterns for those prototypes respectively.

The measure results of those prototypes are obtained by using a near-field scanning system in anechoic chamber. Electromagnetic fields near to the aperture of reflectarrays are measured and recorded. With aperture equivalence principle, a Matlab clode is developed to calculate the field patterns on the plane $50\lambda_0$ away from the reflectarray by using the near-field measurement data. The intensity patterns and the phase patterns of the three prototypes are shown in Fig. 14 and accord with thoe simulated results well.

V. CONCLUSIONS

Reflectarray technique is used to generate the vortex electromagnetic wave in this paper. Design of the reflectarray with different feed mode and different OAM mode has been demonstrated. The HFSS software is used to calculate the phase shift of the double square loops element and the FEKO software to simulate the OAM performance of the reflectarray. Prototypes and experimental results are introduced to validate the design. The proposed antenna in this paper can be used as a substitute for the twisted parabolic antenna to generate the electromagnetic wave with beam vorticity. The next step of our work is to develop an experimental transmit and receive system for radio vortex.

REFERENCES

[1] S. M. Mohammadi, et al., "Orbital angular momentum in radio - A system study," *IEEE Trans. Antennas Propagat.*, vol. 58, no. 2, pp. 565-572, Feb. 2010.

[2] F. Tamburini, "Encoding many channels on the same frequency through radio vorticity: First experimental test," *New J. Phys.*, vol. 14, Mar. 2012.

[3] T. Yuan, et al., "Generation of OAM radio beams with modified uniform circular array antenna," *Electron. Lett.*, vol. 52, no. 11, pp. 896-898, 2016.

[4] Q. Bai, et al., "Experimental circular phased array for generating OAM radio beams," *Electron. Lett.*, vol. 50, no. 20, pp. 1414-1415, Sep. 2014.

[5] Y. Chen, et al., "Half-mode substrate integrated waveguide antenna for generating multiple orbital angular momentum modes," *Electron. Lett.*, vol. 52, no. 9, pp. 684-686, 2016.

[6] L. Cheng, W. Hong, and Z. Hao, "Generation of electromagnetic waves with arbitrary orbital angular momentum modes," *Scientific Report* 4, Article number: 4814 , 2014.

[7] J. Huang and J. A. Encinar, *Reflectarray Antennas*. Hoboken, NJ, USA: Wiley, 2008.

[8] B. Devireddy, A. Yu, F. Yang, and A. Z. Elsherbeni, "Gain and bandwidth limitations of reflectarrays," *Appl. Comp. Electro. Society (ACES)*

Journal, vol. 26, no. 2, pp. 170-178, 2011.

[9] P. Nayeri, F. Yang, and A. Elsherbeni, "Beam scanning reflectarray antennas: A technical overview and state of the art," *IEEE Antennas Propagation Magazine*, vol. 57, no. 4, pp. 32-47, Aug. 2015.

[10] Z. Chang, B. You, L.-S. Wu, et al., "A reconfigurable graphene reflectarray for generation of vortex THz waves," *IEEE Antennas and Wireless Propagation Letters*, vol. 15, pp. 1537-1540, 2016.

[11] P. Nayeri, A. Z. Elsherbeni, and F. Yang, "Design, full-wave analysis, and near-field diagnostics of reflectarray antennas," *Appl. Comp. Electro. Society (ACES) Journal*, vol. 28, no. 4, pp. 284-292, 2013.

[12] M. L. N. Chen, L. J. Jiang, and W. E. I. Sha, "Ultrathin complementary metasurface for orbital angular momentum generation at microwave frequencies," *IEEE Trans. Antennas Propagat.*, vol. 65, no. 1, pp. 396-400, Jan. 2017.

Hai-Tao Chen was born in 1979. He received the B.S. degree in Electronic Engineering from Nanjing University of Science and Technology, Nanjing, China, in 2000 and the Ph.D. degree in Radio Physics from Wuhan University, Wuhan, China, in 2008. Currently, he is a Research Professor at the Department of Antennas Research, Wuhan Maritime Communication Research Institute, Wuhan, China. His current research focus is in the area of antenna design and electromagnetic theory and numerical techniques.

Rui Pan was born in 1983. He received bachlor's degree in Huazhong University of Science and Technology in 2007 and Master's degree in Huazhong University of Science and Technology, Wuhan, China, in 2009. Currently, he is a Research Engineer in the Department of Technological Development, Wuhan Maritime Communication Research Institute, Wuhan, China, devoted mainly in the research of communication engineering.

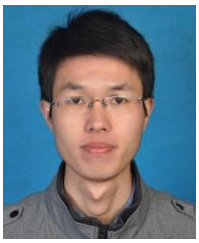

Wei-zhong Sun received the B.S. degrees in Electronic Engineering from Northwestern Polytechnical University, Xi'an, Shaanxi, China in 2010 and the M.E. degrees in Electromagnetic Fields and Microwave Technology from Nanjing Research Institute of Electronics Technology, Nanjing, Jiangsu, China in 2013, respectively. He is currently an Engineer in Wuhan Maritime Communication Research Institute, Wuhan, Hubei, China. His current research interests include array antennas and array signal processing.

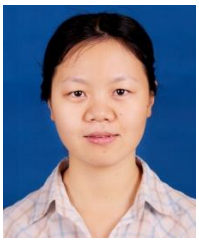

Si-Yuan He was born in China, in 1982. She received the Telecommunication Engineering degree and the Ph.D. degree in Radio Physics from Wuhan University, Wuhan, China, in 2003 and 2009, respectively. From 2005 to 2006, she was a Research Assistant in the Wireless Communications Research Center, City University of Hong Kong, Hong Kong. From 2009 to 2011, she worked as a Postdoctoral Researcher at Wuhan University. She is currently a Professor with the School of Electronic Information, Wuhan University. Her research interest includes electromagnetic theory and its application, computational electromagnetics, radar imaging, and electromagnetic inverse scattering.

Printable Chipless Tag and Dual-CP Reader for Internet of Things

Guoqing Dong, Yizhu Shen, Hongfu Meng, Na Chen, Wenbin Dou, and Sanming Hu

State Key Laboratory of Millimeter Waves
Southeast University, Nanjing, 210096, China
sanming.hu@seu.edu.cn

Abstract ─ This paper proposes a printable chipless tag that encodes more bits than a conventional tag, and also a dual circularly polarized (CP) reader that achieves high isolation with insensitive orientation. To demonstrate this concept, a radio-frequency identification (RFID) tag of 13mm×13mm is designed to encode 5 bits covering 6 - 9 GHz. This tag is investigated and measured with dual-CP backscattering characteristics for the first time. The versatile dual-CP reader, along with this tag which is feasible to print on other flexible substrate including papers, clothes and plastics, are promising to benefit the Internet of Things (IoT).

Index Terms ─ Chipless tag, dual circular polarization, Internet of Things (IoT), Radar Cross Section (RCS), Radio-Frequency Identification (RFID).

I. INTRODUCTION

Different from the widely employed barcode technology, radio frequency identification (RFID) adopts electromagnetic wave to identify targets [1]. RFID has been widely applied to many scenarios including transportation tolls, animal ID, and anti-thief systems, etc. [2]. RFID system usually consists of three parts: tags that carry binary information, readers that extract the encoded data, and a general platform connected with the Internet. Printable RFID tags, which features long reading range, non-line-of-sight (NLOS) reading, and automated identification and tracking, have the potential to supplement the existing barcode technology [3]. The popularity of RFID is mainly dependent on the cost of the tag, especially the cost of silicon chip in a tag. Therefore, chipless RFID tag without expensive chips has become the industry trend and attracts intensive research interest for low-cost, and massive item identification and tracking.

A chipless tag contains neither IC chips nor battery. Therefore, it's very challenging to encode as many data bits as chipped tag. To solve this problems, four encoding methods based on time, frequency, phase, and image are investigated. Among these, the frequency-domain-based approach are demonstrated with the highest data storage capabilities [4]. Using this method, chipless tags are designed with resonators to encode data into predetermined spectrum, and each data bit is associated with the presence or absence of a resonant peak [3]. Based on this principle, many different tags are proposed in [5-7]. However, to date, there still exist two issues. Firstly, the reading accuracy is seriously dependent on the position, orientation, and polarization of chipless tags. Secondly, the RFID system generally requires high isolation between transmitting (Tx) and receiving (Rx) antennas in reader, which causes the complexity and high cost of reader [8].

To alleviate the above issues, this paper demonstrates a novel dual circularly-polarized (dual-CP) RFID system as proposed in [9]. This dual-CP RFID system includes a compact linearly-polarized tag and a pair of reader antennas operating with left-handed circular polarization (LHCP) and right-handed circular polarization (RHCP) respectively. This system features high isolation between Tx and Rx, which not only alleviates the complexity of the following front-end circuits for signal extraction, but also makes the tags orientation insensitive. Additionally, by introducing a dummy structure, one more bit is achieved in the upper ultra-wideband (UWB) frequency range of 6-9 GHz. This paper is organized as follows. Section II introduces the design and analysis of chipless tag and presents the RCS measurements of chipless RFID tags. Section III shows the tag's performance as well as the measurement of RCS for the tag. And last part, Section IV is the conclusion.

II. TAG DESIGN AND MEASUREMENT PRINCIPLE

A. Tag design principle

The proposed dual-CP RFID system is shown in Fig. 1. It consists of two antennas with crossed polarization, i.e., LHCP and RHCP, for transmitting and receiving respectively. Therefore, the isolation between Tx and Rx of the RFID readers is significantly increased. Moreover, this dual-CP configuration enables the proposed RFID system to detect tags with arbitrary orientation. The operation frequency is set as 6-9 GHz which is assigned by the Ministry of Industry and Information Technology of the People's Republic of China for ultra-wideband

Submitted On: September 30, 2017
Accepted On: April 21, 2018

applications [10].

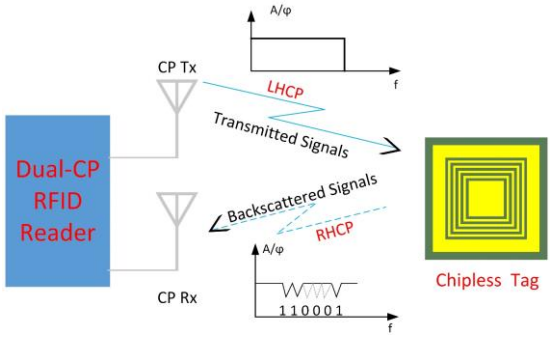

Fig. 1. The proposed RFID system with a dual-CP reader and a chipless tag.

Coplanar square slots with nested concentration structure are used for the tag design. The structure features narrower bandwidth than other resonators such as circular rings. In addition, square slots are more reluctant to the printing errors than other shapes [4], especially when the operating frequency is much higher than the ultra-high-frequency (UHF), the printing accuracy should be the first priority.

For the square-slots, the length dimension of each half-loop should be a multiple of the half-wavelength for resonance to occur, which means each half-loop is acting as a dipole element and the length dimension of the whole loop needs, therefore, to be a multiple of one full wavelength. However, to avoid weak resonances of re-radiated energy in hemisphere of a single element, the length of the loop must be one wavelength instead of a multiple-wavelength [11].

Square slots resonators with different lengths are formulated to generate different signature to represent one bit. Actually, each square slot works as a λ resonator, which means its circumference is equal to one phase wavelength (λ_g) as expressed in Equation (1):

$$\lambda_g = 2(L_i + L_i - 2W_i), \quad (1)$$

and

$$L_i = L_{i-1} - W_{i-1} - G_{i-1}, \quad (2)$$

where L_i is the side length of corresponding slot resonator, W_i is the width of corresponding square slot, G_i is the gap between them. However, the loop width (W) and substrate thickness (h) are also considered for calculating the guided wavelength (λ_g) of the square loop resonator. These empirical equations are derived from least square curve fitting techniques [12] which is quite complex to construct the design.

For simplicity, we can derive the resonant frequency as:

$$f_i = \frac{c}{2(L_i+L_i-2W_i)}\sqrt{\frac{2}{\varepsilon_r+1}}, \quad (3)$$

where c is the speed of light in free space, L_i is the side length of corresponding square slot resonator, and ε_r is the relative permittivity of the substrate.

Therefore, if N square slots of different lengths are placed concentrically, it will generate signatures with N different frequencies. Meanwhile, the harmonics have no effect on the tag's performance: the second harmonics of the resonance are absent in the backscattered signal, while the third harmonics are out of the operation band (6-9 GHz) and small enough to be neglected.

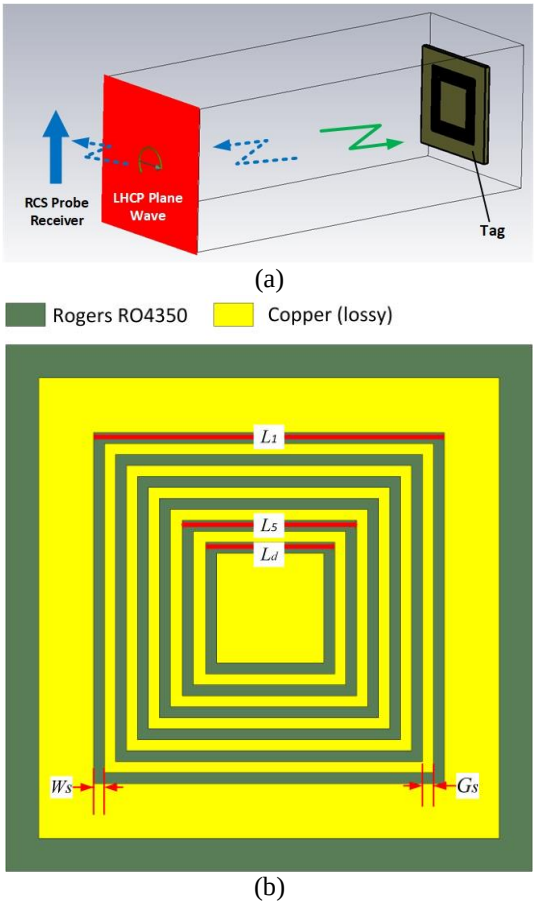

Fig. 2. The proposed chipless tag: (a) design schematic and (b) tag parameters.

As shown in Fig. 2 (a), the tag is excited by LHCP plane wave and the frequency-encoded backscattered signal from the tag is received by an RCS probe placed at 50 mm away. Open (add space) boundary condition is used during the simulation.

The layout of the proposed 5-bit tag is shown in Fig. 2 (b) with design parameters, where L_1 and L_5 are the side lengths of the outermost and innermost square slot resonator respectively, L_d is the side length of the dummy structure. The square slots are with the same width of W_s and gap of G_s between each other. They are calculated using Equation (1), with detailed parameters of L_1 = 8.4mm, L_5 = 6.0mm, L_d = 5.4mm, and W_s = G_s = 0.15mm. The substrate is Rogers RO4350, with dielectric constant of

3.48, and a thickness of 0.76 mm.

The resonators are numbered according to their lengths: resonator 1 is the longest resonator and generates the lowest frequency, which is denoted as most significant bit (MSB); while resonator 5 with highest frequency is denoted as least significant bit (LSB).

When the incident plane wave excites this square slot tag as shown in Fig. 2 (a), a frequency-selective behavior with deep notches appear at the resonant frequencies in the backscattered signal. However, because of the same width and gap of these square loops, the resonant quality factor will drop at higher resonant frequency points, with increased resonant bandwidth. Therefore, a dummy structure is innovatively proposed and located at the inner part of resonator 5. This introduced dummy structure will bring one more bit.

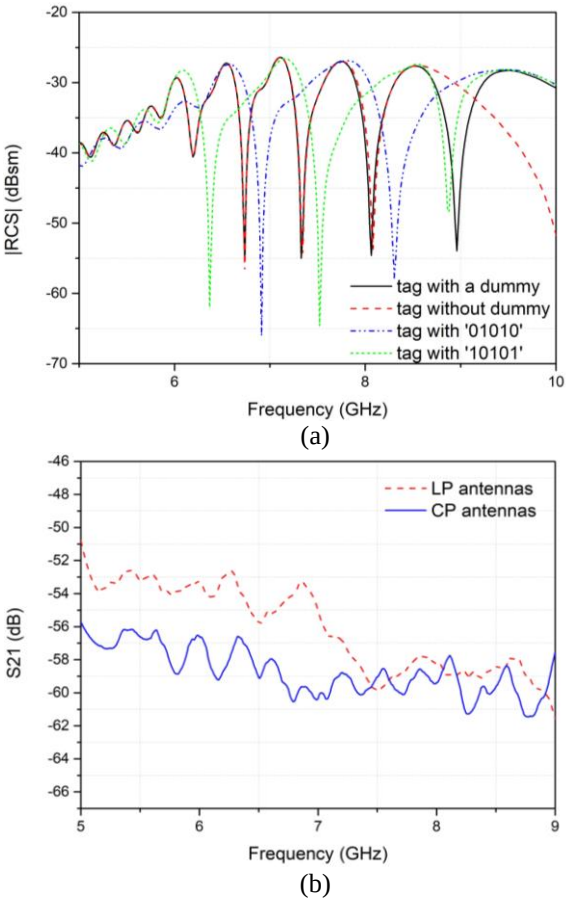

Fig. 3. (a) RCS performance of the four different tags, and (b) the isolation between two horn antennas in the two different RFID systems (@200mm distance).

As shown in Fig. 3 (a), if employing the conventional structure with five square resonators, the six resonant frequency is out of the frequency range of 6-9 GHz, and its Q-factor is too low to be detected as a resonance. Thus, a dummy is innovatively added at the inner of the shortest square resonator to narrow the bandwidth of the highest resonance.

The isolation between two CP and LP horn antennas was demonstrated respectively. The two antennas were placed straightly at 200mm distance. As depicted in Fig. 3 (b), at comparatively lower frequency (5-7 GHz), the isolation between the two LP horn antennas is quite lower compared with CP ones. Since the RCS response of single tag is weak, one tag reading range is quite limited in LP RFID system. As a result, our dual-CP RFID system is free from poor isolation performance, and thus has a farther reading range of tags than conventional LP RFID system.

B. RCS measurement methods

RCS measurement is usually based on the far-field measurement of the backscattered power from the target, namely the tag in this circumstance. The value can be obtained by using vector network analyzer (VNA). As illustrated in Fig. 4, there are two possible measurement configurations: the bi-static bench with two antennas and the mono-static bench with only one antenna. The backscattered power transfer is characterized by the transmission coefficient in bi-static bench and the reflection coefficient in mono-static bench [13].

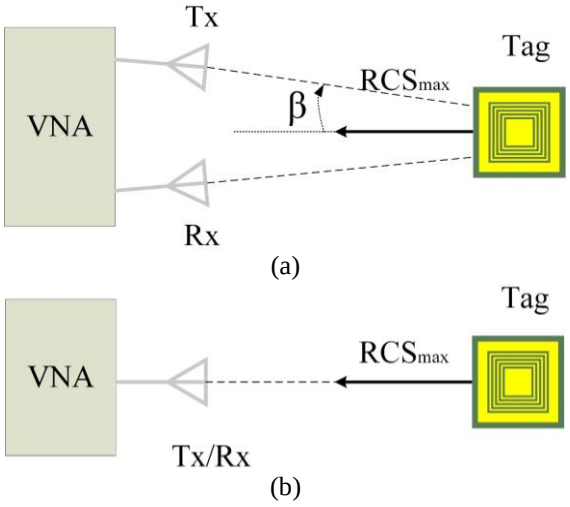

Fig. 4. Configuration of two possible measurement benches: (a) bi-static (measurement of the S_{21} parameter), and (b) mono-static (measurement of the S_{11} parameter).

If the target responds in cross-polarization, a dual-CP antenna can be used as probe, avoiding the environmental contribution such as in [14] and overcoming the incident angle issue [13]. In this configuration, the isolation between the two ports of this antenna will be a critical parameter of the testing accuracy. Hence, we use bi-static RCS measurement configuration. RFID systems can be treated as radar systems because the backward communication link (from tags to the reader) is purely

scattering.

Basically, the RCS can be determined by measuring the backscattered power and using the radar equation in which transmitting power and receiving power have relation formulating in Equation (4) [15]:

$$P_r = \frac{P_t G_t G_r \lambda^2 \sigma}{(4\pi)^3 R^4}, \quad (4)$$

where P_t is transmitting power, P_r is receiving power, G_t, G_r are respectively gain of Tx and Rx, λ is transmitting wave length, R is distance between antenna and tag, σ is the RCS of the tag. The Tx and Rx transmission coefficient from VNA can be obtained using Equation (5):

$$P_r / P_t = |S_{21}|^2 . \quad (5)$$

As a result, the RCS of the tag is calculated with (2) and (6):

$$\sigma = \frac{(4\pi)^3 R^4 |S_{21}|^2}{G_t G_r \lambda^2}, \quad (6)$$

Another RCS calculation method can be found in [16] that RCS σ_{tag} of tags under test is as a function of the frequency based on the known RCS σ_{ref} of the reference scatter:

$$\sigma_{tag} = \left[\frac{S_{21}^{tag} - S_{21}^{background}}{S_{21}^{ref} - S_{21}^{background}} \right]^2 \sigma_{ref}, \quad (7)$$

where $S_{21}^{background}$ is measured S_{21} parameter when nothing is mounted and S_{21}^{ref} is measured S_{21} parameter when the reference scatter is mounted. Normally, a flat metal plate or a metal ball is used as the reference target.

When a perfectly-conducting square flat plate, of side length a, is considered, its RCS can be expressed as [17]:

$$\sigma = \frac{4\pi a^4}{\lambda^2}, \quad (8)$$

or in general, for a plate of area A,

$$\sigma = \frac{4\pi A^2}{\lambda^2}, \quad (9)$$

the RCS has units of m^2 and is often expressed in decibels relative to square meter (dBsm):

$$\sigma(\text{dBsm}) = 10\log_{10}[\sigma(m^2)]. \quad (10)$$

III. RESULTS

Tag measurement was setup in the bi-static form as shown in Fig. 5 (a). The tag doesn't have ground plane; therefore, when the tag was illuminated with LHCP wave, EM waves can be received at both sides of the tag. Figure 6 (a) shows the backscattered signal. The RHCP component is dominant and in the front direction, i.e., the ratio of RHCP/LHCP is much higher than 0 dB. On the contrary, as shown in Fig. 6 (b), LHCP is dominant from the back side. Therefore, it is feasible to use dual-CP antennas to detect these tags.

To improve the RCS response of proposed chipless tags, we fabricated the tag in the form of 4×4 arrays as depicted in Fig. 5 (b). From Equation (4), we can derive the relation between the two RCS response of array and unit:

$$\sigma_{array}(dB) - \sigma_{unit}(dB) = 10log_{10}(16)=12.04. \quad (11)$$

The RCS response in Fig. 7 shows that, when the incident plane wave has limited angle with the tag, there is almost no obvious orientation mismatch, i.e., the proposed dual-CP system can read tags with different orientation.

As Fig. 4 depicts, when we employ the bi-static measurement of S-parameter or RCS response, deviation is unavoidable as the angle deviation increases. Given in Fig. 8, keeping the resonant frequency within acceptable range, the angle between the two antennas can be up to 45 degrees, which is enough for real applications.

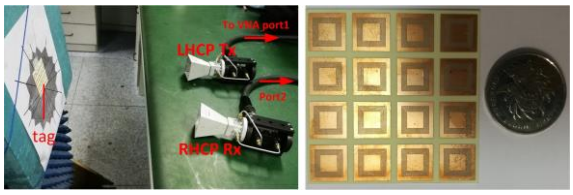

(a) (b)

Fig. 5. (a) Tag measurement setup using two CP horn antennas, and (b) prototype of proposed tag with '11111' (4x4 array).

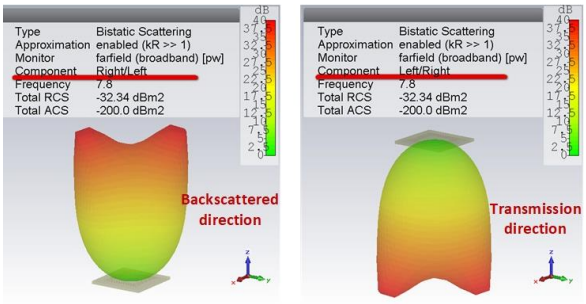

(a) (b)

Fig. 6. Dual-CP backscattering characteristics of the proposed tag: (a) RHCP/LHCP ratio at the front side, and (b) LHCP/RHCP ratio at the back side.

IV. CONCLUSION

A dual-CP RFID system with high isolation and printable chipless nested square slots tag with higher density is proposed and demonstrated. By introducing a dummy, we achieved 1 more bit covering 6−9 GHz. This tag can be directly printed on versatile substrate. In addition, the dual-CP system is orientation insensitive and have 45 degrees tolerance between Tx and Rx. The measured results show that, the proposed dual-CP

system with chipless tag is promising for low-cost IoT applications.

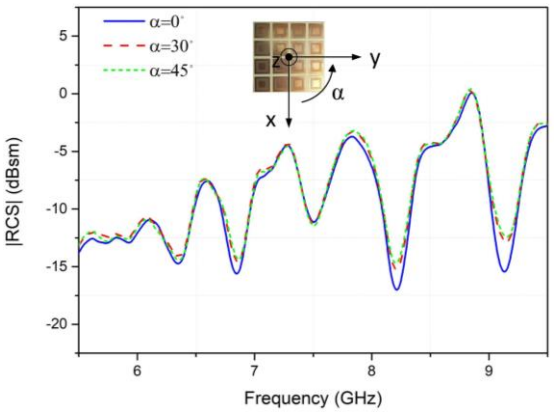

Fig. 7. Measured RCS results for tag with dummy structure, for three angles of incident wave (tag lying on the xoy plane).

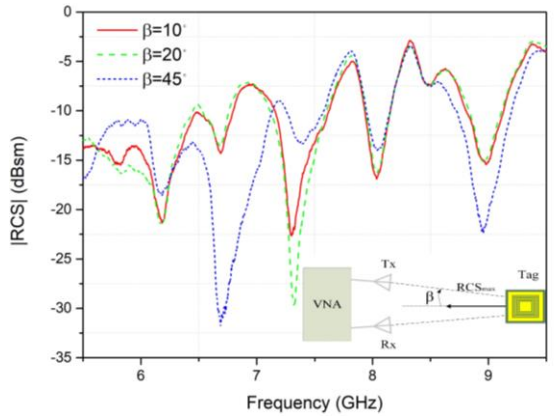

Fig. 8. Angle deviation tolerance of tag with dummy structure for example.

ACKNOWLEDGMENT

This work was supported in part by the National Natural Science Foundation of China under Grants 61701111 and 61701112, and in part by the Open Project Program of the State Key Laboratory of Millimeter Waves under Grants Z201701 and Z201702.

REFERENCES

[1] H. Stockman, "Communication by means of reflected power," *Proc. IRE*, pp. 1196-1204, 1948.

[2] K. Finkenzeller, *RFID Handbook: Fundamentals and Applications in Contactless Smart Cards, Radio Frequency Identification and Near-Field Communication*. New York, NY, USA: Wiley, 2010.

[3] S. Preradovic and N. C. Karmakar, "Chipless RFID: Bar code of the future," *IEEE Microw. Mag.*, pp. 87-97, 2010.

[4] M. A. Islam and N. C. Karmakar, "Real-world implementation challenges of a novel dual-polarized compact printable chipless RFID tag," *IEEE Trans. Microw. Theory Techn.*, vol. 63, no. 12, pp. 4581-4591, 2015.

[5] Md. Aminul Islam, "Compact Printable Chipless RFID Systems," Ph.D. Thesis, Monash University, Melbourne, Australia, 2014.

[6] R. Rezaiesarlak and M. Manteghi, *Chipless RFID, Design Procedure and Detection Techniques.* New York, NY, USA: Springer, 2015.

[7] S. Preradovic, *et al.*, "Multiresonator-based chip item tracking," *IEEE Trans. Microw. Theory Techn.*, vol. 57, pp. 1411-1419, 2009.

[8] T. Björninen, *et al.*, "Circularly polarized tag antenna for UHF RFID," in *26th Annual Review of Progress in Applied Computational Electromagnetics*, Tampere, 2010.

[9] G. Dong, Y. Shen, H. He, J. Virkki, and S. Hu, "Chipless graphene tag and dual-CP reader for Internet of Things," in *2017 International Applied Computational Electromagnetics Society Symposium*, Suzhou, 2017.

[10] Ministry of Industry and Information Technology of the People's Republic of China, April 3, 2013. [Online]. Available: http://www.miit.gov.cn/n1146285/n1146352/n3054355/n3057735/n3057748/n3057752/c3653822/content.html

[11] J. Huang and S. W. Lee, "Tri-band frequency selective surface with circular ring elements," in *Antennas and Propagation Society International Symposium*, pp. 204-207, 1991.

[12] R. Janaswami and D. H. Schaubert, "Characteristic impedance of a wide slot line on low permittivity substrates," *IEEE Trans. Microw. Theory Techn.*, vol. 34, no. 8, pp. 900-902, 1986.

[13] D. Hotte, R. Siragusa, Y. Duroc, and S. Tedjini, "Radar cross-section measurement in millimetre-wave for passive millimetre-wave identification tags," *IET Microw. Antennas Propag.*, vol. 9, pp. 1-7, 2015.

[14] A. Vena, E. Perret, and S. Tedjni, "A depolarizing chipless RFID tag for robust detection and its FCC compliant UWB reading system," *IEEE Trans. Microw. Theory Techn.*, vol. 61, no. 8, pp. 2982-2994, 2013.

[15] M. I. Skolnik, *Radar Handbook.* New York: McGraw-Hill, 1970.

[16] A. Vena, E. Perret, and S. Tedjini, "A fully printable chipless RFID tag with detuning correction technique," *IEEE Microw. Wireless Compon. Lett.*, vol. 22, no. 4, pp. 209-211, 2012.

[17] M. A. S. Miacci, E. L. Nohara, I. M. Martin, *et al.*, "Indoor radar cross section measurements of simple targets," *J. Aerosp. Technol. Manag.*, vol. 4, pp. 25-32, 2012.

Adaptive Compensation Loop Control Method for Dynamic Range Wireless Power Transfer in Endoscopic Capsules Applications

Hao Zhang [1,2], Zheng Zhong [2], and Wen Wu [1]

[1] School of Electronic and Optical Engineering
Nanjing University of Science and Technology, Nanjing, 210094, China
18501566409@163.com, wuwen@mail.njust.edu.cn

[2] Department of Electrical and Computer Engineering
National University of Singapore, Singapore, 117583, Singapore
elezhon@nus.edu.sg

Abstract ─ In this paper, an adaptive compensation loop control method is presented for dynamic range wireless power transfer (WPT) based wireless endoscopic capsules (WEC) applications. Rather than a fixed external resistor feedback network utilized in the DC-DC converter with maximum power point control (MPPC) capability, an enhanced nMOSFET based adaptive compensation loop is introduced to extract maximum power transfer from the RF-DC rectifier within overall operational power range of the WEC system. Simulation in ADS and measurement among three rectifiers with an LDO, a fixed external resistor feedback network and an adaptive compensation loop control are performed respectively to achieve a steady 3.3V on a resistive load of 100Ω, which validates that the proposed adaptive compensation loop control method realizes an extended dynamic power range with a lower limit of 21.5dBm to realize a minimum 100mW load DC power delivery for the IPT enabled WEC system.

Index Terms ─ Adaptive compensation loop, dynamic range, enhanced nMOSFET, MPPC, resistor feedback network, WEC, WPT.

I. INTRODUCTION

Wireless endoscopic capsules (WEC) technology has been developing and researching rapidly in recent years since it provides an alternative solution to the traditional endoscopies for the painless diagnosis of cancer or other diseases affecting the gastrointestinal tract [1]. It releases patients from the painful surgical operations thanks to its specific attributes of the convenience and non-invasion compared with a traditional endoscopy, which enables the patients to have more comfortable medical check-ups and allow a doctor to get a comprehensive profile of the patients' physiological conditions.

However, the power capacity limitation of the cell batteries has become a bottleneck in the WEC's wide applications. Typically, an inductive power transfer (IPT) [2] is introduced to get rid of this constraint (see Fig. 1). A receiving coil captures the alternative magnetic field generated by a transmitting coil to convert into the alternative electrical field as a power source. Then this portion of power is delivered into an RF-DC rectifier for the rectification to achieve a direct voltage V_{in}. However V_{in} is usually not stable for the DC voltage supply requirement of some commercial electronics, such as a micro-programmable control unit (MCU) and sensors. Therefore it's needed to regulate V_{in} by a DC-DC converter (see Fig. 1). In the traditional IPT system, a low dropout (LDO) regulator is typically adopted as the DC-DC converter. When V_{in} is slightly more than the rated operational voltage V_o, LDO is an effective and simple choice for the battery-powered applications [3]. Nevertheless, if V_{in} is much more than V_o, LDO will introduce much power loss as its operation mechanism is only to regulate V_{in} without considering the DC-DC conversion efficiency.

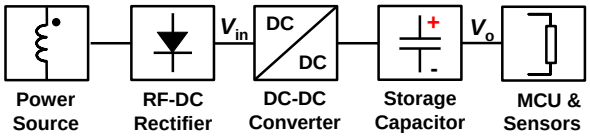

Fig. 1. Block diagram of a IPT receiver.

Therefore, it's essential to adopt a DC-DC bulk with a maximum power point control (MPPC) capability instead of a traditional LDO, which enables a maximum power transfer extraction from a non-ideal DC voltage source when V_{in} is much more than V_o in the IPT system. Nevertheless, some commercial DC-DC converters (e.g., LTC3129-1) can only be controlled with a fixed external

Submitted On: September 30, 2017
Accepted On: April 10, 2018

high resistor feedback network, which maximizes power transfer from a specific and fixed non-ideal DC voltage source [4].

In this paper, rather than a fixed external high resistor feedback network employed in the DC-DC converter, an enhanced nMOSFET Si2342DS based adaptive compensation loop control is proposed to extract the maximum power transfer from the HSMS282P based voltage doubler rectifier over a wide dynamic range of the WEC system. Measurement and fabrication validate that the proposed adaptive compensation loop control enables an extended dynamic power range with a lower limit of 21.5dBm (22.5dBm for the fixed external high resistor network and 25dBm for the LDO SPX3819 in our previous work [8]) to realize a minimum 100mW load DC power delivery, which brings a practicality for the IPT enabled WEC applications.

II. THEORY ANALYSIS

To maximize power extraction from a non-linear DC power source, the DC-DC converter maximum power transfer incident voltage $V_{\text{in(MPPC)}}$ can be controlled by a constant external resistor feedback network consisting of two high resistors R_{high} and R_{low} as:

$$V_{\text{in(MPPC)}} = V_{\text{ref}}\left(\frac{1 + R_{\text{low}}/R_{\text{high}}}{R_{\text{low}}/R_{\text{high}}}\right), \quad (1)$$

where V_{ref} is the reference voltage of the implemented DC-DC converter (e.g., V_{ref} =1.175V in LTC3129-1).

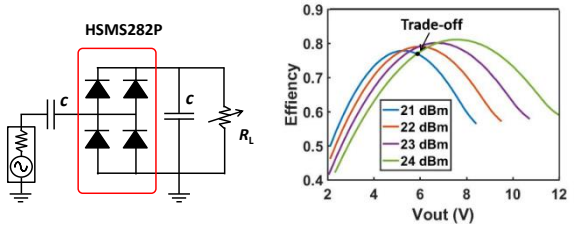

(a) (b)

Fig. 2. (a) HSMS282P based voltage doubler rectifier; (b) power conversion efficiency versus output voltage.

However, the RF-DC rectifier, as a non-ideal power source, can generate different $V_{\text{in(MPPC)}}$ as the incident voltage supply of the LTC3129-1 within various incident powers [5]. Therefore, it addresses an extreme challenge for the fixed voltage $V_{\text{in(MPPC)}}$ in (1) to extract a maximum power transfer within a wide dynamic range IPT enabled WEC system, which requires an adaptive compensation loop to dynamically adjust the ratio of $R_{\text{low}}/R_{\text{high}}$. For the validation, a HSMS282P based voltage doubler rectifier (see Fig. 2 (a)) is designed with harmonic balance (HB) simulation in ADS at 200KHz by sweeping a resistive load R_{L}. Incident power varies from 21dBm to 24dBm, which covers a WEC system's operational power range. Parallel-diode topology of HSMS282P is implemented to reduce the semiconductor resistive loss of R_{s} in its current path when charging and discharging during the procedure of RF-DC rectification [6]. Power conversion efficiency versus output voltage is then calculated in Fig. 2 (b). Thus $V_{\text{in(MPPC)}}$ of HSMS282P based voltage doubler rectifier with the maximum power transfer efficiency is confirmed to be increased with its incident powers [5]. When a trade-off $V_{\text{in(MPPC)}}$=6V is selected with a fixed ratio $R_{\text{low}}/R_{\text{high}}$ around 0.24, a maximum overlap RF-DC conversion efficiency of 74% can only be achieved over power range from 21dBm to 24dBm. Even worse, when the IPT receiver acquires more conversion efficiency, there may be no trade-off $V_{\text{in(MPPC)}}$ for the input voltage supply of the DC-DC converter, which degrades a WEC system performance considerably. Detailed simulation and calculation of a HSMS282P based voltage doubler rectifier (see Fig. 2 (a)) is provided in Table 1 over the WEC operational power range from 21dBm to 24dBm. $V_{\text{in(MPPC)}}$ of the implemented DC-DC converter equals output voltage V_{out} with the maximum power conversion efficiency $E_{ff\text{max}}$ in Fig. 2 (b). Ratio of $R_{\text{low}}/R_{\text{high}}$ can be calculated by reference to the Equation (1). Consequently, $V_{\text{in(MPPC)}}$, $E_{ff\text{max}}$ and $R_{\text{low}}/R_{\text{high}}$ can be determined within different power levels (i.e., Table 1). Noticeably, it's observed an obvious $R_{\text{low}}/R_{\text{high}}$ variation occurs, which seriously degrades the $V_{\text{in(MPPC)}}$ extraction for the LTC3129-1 to maximize power transfer from a non-ideal DC voltage source (i.e., a rectifier in Fig. 2 (a)).

Table 1: Simulation data of the rectifier in Fig. 2 (a)

P_{in} (dBm)	$V_{\text{in(MPPC)}}$ (V)	$E_{ff\text{max}}$ (%)	$R_{\text{low}}/R_{\text{high}}$
21	5.27	79	0.29
22	5.98	79.2	0.25
23	6.74	80.1	0.21
24	7.61	81.1	0.18

So as to get rid of the constraint mentioned, ratio of $R_{\text{low}}/R_{\text{high}}$ in the external high resistor feedback network should be compensated dynamically to achieve $V_{\text{in(MPPC)}}$ within different incident power levels. In order to enable a simple and compact circuit, dynamic adjustment of R_{low} is introduced in this research. Moreover, the voltage drop along R_{low} is constant and equal to the internal V_{ref} of 1.175V [4] under maximum power transfer condition of HSMS282P based voltage doubler based rectifier. Thus, an initial rectifier design with an adaptive loop control is proposed in Fig. 3 with a compensation resistor R_{c}, which functions to dynamically adjust the current (i.e., I_3) in the external high resistor feedback network.

When input power increases, the output current I_1 of RF-DC rectifier rises accordingly along with the input voltage V_{in}. Then it requires a higher $V_{\text{in(MPPC)}}$ for the input supply of the LTC3129-1 in Table 1 to extract the maximum power transfer efficiency. Therefore the compensation resistor R_{c} should be reduced to increase

I_3 until the voltage at MPPC pin equals the internal reference V_{ref}. Then the input voltage $V_{in(MPPC)}$ of the DC-DC converter can be expressed:

$$V_{\text{in(MPPC)}} = V_{\text{ref}} + R_{\text{high}} I_3. \tag{2}$$

In this research, an enhanced nMOSFET based compensation control is introduced to function as R_c in Fig. 3. Typically V_{GS} biased nMOSFETs are applied to achieve a variable resistor in its deeply linear operational region and the drain-to-source channel current I_D before approaching its saturation value can be expressed as:

$$I_{\text{D}} = \mu_{\text{n}} C_{\text{ox}} \frac{W}{L}\left[(V_{\text{GS}} - V_{\text{TH}})V_{\text{DS}} - \frac{1}{2}V_{\text{DS}}^2\right], \tag{3}$$

where W is gate width, L is gate length, μ_n is a foundry concerned constant, C_{ox} is the capacitance in the oxide layer and V_{TH} is the intrinsic threshold voltage.

Therefore V_{GS} controls the value of channel current I_D. When I_D reaches its saturation with $V_{DS} \geq V_{GS}-V_{TH}$, the maximum channel current remains constant as:

$$I_{\text{D,max}} = \frac{1}{2}\mu_{\text{n}} C_{\text{ox}} \frac{W}{L}(V_{\text{GS}} - V_{\text{TH}})^2. \tag{4}$$

Typically, if $V_{DS} << 2(V_{GS}-V_{TH})$, the nMOSFET operates in its deeply linear operational region and the DC-IV characteristic can be simplified as:

$$I_{\text{D}} \approx \mu_{\text{n}} C_{\text{ox}} \frac{W}{L}(V_{\text{GS}} - V_{\text{TH}})V_{\text{DS}}. \tag{5}$$

Thus, the drain-to-source channel can be expressed as a V_{GS} controllable resistor R_{DS}:

$$R_{\text{DS}} = \frac{1}{\mu_{\text{n}} C_{\text{ox}} \frac{W}{L}(V_{\text{GS}} - V_{\text{TH}})}. \tag{6}$$

Then R_{DS} is regarded as a linear function of V_{DS} when V_{GS} remains constant. However, when V_{GS} decreases, R_{DS} increases inversely. Therefore, variable drain-to-source channel resistor R_{DS} can be realized with variation of V_{GS}. However, the value of R_{DS} in its deeply linear operational region of nMOSFET is typically not high enough for the compensation resistor R_c variation requirement in Fig. 3.

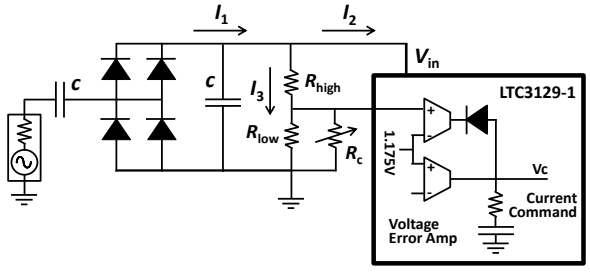

Fig. 3. Proposed circuit with a compensation resistor R_c.

In order to realize an efficient adaptive compensation control loop design, the internal reference voltage V_{ref} of the implemented DC-DC converter is utilized. As shown in Fig. 3, the function of R_c is to dynamically adjust I_3 through the external high resistor feedback network. Rather than the application of R_{DS} in its deeply linear region, V_{GS} biased nMOSFET current source is adopted to enable the current I_3 control with V_{DS} equal the internal voltage reference V_{ref} of the implemented DC-DC bulk under the maximum transfer from the rectifier in Fig. 2 (a). Therefore, V_{GS} biased current source can replace R_c to behave like an equivalent enhanced variable resistance $R_{DS,en}$, which functions to dynamically adjust I_3 within different powers. When $V_{DS} \geq V_{GS}-V_{TH}$, I_D maintains its maximum value $I_{D,max}$ in (4). Hence, the drain-to-source channel can still be controlled by the V_{GS} while V_{DS} maintains constant with V_{ref} of 1.175V. Under this condition, the equivalent enhanced $R_{DS,en}$ functions as the compensation R_c:

$$\begin{aligned} R_{\text{DS,en}} &= \frac{V_{\text{DS}}}{I_{\text{D,max}}} = \frac{2V_{\text{DS}}}{\mu_{\text{n}} C_{\text{ox}} \frac{W}{L}(V_{\text{GS}} - V_{\text{TH}})^2} \\ &= \frac{2V_{\text{DS}}}{(V_{\text{GS}} - V_{\text{TH}})} R_{\text{DS}}. \end{aligned} \tag{7}$$

Therefore, the current I_3 adjusting capability from R_{DS} is enhanced by a coefficient of $2V_{DS}/(V_{GS}-V_{TH})$ when $V_{DS}=V_{ref} \geq V_{GS}-V_{TH}$ under the maximum power extraction from the rectifier in Fig. 2 (a). When an ultra-small V_{GS} is selected, the ultra-high channel equivalent $R_{DS,en}$ in (7) can be realized to satisfy R_c requirements for I_3 current variation in the external high resistor feedback network. Thus, $V_{in(MPPC)}$ can be dynamically adjusted to enable the maximum power extraction from the HSMS282P based voltage doubler rectifier (see Fig. 2 (a)). If the applied nMOSFET is ultra-sensitive, the drain-to-source channel can be threshold with a current of several μA under ultra-small V_{GS} bias. Then equivalent $R_{DS,en}$ is achieved with a super I_3 current adjusting capability for the adaptive compensation loop control. When input power increases, the output current I_1 of the RF-DC rectifier rises as well as V_{in} in Fig. 3. Therefore, the implemented nMOSFET achieves more V_{GS} from the input voltage of LTC3129-1 with more $I_{D,max}$ to enable higher I_3. Then higher $V_{in(MPPC)}$ can be achieved in (2) since R_{high} is fixed, by which the adaptive compensation control is realized.

III. CIRCUIT DESIGN

In order to implement the internal reference V_{ref} for the adaptive compensation control design, nMOSFET drain connects the MPPC pin of the applied DC-DC converter to enable a constant V_{DS}=1.175V under maximum power transfer condition. While V_{GS} is biased through a high resistor voltage divider consisting of R_a and R_b to achieve an ultra-small $V_{GS}=V_{in}R_b/(R_a+R_b)$.

As $V_{in(MPPC)}$ increases with the incident power in

Table 1, the implemented high resistor voltage divider captures $V_{in(MPPC)}$ variation within incident powers from 21dBm to 24dBm. Then the captured $V_{GS}=V_{in}\cdot R_b/(R_a+R_b)$ biases the nMOSFET gate to enable current I_3 adjustment of the drain-to-source channel. Therefore, the equivalent current command $R_{DS,en}$ is realized, which compensates the $V_{in(MPPC)}$ in (2) dynamically for the maximum power extraction from a non-ideal source (e.g., a rectifier in Fig. 2 (a) once the incident RF power changes.

Accordingly, it demands the adopted nMOSFET with a high current sensitivity with small V_{GS} bias to threshold the drain-to-source current channel. Thus, an enhanced nMOSFET Si2342DS [7] is implemented to realize V_{GS} controlled $R_{DS,en}$ in (7). Meanwhile, V_{GS} should be ultra-small to ensure $R_{DS,en}$ ultra-high to minimize the current flowing through the drain-source channel of Si2342DS with V_{DS}=1.175V, due to which the voltage divider of R_a and R_b is high enough for current I_3 in (2) control requirement to capture different $V_{in(MPPC)}$ (see Table 1) simultaneously with a subtle power consumption. For accurate DC-IV measurement of the Si2342DS, an SMA based 24mil FR4 test fixture is fabricated in Fig. 4 (a). V_{GS} is swept from 0.4V to 0.58V with a high resistor voltage divider of R_a=620KΩ and R_b=51KΩ to sense and capture $V_{in(MPPC)}$ variation from 5.27V to7.61V exactly according to $V_{GS}=V_{in}R_b/(R_a+R_b)$ and maintains $V_{DS}=V_{ref}$ of the implemented DC-DC converter. The compensated ratio of R_{low}/R_{high} can be plotted with R_{low}=27KΩ and R_{high}=100KΩ, which is shown by the blue dotted curve (i.e., *Ratio-Compensate*) in Fig. 4 (b). By contrast, a fixed ratio of R_{low}/R_{high}=0.24 is provided with R_{low}=24 KΩ and R_{high}=100KΩ by a black dash curve (i.e., *Ratio-Fixed*) and optimal ratio of R_{low}/R_{high} is calculated with various $V_{in(MPPC)}$ from 5.27V to 7.61V in Table 1, which is plotted by a solid red curve (i.e., *Ratio-Optimal*).

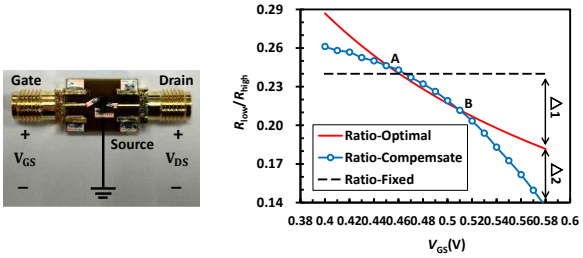

(a) (b)

Fig. 4. (a) SMA based DC-IV 24mil FR4 test fixture; (b) measurement of *Ratio-Compensate* with blue curve.

In this research, different V_{GS} would adaptively adjust the current I_3 in Fig. 5 based on $V_{in(MPPC)}$ from 5.27V to 7.61V in Table 1. The current I_3 with different V_{GS} can be precisely measured by the test fixture in Fig. 4 (a). Therefore, $V_{in(MPPC)}$ in (2) can be calculated with a fixed R_{high}=100KΩ. Then the ratio of R_{low}/R_{high} in (1) is achieved, which can be plotted as *Ratio-Compensate* curve in Fig. 4 (b) under different V_{GS}. For the comparison with the *Ratio-Compensate* curve, $V_{in(MPPC)}$ from 5.27V to 7.61V is normalized by $(R_a+R_b)/R_b$ (i.e., $V_{GS}=V_{in(MPPC)}R_b/(R_a+R_b)$) in the *Ratio-Optimal*. Then *Ratio_Optimal* can be achieved from R_{low}/R_{high} in Table 1 under different $V_{GS}=V_{in(MPPC)}R_b/(R_a+R_b)$. Thus, *Ratio-Compensate* and *Ratio-Optimal* can be plotted with same horizontal coordinate in Fig. 4 (b). There are two intersection points A and B between the *Ratio-Optimal* and *Ratio-Compensate* curves. When V_{GS} < 0.46V (i.e., $V_{in(MPPC)}$ =6.05V) satisfies at A, *Ratio-Compensate* curve is closer to *Ratio-Optimal* than *Ratio-Fixed*. Especially between A and B, *Ratio-Compensate* and *Ratio-Optimal* are almost unanimously. Whereas the *Ratio-Compensate* and *Ratio-Fixed* deviate in opposite direction compared to *Ratio-Optimal* when V_{GS} > 0.515V (i.e., $V_{in(MPPC)}$= 6.78V) at the intersection point B, delta ratio of the *Ratio-Fixed* and the *Ratio-Compensate* between *Ratio-Optimal* could be calculated with Δ_1=0.06 and Δ_2=0.04, which indicates the *Ratio-Compensate* precedes *Ratio-Fixed* even with a maximum input voltage V_{GS} = 0.58V (i.e., $V_{in(MPPC)}$=7.6V). Therefore, when V_{GS} increases from 0.4V to 0.58V (i.e., $V_{in(MPPC)}$ from 5.27V to7.61V in Table 1), the proposed adaptive compensation loop satisfies variation requirement of R_{low}/R_{high} for the overall $V_{in(MPPC)}$ in Table 1 within all power ranges of the implemented LTC3129-1 to maximize DC power transfer from HSMS282P based voltage doubler rectifier.

However, in the circuit design, it suggests that the bulk-boost DC-DC converter LTC3129-1 should be restricted with a maximum input voltage up to 15V [4]. Though HSMS282P based voltage doubler rectifier has a limited maximum output voltage of 15V due to its breakdown voltage [5], the semiconductor fabrication variation or other factors may cause breakdown voltage V_{br} more than 15V slightly, which will make its maximum output voltage more than 15V to damage LTC3129-1 permanently. Therefore, a 15V Zener diode is adopted for protection as shown in Fig. 5.

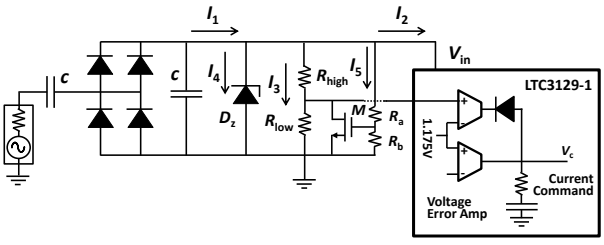

Fig. 5. Final proposed circuit with nMOSFET Si2342DS and 15V Zener diode (D_z).

The power conversion efficiency is more concerned in a WEC system. Thus, the power consumption caused

by Zener diode is analyzed and proven to be ultra-low if the switching frequency of LTC3129-1 is high enough. When open circuit voltage of HSMS282P based voltage doubler rectifier is more than 15V, a limited 15V for protection could only be applied as input voltage of the DC-DC converter LTC3129-1. Then the high resistor feedback network captures the input voltage to dynamically increase I_2 until the input voltage less than 15V. Meanwhile, linkage current I_4 of the Zener diode decreases to zero when input voltage less than 15V. This procedure responds transiently as switching frequency at PWM mode of LTC3129-1 is ultra-high of 1.2MHz [4] with a subtle power consumption. Therefore, the final circuit with a Si2342DS based adaptive compensation loop is proposed for the DC-DC converter to extract the maximum power transfer from the RF-DC rectifier as shown in Fig. 5.

IV. MEASUREMENT AND RESULTS

Three WPT receiver circuits are fabricated with LDO SPX3819 [3] and DC-DC bulk LTC3129-1 with/without nMOSFET based adaptive compensation control loop respectively as shown in Fig. 6 (a). HSMS282P Schottky diodes and several 0603 packaging passive elements are soldering on the 24mil FR4. For the measurement setup, signal generator AV1441A outputs 200 KHz RF signal. Then the RF signal is amplified by a commercial power amplifier (PA) and pre-calibrated by the spectrum analyzer AV4037. A 100 Ω load resistor is employed as a representative of the MCU and sensor networks. As these three WPT receiver circuits are designed with a fixed output steady DC voltage of 3.3V to satisfy minimum 100mW load power supply requirement, thus the output voltages along R_L are measured as shown in Fig. 6 (c). When the input power approaches 22.5dBm, the WPT receiver with a fixed ratio R_{low}/R_{high}=0.24 satisfy 100mW load power supply requirement at input power 22.5dBm and outperforms one with LDO SPX3819 from 22.5dBm to 24.5dBm. By comparison, Si2342DS based adaptive compensation loop of LTC3129-1 can further extract maximum DC power transfer from HSMS282P based voltage doubler rectifier over lower input powers. Measurement indicates that the power supply of 100mW with a output voltage around 3.3V can be achieved by the adaptive compensation loop based WPT receiver at 21.5dBm, which realizes an extended dynamic power range with a lower limit of 21.5dBm (22.5dBm for the fixed external high resistor network and 25dBm for the LDO SPX3819 in our previous work [8]) to realize a minimum 100mW load DC power delivery for the IPT enabled WEC system.

V. CONCLUSION

In this paper, an adaptive compensation loop control method is presented for dynamic range wireless power transfer (WPT) based wireless endoscopic capsules (WEC) applications. Rather than a fixed external resistor feedback network utilized in the DC-DC converter LTC3129-1, an enhanced nMOSFET Si2342DS based adaptive compensation loop is introduced to facilitate the maximum power transfer of the HSMS282P based voltage doubler rectifier from 21dBm to 24dBm, which can cover overall operational incident powers of the WEC system. Measurement validates that the proposed adaptive compensation loop control method realizes an extended dynamic power range with a lower limit of 21.5dBm to realize a minimum 100mW load DC power delivery for the IPT enabled WEC system. The method presented in this paper can be applied to combine with numerical solution to enable fast simulation of maximum power transfer efficiency based on coils modeling, which brings a practicality for an efficient IPT enabled WEC system.

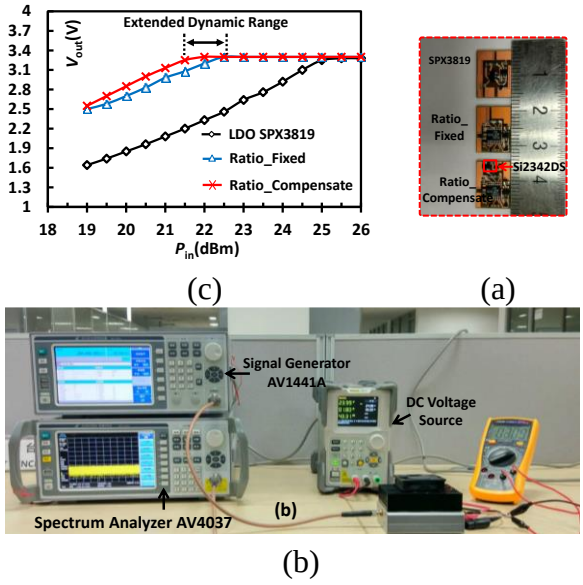

Fig. 6. (a) Fabrications of three applied WPT receivers; (b) measurement setup; (c) measurement results.

ACKNOWLEDGMENT

This work was supported in part by Singapore National Research Foundation Industry-IHL Partnership grant, in part by National Natural Science Foundation of China under the Grant No. 61401296, in part by the Natural Science Foundation for Youths of Jiangsu Province, China under Grant No. BK20130375 and Suzhou Science and Technology Council, China under Grant SYG201618.

REFERENCES

[1] G. Tortora, F. Mulana, G. Ciuti, P. Dario, and A. Menciassi, "Inductive-based wireless power recharging system for an innovative endoscopic capsule," *Energies*, vol. 8, no. 9, pp. 10315-10334,

2015.
[2] J. Zhiwei, Y. Guozheng, W. Zhiwu, and L. Hua, "Efficiency optimization of wireless power transmission systems for active capsule endoscopes," *Physiol. Meas.*, vol. 32, no. 10, p. 1561, 2011.
[3] T. A. Circuit, "Spx 3819 Electrical Characteristics," no. 510, 2008.
[4] Linear Technology, "LTC3129: 15V, 200mA Synchronous Buck-Boost DC/DC Converter with 1.3µA Quiescent Current," pp. 1-30, 2013.
[5] T.-W. Yoo and K. Chang, "Theoretical and experimental development of 10 and 35 GHz rectennas," *IEEE Trans. Microw. Theory Tech.*, vol. 40, no. 6, pp. 1259-1266, 1992.
[6] E. Falkenstein, M. Roberg, and Z. Popovic, "Low-power wireless power delivery," *IEEE Trans. Microw. Theory Tech.*, vol. 60, no. 7, pp. 2277-2286, 2012.
[7] Datasheet of Si2342DS: N-Channel 8V (D-S) MOSFET, Vishay Siliconix.
[8] H. Zhang, Z. Zhong, and W. Wu, "Extracting maximum efficiency of wireless power transfer in endoscopic capsule applications," in *Applied Computational Electromagnetics Society Symposium (ACES), 2017 International*, pp. 1-2, 2017.

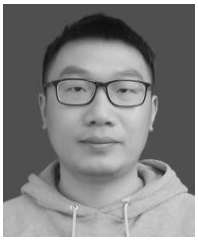

Hao Zhang was born in Jiangsu, China, in 1990. He received the B.Eng. degree from the School of Electronic and Optical Engineering, Nanjing University of Science and Technology, Nanjing, China, in 2014, where he is currently pursuing his Ph.D. degree. He was a Visiting Scholar with the Department of Electrical and Computer Engineering, National University of Singapore from July 2016 to July 2017. His current research interests include RF energy harvesting and wireless power transfer for biomedical applications and Internet of Things (IoTs).

Zheng Zhong received the B.Eng. and M.E. degrees from the University of Science and Technology of China, Hefei, China, in 2003 and 2006, respectively, and the Ph.D. degree in Microwave Engineering from the National University of Singapore (NUS), Singapore, in 2010. He has been a Research Fellow with the Department of Electrical and Computer Engineering, NUS, since 2010. His current research interests include RF/microwave semiconductor devices modeling and characterization, microwave and millimeterwave microwave integrated circuit/MMIC circuits design, and RF energy harvesting.

Wen Wu received the Ph.D. degree in Electromagnetic Field and Microwave Technology from Southeast University, Nanjing, China, in 1997. He is currently a Professor with the School of Electronic Engineering and Optoelectronic Technology, and an Associate Director of the Ministerial Key Laboratory of JGMT with the Nanjing University of Science and Technology, Nanjing, China. He has authored or co-authored over 240 journal and conference papers. He holds 14 patents. His current research interests include microwave and millimeter-wave theories and technologies, microwave and millimeter-wave detection, and multimode compound detection. Mr. Wu was the recipient of the Ministerial and Provincial-Level Science and Technology Awards six times.

Precision Loss Analysis and Its Solution in Calculation of Electromagnetic Wave Propagation in Reentry Plasma Sheath

Xuyang Chen [1], Fangfang Shen [1], Yanming Liu [1], Wei Ai [2], and Xiaoping Li [1]

[1] School of Aerospace Science and Technology
Xidian University, Xi'an, Shaanxi 710071, China
xychen@mail.xidian.edu.cn, ffshen@mail.xidian.edu.cn, ymliu@xidian.edu.cn, xpli@xidian.edu.cn

[2] Science and Technology on Space Physics Laboratory
China Academy of Launch Vehicle Technology, Beijing 100076, China
27821126@qq.com

Abstract — In this paper, the precision loss problem in calculation of EM wave propagation in the extreme reentry plasma sheath environment is analyzed. Furthermore, we propose a numerical calculation method with controllable precision to deal with this problem. The simulation results show the effect of computational precision loss on EM wave propagation in reentry plasma sheath and also illustrate the validity of the controllable precision calculation method.

Index Terms — Controllable precision, EM wave propagation, numerical calculation, precision loss, reentry plasma sheath.

I. INTRODUCTION

It has generated increasing concern about the interactions of electromagnetic (EM) wave with plasma in recent decade years [1-6], which refers to several applications, such as, analysis of reentry plasma sheath, plasma stealth, nuclear fusion control, etc. The reentry plasma sheath, as a special type of plasma, has several distinct characteristics, such as, extreme electron density and time variation, which severely influence the communication with the reentry object and the radar detection of the object. The extreme parameters (especially for the electron density) will cause precision loss in calculation of EM wave propagation, further causing computational error or even misdirection in EM calculation and simulation. The extreme characteristics mainly occur at the head location of a plasma-covered object. For the electron density, it has reached $10^{19}/m^3$ or even $10^{20}/m^3$ at the head location in a reentry flight [7,8]. However, the researchers [1-3, 9-11] studying the interaction between EM wave and reentry plasma sheath mainly focus on the side or tail locations of the object, where the plasma is far less extreme than that at the head location. Certainly, due to this reason, the computational error in their studies is trivial and can be ignored. Whereas, the plasma influence with extreme parameters (especially for the head location of object) cannot be ignored. This will inevitably give rise to the precision loss problem.

In our previous work [12], we have pointed out that the precision loss problem in calculation of EM wave propagation in plasma sheath lies in the limited numerical calculation precision of computer (usually it is double precision). In this paper, we will give further qualitative and quantitative analysis on the precision loss problem. Then, we propose a computing method with controllable precision based on python platform. By this method, the EM wave propagation in plasma sheath can be computed in a much higher precision by a controllable number of digits, eliminating the precision loss problem. In the simulation, the effect of computational precision loss on EM wave propagation is presented, and the validity of the controllable precision calculation method is illustrated.

The remainder of the paper is organized as follows. Sec. II presents the background of EM wave propagation in plasma. The precision loss analysis and its solution in calculation of EM wave propagation in plasma sheath are shown in Sec. III. Section IV shows the simulation results. The conclusions are finally given in Sec. V.

II. BACKGROUND OF EM WAVE PROPAGATION IN PLASMA

A typical stratification model [4,13] for EM wave propagating in plasma environment is presented in Fig. 1. As can be seen in Fig. 1, an EM plane wave (with its electric part labeled by E_i) is transmitted along x-axis into a nonuniform plasma slab. In each sub-slab (or layer), the plasma is thought to be uniform. The layers are labeled by $l_0, l_1, ..., l_p$ from front-layer (where the EM wave enters into the plasma) to bottom-layer (usually

Submitted On: October 14, 2017
Accepted On: January 22, 2018

corresponding to the metallic surface of an object), respectively. The thickness of layer l_m is represented by $d_{m+1}-d_m$, $m\in\{0,1,2,...,p\}$ (note: d_1=d_0=0), and B denotes the background magnetic field in the plasma environment.

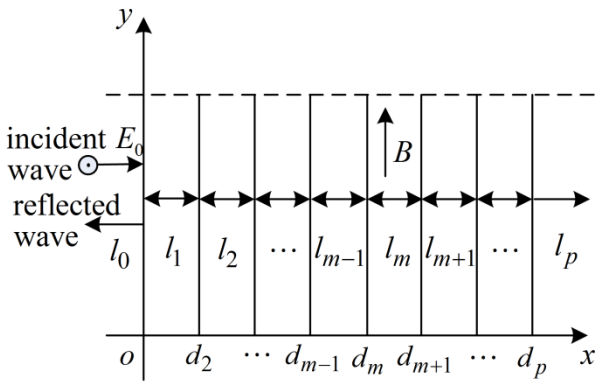

Fig. 1 Stratification model of nonuniform plasma.

The total electric field in layer l_m can be expressed as the following form:

$$E_z^{(m)}(x)=E_0B_m\exp\left(-jk_x^{(m)}(x-d_m)\right)+E_0C_m\exp\left(jk_x^{(m)}(x-d_m)\right),\quad x\in[d_m,d_{m+1}),\tag{1}$$

where E_0 is the input electric field at location x=0, $k_x^{(m)}$ is the complex propagation coefficient in layer l_m, and B_m and C_m are the transmission coefficient and the reflection coefficient at the interface between layers l_{m-1} and l_m, respectively. The detailed expression of $k_x^{(m)}$ can be found in Appendix Section.

There are two important parameters: the total reflection coefficient C_0 and the total transmission coefficient B_p, which reflect the EM reflection and transmission properties of the whole plasma, respectively. These two parameters can be obtained by iteratively solving the equations of boundary conditions [4,14]:

$$\begin{cases} B_m + C_m = B_{m-1}\exp(-jk_x^{(m-1)}(d_m-d_{m-1})) + C_{m-1}\exp(jk_x^{(m-1)}(d_m-d_{m-1})) \\ k_x^{(m)}B_m - k_x^{(m)}C_m = k_x^{(m-1)}B_{m-1}\exp(-jk_x^{(m-1)}(d_m-d_{m-1})) - k_x^{(m-1)}C_{m-1}\exp(jk_x^{(m-1)}(d_m-d_{m-1})) \end{cases},$$
$$m\in\{1,2,...,p\},\tag{2}$$

For conveniently analysis in next section, the Equation (2) is expressed as a matrix form by:

$$\begin{pmatrix}B_m\\C_m\end{pmatrix}=\mathbf{S_m}\begin{pmatrix}B_{m-1}\\C_{m-1}\end{pmatrix},\quad m\in\{1,2,...,p\},\tag{3}$$

where $\mathbf{S_m}$ is called scattering matrix, expressed by:

$$\mathbf{S_m}=\begin{pmatrix}1 & 1\\ k_x^{(m)} & -k_x^{(m)}\end{pmatrix}^{-1}\times\begin{pmatrix}\exp(-jk_x^{(m-1)}(d_m-d_{m-1})) & \exp(jk_x^{(m-1)}(d_m-d_{m-1}))\\ k_x^{(m-1)}\exp(-jk_x^{(m-1)}(d_m-d_{m-1})) & -k_x^{(m-1)}\exp(jk_x^{(m-1)}(d_m-d_{m-1}))\end{pmatrix}.\tag{4}$$

The iterative description of (3) containing the coefficients C_0 and B_p can be expressed by:

$$\begin{pmatrix}B_p\\0\end{pmatrix}=\prod_{m=p}^{1}\mathbf{S_m}\begin{pmatrix}1\\C_0\end{pmatrix}=\mathbf{S_g}\begin{pmatrix}1\\C_0\end{pmatrix},\tag{5}$$

where $\mathbf{S_g}=\prod_{m=p}^{1}\mathbf{S_m}$ is the cascaded scattering matrix. The coefficients C_0 and B_p can then be obtained by solving (5).

III. PRECISION LOSS AND ITS SOLUTION IN CALCULATION OF EM WAVE PROPAGATION IN PLASMA SHEATH

A. Analysis of precision loss

The extreme plasma environment almost always occurs in the reentry flight of a reentry vehicle, especially for the head portion of the vehicle, accompanied by extreme plasma parameters [8]. Among those parameters shown in Sec. II, $k_x^{(m)}$ is a key one, since it is included in the exponent part of the term $\exp(\bullet)$. A larger $|k_x^{(m)}|$ will lead to a much higher rate of increase or decrease of the term $|\exp(\bullet)|$. This will produce a quasi-singular form of the scattering matrix $\mathbf{S_m}$. In detail, it is due to the coexist of the term $\exp(-jk_x^{(m-1)}(d_m-d_{m-1}))$ and its reverse form $\exp(jk_x^{(m-1)}(d_m-d_{m-1}))$ in matrix $\mathbf{S_m}$ as shown in (4). The quasi-singular expression of (4) is adverse to the iterative solution of coefficients and may cause the precision loss. For simplifying description below, let:

$$\xi_{(m-1)}=\exp(jk_x^{(m-1)}(d_m-d_{m-1}))$$
$$\text{and }\xi_{(m-1)}^{-1}=\exp(-jk_x^{(m-1)}(d_m-d_{m-1})).$$

It is not difficult to find that the iterative calculation of (3) and (4) can be divided into the four basic operations: add, subtraction, multiplication, and division. For the case of extreme parameters, the precision loss is possible to occur in the operation of the subtraction of two large quantities with the same sign or approximate argument. Specifically, when the two large numbers are numerically approximate, the precision loss is highly probable to occur. Putting the quasi-singular expression of (4) into consideration, we find that the subtraction operations of two large numbers with numerically approximation occur in a high probability in the iterative calculation of coefficients. It should be noted that the

number of valid digits of a double-precision number (adopted by most computers) is only 16. Whereas, the digits of the term $|\xi_{(m-1)}|$ in (4) may be significantly larger than 16 for the extreme plasma sheath. If this case occurs, the subtraction of two big numbers in calculation of (4) will result in obvious or even huge precision loss. The exact estimation of the digits of $|\xi_{(m-1)}|$, however, is intractable, which relates to a complicated interaction of several parameters as shown in Appendix Section. As an available way, the numerical estimation on digits and on precision loss under selected reasonable parameters will be workable.

Before the presentation of numerical estimation, the computational error of the total reflection coefficient C_0 and that of the total transmission coefficient B_p caused by the precision loss should be analyzed. Based on our analysis, we find that the precision loss is not applied equally to C_0 and B_p, but most of it is applied to B_p. This can be explained by exploring the equation form of (5). For clear description, the Equation (5) is rewritten as the following form:

$$\begin{pmatrix} B_p \\ 0 \end{pmatrix} = \begin{pmatrix} S_{g11} & S_{g12} \\ S_{g21} & S_{g22} \end{pmatrix} \begin{pmatrix} 1 \\ C_0 \end{pmatrix}, \tag{6}$$

where S_{g11}, S_{g12}, S_{g21}, S_{g22} are the four elements of matrix $\mathbf{S_g}$. Suppose we have had the prior knowledge that the elements of $\mathbf{S_g}$ are large numbers. Then, one can find that the solution of C_0 relates to the division of S_{g21} by S_{g22}, which will generate little or trivial precision loss. Whereas, the solution of B_p refers to the add (or subtraction) of two large numbers S_{g11} and $S_{g12}C_0$, which will generate obvious precision loss.

Table 1: Calculated plasma parameters for three selected electron densities

Calculated Parameters	Electron Density n_e (m^{-3})		
	10^{18}	10^{19}	10^{20}
$\lvert\xi_{(1)}\rvert$	1.87×10^{2}	1.24×10^{22}	5.03×10^{74}
C_0	$0.19+0.18j$	$-0.62+0.56j$	$-0.92+0.22j$
B_p	$3.98\times10^{-6}-1.71\times10^{-6}j$	$5.24\times10^{5}j$	$3.14\times10^{57}j$
Abs. Err. of C_0	1.00×10^{-16}	0	3.38×10^{-16}
Abs. Err. of B_p	4.25×10^{-15}	5.24×10^{5}	3.14×10^{57}

To show the precision loss as well as the number of digits in a numerical view, we give an example of the absolute calculation errors for three selected electron densities as shown in Table 1. The main selected constant parameters in Table 1 are shown below: number of layers p=2, plasma thickness d_p=0.1m, collision frequency $f_v = 5\text{GHz}$, incident frequency of EM wave $f = 10\text{GHz}$, material of floor media: titanium alloy with conductivity $\sigma = 2.3\times10^{6}\text{S/m}$.

The calculated parameters $|\xi_{(1)}|$, C_0, and B_p in Table 1 are computed in double precision based on the algorithm in Sec. II. For the true coefficients C_0 and B_p (not the calculated ones in Table 1), they are obtained in an analytic way that is only possible for the ideal plasma case with 2 layers in Table 1 but almost impossible for realistic case. The detailed relation between the electron density n_e and the complex propagation coefficient $k_x^{(m)}$ can be found in Appendix for interested readers.

As shown in Table 1, the calculated parameters for the three electron densities n_e are very different. Only the case for $n_e = 10^{18}/\text{m}^3$ generates no or trivial calculation errors. Whereas, with the increase of n_e, the parameter $|\xi_{(1)}|$ changes quite rapidly and generates large calculation errors. But, coinciding with our analysis, only the calculation of B_p generates large errors but that of C_0 nearly produces no error.

B. Solution of precision loss

The precision loss in the calculation of EM wave propagation can be traced to the shortage of precision in numerical calculation of computer. The commonly used data representation format in most computer systems is double precision with 64-bit. This data format shows limitation when it is used to calculate the EM wave propagation in the extreme environment of reentry plasma sheath. One solution is to increase the numerical calculation precision. There are two ways which can be used to implement it. 1) increasing the float representation bits, such as, 128-bit, 256-bit; 2) converting to integer representation. Considering the complexity and availability, we use the second way.

A matrix calculation technique with controllable precision is put forward here to deal with the precision loss problem. It can be found that the matrix computation procedure shown in Sec. II can be decomposed into the four fundamental arithmetic operations of the elements of the matrixes. To carry out the high-precision calculation, each element of the matrixes is expressed by an integer form (including real part and imaginary part) with fixed digitals. Then, the whole EM wave calculations can be implemented in integer arithmetic operations.

For any a complex element number $\chi = \chi_{real} + j\chi_{imag}$, its integer form can be expressed by:

$$\chi_{\mathrm{INT}} = \left\lfloor 10^n \chi_{real} \right\rfloor + j\left\lfloor 10^n \chi_{imag} \right\rfloor, \quad (7)$$

where '$\lfloor \cdot \rfloor$' denotes the 'round down' operation, and n is the fixed digital number. The add or subtraction of two numbers $\chi^{(1)}$ and $\chi^{(2)}$ is simple and not shown here. For the multiplication of the two numbers, it is implemented by:

$$\mathrm{mul}(\chi^{(1)}, \chi^{(2)}) \underline{\underline{def}} \frac{\chi_{\mathrm{INT}}^{(1)} \cdot \chi_{\mathrm{INT}}^{(2)}}{10^n}, \quad (8)$$

where '$\mathrm{mul}(\cdot)$' denotes the integer multiplication operation, and $\chi_{\mathrm{INT}}^{(1)}$ and $\chi_{\mathrm{INT}}^{(2)}$ are the integer expressions of the numbers $\chi^{(1)}$ and $\chi^{(2)}$, respectively. The division of the two numbers is implemented by:

$$\mathrm{div}(\chi^{(1)}, \chi^{(2)}) \underline{\underline{def}} \frac{\chi_{\mathrm{INT}}^{(1)} \cdot \chi_{\mathrm{INT}}^{(2)*} \cdot 10^n}{\left|\chi_{\mathrm{INT}}^{(2)}\right|^2}, \quad (9)$$

where '$div(\cdot)$' denotes the integer division of $\chi^{(1)}$ by $\chi^{(2)}$, and $\chi_{\mathrm{INT}}^{(2)*}$ is the conjugation of $\chi_{\mathrm{INT}}^{(2)}$.

Complying with the above operations, one can calculate the total reflection and transmission coefficients C_0 and B_p in a high accuracy. Clearly, the more digitals n is set, the more accuracy in calculation one gains. Here, we suggest this technique is implemented by Python, in which the setting of digital numbers has no limit.

Finally, we talk about the computational complexity of the algorithm. The stratification algorithm shown in Sec. II has the complexity of $O(pN_f)$ (with p: number of layers, and N_f: samples of incident frequency for analysis). When the controllable-precision method is put into consideration, the complexity becomes to be $O(npN_f)$, where n is the digital number.

IV. SIMULATIONS

The EM wave propagation in reentry plasma sheath with extreme parameters is simulated by both the commonly used double precision and the proposed controllable-precision method. The Python (Version 2.7.6) is utilized to implement the calculation with controllable precision. The digit number for controllable-precision calculation is set as n=80 (referring to Table 1). The incident frequency f ranges from 1MHz to 30GHz (creating 50 frequency samples). The collision frequency of plasma is set to be a constant 5GHz. The number of plasma layer is set as p=13.

Figure 2 shows the simulation results of magnitudes of total transmission coefficient B_p. Figure 2 (a) and Fig. 2 (c) are the results calculated by double precision, and Fig. 2 (b) and Fig. 2 (d) are the results calculated by controllable-precision method. In Fig. 2 (a) and Fig. 2 (b), the electron density is set to be $10^{19}/m^3$. In Fig. 2 (c) and Fig. 2 (d), the electron density n_e ranges from $10^{18}/m^3$ to $10^{20}/m^3$, generating 50 samples of n_e. It should be noted that the setting of parameters above is reasonable and complies with the realistic case. The results of total reflection coefficient C_0 are not presented here due to the weaker comparison effect.

It can be found from Fig. 2 (a) that the precision losses or calculation errors by double precision are prevalent for most of the tested incident frequency f (see the error regions), whereas the correct points or regions occupy a small range of f. This wrong result is severe which even gives a misleading wrong trend. Further considering the variation of electron density n_e in Fig. 2 (c), one can find clearly that the precision loss changes toward larger and wider directions with the increase of n_e. Whereas, the controllable-precision method shows accurate results for all the tested incident frequencies f and electron densities n_e as shown in Figs. 2 (b) and (d).

For the time consumption, it is 0.24s for the controllable-precision method (Fig. 2 (b)) and 0.11s for the commonly used double precision case (Fig. 2 (a)) for the 1-D figures. For the 2-D figures, it is 10.91s for the controllable-precision method (Fig. 2 (d)) and 2.67s for the double precision case (Fig. 2 (c)). Based on the complexity analysis in Sec. III-B, the complexity of the algorithm combined by the controllable-precision method is a multiple of that of the original algorithm with double precision. According to the simulation result and theoretical analysis, this multiple is estimated to be in the range 0.02n~0.06n (n is the digital number). Although there is some time-consuming increase of the controllable-precision method, it is acceptable compared to its gain in precision improvement.

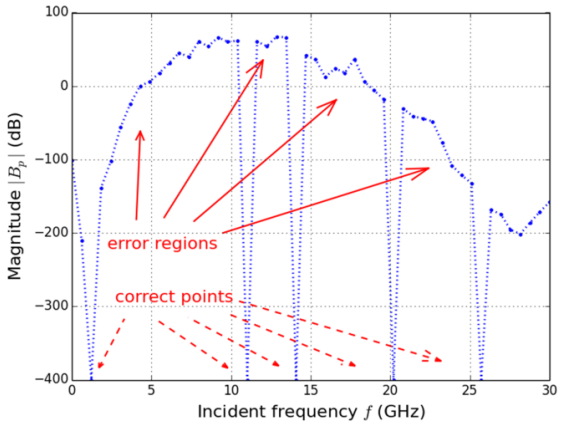

(a)

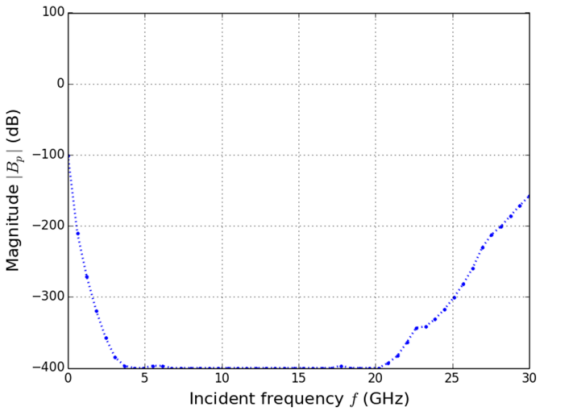

(b)

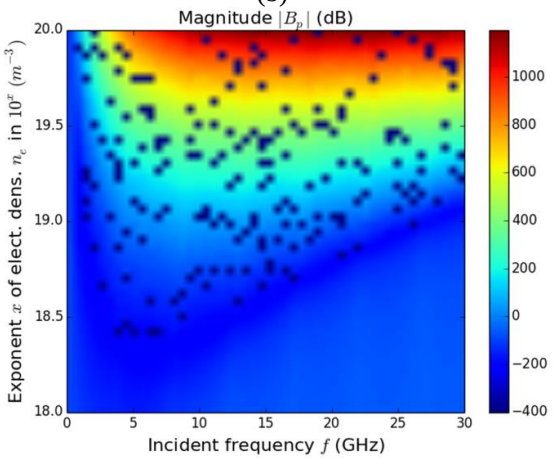

(c)

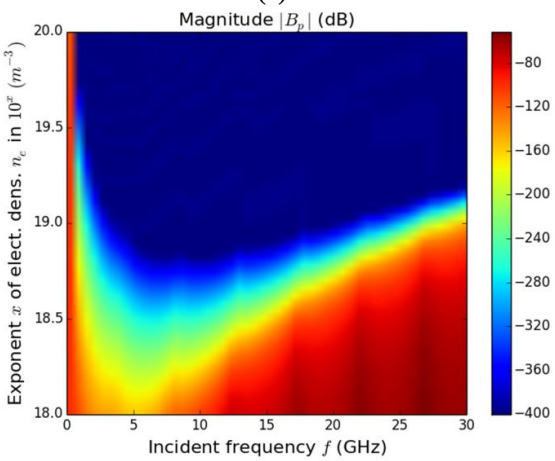

(d)

Fig. 2. Magnitude of transmission coefficient $|B_p|$ calculated by double-precision method and that by controllable-precision method. (a) $|B_p|$ vs. f by double precision with fixing $n_e = 10^{19}/m^3$, (b) $|B_p|$ vs. f by controllable-precision method with fixing $n_e = 10^{19}/m^3$, (c) $|B_p|$ vs. f and n_e by double precision, and (d) $|B_p|$ vs. f and n_e by controllable-precision method.

V. CONCLUSION

The precision loss problem in calculation of EM wave propagating in reentry plasma sheath is analyzed in this paper, and then a solution by numerical calculation with controllable precision is put forward to deal with it. The simulation shows the effect of the precision loss clearly. Also, the proposed controllable-precision calculation method is illustrated to be effective in solving the precision loss problem.

APPENDIX

Relation of propagation coefficient $k_x^{(m)}$, relative complex permittivity $\tilde{\varepsilon}_r^{(m)}$, and electron density n_e [4,15].

The propagation coefficient $k_x^{(m)}$ of the nonuniform plasma in layer l_m is an important parameter related to the EM wave propagation in plasma as described in (1). $k_x^{(m)}$ can be expressed by:

$$k_x^{(m)} = \frac{\omega}{c}\sqrt{\tilde{\varepsilon}_r^{(m)}}, \quad m \in \{0,1,2,...,p\}, \tag{A1}$$

where c is the light speed in vacuum, $\omega = 2\pi f$ is the radian frequency of incident EM wave, and $\tilde{\varepsilon}_r^{(m)}$ is the relative complex permittivity. $\tilde{\varepsilon}_r^{(m)}$ is related to the electric characteristics of a medium. For the plasma medium with layer l_m as shown in Fig. 1, $\tilde{\varepsilon}_r^{(m)}$ can be expressed by:

$$\tilde{\varepsilon}_r^{(m)} = 1 - \frac{\omega_{p,m}^2/\omega^2}{1 - j\frac{\nu_m}{\omega} - \frac{\omega_{ce}^2/\omega^2}{1-\omega_{p,m}^2/\omega^2 - j\nu_m/\omega}}, \quad m \in \{0,1,2,...,p\}, \tag{A2}$$

where $\omega_{p,m}$ and ν_m are the plasma frequency and the collision frequency in m-th layer, respectively, ω_{ce} is the cyclotron frequency of background magnetic field, and all the above symbols are with unit of *rad/s*. The plasma frequency $\omega_{p,m}$ is expressed by:

$$\omega_{p,m} = \sqrt{\frac{n_{e,m}e^2}{\varepsilon_0 m_e}}, \quad m \in \{0,1,2,...,p\}, \tag{A3}$$

where $n_{e,m}$ is the electronic density in plasma layer l_m, ε_0 is the permittivity of vacuum, e and m_e are the electronic quantity and the mass of an electron, respectively.

All the detailed deduction of the above equations (A1~A3) can be found from [15].

ACKNOWLEDGMENT

This work was supported by the National Science Foundation of China under Grants 61701380, the

Science and Technology on Space Physics Laboratory Funds, and the China Postdoctoral Science Foundation (No. 2016M592758).

REFERENCES

[1] K. Xie, M. Yang, B.-W. Bai, X.-P. Li, H. Zhou, and L.-X. Guo, "Re-entry communication through a plasma sheath using standing wave detection and adaptive data rate control," *J. Appl. Phys.*, vol. 119, no. 2, p. 023301, 2016.

[2] S.-H. Liu and L.-X. Guo, "Analyzing the electromagnetic scattering characteristics for 3-D inhomogeneous plasma sheath based on PO method," *IEEE Trans. Plasma Sci.*, vol. 44, no. 11, pp. 2838-2843, Nov. 2016.

[3] M. Yang, X.-P. Li, K. Xie, and Y.-M. Liu, "Parasitic modulation of electromagnetic signals caused by time-varying plasma," *Phys. Plasmas*, vol. 22, no. 2, p. 022120, 2015.

[4] B.-J. Hu, G. Wei, and S.-L. Lai, "SMM analysis of reflection, absorption, and transmission from nonuniform magnetized plasma slab," *IEEE Trans. Plasma Sci.*, vol. 27, no. 4, pp. 1131-1136, Apr. 1999.

[5] H. Torres-Silva, N. Reggiani, and P. H. Sakanaka, "Electromagnetic properties of a chiral-plasma medium," *ACES Journal*, vol. 12, no. 1, pp. 14-18, 1997.

[6] B. T. Nguyen, A. Samimi, and J. J. Simpson, "Recent advances in FDTD modeling of electromagnetic wave propagation in the ionosphere," *ACES Journal*, vol. 29, no. 12, pp. 1003-1012, 2014.

[7] J. P. Rybak and R. J. Churchill, "Progress in reentry communications," *IEEE Trans. Aerosp. Electron. Syst.*, vol. AES-7, no. 5, pp. 879-894, Sept. 1971.

[8] P. W. Huber, N. D. Akey, W. F. Croswell, and C. T. Swift, "The entry plasma sheath and its effects on space vehicle electromagnetic systems," *NASA Tech. Note*, no. SP-252, pp. 1-630, 1971.

[9] S. Liu and S.-Y. Zhong, "Analysis of back-scattering RCS of targets coated with parabolic distribution and time-varying plasma media," *Optik*, vol. 124, no. 24, pp. 6850-6852, 2013.

[10] T. C. Lin and L. K. Sproul, "Influence of reentry turbulent plasma fluctuation on EM wave propagation," *Comput. Fluids*, vol. 35, no. 7, pp. 703-711, 2006.

[11] G.-L. He, Y.-F. Zhan, N. Ge, and Y. Pei, "Measuring the time-varying channel characteristics of the plasma sheath from the reflected signal," *IEEE Trans. Plasma Sci.*, vol. 42, no. 12, pp. 3975-3981, 2014.

[12] X.-Y. Chen, Y.-G. Zhou, Y.-Y. Liu, K.-X. Li, and X.-P. Li, "Precision loss and its solution in calculation of EM wave propagation in plasma environment," in *2017 International Applied Computational Electromagnetics Society Symposium (ACES 2017)*, China: Suzhou, p. 1804, Aug. 2017.

[13] X. Yin, H. Zhang, S.-J. Sun, Z.-W. Zhao, and Y.-L. Hu, "Analysis of propagation and polarization characteristics of electromagnetic waves through nonuniform magnetized plasma slab using propagator matrix method," *Prog. Electromagn. Res.*, vol. 137, no. 1, pp. 159-186, 2013.

[14] W. C. Chew, *Wave and Fields in Inhomogeneous Media*. New York, NY, USA: Van Nostrand Reinhold, 1990.

[15] M. A. Heald and C. B. Wharton, *Plasma Diagnostics with Microwaves*. New York, NY, USA: Krieger, 1978.

Xuyang Chen was born in Hebei, China, in 1980. He received the B.S., M.S., and Ph.D. degrees in Electronic Engineering from Xidian University, Xi'an, China, in 2005, 2008, and 2011, respectively. He joined the CAST-Xi'an Institute of Space Radio Technology, Xi'an, as an Engineer in 2011, where he is involved in radar detection and space navigation. He is currently a Teacher with the School of Aerospace Science and Technology, Xidian University. His current research interests include the radar detection of reentry vehicles covered by plasma sheath.

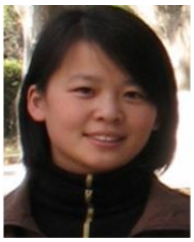

Fangfang Shen received the B.S., M.S. and Ph.D. degrees in Telecommunications Engineering from Xidian University, Xi'an, China, in 2006, 2009, and 2015, respectively. She is currently a Teacher with the School of Aerospace Science and Technology, Xidian University. Her research interests include high-resolution radar imaging and DOA estimation.

Yanming Liu was born in Shaanxi, China, in 1966. He received the B.S., M.S., and Ph.D. degrees from Xidian University, Xi'an, China, in 1989, 1993, and 2003, respectively. He is currently a Full Professor with the School of Aerospace Science and Technology, Xidian University. His current research interests include telecommunication network technology and wireless communication.

Wei Ai was born in Shanxi, China, in 1977. He received the B.S. degree from North University of China in 2000, and M.S. degrees from China Academy of Launch Vehicle Technology in 2011. He is currently a Senior Engineer with China Academy of Launch Vehicle Technology. His current research interests include communication technique and system integration design.

Xiaoping Li was born in Shanxi, China, in 1961. She received the B.S., M.S., and Ph.D. degrees from Xidian University, Xi'an, China, in 1982, 1988, and 2004, respectively. She is currently a Full Professor with the School of Aerospace Science and Technology, Xidian University. Her current research interests include telemetry, tracking and command, and communication technology.

Post-processing Techniques for Polarimetric Passive Millimeter Wave Imagery

L. Wu [1,2], J. Q. Zhu [1], S. S. Peng [1], Z. L. Xiao [1], and Y. K. Wang [1]

[1] School of Electronic and Optical Engineering
Nanjing University of Science & Technology, Nanjing, 210094, China
li_wu@njust.edu.cn, zhujiaqi3301@163.com, pengshusheng@njust.edu.cn, zelongxiao@njust.edu.cn, wykkerry@163.com

[2] Ministerial Key Laboratory of JGMT
Nanjing University of Science & Technology, Nanjing, 210094, China

Abstract ─ Post-processing techniques for polarimetric passive millimeter wave (MMW) imagery are proposed to display imaging information comprehensively. Initially an image fusion method based on two-scale decomposition is proposed to realize polarimetric passive imagery fusion. The fusion rules are separately designed for base layer and detail layer to reconstruct weight maps. Then an improved technique for displaying polarization information through color is proposed to present polarization features simultaneously with unpolarized imagery. Experimental results demonstrate that the proposed post-processing techniques are capable of presenting more informative imagery.

Index Terms ─ Millimeter wave passive imaging, polarimetric imaging, remote sensing.

I. INTRODUCTION

Millimeter wave (MMW) passive imaging sensor constructs the MMW images of the observed scene by recording radiometric temperature distributions. Recently passive MMW imaging sensors have been increasingly applied in a variety of fields, including security screening, surveillance and person recognition due to their ability to image through textiles, smoke, fog, light rain, dust storms [1-2]. Moreover, several polarimetric passive MMW imaging sensors have already been developed to provide polarimetric information of the observed scene [3-5].

Due to the wide applications of polarimetric passive MMW imaging system, how to process polarimetric information of objects is becoming an important research topic. Polarimetric brightness temperatures have been successfully used for remote sensing of wind speed and direction over sea surfaces [5-6]. Polarization-based techniques are presented to classify materials and acquire object surface orientation information using polarimetric passive MMW imagery [7-8]. A linear polarization sum imaging method which is based on the combination of the different polarization images is presented in [9] to increase the intensity contrast between the target area and background area. In our previous work [10], linear polarization characteristics of various terrains at MMW band for image interpretation were experimentally investigated. And it was proved that polarization has a decisive advantage over the single intensity for terrain identification.

However, there are few literatures have discussed the post-processing techniques for polarimetric passive MMW imagery collected by polarimetric imaging sensors. Siegenthaler et al. illustrated the image registration and fusion for the MMW images of 91 GHz Scanning Polarimetric Imaging Radiometer (SPIRA) and optical images [11]. A technique defined as polarization display through Color (PDC) is proposed in [12] to display polarization information from passive MMW sensors within a single image.

As the fused information is useful for the understanding enhancement of surroundings and is beneficial to human and machine vision for planning and decision-making, a method based on computationally efficient two-scale decomposition is proposed for polarimetric passive MMW imagery fusion. In addition, an improved technique for displaying polarization information through color which is capable of providing more details compared with the conventional PDC is also presented in this paper.

II. STOKES VECTOR DEFINITION

The signal received by MMW radiometer comes from the emitted radiation of objects and refracted or reflected radiation of objects and background. Therein, MMW radiation emitted by objects are not polarized. However, it differs in the reflection and refraction of

Submitted On: September 28, 2017
Accepted On: April 10, 2018

polarized radiation from various media and leads to partial polarization of radiation energy collected by MMW radiometer. Stokes parameters are commonly employed to characterize the polarization of electromagnetic wave and are well applied to describe the polarimetric information of passive MMW imagery. The expression of Stokes parameters is comprised of four elements, which can be written as:

$$\begin{pmatrix} S_0 \\ S_1 \\ S_2 \\ S_3 \end{pmatrix} = \begin{pmatrix} (T_h + T_v)/2 \\ T_v - T_h \\ T_{45^\circ} - T_{-45^\circ} \\ T_{RHC} - T_{LHC} \end{pmatrix}, \quad (1)$$

where, S_0, S_1, S_2 and S_3 represent the total intensity of radiation in all polarizations, the difference in intensity between two orthogonal linear polarization states, the degree of linear polarization at an angle of 45° to the horizontal and the degree of right-hand circular polarization respectively [5]. *T* denotes the radiometric temperature with different polarization modes, the subscripts of *h, v,* 45°, -45°, *RHC* and *LHC* represent horizontal, vertical, linear 45°, linear -45°, right-hand circular and left-hand circular polarization mode respectively.

Polarimetric passive MMW imaging systems are usually constructed with incoherent or coherent methods. For the incoherent PMMW imaging system, it requires simpler hardware with one receiver, thus it cannot measure Stokes parameters simultaneously. One the other hand, correlation polarimetric MMW system with parallel receivers is preferable to measure all Stokes parameters at a time. But the additional components will lead to higher cost and decreased performance of imaging system. To make that the proposed techniques can be applied to both incoherent and coherent imaging systems, the first two Stokes parameters, i.e., the sum and difference between the vertical and horizontal polarization states, are easily obtained for both kinds of imaging systems and thus will be processed to demonstrate the proposed post-processing techniques.

III. POST-PROCESSING TECHNIQUES

A. Polarimetric imagery fusion

It is known from the Rayleigh-Jeans law that the radiation emitted from the object is linear with the temperature at MMW frequencies, the retrieved parameter of imaging radiometer is radiometric temperature instead of intensity by calibrating the sensor with hot and cold calibration sources. So the measured Stokes parameter S_0 is the average of horizontal and vertical radiometric temperatures and it can be regarded as the unpolarized image, whereas Stokes parameter S_1 is radiometric temperature difference between the two orthogonal linear polarization states In this section, an image fusion algorithm which retains both radiometric intensity and polarimetric difference features is proposed to improve image readability. The processes sketch of the presented method for polarimetric passive MMW imagery fusion is presented in Fig. 1.

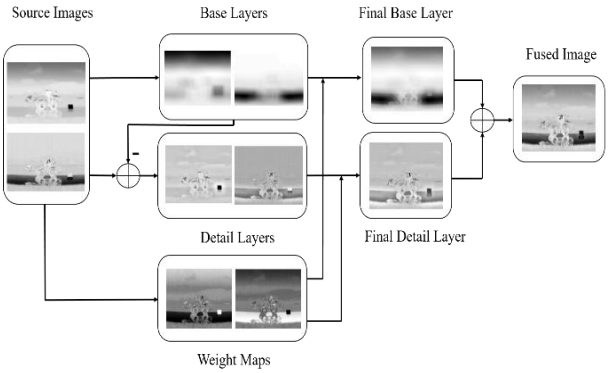

Fig. 1. Schematic diagram of the proposed fusion method for polarimetric passive MMW imagery.

An average filter based two-scale decomposition [13] is employed to decompose the polarimetric passive MMW images into the base layers and detail layers. The base layer of each source image is expressed as:

$$B_n = S_n * Z, \quad (2)$$

where S_n is the polarimetric passive MMW source image, *Z* is the average filter. The detail layer of the decomposed image can be obtained based on base layer with the following expression:

$$D_n = S_n - B_n. \quad (3)$$

By performing the above decomposition steps, each separate passive MMW image is decomposed into a base layer containing the large-scale variations in intensity and a detail layer containing the small-scale details. Based on achievements of the base layer and detail layer which correspond to the low-frequency and high-frequency components separately, the fusion of the base layer and detail layer can be respectively completed by constructing proper weights with:

$$\overline{B} = w_{S_0}^B B_{S_0} + w_{S_1}^B B_{S_1}, \quad (4)$$

$$\overline{D} = w_{S_0}^D D_{S_0} + w_{S_1}^D D_{S_1}, \quad (5)$$

where, $w_{S_0}^B$ and $w_{S_1}^B$ are the weight factors constructed for the base layer fusion, and $w_{S_0}^D$ and $w_{S_1}^D$ are the weight factors constructed for the detail layer fusion. The final fused image can be constructed by the addition of the updated base layer and the updated detail layer:

$$F = \overline{B} + \overline{D}. \quad (6)$$

The human perception system is sensitive to the contrast of visual signals, such as color, intensity and texture, and this phenomenon is regarded as the spatial attention [16]. As the low-frequency component is the

approximation of an image, the visual spatial attention based fusion rule is employed for the low-frequency component to keep the salient profiles of the both source images as much as possible. Based on the saliency map proposed in [14] which is built upon the color contrast between image pixels, a similar saliency value of a pixel P_k in image P is computed as:

$$SalS(P_k) = \sum_{\forall P_i \in P} \|P_k - P_i\|. \quad (7)$$

where, $\|\cdot\|$ denotes the radiometric temperature distance metric. Assumed that the gray value of the pixel P_k is a_m after mapping the measured radiometer temperatures linearly to range of [0,255], the above expression can be rewritten as:

$$SalS(a_m) = \sum_{n=0}^{255} f_n \|a_m - a_n\|. \quad (8)$$

where f_n denotes the frequency of pixel value a_n in the image and it can be obtained in histograms. Subsequently, the saliency maps $SalS(x,y)$ of the source images can be constructed and the fusion weight factors are determined using the following expression:

$$w_{S_0}^B(x,y) = \frac{SalS_{S_0}(x,y)}{SalS_{S_0}(x,y) + SalS_{S_1}(x,y)}, \quad (9)$$

$$w_{S_1}^B(x,y) = \frac{SalS_{S_1}(x,y)}{SalS_{S_0}(x,y) + SalS_{S_1}(x,y)}. \quad (10)$$

The detail layer of the image presents detailed features, such as texture, edge. The local energy based weighted average method is used to keep detailed information. The local energy within region R of each pixel in source image is given as:

$$E(x,y) = \sum_{m,n \in R} a^2(x+m, y+n), \quad (11)$$

where, $a(x,y)$ represents the gray level of the pixels. Based on the constructed local energy maps of source images, the fusion weight factors can be determined by:

$$w_{S_0}^D(x,y) = \frac{E_{S_0}(x,y)}{E_{S_0}(x,y) + E_{S_1}(x,y)}, \quad (12)$$

$$w_{S_1}^D(x,y) = \frac{E_{S_1}(x,y)}{E_{S_0}(x,y) + E_{S_1}(x,y)}. \quad (13)$$

As above, the base layer and detail layer weigh maps construction method is able to keep salient and interested features of the source images, it will lead to a better fusion performance compared to most weight factors construction methods like simply averaging of the source images.

B. Polarization information display

Though the fused image preserves the details of separate polarimetric passive MMW images, it provides less information than a color image due to the limitations of image grayscale. There is an alternative approach to display polarimetric information of passive MMW imagery with a color image determined by polarization. An example of that is the technique named PDC (polarization display through color) introduced in [12]. For the convenience of comparison, the hue, saturation, lightness cylindrical-coordinate color mapping system is used to deliver a color image in this paper as done in [12].

As the difference between the two orthogonal linear polarization states is applied to target identification in some biological systems, the imaged scene is classified into three categories by setting thresholds for the Stokes parameter S_1. Here the mean value of S_1 is employed as the offset T_{offset} which is resulted by the kinetic temperature of object. And the threshold δ is determined with the following expression:

$$\delta = (T_{med} + T_{df})/2, \quad (14)$$

where T_{med} is the median of S_1, T_{df} is the difference between T_{med} and the maximum or minimum value of S_1 which leads to a smaller number. So the pixels of image will be classified into three groups by determining the values position relative with thresholds of $T_{offset} \pm \delta$, including pixels smaller than T_{offset}-δ, pixels between T_{offset}-δ and T_{offset}+δ, and pixels larger than T_{offset}+δ. And the hue value of each pixel in the color image is assigned to one of the three different constants which would determine the color of the image depending on the classification results. As for the saturation, it is shaped with the values of Stokes parameter S_1 which are linearly scaled to a range of $[\lambda_{sat}, 1]$ for each classification. Compared with a constant saturation value, more details can be provided by the varying color saturation. At last the unpolarized image is mapped to the lightness of color mapping system, where the maximum is scaled to 1 and the minimum is scaled to 0.

IV. EXPERIMENTAL RESULTS

A. Fusion results and evaluation analysis

Several polarimetric passive MMW images collected by the raster-scanned polarimetric imaging sensor [15] are processed with the proposed method. The window size of the average filter Z in Equation (2) is set to 31*31 for numerical results as suggested in [13], [18]. And the size of region R in Equation (11) is 2*2 to obtain optimal comprehensive performances. A scene of the experiment is shown in Fig. 2 (d). It can be seen that a digger is adjacent to an asphalt road which went laterally across the lawn. A metal plate with a tilting angle of 45° to the horizon is put on the right side of the vehicle. Behind the lawn there are mountains and buildings as well. The first

two Stokes parameters of collection are shown in Fig. 2 (a) and Fig. 2 (b) respectively. Disturbances resulted from the radio frequency interference of the second imaging sensor working simultaneously can be clearly seen around the cab, and the temperature range is adapted to display more details.

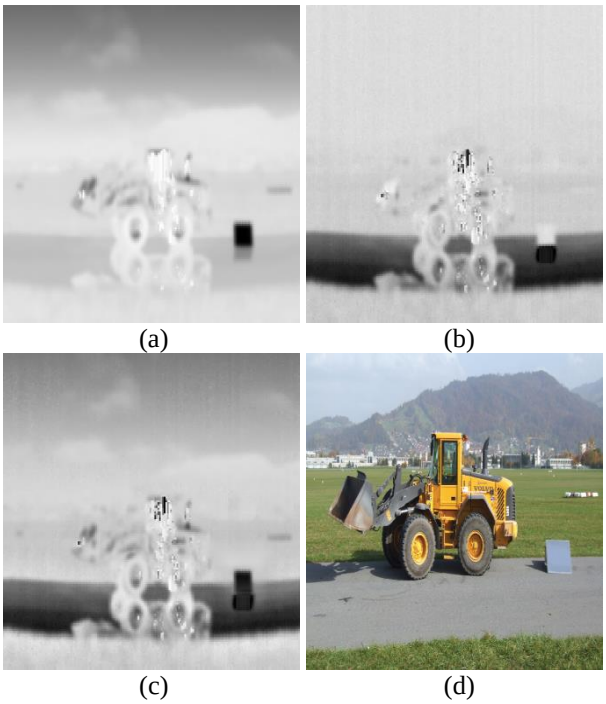

Fig. 2. Polarimetric MMW imagery and fusion result of a digger. (a) Unpolarized image S_0, (b) polarization difference image S_1, (c) fused polarimetric image, and (d) photo of the imaging scene.

It can be seen in Fig. 2 (a) that the sky and the tilted metal plate have a lower radiometric temperature. The cold temperature of metal plate is resulted by the reflection of sky due to its high reflectivity close to 1. The radiometric temperature of the asphalt road is lower than that of the lawn due to a higher reflectivity. The above results can be explained with the expression of detected radiometric temperature given by:

$$T_a(x,y) = R(x,y)T_{inc}(x,y) + \left[1\text{-}R(x,y)\right]T_{obj}(x,y), \quad (15)$$

where T_a is the radiometric temperature, R denotes the reflectivity, T_{inc} stands for the radiometric temperature incident on the object at the reflection angle, T_{obj} is the kinetic temperature of the object. For the observed scene, radiometric temperature incident on the objects is the radiometric temperature of clear sky which is a cold source. As the reflectivity of the metal plate is close to 1, it is known from the above equation that T_a is almost the same with the radiometric temperature of sky and thus it resulted in a low temperature of the metal plate. Also, it can be concluded from Equation (15) that a higher reflectivity will bring a lower radiometric temperature if two targets have the same kinetic temperatures.

In Fig. 2 (b), radiometric temperature difference between horizontal and vertical states for the asphalt road is higher which is caused by a big Fresnel coefficient difference between the orthogonal states. Also the inverted reflections of the vehicle and the tilted metal plate on the road are also obvious from the both figures. With the proposed fusion method, more details can be found in the fused image compared with the source images.

As shown in Fig. 3 (d), a basin full of water is placed on the lawn and imaged with the polarimetric MMW imaging system. The delivered polarimetric images are presented in Fig. 3 (a) and Fig. 3 (b) respectively.

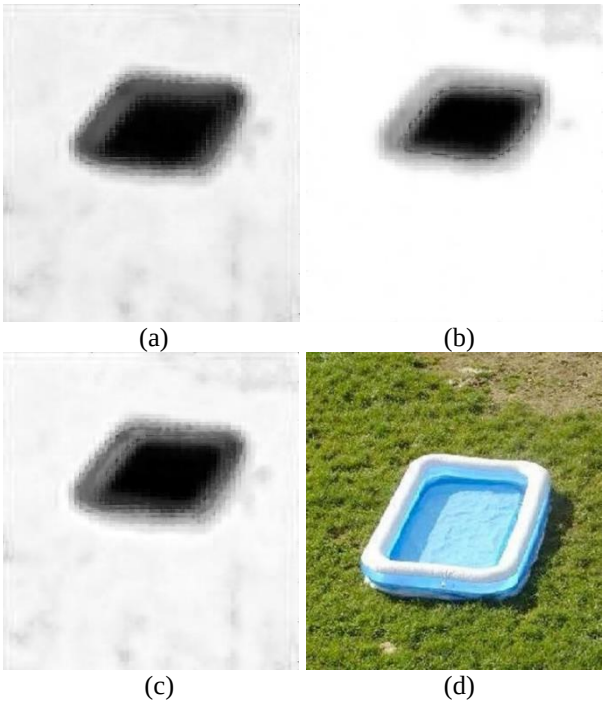

Fig. 3. Polarimetric MMW imagery and fusion result of a basin. (a) Unpolarized image S_0, (b) polarization difference image S_1, (c) fused polarimetric image, and (d) photo of the imaging scene.

It is seen from the imaging results that the radiometric temperature of water is lower than that of the lawn because it reflects more radiation of the cold sky. Also a big polarization difference is observed for water because the reflectivity difference between horizontal and vertical polarization is larger. And the horizontal radiometric temperature of water is lower due to a lager reflectivity in this polarization. The fused image obtained with the proposed method is shown in Fig. 3 (c). It can

be also found that the fused image provides more details than any single source image.

Though the subject evaluation is a direct and effective method, it varies a lot as this depends on the individuals' experiences. As a result, some metrics such as standard deviation (SD), entropy (EN), mean gradient (MG), and spatial frequency (SF) are employed to evaluate the quality of the fused images objectively.

The standard deviation delivers an overview of the contrast of image. A larger standard deviation means a higher image contrast. In the field of imaging processing, information entropy denotes the average information included in the image. A larger information entropy means a better fusion effect as it provide more details and information in the image. The mean gradient indicates the clarity of image and detailed texture features. The spatial frequency computed in the spatial domain is used to measure the overall activity level of an image.

The objective performances of the proposed fusion method are summarized in Table 1. Also the fusion quality indexes of the multi-scale transform based dual-tree complex wavelet transform (DTCWT) with a decomposition level of 4 [16, 17] and two-scale image fusion using saliency detection (TS-SD) [18] are given for comparison.

Table 1: Quality metrics of various fusion methods for polarimetric MMW imagery

Source Images	Metrics	DTCWT	TS-SD	Proposed
Digger	SD	32.7446	34.4488	47.5733
	MG	3.7212	3.0040	3.7862
	EN	6.6312	6.5985	7.0216
	SF	13.4614	10.4936	13.4021
Basin	SD	63.4588	64.5289	65.5313
	MG	1.8458	1.6210	1.8706
	EN	5.2473	5.3465	5.4157
	SF	7.0857	5.7857	6.8539

As shown in Table 1, the proposed fusion method is able to outperform TS-SD in terms of all quality metrics for the both experiments. The proposed method also has a better performance than DTCWT in most quality indexes except SF. We think that the excellent ability of details preservation contributes a better performance in SF for the DTCWT. Given that the passive MMW imaging sensors suffer from a problem of low resolution compared with high resolution optical imagery, the spatial attention model introduced for fusion weight maps construction plays a significant role to achieve the best performances in most cases for the proposed method.

To evaluate the computational performance of the presented fusion method, the computational time for processing the digger and basin images is summarized in Table 2, and time for DTCWT and TS-SD algorithms is presented for comparison. Experiments are conducted on a computer with 2.6 GHz CPU and 8 GB RAM. The decomposition level of DTCWT is 4 in the experiment. From the above experimental results, it is concluded that two-scale decomposition based methods are more efficient than DTCWT, and the proposed method runs a bit faster than TS-SD.

Table 2: Computational time of various methods

Source Images	Computational Time in Seconds		
	DTCWT	TS-SD	Proposed
Digger	0.219	0.020	0.016
Basin	0.275	0.029	0.022

B. Polarization information display results

Also, the above collected polarimetric passive MMW imagery is dealt with the proposed polarization information display technique. Here the minimum saturation value λ_{sat} is set to 0.3 for a better visual effect. The color images obtained with the proposed method and PDC are presented in Fig.4 and Fig.5 for the digger imagery respectively. The parameters for PDC are chosen with the second method which would produce the most informative images qualitatively [12].

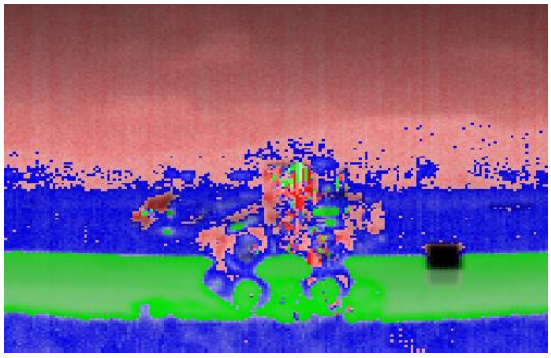

Fig. 4. Polarimetric passive MMW imagery of the digger displayed with the proposed technique.

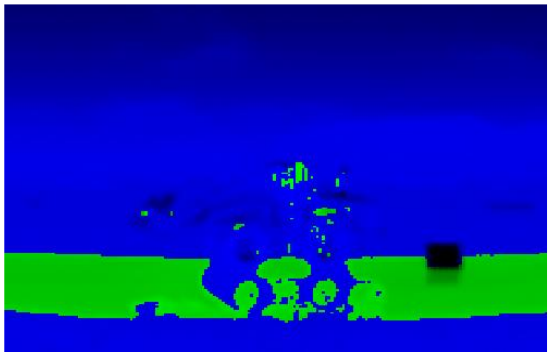

Fig. 5. Polarimetric passive MMW imagery of the digger displayed through PDC.

It can be found from the figures that a color image provides a more intuitive effect as objects are differentiated by color. Compared with PDC, the proposed technique in this paper offers a superior ability of object classification. Moreover, more details are featured with a various color saturation for each classification. Though the lawn is marked with green color, there is a minor difference between the lawn covered and uncovered by the reflection of digger. In addition, the radio frequency interference spots on the digger can be easily distinguished due to the highest saturation level.

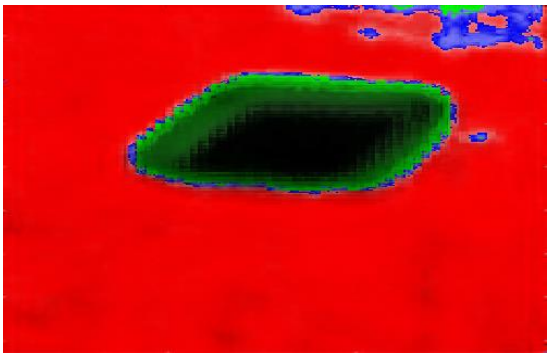

Fig. 6. Polarimetric passive MMW imagery of the basin displayed with the proposed technique.

The color basin polarimetric passive MMW imagery displayed with the proposed method and PDC are presented in Fig. 6 and Fig. 7 respectively. It can be seen from the results that the lawn and gravel ground are separated with different colors by the proposed technique, whereas the difference cannot be distinguished in the color image generated with PDC.

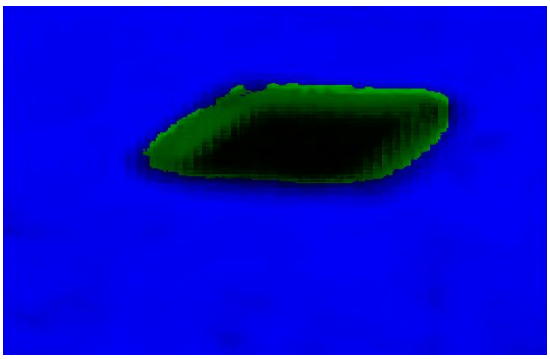

Fig. 7. Polarimetric passive MMW imagery of the basin displayed through PDC.

V. CONCLUSION

As the polarimetric radiation of object provides supplementary information for passive MMW imaging, the post-processing techniques are increasingly significant for polarimetric passive MMW imagery analysis and understanding. The polarimetric imagery fusion method and polarization display technique are discussed in this paper. The performances of the proposed fusion method are better than the methods of DTCWT and TS-SD in terms of objective imagery quality metrics. Additionally, it's simple and computing efficient due to that the two-scale decomposition does not rely on complex image decomposition steps. Also a technique for displaying polarization information through color is presented to provide a more informative image. The unpolarized image can be displayed simultaneously with the polarization. Compared with the conventional PDC technique, the proposed method has a better performance in the object classification and details presentation.

As for the future work, more experiments will be conducted to further verify the performances of the proposed post-processing techniques for polarimetric passive MMW imagery. Additionally, there is a large quality of fusion algorithms which are applied in optical and infrared image processing. More efficient and better fusion methods can be explored to demonstrate the potential of radiometric polarization information application.

ACKNOWLEDGMENT

The authors would like to express their deepest gratitude to Dr. Murk Axel from University of Bern for providing the imaging data. This work was supported by the National Natural Science Foundation of China (No. 61501234), and the Fundamental Research Funds for the Central Universities (No. 30920140122005).

REFERENCES

[1] E. Gonzalez-Sosa, R. Vera-Rodriguez, J. Fierrez, and V. Patel, "Exploring body shape from mmW images for person recognition," *IEEE Trans. Inf. Forensics Security*, vol. 12, pp. 2078-2089, 2017.

[2] L. Wu, S. Peng, Z. Xiao, and J. Xu, "Sensitivity analysis and tipping calibration of a W-band radiometer for radiometric measurements,"*Appl. Comput. Electromagn. Soc. J.*, vol. 31, 2016.

[3] S. Liao, N. Gopalsami, T. W. Elmer, E. R. Koehl, A. Heifetz, K. Avers, E. Dieckman, and A. C. Raptis, "Passive millimeter-wave dual-polarization imagers," *IEEE Trans. Instrum. Meas*., vol. 61, pp. 2042-2050, 2012.

[4] J. P. Wilson, C. A. Schuetz, C. E. Harrity, S. Kozacik, D. L. Eng, and D. W. Prather, "Measured comparison of contrast and crossover periods for passive millimeter-wave polarimetric imagery," *Opt. Express*, vol. 21, pp. 12899-12907, 2013.

[5] A. Duric, A. Magun, A. Murk, C. Matzler, and N. Kampfer, "The fully polarimetric imaging radiometer SPIRA at 91 GHz," *IEEE Trans. Geosci. Remote Sens.*, vol. 46, pp. 2323-2336, 2008.

[6] P. S. Narvekar, G. Heygster, T. J. Jackson, R.

Bindlish, G. Macelloni, and J. Notholt, "Passive polarimetric microwave signatures observed over Antarctica," *IEEE Trans. Geosci. Remote Sens.*, vol. 48, pp. 1059-1075, 2010.

[7] Y. Cheng, F. Hu, L. Gui, L. Wu, and L. Lang, "Polarization-based method for object surface orientation information in passive millimeter-wave imaging," *IEEE Photon. J.*, vol. 8, pp. 1-12, 2016.

[8] F. Hu, Y. Cheng, L. Gui, L. Wu, X. Zhang, X. Peng, and J. Su, "Polarization-based material classification technique using passive millimeter-wave polarimetric imagery," *Appl. Opt.*, vol. 55, pp. 8690-8697, 2016.

[9] S. Yeom, D. Lee, H. Lee, J. Son, and V. P. Gushin, "Vector clustering of passive millimeter wave images with linear polarization for concealed object detection," *Prog. Electromagn. Res. Lett.*, vol. 39, pp. 169-180, 2013.

[10] X. Lu, Z. Xiao, and J. Xu, "Linear polarization characteristics for terrain identification at millimeter wave band," *Chin. Opt. Lett.*, vol. 12, pp. 101201, 2014.

[11] S. Siegenthaler, M. Canavero, and A. Murk, "Post-processing techniques for radiometric images," *IEEE Geoscience and Remote Sensing Symposium*, Munich, pp. 2316-2319, July 2012.

[12] J. P. Wilson, C. A. Schuetz, T. E. Dillon, D. L. Eng, S. Kozacik, and D. W. Prather, "Display of polarization information for passive millimeter-wave imagery," *Opt. Eng.*, vol. 51, pp. 091607, 2012.

[13] S. Li, X. Kang, and J. Hu, "Image fusion with guided filtering," *IEEE Trans. Image Process.*, vol. 22, pp. 2864-2875, 2013.

[14] Y. Zhai and M. Shah, "Visual attention detection in video sequences using spatiotemporal cues," *Proceedings of the 14th ACM International Conference on Multimedia*, Santa Barbara, CA, pp. 815-824, Oct. 2006.

[15] O. Stähli, "Novel Measurements with the Imaging Polarimeter SPIRA (91 GHz) after Technical Upgrades," Master Thesis, Inst. Appl. Physics, University of Bern, Switzerland, 2009.

[16] Y. Liu, S. Liu, and Z. Wang, "A general framework for image fusion based on multi-scale transform and sparse representation," *Inf. Fusion*, vol. 24, pp. 147-164, 2015.

[17] J. J. Lewis, R. J. O'Callaghan, S. G. Nikolov, D. R. Bull, and N. Canagrajah, "Pixel-and region-based image fusion with complex wavelets," *Inf. Fusion*, vol. 8, pp. 119-130, 2007.

[18] D. P. Bavirisetti and R. Dhuli, "Two-scale image fusion of visible and infrared images using saliency detection," *Infrared Phys. Tech.*, vol. 76, pp. 52-64, 2016.

L. Wu received the B.S., M.S. and Ph.D. degrees all in Electrical Engineering from Nanjing University of Science and Technology (NUST), Nanjing, China, in 2003, 2005 and 2009, respectively. Since 2009, he has been a Lecturer with School of Electronic and Optical Engineering at NUST. His research interests involve passive imaging, remote sensing, millimeter wave radar system and application.

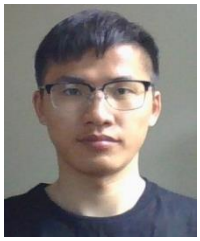

J. Q. Zhu received the B.S. and M.S. degrees all in Electrical Engineering from Nanjing University of Science and Technology (NUST), Nanjing, China, in 2015 and 2018. His research interest is millimeter wave passive imaging.

Uncertainty Analysis of Reflection Coefficient for a Coating with Random Flaws Using Adaptive Mesh and DGTD Method

Huiping Li [1,2], Ishfaq Hussain [1], Yi Wang [1], and Qunsheng Cao [1]

[1] College of Electronic and Information Engineering
Nanjing University of Aeronautics and Astronautics, Nanjing, 211106, China
lihp@nuaa.edu.cn, ishfaqhussain05@nuaa.edu.cn, jflsjfls@nuaa.edu.cn, qunsheng@nuaa.edu.cn

[2] School of Physics and Electronics
Henan University, Kaifeng 475004, China

Abstract ─ An imperfect coating shall cause uncertainties in the analysis of electromagnetic properties. To quantify the influence of irregularity, complexity, and uncertainty of the coatings for electronic devices, an adaptive mesh algorithm combined with the discontinuous Galerkin time domain (AM-DGTD) method is developed. The uncertain variations are incorporated into the proposed algorithm by an appropriate parameterization. The standard statistical analysis is performed to calculate the appropriate moments, i.e., mean and variance. The developed method is validated by modeling a dielectric coating with uncertain flaws in an adaptive mesh grid. The computed quantities of interest from numerical estimations are compared with the analytical values, these results agree with the physical explanation, and are in good agreement with the exact values, as demonstrated by numerical experiments.

Index Terms ─ AM-DGTD method, reflection coefficient, statistical analysis, uncertainty quantification.

I. INTRODUCTION

Dielectric coatings applied to surfaces of aircraft frames, automobile frames and ship hull are able not only to protect objects from sunlight, moisture, dust and abrasion but also to improve their appearance [1]. For example, cracks, voids, inclusions, structural flaws and material defects [2], these uncertain flaws may impact the coating's electromagnetic performance and cause difference from the ideal manufacturing objectives, or to damage the essential functions of the dielectric coatings. In order to engage in the practical analysis and simulation, one must find a suitable, flexible and efficient method to deal with these electromagnetic problems.

In the recent years, the method of moments (MoM) with probabilistic technique outlined in [3] was applied to determine the uncertainty in practical EM compatibility measurements. Polynomial chaos technique was used in the finite difference time domain (FDTD) method to study microwave circuits and free-space scattering problems [4]-[5]. An efficient stochastic finite difference time domain (S-FDTD) method [6], which uses truncated Taylor series approximations in the derivation, is employed for evaluating statistical variation in the EM fields caused by variability or uncertainty in the electrical properties of the materials in the model. To obtain static response characteristics of graphite/epoxy composite laminates with random material properties, Navaneetha Raj *et al.* employed Monte Carlo simulation and the finite element method (FEM) with different boundary conditions [7]. A hybrid approach was adopted in the spectral stochastic finite element method (SSFEM) and polynomial chaos expansion (PCE) to provide response analysis of a linear structure with uncertainties in both the structural parameters and the external excitation [8]. In [9], a probabilistic approach based on high-order accurate expansions of general stochastic processes and high-order discontinuous Galerkin method was applied to solve the time-domain electromagnetic problems with uncertainty in initial conditions, boundary conditions, sources, materials, computational domain, and/or geometries. In [10], Li *et al.* proposed a hybrid method which integrated an adaptive hierarchical spare grid collocation (ASGC) method and the discontinuous Galerkin time-domain (DGTD) method. The ASGC method is employed to approximate the stochastic observables of interest using interpolation functions over a set of collocation points determined by the Smolyak's algorithm integrated with an adaptive strategy. Owing to the random flaws in the coatings are generally smaller, irregular, and more arbitrary in nature. Moreover, the DGTD method offers high-order accuracy to a coarse resolution, geometrical flexibility through fully unstructured grids and higher computational efficiency, so it could be more suitable to be employed for the uncertainty quantization [9]-[14].

In this work, using the node displacement method and the node insertion method[15]-[17], we develop an

Submitted On: August 9, 2017
Accepted On: January 22, 2018

adaptive spatial discrete algorithm for the high order DGTD method to generate an optimal number of mesh elements and to adapt the locations of the global nodes for uncertain and complex structures. The AM-DGTD method is used to evaluate the statistical variations of reflection coefficients of dielectric coating with random flaws in one-dimensional model. Firstly, we compare the high-order convergence of the AM-DGTD algorithm for different values of the number of element K and the order of polynomial N. Then, we solve three typical uncertain flaw problems using the developed approach: (i) slight deviation in the permittivity of the dielectric coating, (ii) variable tolerance in the thickness of coating, and (iii) uncertain holes in the coating. For the first two cases, there is only one uncertain input parameter, i.e., permittivity and thickness, respectively. For the third case, we investigate multivariable situation, e.g., the diameter, position, and number of holes as the stochastic variables. Furthermore, this article not only provides results of uncertainties but also insight into the expected statistical properties.

II. ADAPTIVE MESH DGTD METHOD

To use unstructured finite element methods, the computational domain must be decomposed into geometric elements, e.g., lines in one dimension, triangles in two dimensions and tetrahedral in three dimensions. Suppose one-dimensional computational domain is $\Omega = [xmin, xmax]$, which can be tessellated by K equidistant nodes. If the meshes are uniform then each element has the same size $h = \Omega/K$. When the desired nodes, which represent the interfaces of the structure under study, do not coincide with the positions of the equidistant nodes, the uniform meshes are terrible and unserviceable. If setting a larger h, the discretization error will increase; if setting a smaller h for capturing fine details and maintaining Courant-Friedrichs-Levy (CFL) condition of the numerical methods, the computational memory and execution time will increase.

For problems with uncertain desired nodes, dynamic, intelligent, and more robust meshes are needed to achieve accurate identification for the random objects. In this work, two types of adaptive mesh generation techniques are proposed as below:

A. Node insertion mesh

Firstly, the computational domain Ω is discretized into K equidistant non-overlapping line segments. Each line segment has two end nodes. Vx is introduced to stand for the global uniform node vector (UNV). Using the insertion algorithm, the desired node vector (DNV) can be added adaptively into UNV and the resulting vector is sorted to achieve overall discretization scheme. The new global node vectors could become nonuniform. Note that the number of global nodes is increased as inserting DNV, as shown in Fig. 1.

The node insertion method is simple, however, it is time and resource-consuming, because the insertion of DNV into V_x cause reduction in the minimum distance between adjacent nodes, then the smaller time step has to be employed to maintain the CFL condition. Pseudo algorithm for this adaptive mesh by inserting node is provided in Algorithm 1.

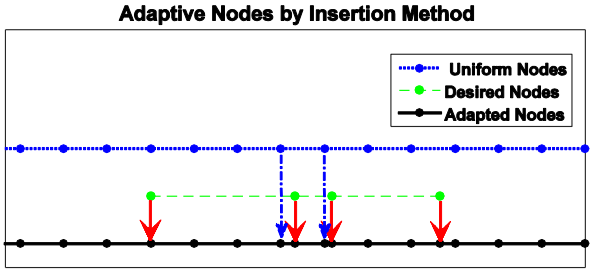

Fig. 1. The mesh cell mappings for node inserting mesh algorithm.

Algorithm 1 Insertion algorithm for desired nodes

Input: computational domain Ω=[*xmin*, *xmax*], number of elements K, desired node vectors *DNV*
Output: updated number of elements K*, updated global node vector V_x*

for i←1 to K do
  /* Generate a simple equidistant grid and uniform node vectors V_x */
  V_x(i) ← (*xmax*−*xmin*)*(*i*-1)/K + *xmin*
/* Insert the *DNV* into the uniform node vector V_x */
/* Sort and return the unique values */
V_x*←unique ([V_x *DNV*])
K*←length(V_x*)-1
Return K*, V_x*

B. Node displacement mesh

In this type of adaptive mesh generation, the adaptation can be achieved through suitably displacing the UNV. The algorithm identifies the nodes from the UNV which are nearest to the set of DNV and shifts these nodes to the desired locations. If a DNV coincides with one of the UNV, such as the node ① and ②, then no displacement is needed; if a structure represented by any two of the DNV (e.g., node ② and ③) is much larger than uniform elements, then the nearest uniform nodes are modified at the boundaries; if a structure is very small, such as the segment composed by node ⑤ and ⑥, the algorithm makes sure that at least one element is contained. Hence, only optimal numbers of element are generated, as shown in Fig. 2.

Note that the number of global nodes remains unchanged, that is, K* = K. This algorithm generates optimal density of mesh cells over the whole Ω,

regardless of geometry structure. The displacement of nodes to different position caused non-uniformity in the distribution of global nodes. Realization for this adaptive mesh algorithm is given below in Algorithm 2.

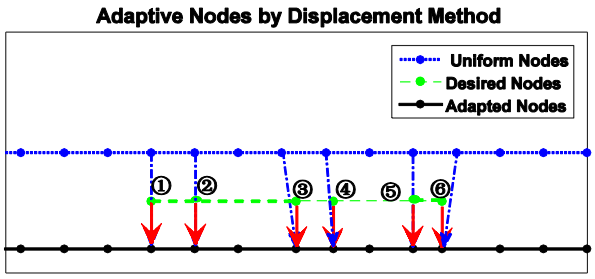

Fig. 2. The mesh cell mappings for node displacing mesh algorithm.

Algorithm 2 Displacement algorithm for desired nodes

Input: computational domain Ω=[*xmin*, *xmax*], number of elements *K*, desired node vectors *DNV*
Output: updated number of elements *K**, updated global node vector V_x*

```
for i←1 to K do
    /* Generate a simple equidistant grid and uniform
       node vectors Vx */
    Vx(i) ← (xmax−xmin)*(i-1)/K + xmin
if length(Vx) > 2*length(DNV)+2 then
    for q← 1 to length(DNV) do
        /*Generate index of DNV in set of the uniform
          node vectors UNV */
        [Val(q) Index(q)] ← min(abs(Vx−DNV(q)))
        /* Deal with nodes which near boundary of
        the domain */
        ConflictIndex ← find( Index(end)==Index)
            if length(ConflictIndex) > 1 then
                Index(end) ← Index(end)+1
            return
        Vx (Index(q)) ← DNV(q)
    Vx*←Vx
    K*←length(Vx*)-1
return
Return K*, Vx*
```

C. Numerical scheme for one-dimensional case

To compute the reflection coefficients of the dielectric coating with random flaws, we solve the one-dimensional Maxwell's equations in the time domain, subject to a broadband initial condition, and collect one time-trace at an observed point in the computational domain. Consider a lossless material TEM_z case, the time-dependent Maxwell's equations can be written as follows:

$$\varepsilon(z)\frac{\partial E_x}{\partial t}+\frac{\partial H_y}{\partial z}=0,\qquad \mu(z)\frac{\partial H_y}{\partial t}+\frac{\partial E_x}{\partial z}=0, \tag{1}$$

where E_x, H_y, ε and μ represent the electric field, the magnetic field, the local electric permittivity, and the local magnetic permeability, respectively.

Using the aforementioned adaptive mesh approaches, the computational domain $\Omega = [l, r]$, which is tessellated by K^* subdomains, i.e., any one of elements of the physical space D^k is equal to $[z_l^k, z_r^k], k = 1...K^*$. The solution of Equation (1) will be discontinuous between elements. In an arbitrary element D^k, the fields can be approximately expanded using local high-order Lagrange interpolation polynomial $\ell_i^k(z)$:

$$\begin{bmatrix}E_x^k(z,t)\\H_y^k(z,t)\end{bmatrix}\approx\begin{bmatrix}E_{xh}^k(z,t)\\H_{yh}^k(z,t)\end{bmatrix}=\sum_{i=1}^{N_p}\begin{bmatrix}E_{xh}^k(z_i^k,t)\\H_{yh}^k(z_i^k,t)\end{bmatrix}\ell_i^k(z), \tag{2}$$

where N_p stands for the number of the local expansion. E_{xh}^k and H_{yh}^k contain a N_p-vector of expansion coefficients to be solved. $\ell_i^k(z)$ signifies an N_pth order Lagrange polynomial. The relationship between N_p and the polynomial expansion order N is $N_p = N+1$. On account of the fact that correctly choosing interpolation nodes can bring about good numerical behaviors, this work employs the Legendre-Gauss-Lobatto (LGL) interpolating nodes as z_i [21]-[23].

Next, multiplying (1) by a test function $\ell_i^k(z)$ in an element D^k, yields:

$$\begin{aligned}&\int_{D^k}\left(\varepsilon^k(z)\frac{\partial E_x^k(z,t)}{\partial t}+\frac{\partial H_y^k(z,t)}{\partial z}\right)\ell_i^k(z)\,dz=0,\\&\int_{D^k}\left(\mu^k(z)\frac{\partial H_y^k(z,t)}{\partial t}+\frac{\partial E_x^k(z,t)}{\partial z}\right)\ell_i^k(z)\,dz=0.\end{aligned} \tag{3}$$

In order to couple with adjacent elements, Equation (3) are manipulated with integration by parts twice, and the strong variational formulation can be obtained as [21]:

$$\begin{aligned}&\int_{D^k}\left(\varepsilon^k\frac{\partial E_x^k}{\partial t}+\frac{\partial H_y^k}{\partial z}\right)\ell_i^k(z)\,dz=\int_{\partial D^k}\hat{\boldsymbol{n}}\cdot\left(\frac{\partial H_y^k}{\partial z}-\frac{\partial H_y^*}{\partial z}\right)\ell_i^k(z)\,dz,\\&\int_{D^k}\left(\mu^k\frac{\partial H_y^k}{\partial t}+\frac{\partial E_x^k}{\partial z}\right)\ell_i^k(z)\,dz=\int_{\partial D^k}\hat{\boldsymbol{n}}\cdot\left(\frac{\partial E_x^k}{\partial z}-\frac{\partial E_x^*}{\partial z}\right)\ell_i^k(z)\,dz.\end{aligned} \tag{4}$$

Here, $\hat{\boldsymbol{n}}$ denotes the local outward pointing normal. On the right-hand side (RHS) of (4) (E_x^*, H_y^*) are numerical fluxes to exchange the coupling between neighboring elements. Using the Riemann conditions

and for stability reasons, we use a pure upwind flux [21] which could strongly damp unphysical modes,

$$E_x^* = \frac{1}{\{\{Y\}\}}\left(\left\{\left\{YE_x^k\right\}\right\} + \frac{1}{2}[[H_y^k]]\right)$$
$$H_y^* = \frac{1}{\{\{Z\}\}}\left(\left\{\left\{ZH_y^k\right\}\right\} + \frac{1}{2}[[E_x^k]]\right), \quad (5)$$

where $Z = (Y)^{-1} = \sqrt{\mu/\varepsilon}$, represents the impedance of the medium.

Now substitute the expansions in (2) with the numerical flux of (5) into (4) and assume a smooth material in each element. After some algebraic computations, the explicit semi-discrete scheme in matrix-vector form can be obtained as follows:

$$\frac{dE_{xh}^k}{dt} = \frac{1}{J^k\varepsilon^k}\left\{-\mathcal{D}_r H_{yh}^k + \frac{1}{\mathcal{M}^k}\left[\ell^k(z)\left(H_{yh}^k - H_y^*\right)\right]_{z_l^k}^{z_r^k}\right\},$$
$$\frac{dH_{yh}^k}{dt} = \frac{1}{J^k\mu^k}\left\{-\mathcal{D}_r E_{xh}^k + \frac{1}{\mathcal{M}^k}\left[\ell^k(z)\left(E_{xh}^k - E_x^*\right)\right]_{z_l^k}^{z_r^k}\right\}. \quad (6)$$

Here, the matrices J^k, D_r, and M^k represent the local transformation Jacobian, differentiation matrix and mass-integration matrix, respectively (see [21] for details).

The semi-discrete system of (6) is ordinary differential equations with respect to time. The forth-order low-storage explicit Runge-Kutta (LSERK) solver is employed for the time integration of (6) [24].

III. AM-DGTD FOR DETERMINISTIC PARAMETERS

A. Computation model

The objective of this article is to analyze the characteristics of a dielectric coating. To reduce the complexity of the problem, this coating is located at the center (i.e., $x^{left} = 0$) of the computational domain Ω = [-6.0cm, 6.0cm]. Free space is set on the both sides of the coating and the relative parameters $\varepsilon_r = 1$ and $\mu_r = 1$. The main sensitive variables with uncertainty are supposed to be mean values, i.e., the average thickness of the coating $d = 2.0$cm and its average relative permittivity $\varepsilon_r = 4$.

To model the excitation source, an x-polarized, z-directed Gaussian pulse with respect to space is used and the following initial conditions ($t=0$) are adopted as:

$$E_x = \exp\left(-4\pi\frac{(z-z_0)^2}{z_\tau^2}\right),\ z_0 = -3.5cm, z_\tau = 0.5cm$$
$$H_y = 0 \quad (7)$$

where z_0 and z_τ are the center position and the width of the Gauss curve, respectively. This Gaussian pulse traveling in free space normally incident upon the dielectric coating, as illustrated in Fig. 3.

We collect one time-trace at the observation point (P = -1.0cm) in the computational domain. The frequency response is obtained by using fast Fourier transformation (FFT). Moreover, the Mur's absorbing boundary conditions (ABC) [25] is employed to truncate the open domain.

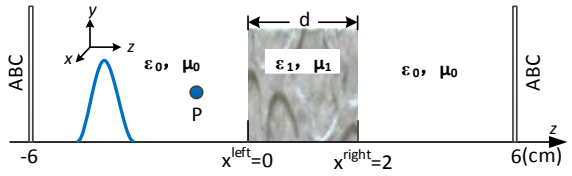

Fig. 3. The sketch map of the dielectric coating with uncertain flaws.

B. Reflection coefficient

The reflection coefficients at the observation point are calculated by using the AM-DGTD method. The coating is assumed to be removed at first, that is, the whole computational domain lies in free space. The electric field data at the observation point can completely represent the incident field, E^{inc}. Then, the complete model is simulated again. Because of the discontinuous interface, when the incident wave encounters the interface, a fraction of the wave energy will be reflected and part will be transmitted. Hence, the electric field data at the same observation point represents the total field E^{tot}, which includes incident and reflected electric field components. The formulation for the reflected fields is given by $E_x^{ref} = E_x^{tot} - E_x^{inc}$. Figure 4 illustrates the relationship of incident, total, and reflected electric field with time at the observation point.

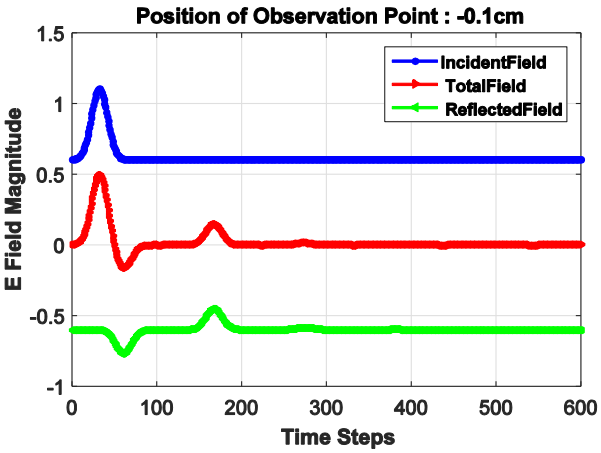

Fig. 4. The relationship of incident, total, and reflected electric field.

Using FFT, the frequency responses of the incident and reflected electric fields are obtained, then the reflection coefficients $\Gamma = E^{ref}/E^{inc}$ are achieved.

When uncertain parameters impact on the computational model, supposing θ is independent random

parameter with probability density function (PDF). The random parameter may come from uncertain material parameters, geometrical shapes, boundary conditions, initial conditions, computational domain, etc. To model the impact of these randomness and uncertainty on the propagation of EM waves, the solution of E^{inc} and E^{ref} can be expressed as $E^{inc}(z,t,\theta)$ and $E^{ref}(z,t,\theta)$, they are not only a function of (z, t) but also of θ. Therefore, the reflection coefficient Γ are uncertain and stochastic, correspondingly. The statistical moments of the solutions, such as mean and variance of Γ can be quantified [18]-[20] as:

$$E[\Gamma]=\frac{1}{M}\sum_{m=1}^{M}\Gamma_m$$

$$Var[\Gamma]=E[(\Gamma-E[\Gamma])^2]=\frac{1}{M}\sum_{m=1}^{M}(\Gamma_m-E[\Gamma])^2, \quad (8)$$

$$Std[\Gamma]=\sqrt{Var[\Gamma]}$$

$$CI[\Gamma]:\left(E[\Gamma]-n\cdot Std[\Gamma],E[\Gamma]+n\cdot Std[\Gamma]\right)$$

where M represents the samples of the stochastic parameters, which are generated by using a random number generator. $E[\Gamma]$ stands for the mean of the random variable Γ; $Var[\Gamma]$ and $Std[\Gamma]$ are the variance and standard deviation of the random variable Γ, respectively; $CI[\Gamma]$ denotes the confidence interval with an upper and lower bounds. The n is used as the critical value. This value is only dependent on the confidence level of the test. A typical two-sided confidence level is as n = 1.96, which corresponds to the confidence interval as 95% (see [18] for details).

C. Results and analysis

To validate the approach discussed above, the reflection coefficients are calculated by the AM-DGTD method for the sensitive variables given. The constitutive parameters are the same as in Subsection A.

Figure 5 plots the computed solution at final time T = 10s as a function of the number of adaptive elements, K, and the order of the local approximation, N. Comparing with analytic solutions, it shows a good agreement for different parameter sets (N, K). There are two ways to improve the accuracy of Γ: (i) keep N fixed, and increase K, known as h-refinement, and (ii) keep K fixed, and increase N, known as order or p-refinement [21]. As shown in the magnified image at around 1.85 GHz, simulation results using larger N or K are closer to analytic results.

Figure 6 shows the results of absolute errors (compared to analytic results). The errors decay fast with increasing N or K, while both lead to a better approximation. Because of smaller errors at the extreme points, there is better manner at the maximum and minimum of the reflection coefficient Γ, i.e., at 1.85 GHz and 3.75 GHz. But with increasing frequency, the error values become somewhat large.

Inspecting results in Fig. 6, one observes that the results of AM-DGTD scheme are clearly convergent for increasing K and/or N. However, the high accuracy comes at a price. The higher accuracy needs the greater execution time. Table 1 has listed the root mean square (RMS) error and the execution time at different combinations of (N, K). Consider, as an example, an error of O (3.0e-5). From the results in Table 1, we see that this can be achieved through (2, 40), (2, 160), (3, 40), and (4, 20) (the bold font). Comparing with these results, the combination of (2, 40) has the highest order of approximation and the fastest running time in which the hosting CPU is Intel Core i3-4150 with four cores and clock speed of 3.5 GHz.

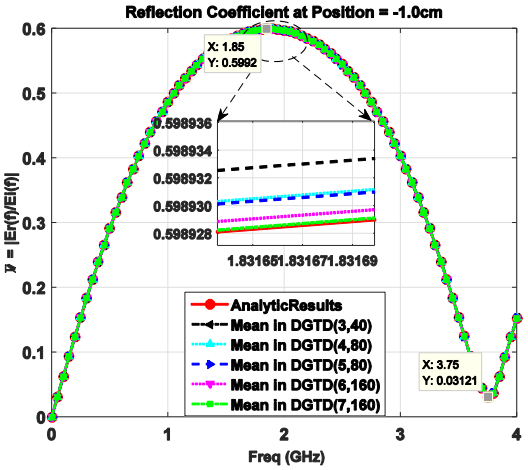

Fig. 5. The reflection coefficient for different sets of parameters (N, K) compared against the exact solution.

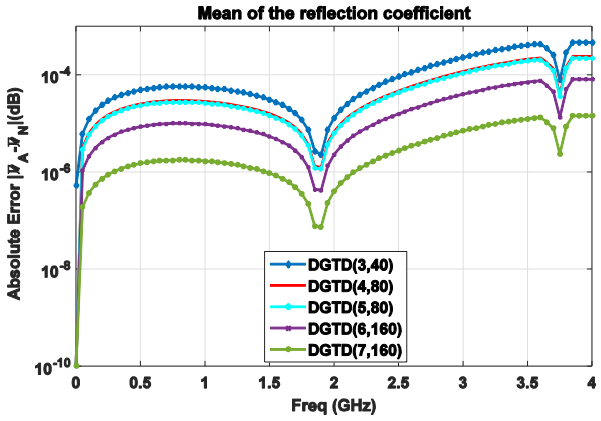

Fig. 6. Absolute errors for different sets of parameters (N, K) compared against the exact solution.

Because the stochastic problems require generally a large number of the variables to calculate statistical properties, one must make a trade-off between accuracy and execution time for the employed method. According

to the results of Table 1, the combination of (N, K) = (2, 40) has been chosen, because of its higher accuracy and lesser time.

To analyze execution time efficiency, an ultra-thin coating is handled by the AM-DGTD method. Comparing with traditional DGTD method, the AM-DGTD approach can save more execution time. For example, when the thickness of the ultra-thin coating is 0.05cm, the execution time is 1724.4648s and 205.0989 s, respectively, using the traditional DGTD and the AM-DGTD methods. It is clearly exhibiting that the AM-DGTD technique helps achieving very fast numerical computations.

Table 1: RMS error (GHz), total execution time (s)

N \ K	20	40	80	130	160
1	5.3615e-3	1.1319e-3	2.8409e-4	1.0901e-4	7.1152e-5
	5.1219	6.4955	10.0083	14.0528	16.5547
2	1.8919e-3	**2.4724e-5**	5.1515e-5	1.4265e-5	**2.7230e-5**
	6.5837	**9.6089**	16.4490	24.8534	**30.1344**
3	5.3715e-5	**2.7734e-5**	1.9115e-5	2.0471e-5	1.2255e-5
	9.1618	**15.0469**	26.7811	42.7873	52.5584
4	**3.0970e-5**	2.3152e-5	2.0652e-5	1.3980e-5	1.2212e-5
	12.5116	21.9100	41.4415	67.3585	82.5465
5	2.4773e-5	1.3339e-5	1.3075e-5	1.5433e-5	1.3684e-5
	17.1342	30.7708	59.2901	97.0274	120.9001
6	3.1082e-5	1.7996e-5	1.5677e-5	1.4709e-5	1.2306e-5
	22.2469	41.6919	81.7953	134.7709	167.9819
7	1.6191e-5	1.9432e-5	1.3092e-5	1.3431e-5	1.3097e-5
	28.1425	54.0226	106.8370	176.5143	220.7351

IV. AM-DGTD FOR STOCHASTIC PARAMETERS

The actual form of flaws in the dielectric coating may not be known, causing the introduction of the uncertainty in some sensitive parameters. These uncertainties can be based on pure speculation, on measured data, or on other available information. In this section, a few typical uncertain flaws are discussed and validated by the AM-DGTD approach. To reduce the complexity of the simulations, the uncertain flaws are expressed as stochastic variables, characterized with appropriate probability distributions. And these stochastic variables are statistically independent.

A. Uncertainty in material

Deterministic solutions require accurate input parameters, however, there always exist uncertain material properties such as from imprecise measurement or manufacturing. In this section, the case of uncertainty in permittivity is considered, that is, tolerances and uncertainties lie in the relative permittivity ε_r.

For the model in Fig. 3, a randomness in the relative permittivity of the dielectric coating is assumed as [9]:

$$\varepsilon_r(x,\theta)=\begin{cases}1 & x\notin coating\\ 4\cdot\left(1+\dfrac{0.1\cdot\theta^2}{1+\theta^2}\right) & otherwise\end{cases}, \tag{9}$$

where θ is a Gaussian variable with zero mean and unit variance. With the uncertainty of the formula (9), the relative permittivity ε_r is guaranteed to remain positive in the domain of the dielectric coating. Note that our concern is not the correctness of the probabilistic law chosen in (9) for the uncertainty of the ε_r, since for any reasonable law, the techniques presented in this paper should work equally well.

Other parameters are fixed as the computational domain Ω = [-6.0cm, 6.0cm], the thickness of the coating d = 2.0cm, the position of the observed point P = -0.1cm, the total computational time T = 10s.

The mean and standard deviation of the reflection coefficient Γ of have been evaluated by the AM-DGTD method at the observation point. Table 2 shows the results of the quantitative uncertainties of the Γ versus different tolerances of the relative permittivity ε_r, i.e., the minimum, maximum, mean and 95% confidence intervals (CI) of Γ at the maximum 1.85 GHz. With the increasing of the $\Delta\varepsilon_r$, it has been found that the $E[\Gamma]$ is far away from the value of $\Delta\varepsilon_r = 0$. When the $\Delta\varepsilon_r$ is negative, i.e., the value of ε_r turns small, the $E[\Gamma]$ is reduced and the region of 95% $CI[\Gamma]$ widens, e.g., ε_r = 3.8612, then $E[\Gamma]$ = 0.5878, $CI[\Gamma]$ = [0.5690, 0.6067]. On the contrary, the $\Delta\varepsilon_r$ is positive, i.e., the value of ε_r turns big, the $E[\Gamma]$ is increased and the region of 95% $CI[\Gamma]$ also widens, e.g., ε_r = 4.2994, then $E[\Gamma]$ = 0.6214, $CI[\Gamma]$ = [0.5924, 0.6505].

To study the relationship of the deviation of reflection coefficient Γ and permittivity ε_r, another 1000 independent random variables are used. The results of uncertainty quantification of reflection coefficient with different deviations in permittivity ε_r over a 0-4 GHz frequency range are shown in Fig. 7. It is obvious that the minimum

reflection point, i.e., 3.75 GHz, turn worse with the tolerances of ε_r increase. When the tolerance of ε_r is changed, the value of this point is increased, i.e., the value of ε_r decreases, this point shifts a bit to higher frequency; when the values of ε_r increases, the point shifts a bit to lower frequency. The increased offset indicates an increased tolerance existing in the results.

Table 2: Uncertainty quantification of Γ versus different deviation in ε_r

$\Delta\varepsilon_r$ \ Γ	Min	Max	Mean	95% CI
-0.4056	0.4737	0.5999	0.5595	[0.4905, 0.6286]
-0.2831	0.5287	0.5999	0.5735	[0.5311, 0.6159]
-0.1388	0.5681	0.5999	0.5878	[0.5690, 0.6067]
0.0	0.5999	0.5999	0.5999	[0.5999, 0.5999]
0.1287	0.5999	0.6267	0.6098	[0.5943, 0.6253]
0.2994	0.5999	0.6474	0.6214	[0.5924, 0.6505]
0.4232	0.5999	0.6668	0.6286	[0.5882, 0.6690]

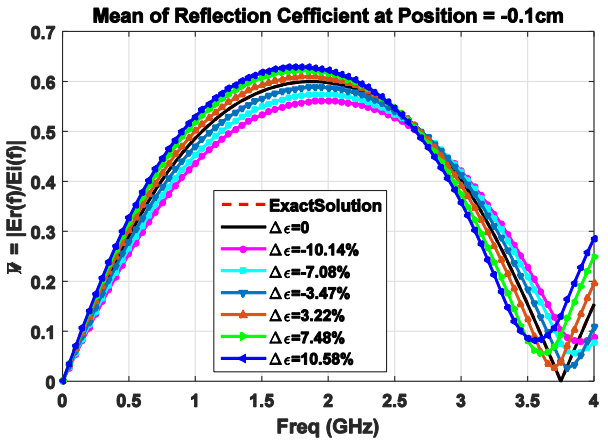

Fig. 7. Distribution of Γ with respect to different deviation in ε_r.

B. Uncertainty in thickness of coating

Suppose that the physical thickness of the dielectric coating is unknown, i.e., when there is uncertainty associated with the position of the right boundary of the coating. Uncertainty in the thickness of d can be modeled by choosing x^{right} a random variable and keeping x^{left} as constant. And the randomness x^{right} is a random parameter with some associated PDF.

The uncertain deviation in the right boundary position is chosen, so that the thickness of the coating is of variable value. The position of the right boundary is assumed to be $x^{right} = d + g(\theta)$, this allows x^{right} to be positioned on both sides of the mean position. Here $g(\theta)$ (the deviation in thickness Δd) is a uniform variable. The mean is chosen as ±0.1, ±0.2 and ±0.3 with a tolerance of ±0.01, i.e., $g(\theta)/\Delta d$ is uniformly distributed in the interval [±0.09cm, ±0.11cm], [±0.19cm, ±0.21cm], and [±0.29cm, ±0.31cm], respectively.

Figure 8 shows how the uncertain deviation in thickness of the dielectric coating affects the reflection coefficient Γ at the observation point P = -0.1cm, which are computed using the AM-DGTD formulation outlined in Section III. In the frequency 0-5 GHz range, the magnitude of the mean of Γ for 1000 samples of the random thickness is shown in the Fig. 8. When Δd = 0, the numerical results are in good agreement with analytic solutions. With the thickness d decreasing, e.g., the average thickness is from 2.3cm to 1.7cm, it has been observed obviously that the curves of the reflection coefficient Γ are extended towards the x axis and the minimum reflection frequency points shift from low to high frequency.

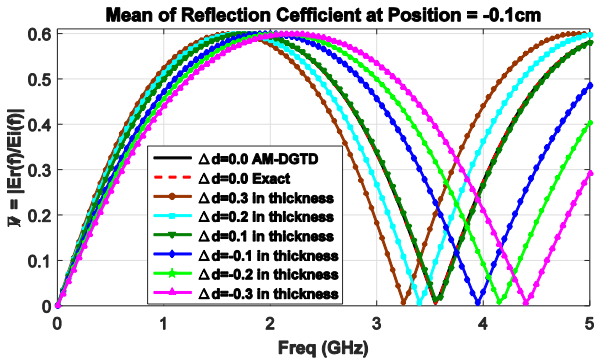

Fig. 8. Mean of Γ for 1000 samples drawn from the AM-DGTD simulations.

C. Random holes in coating

In this experiment, the AM-DGTD method is employed to analyze the reflection coefficients of imperfect dielectric coating caused by blotch, bubble, or recessed hole on a film. The different number, different radius, and random positions of holes in the dielectric coating of the range of [0.0cm, 2.0cm] are simulated.

1) Single hole

The hole parameters are assumed as ε_{rh} = 1, μ_{rh} = 1. The arbitrary mesh is represented in Fig. 9, the radius and random position of the hole are statistically independent. The number of the elements is set as K = 40. Degrees of two (N = 2) polynomials are enough to ensure that convergence is achieved in the physical space. The randomness of the holes can be incorporated into the AM-DGTD method by introducing uncertainty in the local computational mesh. To accomplish this, a displacement mesh is employed around each uncertain portion of the geometry.

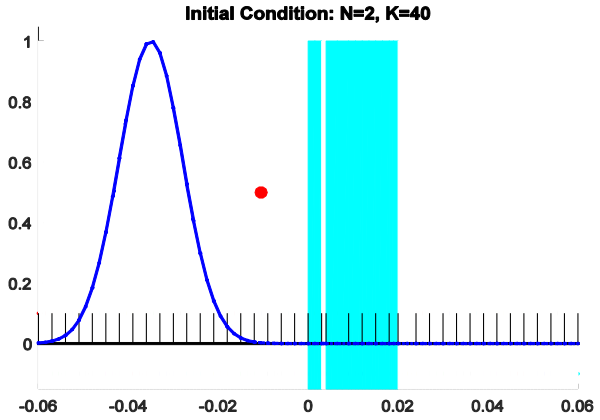

Fig. 9. The sketch of the model with one uncertain hole.

Three cases with random position and radius r as 0.025cm, 0.05cm, and 0.1cm are considered, respectively. Comparisons of the mean of the reflection coefficient Γ with and without these random holes over a 0-10 GHz frequency range are presented in Fig. 10. When the radius r is increased, the mean Γ becomes worse. For instance, the maximum reflection coefficient at 1.85 GHz is decreased, and the minimum value at 3.75 GHz is increased. And the curves of frequency-domain response are shifted a bit to higher frequency.

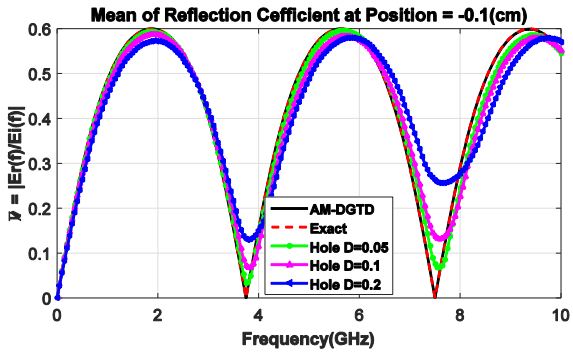

Fig. 10. One hole with random positions and variable diameter.

2) Multiple holes

An arbitrary mesh with two uncertain holes is represented in Fig. 11, all parameters are same as that of single-hole case. With the increasing of hole radius, the mean of reflection coefficient Γ becomes worse. For example, the value of the maximum becomes smaller and the value of the minimum becomes bigger.

The properties of results are similar to those of the single-hole case, but for the two random holes, the curve shifts more bit to the higher frequency, as shown in Fig. 12. The comparison results of the mean of the reflection coefficient of the model with 0-3 random holes are summarized in Fig. 13. It has been found that the mean Γ becomes worse with the number of the holes increasing.

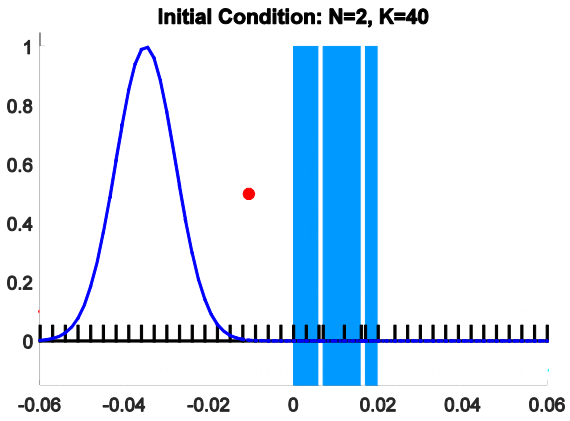

Fig. 11. The sketch of the model with two uncertain holes.

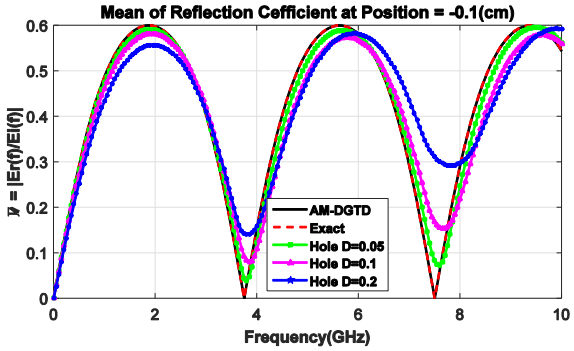

Fig. 12. Two holes with random positions and variable radius.

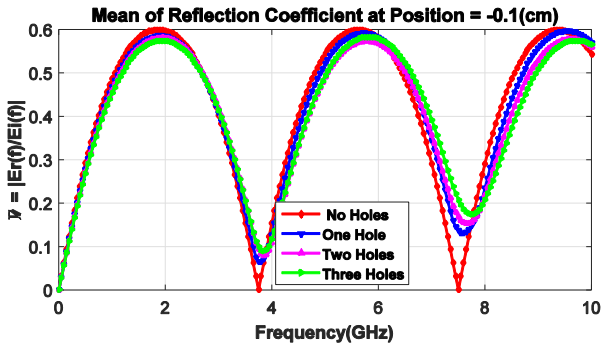

Fig. 13. Comparison of the Γ for different numbers of random hole.

Figure 14 shows the estimation of mean Γ and 95% *CI* for the imperfect dielectric coating with random number of holes computed by the AM-DGTD method. And the radius of hole is supposed to equal to 0.1cm, and the positions of hole are randomly selected. The limits of the 95% *CI* are obtained from the PDF, such that

the 2.5% of the data goes beyond the lower and upper bounds, respectively. The mean Γ of 2.5% quartile near the minimum is observed to perturb slightly and the mean Γ of 97.5% near the maximum is observed to shift slightly, all indicating an increased uncertainty exists in the results.

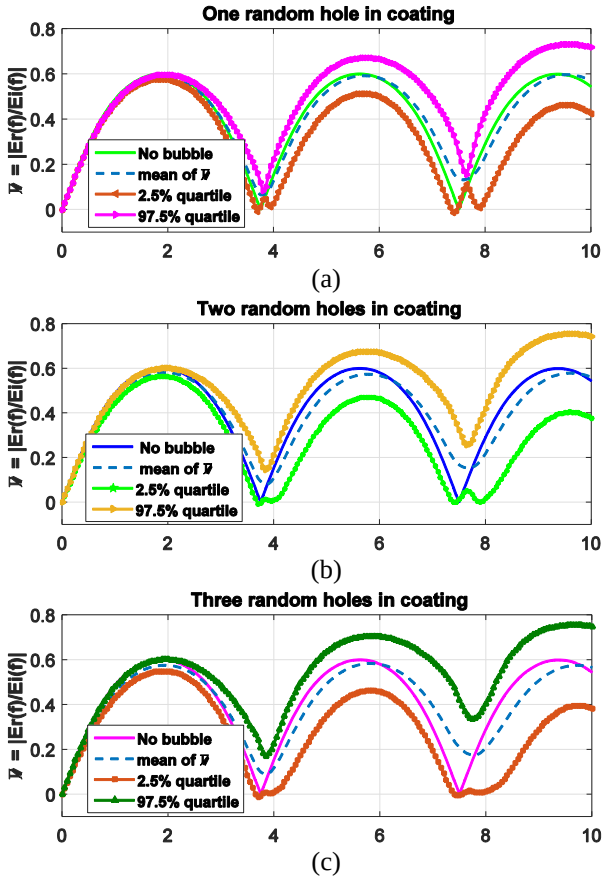

Fig. 14. The deviation in the mean and in 95% confidence intervals for Γ when the solution with stochastic holes is compared against the solution without holes: (a) one hole, (b) two holes, and (c) three holes.

Figure 15 (a) shows the mean of the Γ for the dielectric coating without holes by using the AM-DGTD method. The mean Γ with only one uncertain hole at the maximum 1.85 GHz are concentrated in the interval [0.581, 0.598], however, the values drop to range of [0.562, 0.597] and [0.544, 0.596] for the two and three holes, respectively, as shown in Figs. 15 (b)-(d). These numerical results are agreed with the physical explanation. In term of the value of the interval, we clearly see the smaller mean Γ have worse flaws corresponding to a larger number of holes.

From Fig. 16, it is clearly seen that the mean Γ at different frequencies is different for different numbers of random holes. For $0 \leq \Gamma \leq 0.4$, the values are increased with increasing of the number of the random hole; the $\Gamma = 0.5$ results slightly changed; and for $0.5 < \Gamma \leq 0.6$, the values are decreased with the increasing of the number of the random hole.

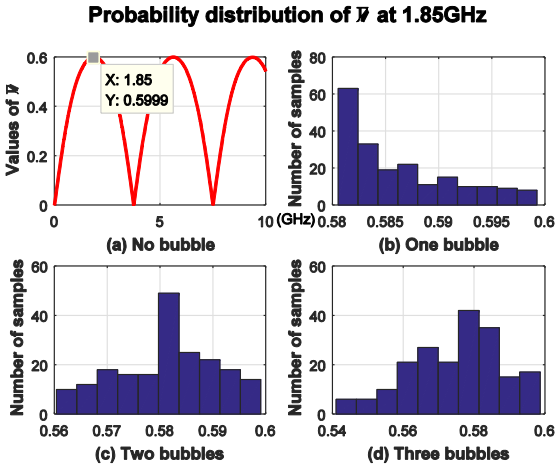

Fig. 15. Distribution of the reflection coefficient with different number of random holes: (a) the analytic solution of Γ without hole, (b) the distribution of Γ with one random hole at 1.85 GHz, (c) the distribution of Γ with two holes, and (d) the distribution of Γ with three random holes.

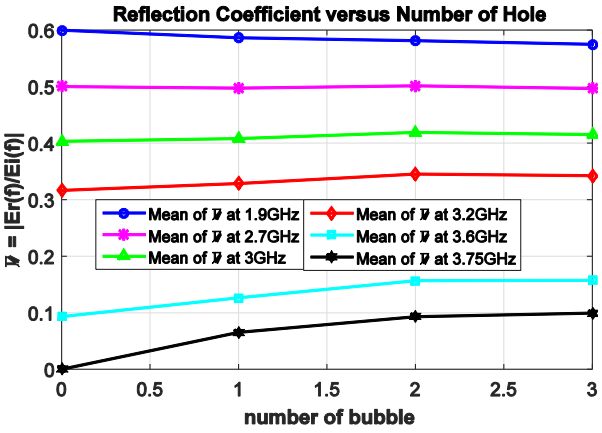

Fig. 16. The relationship between the mean of Γ and the number of hole.

V. CONCLUSION

In this paper, we discussed the use of an adaptive mesh integrated into discontinuous Galerkin method to research the impact of uncertain flaws in the 1D propagation problems. These sources of uncertain flaws are considered: the varied relative permittivity, thickness of coating and multivariable holes in the medium. The adaptive spatial discrete algorithm for the high order accurate DGTD method has been developed to solve

these irregular, complex, and random flaws in the dielectric coating.

The adaptive mesh technology, which generated by the displacement of nodes and the insertion of nodes, can provide efficient and optimum number of mesh elements as compared to simple uniform mesh. The simulation results have been shown that the new approach can save computational resources because of avoiding redundant division of the computational domain. Three typical experiments validate significant advantages of the AM-DGTD approach and show potential for further study of uncertain problems.

ACKNOWLEDGMENT

This work was supported in part by the Natural Science Foundation of China 61401199, Postgraduate Technology Innovation Project of Jiangsu Province KYLX15_0286, and the Technology key Project of the Education Department of Henan Province 14B413010.

REFERENCES

[1] D. Satas, A. A. Tracton, and A. J. Rafanelli, *Coatings Technology Handbook*. 2nd ed., Charleston Advisor, pp. 12-14, 2002.

[2] M. P. Schultz, "Effects of coating roughness and biofouling on ship resistance and powering," *Biofouling*, vol. 23, no. 5, pp. 331-341, Sep. 2007.

[3] L. R. A. X. De Menezes, A. Ajayi, *et al.*, "Efficient extraction of statistical moments in electromagnetic problems solved with the method of moments," in *Microwave and Optoelectronics Conference*, pp. 757-760, 2007.

[4] R. S. Edwards, A. C. Marvin, and S. J. Porter, "Uncertainty analyses in the finite-difference time-domain method," *IEEE Transactions on Electromagnetic Compatibility*, vol. 52, no. 1, pp. 155-163, Feb. 2010.

[5] A. C. M. Austin and C. D. Sarris, "Efficient analysis of geometrical uncertainty in the FDTD method using polynomial chaos with application to microwave circuits," *IEEE Transactions on Microwave Theory & Techniques*, vol. 61, no. 12, pp. 4293-4301, Sep. 2013.

[6] S. M. Smith and C. Furse, "Stochastic FDTD for analysis of statistical variation in electromagnetic fields," *IEEE Transactions on Antennas & Propagation*, vol. 60, iss. 7, pp. 3343-3350, May 2012.

[7] B. Navaneetha Raj, N. G. R. Iyengar, and D. Yadav, "Response of composite plates with random material properties using FEM and Monte-Carlo simulation," *Advanced Composite Materials*, vol. 7, no. 3, pp. 34-39, Apr. 2012.

[8] S. Sarkar and D. Ghosh, "A hybrid method for stochastic response analysis of a vibrating structure," *Archive of Applied Mechanics*, vol. 85, iss. 11, pp. 1607-1626, Nov. 2015.

[9] C. Chauvi, J. S. Hesthaven, and L. Lurati, "Computational modeling of uncertainty in time-domain electromagnetics," *Siam Journal on Scientific Computing*, vol. 28, no. 2, pp. 751-775, Jan. 2006.

[10] P. Li and L. J. Jiang, "Uncertainty quantification for electromagnetic systems using ASGC and DGTD method," *IEEE Transactions on Electromagnetic Compatibility*, vol. 57, no. 4, pp. 754-763, Feb. 2015.

[11] L. D. Angulo, J. Alvarez, *et al.*, "Discontinuous Galerkin time domain methods in computational electrodynamics: State of the art," *Forum for Electromagnetic Research Methods and Application Technologies*, vol. 10, no. 004, pp. 34-39, Aug. 2015.

[12] S. P. Gao, Y. Lu, and Q. Cao, "Hybrid method combining DGTD and TDIE for wire antenna-dielectric interaction," *Applied Computational Electromagnetics Society Journal*, vol. 60, no. 6, pp. 677-681, June 2015.

[13] H. Li, I. Hussain, Y. Wang, *et al.*, "Analysis the electromagnetic properties of dielectric coatings with uncertain flaws using DGTD method," *International Applied Computational Electromagnetics Society (ACES) Symposium*, Aug. 2017.

[14] L. Zhao, G. Chen, and W. Yu, "An efficient algorithm for SAR evaluation from anatomically realistic human head model using DGTD with hybrid meshes," *Applied Computational Electromagnetics Society Journal*, vol. 31, no. 6, pp. 629-635, June 2016.

[15] S. Yan and J. M. Jin, "A dynamic p-adaptation algorithm for the DGTD simulation of nonlinear EM-plasma interaction," *IEEE/ACES International Conference on Wireless Information Technology and Systems, IEEE*, pp. 1-2, May 2016.

[16] H. Edelsbrunner, *Geometry and Topology for Mesh Generation*. Cambridge University Press, 2001.

[17] L. Freitag and C. Ollivier-Gooch, "Tetrahedral mesh improvement using swapping and smoothing," *International Journal for Numerical Methods in Engineering*, vol. 40, no. 21, pp. 3979-4002, Mar. 1997.

[18] S. Swain, *Handbook of Stochastic Methods for Physics, Chemistry and the Natural Sciences*. Springer-Verlag, 1983.

[19] E. L. Bronaugh and J. D. M. Osburn, "A process for the analysis of the physics of measurement and determination of measurement uncertainty in EMC test procedures," in *Electromagnetic Compatibility*, pp. 245-249, Aug. 1996.

[20] D. L. Rumpf, *Statistics for Dummies*. John Wiley & Sons Inc., 2004.

[21] J. S. Hesthaven and T. Warburton, *Nodal Discontinuous Galerkin Methods: Algorithms, Analysis,*

and Applications. Springer Publishing Company, Incorporated, 2008.

[22] I. Hussain, H. Li, Y. Wang, and Q. Cao, "Modeling of structures using adaptive mesh in DGTD method for EM solver," presented at *Progress in Electromagnetics Research Symposium*, 2017.

[23] T. Warburton, "An explicit construction of interpolation nodes on the simplex," *Journal of Engineering Mathematics*, vol. 56, no. 3, pp. 247-262, Sep. 2006.

[24] R. Diehl, K. Busch, and J. Niegemann, "Comparison of low-storage Runge-Kutta schemes for discontinuous Galerkin time-domain simulations of Maxwell's equations," *Journal of Computational & Theoretical Nanoscience*, vol. 7, no. 8, pp. 1572-1580, Aug. 2010.

[25] G. Mur, "Absorbing boundary conditions for the finite-difference approximation of the time domain electromagnetic field equations," *IEEE Trans. Electromagnetic Compatibility*, vol. 23, no. 4, pp. 277-382, Nov. 1981.

Huiping Li received the master's degree in Communication and Information Systems from the Guangxi University, Guangxi, China, in 2007, and she is currently pursuing the Ph.D. degree in Electromagnetic Field and Microwave Technology from Nanjing University of Aeronautics and Astronautics, Nanjing, China, since 2014.

She has been a Lecturer with the School of Physics and Electronics, Henan University, Kaifeng, China, since 2008. Her current research interests include computational electromagnetism, wireless communication and circuit analysis.

Ishfaq Hussain received the B.Sc. degree in Electrical Engineering (Electronics & Communication) from the University of Engineering and Technology (UET) Lahore, Pakistan in 2008. He has been working on microwave systems as a Manager (Technical) with Pakistan-based public sector research and development organization since 2008. Currently, he is pursuing the M.Sc. degree at College of Electronic and Information Engineering, Nanjing University of Aeronautics and Astronautics, Nanjing China. His current research interests include computational electromagnetics and broadband microwave systems.

Yi Wang received the B.S. and Ph.D. degrees in Communication and Information System from Nanjing University of Aeronautics and Astronautics (NUAA), Nanjing, China in 2006 and 2012. After that, Wang joined the College of Electronic and Information Engineering, NUAA, as an assistant Professor.

His research interests includes computational electromagnetics, especially the finite-difference time-domain (FDTD) method, the FDTD modeling of the entire Earth-ionosphere system, the earthquake electromagnetics and radome design.

Qunsheng Cao received the Ph.D. degree in Electronic Engineering from The Hong Kong Polytechnic University, Hong Kong, in 2000. From 2000 to 2005, he was a Research Associate with the Department of Electrical Engineering, University of Illinois at Urbana-Champaign, and with the Army High Performance Computing Research Center (AHPCRC), University of Minnesota, respectively. In 2006, he joined the University of Aeronautics and Astronautics (NUAA), Nanjing, China, as a Professor of Electronic Engineering. He has authored or co-authored over 70 papers in refereed journals and conference proceedings. He has co-authored Multi-resolution Time Domain Scheme for Electromagnetic Engineering (Wiley, 2005).

His current research interests are in computational electromagnetism and antennas designs, particularly in time domain numerical techniques for the study of microwave devices and scattering applications.

Resistive Active Balanced Power Divider Design with Touchstone and Kron's Formalism Hybrid Model

Blaise Ravelo [1,2], Fayu Wan [1], Sebastien Lalléchère [3], and Benoit Agnus [4]

[1] Nanjing University of Information Science & Technology, Nanjing, China 210044

[2] Normandy University, UNIROUEN, ESIGELEC, IRSEEM EA 4353
Technopole du Madrillet, Avenue Galilée, BP 10024, F-76801 Saint Etienne du Rouvray, France

[3] UCA, CNRS, SIGMA Clermont, Institut Pascal, France

[4] Av. Blaise Pascal, F-63178 Aubière, WAVE CONCEPTION, 14000 Caen, France
fayu.wan@nuist.edu.cn

Abstract ─ A resistive active power divider (RAPWD) design based on Kron's model is introduced. The three-way RAPWD topology is essentially constructed with a low noise amplifier (LNA) with input and output matching shunt resistances. The RAPWD S-parameter is analytically expressed from the Kron's method hybridized with the LNA touchstone model. The RAPWD synthesis relation is established in function of the expected gain and matching access. The feasibility of the established Kron's method modelling is validated with a proof-of-concept (POC) using the surface mounted monolithic LNA LEE-9+ from mini-circuits. As expected, S-parameters are in good correlation between simulations and computed results from the proposed hybrid method. A relatively flat transmission gain of about 9+/-0.2 dB is realized in the very wide frequency band 0.5 to 4.5 GHz. The broadband tested RAPWD input and output matching and access port isolations are widely better than 10 dB.

Index Terms─ Active microwave circuit, design method, hybrid model, Kron's formalism, Power Divider (PWD), resistive topology, synthesis relations.

I. INTRODUCTION

The power divider (PWD) is one of the key elements and most useful components for the RF/microwave communication system. The PWD RF/microwave function is usually implemented in different front- and back-end architectures as phased array antennas [1-2] and reflectors [3].

The phased array enables to deploy several functions widely used in military and commercial applications as retrodirective antenna system for example based on the Van Atta Array [4]. Various design technologies have been deployed in function of the substrate structures [5] and improving the 3D radiation beam coverage [6]. The phased array architecture is regularly employed in the radar system. It allows to improve the airborne radar performance as can be found in the atmospheric meteorology research [7]. The phased array architecture is also popularly implemented in radio astronomy stations [8-10]. The array antenna is flexible to operate in low-frequency ranges which are potentially useful for the sky radio scanning [8-12]. In addition, the PWD based phased array architectures are potentially integrable in Silicon based radio frequency integrated circuits (RFICs) [13]. So, the phased array elements are potentially designed and implemented in CMOS technology for microwave and millimeter wave applications as 60-GHz [14] and 77-GHz [15] transceivers.

The PWD function can be designed in three- or multiple N-way topologies [16-19]. Several topologies as coplanar waveguide [17], metamaterial [18] and hybrid-expanded coupled line based structures [19] were proposed. However, one of easiest design and implemented PWD are based on the Tee-shape passive circuit. The most popular in RF/microwave engineering is the Wilkinson PWD [20-25]. The Wilkinson PWD has been widely exploited and implemented in coplanar wave guide [22], microstrip [23] and hybrid technology [24] in both narrow- and broad-band frequencies. The Wilkinson PWD can be also used to design more complex microwave function as Balun [25]. Nevertheless, acting as passive devices, Tee- and Wilkinson PWD components suffer about insertion losses.

To tackle this problem, active topologies may constitute an efficient solution in order to compensate the losses. The PWD active topology can be designed similar to multiport power amplifiers [26]. But to cope with the design complexity, simple implementation circuit as resistive and low-noise amplifier (LNA) active multi-way PWD [27-28] is required. However, the analytical

Submitted On: September 26, 2017
Accepted On: January 9, 2018

modelling should require the consideration of the LNA touchstone model. In this paper, we are introducing a simple and efficient computational method of the resistive active PWD topology by using the Kron's formalism as deployed in [29-32]. This typically unfamiliar computational method is based on the tensorial analysis of network (TAN).

The Kron's formalism was initially developed for the modelling of electrical machine. Then, recently, it was extended to the modelling of complex electronic and electrical system electromagnetic compatibility (EMC) [29]. Combined with the transmission line (TL) Branin approach, the extended Kron's formalism has been employed to the modelling of TL based interconnect printed circuit board (PCB) [30-31]. Moreover, the formalism can be potentially used to determine the S-parameter model of PWD. The fast-computational model of quarter wavelength arm Y-shape unequal PWD is communicated recently in conference ACES-China 2017 [32], the structure is shown in Fig. 1. In progress of this Kron's modelling, we may wonder on applicability of the proposed method for the resistive active PWD (RAPWD) using LNA.

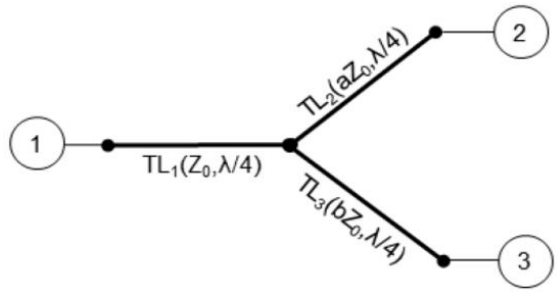

Fig. 1. Y-shape PWD structure [32].

To answer to this technical curiosity, a hybridized model of RAPWD is developed in the present paper. For the better understanding, the paper is organized as follows. Section 2 is dedicated to the proposed circuit computational method. The circuit modelling based on the Kron's formalism and the LNA touchstone model is described. Section 3 addresses the developed hybrid modelling by considering a circuit proof-of-concept (POC). S-parameters simulation results are presented and discussed. Last, Section 4 is the conclusion.

II. THEORY ON THE KRON'S FORMALISM AND TOUCHSTONE HYBRID MODEL OF RESISTIVE ACTIVE POWER DIVIDER

The present section is focused on the hybrid modelling of the three-way PWD. The synoptic of the proposed topology is depicted in Fig. 2. In the present configuration, Port ① is assumed as the input, and Port ② and Port ③ are the outputs.

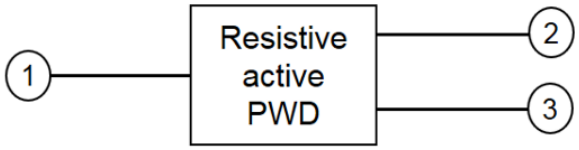

Fig. 2. Synoptic of the RAPWD under study.

The RAPWD is basically implemented by using shut resistances associated with LNA as active elements. Similar to all microwave circuit, in the remainder part of the paper, the proposed theory is established based on the topology S-parameter investigation referenced to the source and load impedance R_0=50 Ω. The calculation principle of the hybrid modelling under study will be illustrated in the coming paragraphs.

A. Resistive and LNA based elementary cell

The elementary cell constituting the proposed RAPWD is sketched in Fig. 3.

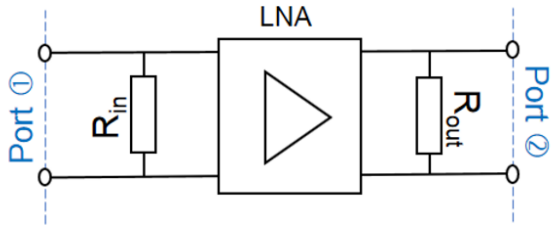

Fig. 3. Considered resistive and active cell constituting the proposed RAPWD.

It consists essentially of an LNA combined with input and output shunt resistances respectively R_{in} and R_{out}. To establish the RAPWD S-parameter, the LNA model is assumed to be provided by the manufacturer in touchstone data. Acting as a two-port S-parameter, the equivalent model can be merely written as:

$$[S_{LNA}(j\omega)]=\begin{bmatrix} S_{LNA_{11}}(j\omega) & S_{LNA_{12}}(j\omega) \\ S_{LNA_{21}}(j\omega) & S_{LNA_{22}}(j\omega) \end{bmatrix}. \quad (1)$$

The LNA is supposed as a unilateral RF/microwave component. Furthermore, it is characterized the input and output matching level equal to S_{LNA11}=S_{LNA22}=r. Meanwhile, the LNA can be represented by the matrix:

$$[S_{LNA}(j\omega)]=\begin{bmatrix} r(j\omega) & 0 \\ t(j\omega) & r(j\omega) \end{bmatrix}. \quad (2)$$

Based on the S-to-Z transform, the equivalent Z-matrix is given by:

$$[Z_{LNA}(j\omega)]=\begin{bmatrix} R_0\dfrac{1+r(j\omega)}{1-r(j\omega)} & 0 \\ 2R_0\dfrac{t(j\omega)}{[1-r(j\omega)]^2} & R_0\dfrac{1+r(j\omega)}{1-r(j\omega)} \end{bmatrix}. \quad (3)$$

B. Graph model of the two-way RAPWD

The RAPWD circuit diagram is illustrated in Fig. 3. The LNAs are inserted at the PWD input and output three arms. The resistance R_1 is connected in shunt at the input for controlling the input matching. Similarly, the resistances R_2 and R_3 are connected in shunt at the outputs for controlling the output matching. The intermediate resistance Rm ensures the stability and the LNA interstage matching. Before setting the Kron's formalism, the system must be traduced in graph representation. The graph equivalent topology of the circuit introduced in Fig. 4. This graph is essentially built by the branches and the black box representing the LNA touchstone S-parameter model. The circuit is fed by voltage sources V_1, V_2 and V_3 respectively connected at Port ①, Port ② and Port ③. It induces the branch currents I_1, I_2 and I_3. The LNA input and output voltages V_α and fictive currents I_α with $\alpha=\{a, b, \dots, i\}$ are indicated in this circuit for mesh law elaboration.

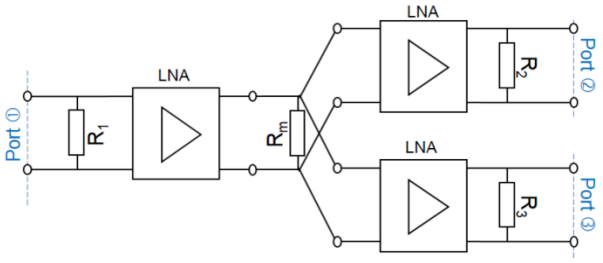

Fig. 4. Circuit topology of the RAPWD.

To construct a symmetrical or balanced PWD, we just have to generate $S_{21}=S_{31}$ and $S_{22}=S_{33}$. This condition can be achieved by implementing same arms at the PWD output branches. In other word, same output shunt resistances $R_2=R_3$ must be used. This idea guarantees the symmetry between the PWD output arms. Consequently, the overall three-port device S-parameter can be determined with the S-parameter of two port system by taking $S_{23}=S_{32}=0$ in addition to the equality $S_{21}=S_{31}$ and $S_{22}=S_{33}$. In this case, the graph introduced in Fig. 5 can be reduced as shown in Fig. 6. The shunt impedance Z_{LNA} represents in the LNA input impedance which is previously given in expression (3).

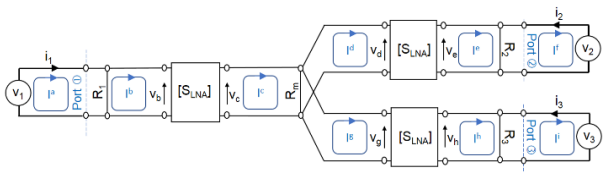

Fig. 5. Equivalent graph topology of the PWD introduced in Fig. 4.

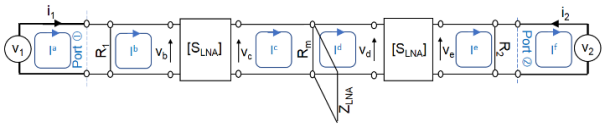

Fig. 6. Reduced equivalent diagram of the graph established in Fig. 5.

C. Discussion on the advantages and the limitation of the RAPWD topology

The combined Kron's formalism and LNA touchstone data hybrid model can be established from the reduced graph proposed in Fig. 6. In order to calculate, the overall system S-parameter, we would start with the three port Z-matrix defined by:

$$\begin{bmatrix} V_1(j\omega) \\ V_2(j\omega) \end{bmatrix} = [Z] \times \begin{bmatrix} I_1(j\omega) \\ I_2(j\omega) \end{bmatrix}, \tag{4}$$

with

$$[Z] = \begin{bmatrix} Z_{11}(j\omega) & Z_{12}(j\omega) \\ Z_{21}(j\omega) & Z_{22}(j\omega) \end{bmatrix}. \tag{5}$$

The analytical expressions governing the system under study can be extracted from the Kron's formalism by assuming that the mesh spaces represented by the current fictive meshes I_α with $\alpha=\{a, b, \dots, i\}$. It implies the following equation system:

$$\begin{cases} V_1(j\omega) = V_b(j\omega) = R_1(I^a(j\omega) - I^b(j\omega)) \\ V_c(j\omega) = V_d(j\omega) = Z_x(I^c(j\omega) - I^d(j\omega)) \\ V_e(j\omega) = V_2(j\omega) = R_2(I^e(j\omega) - I^f(j\omega)) \end{cases}, \tag{6}$$

by denoting the total intermediate impedance as:

$$Z_x = Z_m // Z_{LNA} = \frac{R_0 Z_m (1+r)}{R_0(1+r) + Z_m(1-r)}. \tag{7}$$

In addition to this system, we can consider the LNA model by the transfer matrix:

$$[T(j\omega)] = \begin{bmatrix} T_{11}(j\omega) & T_{12}(j\omega) \\ T_{21}(j\omega) & T_{22}(j\omega) \end{bmatrix}. \tag{8}$$

This transfer matrix is obtained from the LNA touchstone model via the S-to-T transform:

$$\begin{cases} T_{11} = \dfrac{1 + S_{11} - S_{22} - S_{11}S_{22} + S_{12}S_{21}}{2S_{21}} \\ T_{12} = \dfrac{Z_0(1 + S_{11} + S_{22} + S_{11}S_{22} - S_{12}S_{21})}{2S_{21}} \\ T_{21} = \dfrac{1 - S_{11} - S_{22} + S_{11}S_{22} - S_{12}S_{21}}{2S_{21}Z_0} \\ T_{22} = \dfrac{1 - S_{11} + S_{22} + S_{11}S_{22} - S_{12}S_{21}}{2S_{21}} \end{cases}. \tag{9}$$

Therefore, we have the complementary equation system:

$$\begin{cases} V_b(j\omega) = T_{11}(j\omega)V_c(j\omega) + T_{12}(j\omega)I_c(j\omega) \\ I_b(j\omega) = T_{21}(j\omega)V_c(j\omega) + T_{22}(j\omega)I_c(j\omega) \\ V_d(j\omega) = T_{11}(j\omega)V_e(j\omega) + T_{12}(j\omega)I_e(j\omega) \\ I_d(j\omega) = T_{21}(j\omega)V_e(j\omega) + T_{22}(j\omega)I_e(j\omega) \end{cases}. \quad (10)$$

The solution of the combined equations allows to express the unknown voltage in function of the branch currents given by:

$$\begin{cases} V_1(j\omega) = Z_{PWD_{11}}(j\omega)I^b(j\omega) - Z_{PWD_{12}}(j\omega)I^f(j\omega) \\ V_2(j\omega) = Z_{PWD_{21}}(j\omega)I^b(j\omega) - Z_{PWD_{22}}(j\omega)I^f(j\omega) \end{cases}. \quad (11)$$

Finally, the RAPWD S-parameter matrix:

$$\left[S_{PWD}(j\omega)\right] = \begin{bmatrix} S_{PWD_{11}}(j\omega) & S_{PWD_{12}}(j\omega) \\ S_{PWD_{21}}(j\omega) & S_{PWD_{22}}(j\omega) \end{bmatrix}, \quad (12)$$

can be determined from the Z-to-S matrix transform. The expected S-parameter model is given in (13). It can be pointed out that in this ideal case, the PWD isolation losses are zero because of the LNA unilaterality:

$$\begin{cases} S_{PWD_{11}} = \dfrac{2r(j\omega)R_1 - \left[1+r(j\omega)\right]R_0}{2R_1 + \left[1+r(j\omega)\right]R_0} \\ S_{PWD_{12}} = 0 \\ S_{PWD_{21}} = \dfrac{\left\{2r(j\omega)R_2 + \left[1+r(j\omega)\right]R_0\right\}}{\left[1+r(j\omega)\right]\begin{Bmatrix}\left[1+r(j\omega)\right]R_0 + \\ 3\left[1-r(j\omega)\right]R_m\end{Bmatrix}} \\ S_{PWD_{22}} = \dfrac{2R_2 + \left[1+r(j\omega)\right]R_0}{2r(j\omega)R_2 + \left[1+r(j\omega)\right]R_0} \end{cases}. \quad (13)$$

D. Proposed RAPWD synthesis relations

The synthesis relations allowing to determine the RAPWD parameters R_1, R_m and R_2 can be extracted from this equation system in function of the specified PWD:

- Input and output matching level m>0 (assumed to be identical).
- And insertion gain g>0.

Doing this, the proposed RAPWD synthesis formulas are determined from the equations:

$$\begin{cases} \left|S_{PWD_{11}}(R_1)\right| = m \\ \left|S_{PWD_{21}}(R_m)\right| = g \\ \left|S_{PWD_{22}}(R_2)\right| = m \end{cases}. \quad (14)$$

As a matter of fact, the formulas enabling to express the RAPWD parameters are written as:

$$R_1 = \begin{cases} \dfrac{R_0(1+r)(1+m)}{2(r-m)} \; if \; r > m \\ \dfrac{R_0(1+r)(1-m)}{2(m+r)} \; if \; r \le m \end{cases}, \quad (15)$$

$$R_2 = \frac{R_0(1+r)(1-m)}{2(m+r)}. \quad (16)$$

$$R_m = \begin{cases} \dfrac{\alpha_1}{3r^3 g(r+2) - \alpha_2 - 3g} \; if \; S_{PWD_{21}} > 0 \\ -2(1+2m)t^2 \\ \dfrac{\alpha_1}{3g + 2(1-2m)t^2 +} \; if \; S_{PWD_{21}} < 0 \\ 3r^3 g(r+2) - \alpha_2 \end{cases}, \quad (17)$$

with

$$\begin{cases} \alpha_1 = R_0 g(r^4 + 4r^3 + 6r^2 + 4r + 1) \\ \alpha_2 = 2m^2 r^2 \end{cases}. \quad (18)$$

III. SIMULATION VALIDATION RESULTS

This section is focused on the validations of the developed hybrid modelling concept. A POC of RAPWD is designed and fabricated following the synthesis approach described in the previous section. The POC modelled computed results are compared with simulations run in the ADS® environment of the electronic circuit designer and simulator.

A. RAPWD POC description

The PWD POC is a three-port active microwave circuit. This POC was designed with the surface mounted monolithic LNA LEE-9+ from mini-circuits. Figure 7 represents the schematic of the POC circuit prototype.

Initially, the RAPWD expected generating transmission gain of about 9 dB and access port reflection coefficients better than 10 dB was synthesized. Therefore, the calculated RAPWD parameters are R_1=R_2=R_3=200 Ω and R_m=62 Ω. The circuit was biased with V_0=5V_{DC} power supply. The designed, fabricated, simulated and measured POC is represented in Figs. 7. The bias circuits are consisted of self-inductance L=75 nH and C_p=100 pF. The DC blocking capacitors are C=100 pF.

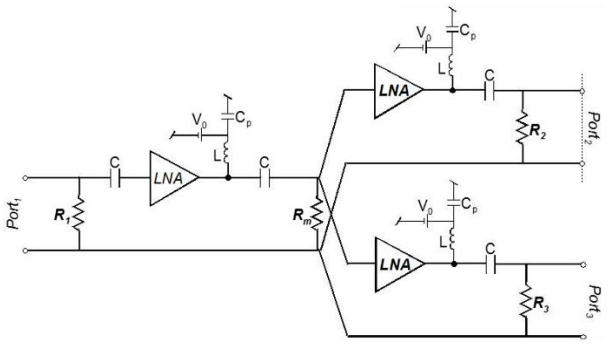

Fig. 7. RAPWD POC simulated circuit design

B. S-parameter results

The validation simulations were performed from 0.5

to 4.5 GHz by using the LNA touchstone model provided by the manufacturer. Figure 8 represents the comparison between the simulated and ideal theory S-parameters obtained from the POC depicted in Fig. 7.

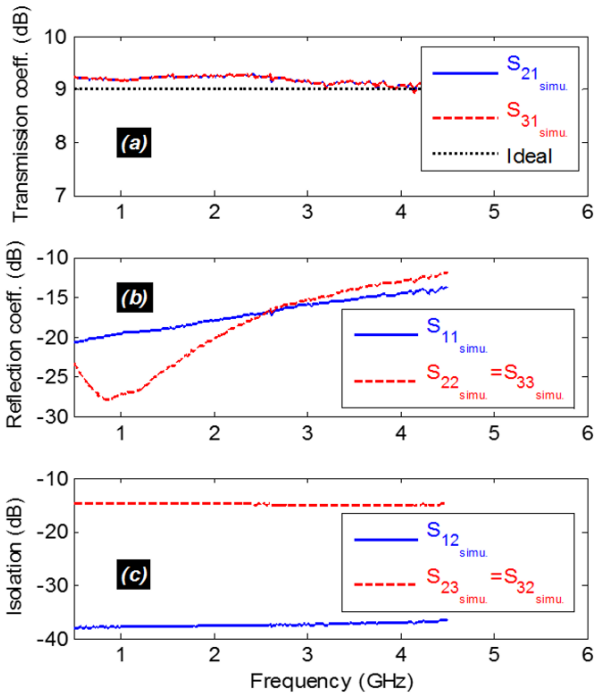

Fig. 8. Comparison of the simulated and ideal theory S-parameters: (a) transmission gains, (b) reflection coefficients, and (c) isolations.

It acts as a very broadband PWD. As seen in Fig. 8 (a), the RAPWD presents a transmission gain with excellent flatness of about 9+/-0.2 dB from 0.5 GHz to 4.5 GHz. Then, as shown in Fig. 8 (c), the isolations are better than 10 dB. The result is very well-correlated to the targeted transmission gain. In addition, as shown in Fig. 8 (b), the three-port access matching is better than 10 dB.

C. Discussion on the advantages and the limitation of the RAPWD topology

The presented RAPWD topology is particularly advantageous in terms of:

- The isolation because of the LNA unilaterality.
- The gain flatness is not easy to achieve for most of passive PWD expected the fully resistive ones. However, with the proposed topology, we have a possibility to generate a very wide bandwidth by choosing the expected LNA.
- The stability which is not, in general, easy to control if the passive PWD to be cascaded with the LNA is not very well matched even out of the operating frequency band.

However, the RAPWD presents drawbacks in matter of:

- The power efficiency because of the shunt resistor which is susceptible to consume and waste energy via Houle effect.
- And the complexity of bias network associated with the DC blocking circuitry.

IV. CONCLUSION

A hybrid modelling methodology of resistive active PWD is investigated. The active topology is mainly consisted of LNA element and shunt resistances. The introduced PWD topology enables to compensate losses and minimize the interbranch isolation in difference with the popular passive PWD topologies. The developed modelling concept is built with the Kron's formalism and the LNA touchstone model. The PWD S-parameter model in function of the LNA S-parameter is established. Then, the synthesis formulas enabling to determine the PWD parameters are expressed. The established theory is validated with resistive active PWD POC. The S-parameter simulation confirms the expected values specified in the synthesis formulas.

It should be emphasized that the proposed RAPWD is advantageous to generate competitive gain flatness, isolation and matching. But it presents some weakness in terms of power efficiency and bias/DC blocking circuitry. In the future, we expect to apply the proposed hybridized Kron's method to more complex active RF/microwave topology by taking into account the power efficiency.

ACKNOWLEDGMENT

The authors address their grateful thanks to Dr. Olivier Maurice for his advice to develop the Kron's formalism based microwave circuit.

This work was supported by NSFC (61601233 and 61750110535). And this work was also partly supported by the FEDER fund from BRIDGE project in Normandy Region, by NSF of Jiangsu (BK20150918), by Defence Research Foundation (6140209050116 ZK53001), by Jiangsu Innovation and Enterprise Group Talents Plan 2015 (SRCB201526), and by PAPD.

REFERENCES

[1] H. A. Wheeler, "Simple relations derived from a phased-array antenna made of an infinite current sheet," *IEEE Trans. AP*, vol. 13, no. 14, pp. 506-514, July 1965.

[2] G. L. Charvat, "Visualization of a phased array antenna system," *Available Online* [2017], https://hackaday.com/2017/01/05/visualization-of-a-phased-array-antenna-system/

[3] B. T. Toland, L. D. Gilger, R. Y. Chan, A. S. Barlevy, and S. J. Hamada, "Deployable phased array of reflectors and method of operation," *Patent US 6268835 B1*, July 2001.

[4] L.Chen, X.-H. Wang, X.-W. Shi, T.-L. Zhang, and

J.-Z. Tong, "Design of a broadband frequency offset van atta array," *PIER Letter*s, vol. 13, pp. 161-171, 2010.

[5] J. B. West and J. C. Mather, "Phased array antenna interconnect having substrate slat structures," *Patent US 7170446 B1*, Jan. 2007.

[6] D. Choudhury, R. Roberts, and U. Karacaoglu, "Wireless antenna array system architecture and methods to achieve 3d beam coverage," *Patent US 20110014878 A1*, Jan. 2011.

[7] E. Loew, J. Salazar, P. S. Tsai, J. Vivekanandan, W. Lee, and V. Chandrasekar, "Architecture overview and system performance of the airborne phased array radar (APAR) for atmospheric research," *Proc. 36rd Conf. on Radar Meteor.*, Breckenrigde, CO, USA, pp. 159-164, 16-20 Sept. 2013.

[8] S. W. Ellingson, "Sensitivity of antenna arrays for long-wavelength radio astronomy," *IEEE Trans. Antennas and Propagation*, vol. 59, no. 6, pp. 1855-1863, June 2011.

[9] G. B. Taylor, S. W. Ellingson, N. E. Kassim, et al., "First light for the first station of the long wavelength array," *J. Astronomical Instrumentation*, vol. 1, no. 1, 1250004, pp. 1-56, 2012.

[10] S. W. Ellingson, T. E. Clarke, A. Cohen, N. E. Kassim, Y. Pihlstrom, L. J. Rickard, and G. B. Taylor, "The long wavelength array," *Proc. IEEE*, vol. 97, no. 8, pp. 1421-1430, Aug. 2009.

[11] M. Harun and S. W. Ellingson, "Design and analysis of low frequency strut-straddling feed arrays for EVLA reflector antennas," *Radio Sci.*, vol. 46, no. 3, RS0M04, pp. 1-12, June 2011.

[12] S. E. Cutchin, J. H. Simonetti, S. W. Ellingson, A. S. Larracuente, and M. J. Kavic, "Constraining the rate of primordial black-hole explosions and extra dimension scale using a low-frequency radio antenna array," *Pub. Astr. Soc. Pacific*, vol. 127, no. 958, pp. 1269-1278, Dec. 2015.

[13] G.-M. Rebeiz and K.-J. Koh, "Silicon RFICs phased arrays," *IEEE Microwave Magazine*, vol. 10, no. 3, pp. 96-103, May 2009.

[14] E. Cohen, M. Ruberto, M. Cohen, O. Degani, S. Ravid, and D. Ritter, "A CMOS bidirectional 32-element phased-array transceiver at 60 GHz with LTCC antenna," *IEEE Trans. MTT*, vol. 61, no. 3, pp. 1359-1375, Mar. 2013.

[15] A. Natarajan, A. Komijani, X. Guan, A. Babakhani, and A. Hajimiri, "A 77-GHz phased-array transceiver with on-chip antennas in silicon: Transmitter and local LO-path phase shifting," *IEEE Journal of Solid-State Circuits*, vol. 41, no. 12, pp. 2807-2819, Dec. 2006.

[16] 16 Way Power Divider, Combiner, Splitter. *Available Online* [2017]. http://www.instockwireless.com/16way-power-splitter-combiner-divider-app.htm

[17] R. N. Simons and G. E. Ponchak, "Coax-to-channelised coplanar waveguide in-phase N-way, radial power divider," *Electronics Letters*, vol. 26, no. 11, pp. 754-756, May 1990.

[18] K. W. Eccleston, "N-way microwave power divider using two-dimensional meta-materials," *Electronics Letters*, vol. 42, no. 15, pp. 863-864, July 2006.

[19] H. Chen and Y. X. Zhang, "A novel compact planar six-way power divider using folded and hybrid-expanded coupled lines," *PIER*, vol. 76, pp. 243-252, 2007.

[20] L. I. Parad and R. L. Moynihan, "Split-tee power divider," *IEEE Trans. MTT*, vol. 13, no. 1, pp. 91-95, Jan. 1965.

[21] N-way Wilkinson Divider. Microwave Encyclopedia-Microwaves101.com. *Available Online* [2017]. https://www.microwaves101.com/encyclopedias/n-way-wilkinson-splitters

[22] J.-S. Lim, H.-S. Yang, Y.-T. Lee, S. Kim, K.-S. Seo, and S. Nam, "E-band Wilkinson balun using CPW MMIC technology," *Electronics Letters*, vol. 40, no. 14, pp. 879-880, July 2004.

[23] M.-A. Antoniades and G.-V. Eleftheriades, "A broadband Wilkinson balun using microstrip metamaterial lines," *IEEE Antennas and Wireless Propagation Letters*, vol. 4, no. 1, pp. 209-212, 2005.

[24] Y. Wu, Y. Liu, S. Li, C. Yu, and X. Liu, "Closed-form design method of an N-way dual-band Wilkinson hybrid power divider," *PIER*, vol. 101, pp. 97-114, 2010.

[25] U.-H. Park and J.-S. Lim, "A 700- to 2500-MHz microstrip balun using a Wilkinson divider and 3-dB quadrature couplers," *Microwave and Optical Technology Letters*, vol. 47, no. 4, pp. 333-335, Sept. 2005.

[26] P. Angeletti and M. Lisi, "Multiport power amplifiers for flexible satellite antennas and payloads," *Microwave Journal*, pp. 96-110, May 2010.

[27] B. Ravelo, "Synthesis of N-way active topology for wide-band RF/microwave applications," *International Journal of Electronics*, vol. 99, no. 5, pp. 597-608, May 2012.

[28] O. Maurice, A. Reineix, P. Hoffmann, B. Pecqueux, and P. Pouliguen, "A formalism to compute the electromagnetic compatibility of complex networks," *Advances in Applied Science Research*, vol. 2, no. 5, pp. 439-448, 2011.

[29] S. Lalléchère, B. Ravelo, and A. Thakur, "Statistical performances of resistive active power splitter," *IoP Conf. Ser.: Mater. Sci. Eng.*, vol. 120, no. 1, pp. 12015-12018, 2016.

[30] B. Ravelo, O. Maurice, and S. Lalléchère, "Asymmetrical 1:2 Y-tree interconnects modelling with Kron-Branin formalism," *Electronics Letters*, vol. 52, no. 14, pp. 1215-1216, July 2016.

[31] B. Ravelo and O. Maurice, "Kron-Branin modelling of Y-Y-tree interconnects for the PCB signal integrity analysis," *IEEE Trans. EMC*, vol. 59, no. 2, pp. 411-419, Apr. 2017.

[32] B. Ravelo, O. Maurice, and S. Lalléchère, "Unequal Y-power divider Kron-Branin model," *Proc. of 2017 International Applied Computational Electromagnetics Society (ACES) Symposium*, Suzhou, China, pp. 1-2, 1-4 Aug. 2017.

B. Ravelo holds his Ph.D. degree in 2008 from Univ. Brest and his dissertation to lead research ("HDR= Habilitation à Diriger des Recherches") in 2012 from Univ. Rouen. He is currently Associate Professor at the graduate engineering school ESIGELEC/IRSEEM in Rouen/ France. His research interests cover the microwave circuit design, electromagnetic compatibility (EMC) and interference (EMI), and signal and power integrity (SI/PI) engineering. He is a pioneer of the negative group delay (NGD) RF/analog and digital circuits and systems. He is (co)-author of more than 200 papers and regularly involved in national/international research projects. He co-supervised and directed 9 Ph.D. students whose 6 Ph.D. candidates defended. He is the coordinator of the European TECS Project funded by the program INTERREG VA 4081, he is in charge of the EM characterization of the platform developed in the CareStore Project funded by FP7-SME-2012 and he participates regularly in large R&D international projects. His current publication h-index is 16 (Reference: Google Scholar 2017).

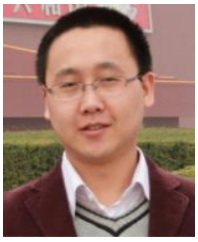

F. Wan received the Ph.D. degree in Electronic Engineering from University of Rouen, Rouen, France, in 2011. From 2011 to 2013, he was a Postdoctoral Fellow in the Electromagnetic Compatibility Laboratory, Missouri University of Science and Technology, Rolla. He is currently a Professor at Nanjing University of Information Science and Technology, Nanjing, China. His current research interests include negative group delay circuit, electrostatic discharge, electromagnetic compatibility, and advanced RF measurement.

S. Lalléchère received the M.Sc. and Ph.D. degrees in Computational Modeling and Electronics from Polytech Clermont and Université Blaise Pascal, Clermont-Ferrand, France, in 2002 and 2006. He is currently an Associate Professor at Université Clermont Auvergne (UCA) and Institut Pascal, Clermont-Ferrand, France. He authored and co-authored more than 120 communications in international journals and conferences. His research interests cover the fields of electromagnetics including electromagnetic compatibility, antennas and propagation, computational electromagnetics, and stochastic modeling in electrical engineering.

Benoit Agnus is the Director of the independent applied research enterprise "Wave Conception." The enterprise is performing research in the areas of electromagnetism, plasmas and multi-parametric servo systems.

Agnus received his Ph.D. in Microwave and Millimeter Wave Engineering Instrumentation and Measurement Techniques in 1994 at the University of Bordeaux 1 in the laboratory of Physics of Interactions Waves Materials ("Physique d'Interaction Ondes Matières = PIOM").

He pursued a 25-year career in industrial Research and Development (R&D) and published several scientific papers. His interest activities are electromagnetic waves, RF/microwave system modeling and post-processing, spatial or terrestrial communication instrumentation, plasma production and control, energy issues for system autonomy, embedded intelligence for the diagnosis and reconfiguration of complex systems, signal processing and RF/microwave transceiver architectures.

An Extension of Cooray-Rubinstein Formula on the Calculation of Horizontal Electric Field from Inclined Lightning Channel

Haojiang Wan, Xiaojia Wang, Yazhou Chen, Xiaodong Pan, and Xinfu Lu

National Key Laboratory on Electromagnetic Environment Effects
Army Engineering University, Shijiazhuang Branch, Shijiazhuang, 050003, China
hbwhj1983@163.com, wangxiaojia0@sina.com, chen_yazhou@sina.com, panxiaodong1980@sina.com, luxinfu123@126.com

Abstract ─ An approximate method to calculate the horizontal electric field from inclined lightning channel in frequency-domain was proposed based on the extension of Cooray formula and Cooray-Rubinstein formula. Validations of these two extended formulas were both performed by comparing their calculation results with those obtained by the numerical solution of Sommerfeld's integrals using Bannister approximations. The results have shown that both the accuracy of these two extended formulas are mainly related to the observation distance and the ground conductivity, and will increase with the increasing ground conductivity and observation distance. The extended Cooray formula could predict the horizontal electric field at ground level accurately at the distance beyond 100m. And the extended Cooray-Rubinstein formula could yield an acceptable approximation on the above-ground horizontal electric field with the exception of the observation point at close range under poor ground conductivity less than 0.0001S/m.

Index Terms ─ Approximate calculation, extended Cooray-Rubinstein formula, frequency-domain, horizontal electric field, inclined lightning channel.

I. INTRODUCTION

The calculation of lightning horizontal electric field at a lossy ground is very important in the field-to-line coupling problem. Generally, the solution of horizontal electric field would lead to the so-called Sommerfeld's integrals, which are highly oscillatory and difficult to evaluate numerically. To overcome this difficulty, many simplified approaches have been proposed, especially in frequency domain. An approximate technique known as the wave tilt formula has been used by several researchers to calculate the horizontal field from lightning at ground level [1, 2]. However, the wave tilt formula is only applicable for the calculation of horizontal field at distances beyond a few kilometers. In order to calculate the horizontal field at close range, Cooray [3] introduced an approximate method in frequency domain to calculated the horizontal field at ground level with the help of the ground surface impedance, which is called as Cooray formula and can be applied for the distances as short as 200m. Based on the Cooray formula, Rubinstein [4] presented another approximate formula, known as Cooray-Rubinstein formula, to evaluate the horizontal electric field off the ground at close, intermediate and far distances. Several researches have shown that the Cooray-Rubinstein formula could yield a satisfactory approximation on the above-ground horizontal electric field at different distances [4-6]. General restrictions of validity of the Cooray-Rubinstein approximation were theoretically examined by Wait [7]. However, he mentioned the possibility that the errors due to the violation of these restrictions may not be practically significant. To improve the accuracy of the Cooray-Rubinstein formula, a simple modification was provided by Cooray [8]. Moreover, his calculations showed that the accuracy of the Cooray-Rubinstein formula may become better when propagation effects were included in the magnetic field used in the surface impedance expression [9]. However, it is worthwhile to note that all these above researches are carried out in the case of vertical lightning channel, including the Cooray formula and Cooray-Rubinstein formula. In fact, the lightning channel is usually inclined or tortuous, which has great influence on the lightning electromagnetic field [10]. Due to traditional analytical methods in time domain are difficult to calculate directly the electromagnetic field from the inclined or tortuous channel at a lossy ground, some researchers used the finite difference time domain (FDTD) method to evaluate the effect of the inclined channel [11, 12]. But this method usually takes a long computation time, and is mainly applicable for close and intermediate distances. To calculate the horizontal field from inclined channel at far distance, Wan et al. [13] proposed an approximate method in frequency domain based on the extension of Cooray formula, which is applicable for the horizontal field at ground level. In this paper, in order to calculate the horizontal electric field from inclined lightning channel above a lossy ground, an extension of Cooray-Rubinstein formula for inclined

Submitted On: September 30, 2017
Accepted On: April 10, 2018

lightning channel is derived, which is applicable for close, intermediate and far distances. Its validity is verified by comparing it with the results from the numerical solution of Sommerfeld's integrals using Bannister approximations, the accuracy of which has already been proved by Cooray [14]. Such an extended Cooray-Rubinstein approximation could be useful for analyzing the interaction of lightning electromagnetic fields with power lines or electrical installations due to the inclined or tortuous lightning channel.

Due to that Cooray formula is an important part of Cooray-Rubinstein approximation, the extension of Cooray formula for inclined lightning channel and its validation are firstly provided in this paper. Then, the extension of Cooray-Rubinstein formula for inclined lightning channel is presented. And the influences of the ground conductivity, the observation distance, and the observation height on the extended Cooray-Rubinstein formula for inclined lightning channel are also discussed, respectively.

II. EXTENSION OF COORAY FORMULA FOR INCLINED LIGHTNING CHANNEL

Figure 1 shows the geometry relevant to the calculation of lightning electromagnetic field from inclined lightning channel. According to the vector superposition principle, the inclined current-carrying channel element $I\mathrm{d}\boldsymbol{l}$ can be decomposed into horizontal component and vertical component [15]:

$$\begin{aligned} I\,\mathrm{d}\boldsymbol{l} &= I\,\mathrm{d}l\left(\sin\alpha\boldsymbol{e}_r+\cos\alpha\boldsymbol{e}_z\right)\\ &= I\,\mathrm{d}l\left(\sin\alpha\cos\varphi'\boldsymbol{e}_x+\sin\alpha\sin\varphi'\boldsymbol{e}_y+\cos\alpha\boldsymbol{e}_z\right), \end{aligned} \tag{1}$$

where I is the channel current, α and φ' are the inclined angle and azimuth angle of lightning channel, respectively. $\boldsymbol{e}_x$, $\boldsymbol{e}_y$, and $\boldsymbol{e}_z$ are the unit vectors. Here we will only deal with the differential segment of the inclined lightning channel since superposition assures the applicability of the result to the complete channel.

According to the Maxwell's equations in frequency-domain, we have:

$$\boldsymbol{E}=\nabla\left(\nabla\cdot\boldsymbol{A}\right)-\gamma_0\boldsymbol{A}, \tag{2}$$

$$\boldsymbol{B}=j\omega\varepsilon_0\left(\nabla\times\boldsymbol{A}\right), \tag{3}$$

where $\boldsymbol{E}$ and $\boldsymbol{B}$ are the total electric field and the total magnetic field generated by the inclined channel respectively. ω is the angular frequency, and $\boldsymbol{A}=A_x\boldsymbol{e}_x+A_y\boldsymbol{e}_x+A_z\boldsymbol{e}_z$ is the magnetic vector potential. $\gamma_0=j\omega\sqrt{\mu_0\varepsilon_0}$, μ_0 and ε_0 are the magnetic permeability and electric permittivity of free space respectively.

We use primed letters for the coordinates of the source points and the unprimed letters for points at which the desired quantities are to be determined. The magnetic vector potential $\mathrm{d}\boldsymbol{A}^x$ generated by the horizontal element $I\,\mathrm{d}x\boldsymbol{e}_x$ can be approximately expressed in the rectangular coordinate system by [16]:

$$\begin{aligned} \mathrm{d}\boldsymbol{A}^x \approx{}& \frac{I\mathrm{d}x'}{2\pi j\omega\varepsilon_0}\frac{e^{-\gamma_0R}}{R}\frac{\sin\theta}{\sin\theta+\Delta^{-1}\sqrt{1-\Delta^2\cos^2\theta}}\boldsymbol{e}_x\\ &-\frac{I\mathrm{d}x'\cos\theta}{2\pi j\omega\varepsilon_0\gamma_1}\frac{\left(x-x'\right)}{\rho}\frac{e^{-\gamma_0R}}{R^2}\\ &\times\left[\left(1+\gamma_0R\Pi\right)-\frac{\sin\theta}{\gamma_1R}\left(2+2\gamma_0R+\gamma_0^2R^2\right)\right]\boldsymbol{e}_z, \end{aligned} \tag{4}$$

where r, φ and z are the cylindrical coordinates, $R=\sqrt{r^2+r'^2+z'^2-2rr'\cos\left(\varphi-\varphi'\right)}$, $\sin\theta=z'/R$, $\rho=\sqrt{\left(x-x'\right)^2+\left(y-y'\right)^2}$, $\gamma_1=\sqrt{j\omega\mu_0\left(\sigma+j\omega\varepsilon_0\varepsilon_r\right)}$, ε_r is the relative dielectric constant, and σ is the conductivity of the ground. $\Delta=\gamma_0/\gamma_1$, $\Delta_1=\Delta\sqrt{1-\Delta^2\cos^2\theta}$, $w=-\gamma_0R\left(\sin\theta+\Delta\right)^2/2$, $F\left(w\right)=1-j\sqrt{\pi w}e^{-w}erfc\left(j\sqrt{w}\right)$, and $\Pi=\left(\Delta_1F\left(w\right)-\sin\theta\right)/\left(\Delta_1-\sin\theta\right)$.

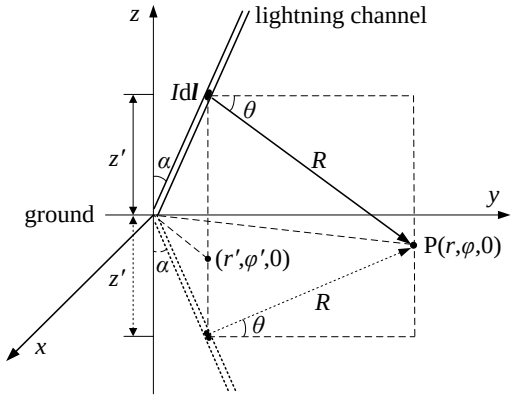

Fig. 1. Geometry relevant to this calculation.

Substituting (4) into (2) and (3), and applying $\left|\Delta^2\right|\ll1$, we can obtain the horizontal electric field $\mathrm{d}E_r^{hx}$ and azimuthal magnetic field $\mathrm{d}B_\varphi^{hx}$ from the horizontal element $I\,\mathrm{d}x'\boldsymbol{e}_x$ at observation point P as:

$$\begin{aligned} \mathrm{d}E_r^{hx}\left(r,0,j\omega\right)=-\frac{I\mathrm{d}x'}{2\pi j\omega\varepsilon_0}\frac{\left(x-x'\right)}{\rho}\gamma_0\Bigg\{&\gamma_0\Delta_1\Bigg[\frac{\sin^2\theta}{\sin\theta+\Delta_1}\\ &-\frac{\Delta^2}{\sin\theta+\Delta_1}F\left(w\right)\Bigg]\frac{e^{-\gamma_0R}}{R}-\frac{\Delta e^{-\gamma_0R}}{\gamma_1R^3}\left(1+\gamma_0R-\gamma_1R\sin\theta\right)\Bigg\}, \end{aligned} \tag{5}$$

$$\begin{aligned} \mathrm{d}B_\varphi^{hx}\left(r,0,j\omega\right)=\frac{\mu_0I\mathrm{d}x'}{2\pi}\frac{\left(x-x'\right)}{\rho}\Bigg\{&\gamma_0\Bigg[\frac{\sin^2\theta}{\sin\theta+\Delta_1}\\ &-\frac{\Delta_1\Delta}{\sin\theta+\Delta_1}F\left(w\right)\Bigg]\frac{e^{-\gamma_0R}}{R}-\frac{e^{-\gamma_0R}}{\gamma_1R^3}\left(1+\gamma_0R-\gamma_1R\sin\theta\right)\Bigg\}. \end{aligned} \tag{6}$$

Note that if $\left|\Delta^2\right| \ll 1$, $\Delta_1 \approx \Delta$. Then (5) and (6) can be reduced to:

$$\mathrm{d}E_r^{hx}\left(r,0,j\omega\right) = -c\mathrm{d}B_\varphi^{hx}\left(r,0,j\omega\right)\frac{\gamma_0}{\gamma_1}, \tag{7}$$

where c is the speed of light in free space.

Likewise, we can obtain the relationship between the on-ground horizontal electric field $\mathrm{d}E_r^{hy}\left(r,0,j\omega\right)$ and azimuthal magnetic field $\mathrm{d}B_\varphi^{hy}\left(r,0,j\omega\right)$ generated by the horizontal element $I\,\mathrm{d}\,y'\boldsymbol{e}_y$ as:

$$\mathrm{d}E_r^{hy}\left(r,0,j\omega\right) = -c\mathrm{d}B_\varphi^{hy}\left(r,0,j\omega\right)\frac{\gamma_0}{\gamma_1}. \tag{8}$$

The relationship between the on-ground horizontal electric field $\mathrm{d}\,E_r^{v}\left(r,0,j\omega\right)$ and azimuthal magnetic field $\mathrm{d}\,B_\varphi^{v}\left(r,0,j\omega\right)$ generated by the vertical element $I\,\mathrm{d}\,z'\boldsymbol{e}_z$ can be given by the original Cooray formula for vertical lightning channel [3]:

$$\mathrm{d}\,E_r^{v}\left(r,0,j\omega\right) = -c\,\mathrm{d}\,B_\varphi^{v}\left(r,0,j\omega\right)\frac{\gamma_0}{\gamma_1}. \tag{9}$$

Performing the vector superposition to the contributions of all channel elements according to (1), (7), (8) and (9), we can obtain the relationship between the horizontal electric field $E_r\left(r,0,j\omega\right)$ and azimuthal magnetic field $B_\varphi\left(r,0,j\omega\right)$ at ground level generated by the inclined channel as follow:

$$E_r\left(r,0,j\omega\right) = -cB_\varphi\left(r,0,j\omega\right)\frac{\gamma_0}{\gamma_1}. \tag{10}$$

The form of Equation (10) is the same as original Cooray formula for vertical lightning channel. Note, however, that here $B_\varphi\left(r,0,j\omega\right)$ is the azimuthal magnetic field at ground level generated by the inclined lightning channel. Moreover, due to all the above derivations are carried out based on an inclined differential segment of the lightning channel in the space, Equation (10) is suitable for even tortuous lightning channel.

III. VALIDATION OF THE EXTENDED COORAY FORMULA

Cooray [14] has shown that the Bannister approximations could basically provide an accurate description of the lightning generated electric fields over finitely conducting ground. Thus, to verify the reliability of the extended Cooray formula, we have calculated the horizontal electric fields at ground level at distances of 100m, 500m, and 1000m from the return stroke by employing the numerical solution of Sommerfeld's integrals using Bannister approximations, and compared the results with those obtained from (10), as shown in Fig. 2. Note that here, for all the following calculations of the fields in the paper, the lightning channel-base current in [17] and MTLE model are adopted, and the return stroke speed is set to 1.5×10^8m/s. All calculations are performed using Matlab codes.

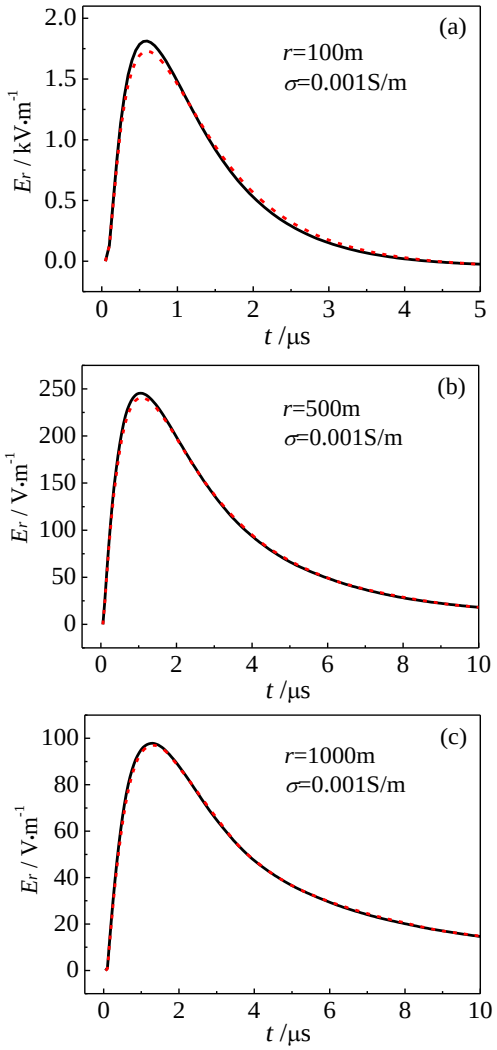

Fig. 2. Comparison of the horizontal fields from the numerical solution of Sommerfeld's integrals (solid line) at ground level with those from the extended Cooray formula (dotted line): (a) r=100m, (b) r=500m, and (c) r=1000m. The inclined angle of lightning channel $\alpha = \pi/6$, the azimuth angle $\varphi = 3\pi/4$, and $\varphi' = \pi/2$.

As follows from Fig. 2, the horizontal electric field waveforms from the extended Cooray formula are essentially coincident with those from the numerical solution of Sommerfeld's integrals beyond 100m. Note that there is only some deviation on the peak value of the waveform for the distance within 100m. The deviation of the peak value is about 4.6% at the distance of 100m.

In order to test the influences of the ground conductivity, the observation distance, the inclined

angle of lightning channel and the azimuth angle of observation point on the accuracy of the extended formula, the peak value ratios *K* of the waveforms from the extended formula to those from the numerical solution of Sommerfeld's integrals are also calculated, as shown in Fig. 3.

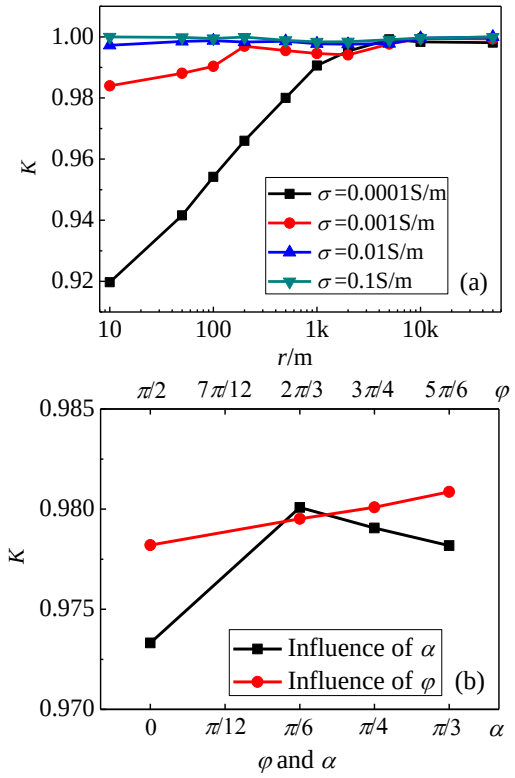

Fig. 3. Influences of the ground conductivity σ, the observation distance *r*, the channel inclined angle α and the observation azimuth angle φ on the accuracy of the extended Cooray formula. (a) The peak value ratios *K* of the waveforms under different σ and *r*, and (b) the peak value ratios *K* of the waveforms under different α and φ.

As shown in Fig. 3 (a), the accuracy of the extended Cooray formula is related to the ground conductivity and the observation distance. The ratio *K* will tend to 1.0 with the increasing ground conductivity σ and observation distance *r*. In other words, the bigger the ground conductivity or the observation distance is, the smaller the deviation of the extended formula is. As shown in Fig. 3 (b), the ratio *K* is less than 0.9733 for different inclined angles α and azimuth angles φ. That is to say, the deviation of the results calculated by the extended formula from the numerical solution of Sommerfeld's integrals is basically less than 2.67% for different inclined angles of lightning channel and different azimuth angles of observation point, which is very small and can nearly be ignored.

IV. EXTENSION OF COORAY-RUBINSTEIN FORMULA FOR INCLINED LIGHTNING CHANNEL

In this Section, we will present the derivation of the extended Cooray-Rubinstein formula for inclined lightning channel. The geometry relevant to this problem is basically the same as Fig. 1 except that the observation point P(*r*, φ, *z*) is off the ground. To calculate the horizontal electric field generated by the inclined channel at a height *z*=*h*, the Faraday's equation for a closed path is employed as following:

$$\oint_{l'} \boldsymbol{E}\cdot \mathrm{d}\boldsymbol{l}' = -j\omega\int_{S} \boldsymbol{B}\cdot \mathrm{d}\boldsymbol{S}, \tag{11}$$

where $\mathrm{d}\boldsymbol{l}'$ is a rectangular path of width d*r* extending from *z*=0 to *z*=*h*, and $\mathrm{d}\boldsymbol{S}$ is the surface surrounded by the rectangular path, as shown in Fig. 4. The direction of the surface $\mathrm{d}\boldsymbol{S}$ is defined by the direction of the contour l' and the right-hand rule.

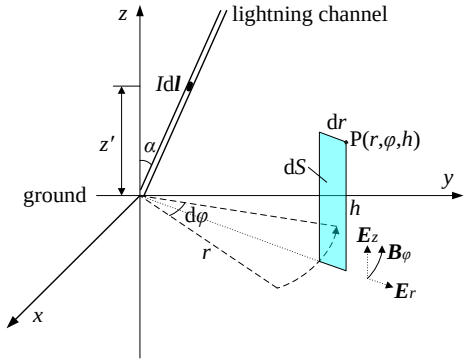

Fig. 4. Geometry relevant to the Faraday's equation shown in (11) for the inclined lightning channel. $\boldsymbol{E}_r$, $\boldsymbol{E}_z$ and $\boldsymbol{B}_\varphi$ are the horizontal electric field, vertical electric field and azimuthal magnetic field generated by the inclined lightning channel, respectively.

Integrating the Faraday's Equation (11), we can obtain:

$$E_r(r,h,j\omega)\,\mathrm{d}r - E_r(r,0,j\omega)\,\mathrm{d}r + \int_0^h E_z(r,z,j\omega)\mathrm{d}z - \int_0^h E_z(r+\mathrm{d}r,z,j\omega)\mathrm{d}z = -j\omega\,\mathrm{d}r\int_0^h B_\varphi(r,z,j\omega)\mathrm{d}z, \tag{12}$$

where $E_z(r,z,j\omega)$, and $E_z(r+\mathrm{d}r,z,j\omega)$ are the vertical electric field generated by the inclined lightning channel at radial distance *r* and *r*+d*r*, respectively.

For the case of a perfectly conducting ground, the horizontal electric field at ground level is zero. Thus, we can write (12) as:

$$E_{rp}(r,h,j\omega)\,\mathrm{d}r + \int_0^h E_{zp}(r,z,j\omega)\mathrm{d}z - \int_0^h E_{zp}(r+\mathrm{d}r,z,j\omega)\mathrm{d}z = -j\omega\,\mathrm{d}r\int_0^h B_{\varphi p}(r,z,j\omega)\mathrm{d}z, \tag{13}$$

where E_{rp}, E_{zp}, and $B_{\varphi p}$ are the horizontal electric field, vertical electric field, and azimuthal magnetic field generated by the inclined lightning channel for the case of a perfectly conducting ground, respectively.

For distances not exceeding several kilometers, several researchers have shown that the perfect ground conductivity assumption is a reasonable approximation for the vertical electric field and the azimuthal magnetic field [4, 5, 10, 18]. Thus, we can approximate the field components B_φ and E_z as:

$$B_\varphi \approx B_{\varphi p}, \text{ and } E_z \approx E_{zp}. \tag{14}$$

Substituting (14) into (12), we can obtain:

$$E_r(r,h,j\omega)\mathrm{d}r - E_r(r,0,j\omega)\mathrm{d}r + \int_0^h E_{zp}(r,z,j\omega)\mathrm{d}z - \int_0^h E_{zp}(r+\mathrm{d}r,z,j\omega)\mathrm{d}z \approx -j\omega\mathrm{d}r\int_0^h B_{\varphi p}(r,z,j\omega)\mathrm{d}z. \tag{15}$$

Comparing equation (13) with (15), we can find that the right sides of these two equations are the same. Thus, Subtracting (13) from (15), we can obtain the total horizontal electric field $E_r(r,h,j\omega)$ generated by the inclined channel at a height $z=h$ as:

$$E_r(r,h,j\omega) = E_r(r,0,j\omega) + E_{rp}(r,h,j\omega). \tag{16}$$

Substituting the extended Cooray formula (10) into Equation (16), we can obtain the extended Cooray-Rubinstein formula as:

$$E_r(r,h,j\omega) = -cB_\varphi(r,0,j\omega)\frac{\gamma_0}{\gamma_1} + E_{rp}(r,h,j\omega). \tag{17}$$

Just like the extended Cooray formula, the form of the extended Cooray-Rubinstein formula for the inclined channel is also the same as that for vertical lightning channel. Note that here $B_\varphi(r,0,j\omega)$ is the azimuthal magnetic field at ground level generated by the inclined lightning channel, and $E_{rp}(r,h,j\omega)$ is the horizontal electric field at a height $z=h$ for the case of a perfectly conducting ground generated by the inclined lightning channel. Moreover, the derivation of the extended Cooray-Rubinstein formula is basically independent of the shape of the lightning channel. Thus, Equation (17) is also suitable for even tortuous lightning channel.

Specially, if the observation point P is at ground level, we have $E_{rp}(r,h,j\omega)=0$ in (17). Then, the extended Cooray-Rubinstein formula will reduce to the extended Cooray formula.

V. VALIDATION OF THE EXTENDED COORAY-RUBINSTEIN FORMULA

To verify the reliability of the extended Cooray-Rubinstein formula, the horizontal electric fields at a height z=10m are calculated by adopting the extended Cooray-Rubinstein formula (17) and the numerical solution of Sommerfeld's integrals using Bannister approximations. Comparisons of the horizontal electric fields from the extended Cooray-Rubinstein formula with those from the numerical solution of Sommerfeld's integrals at different distances are shown in Fig. 5 (for the case of σ=0.0001 S/m) and Fig. 6 (for the case of σ=0.001 S/m). To analyze the influence of the observation distance r on the accuracy of the extended Cooray-Rubinstein formula, the peak time ratios K_t of the waveforms from the extended formula to those from the numerical solution of Sommerfeld's integrals under different distances, as well as the peak value ratios K of the waveforms, are calculated, as shown in Fig. 7.

As follows from Fig. 5 and Fig. 7, the accuracy of the extended Cooray-Rubinstein formula increases gradually with the distance r increases. The closer the distance is, the less the deviations are. For the case of σ=0.0001 S/m, when the observation distance is less than 10 m, there is a visible difference between the horizontal electric field waveforms from the numerical solution of Sommerfeld's integrals and the extended Cooray-Rubinstein formula after the rising edge. At distance r=10m, the deviation of the peak value is about 10.4%, and the deviation of the peak time is about 52.9%. However, when the observation distance exceeds 500m, the horizontal electric field waveforms from the extended Cooray-Rubinstein formula are basically coincident with those from the numerical solution of Sommerfeld's integrals. The deviation of the peak value is less than 6.2%, and the deviation of the peak time is less than 5.3%, as shown in Fig. 7. Thus, it can be concluded that, for the case that the observation height is 10m and the ground conductivity is not less than 0.0001 S/m, the extended Cooray-Rubinstein formula could yield an acceptable approximation on the horizontal electric field at the distance beyond 500m.

Comparing Fig. 5 with Fig. 6, it can be found that the accuracy of the extended Cooray-Rubinstein formula increases with the ground conductivity σ increases. As shown in Fig. 7, the greater the ground conductivity is, the less the deviations are. As shown in Fig. 6, for the case of σ=0.001 S/m, the horizontal electric field waveforms from the extended Cooray-Rubinstein formula are essentially coincident with those from the numerical solution of Sommerfeld's integrals, even at the distance r=10m. As follows from Fig. 7, the deviation of the peak value for the case of σ=0.001 S/m is less than 2.1%, and the deviation of the peak time is less than 6.3%. Especially for the observation distance beyond 500m, there is not any deviation on the peak time between the waveforms from the extended formula and the numerical solution of Sommerfeld's integrals. Thus, it can be concluded that, for the case that the observation height is 10m and the ground conductivity is not less than 0.001 S/m, the extended Cooray-Rubinstein formula could yield a satisfactory approximation on the horizontal electric field at close (10m), intermediate (some kilometers), and far (tens of kilometers) distances.

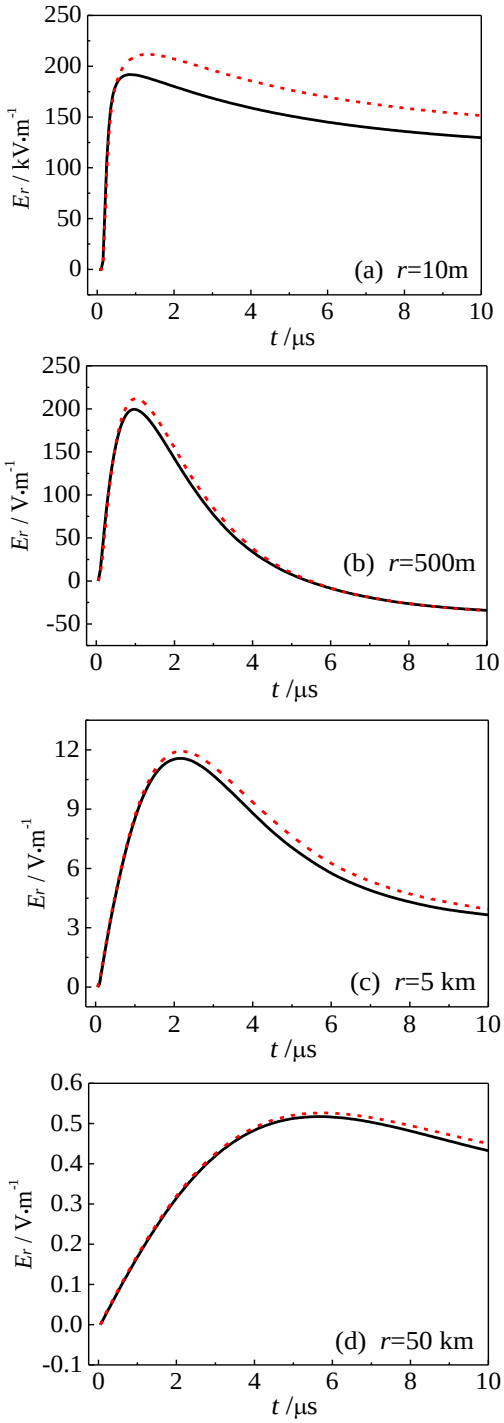

Fig. 5. Comparison of the horizontal field from the numerical solution of Sommerfeld's integrals (solid line) at a height z=10m with that from the extended Cooray-Rubinstein formula (dotted line): (a) r=10m, (b) r=500m, (c) r=5km, and (d) r=50km. The ground conductivity is set to σ=0.0001S/m. The inclined angle of lightning channel $\alpha = \pi/6$, the azimuth angle $\varphi = \pi/2$, and $\varphi' = \pi/4$.

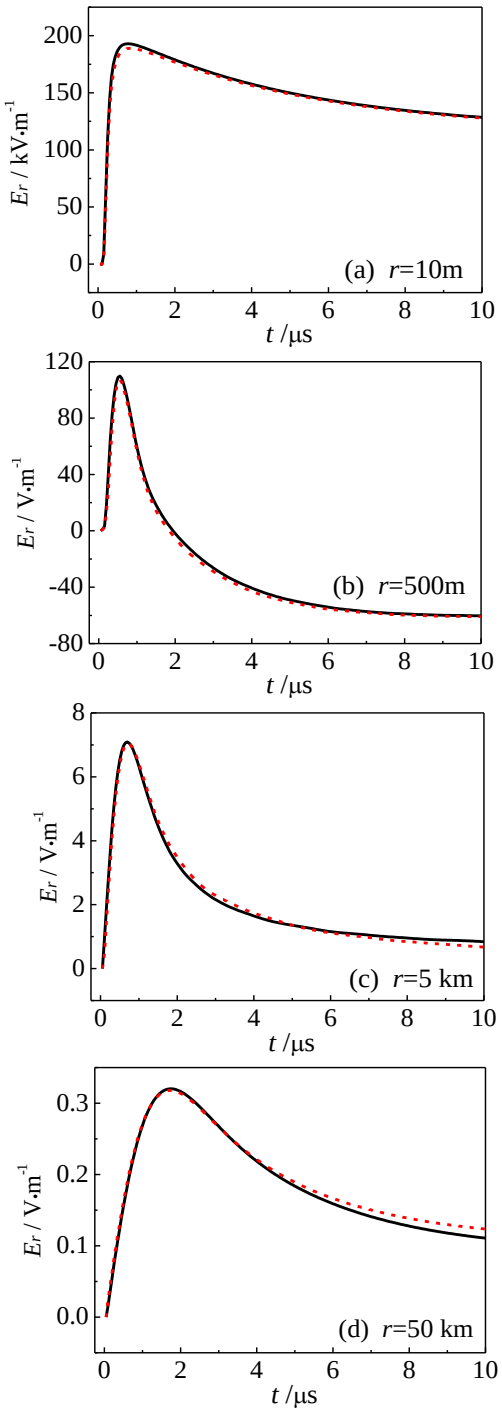

Fig. 6. Comparison of the horizontal field from the numerical solution of Sommerfeld's integrals (solid line) at a height z=10m with that from the extended Cooray-Rubinstein formula (dotted line): (a) r=10m, (b) r=500m, (c) r=5km, and (d) r=50km. The ground conductivity is set to σ=0.001S/m. The inclined angle of lightning channel $\alpha = \pi/6$, the azimuth angle $\varphi = \pi/2$, and $\varphi' = \pi/4$.

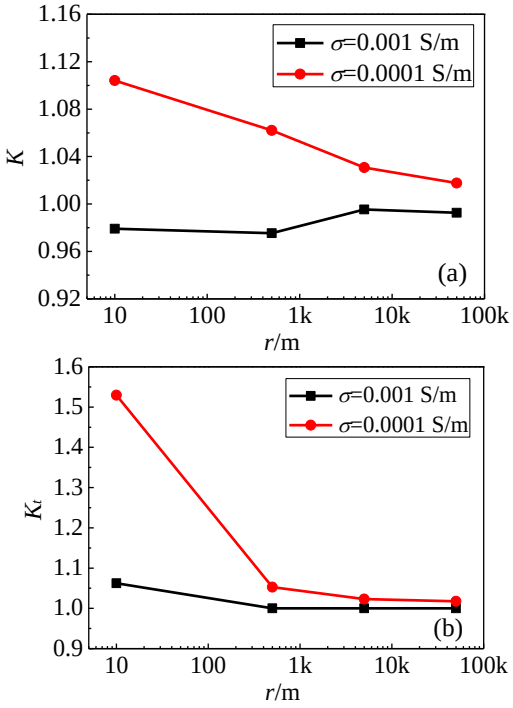

Fig. 7. Influences of the observation distance r on the accuracy of the extended Cooray-Rubinstein formula. (a) The peak value ratios K of the waveforms under different distances, and (b) the peak time ratios K_t of the waveforms under different distances.

Comparing Fig. 5 with Fig. 6, it can be found that the accuracy of the extended Cooray-Rubinstein formula increases with the ground conductivity σ increases. As shown in Fig. 7, the greater the ground conductivity is, the less the deviations are. As shown in Fig. 6, for the case of σ=0.001 S/m, the horizontal electric field waveforms from the extended Cooray-Rubinstein formula are essentially coincident with those from the numerical solution of Sommerfeld's integrals, even at the distance r=10m. As follows from Fig. 7, the deviation of the peak value for the case of σ=0.001 S/m is less than 2.1%, and the deviation of the peak time is less than 6.3%. Especially for the observation distance beyond 500m, there is not any deviation on the peak time between the waveforms from the extended formula and the numerical solution of Sommerfeld's integrals. Thus, it can be concluded that, for the case that the observation height is 10m and the ground conductivity is not less than 0.001 S/m, the extended Cooray-Rubinstein formula could yield a satisfactory approximation on the horizontal electric field at close (10m), intermediate (some kilometers), and far (tens of kilometers) distances.

VI. INFLUENCE OF THE OBSERVATION HEIGHT ON THE EXTENDED COORAY-RUBINSTEIN FORMULA

To evaluate the influence of the observation height on the accuracy of the extended Cooray-Rubinstein formula, the horizontal electric fields at different heights from the extended Cooray-Rubinstein formula and the numerical solution of Sommerfeld's integrals are also calculated here, as shown in Fig. 8. In this calculation, the observation distance is set to r=100m, and the ground conductivity is set to σ=0.001 S/m. Due to that there is basically not any deviation on the peak time between the waveforms from the extended formula and the numerical solution of Sommerfeld's integrals, only the peak value ratios K of the waveforms are calculated here to evaluate the influence of the observation height, which are also shown in Fig. 8.

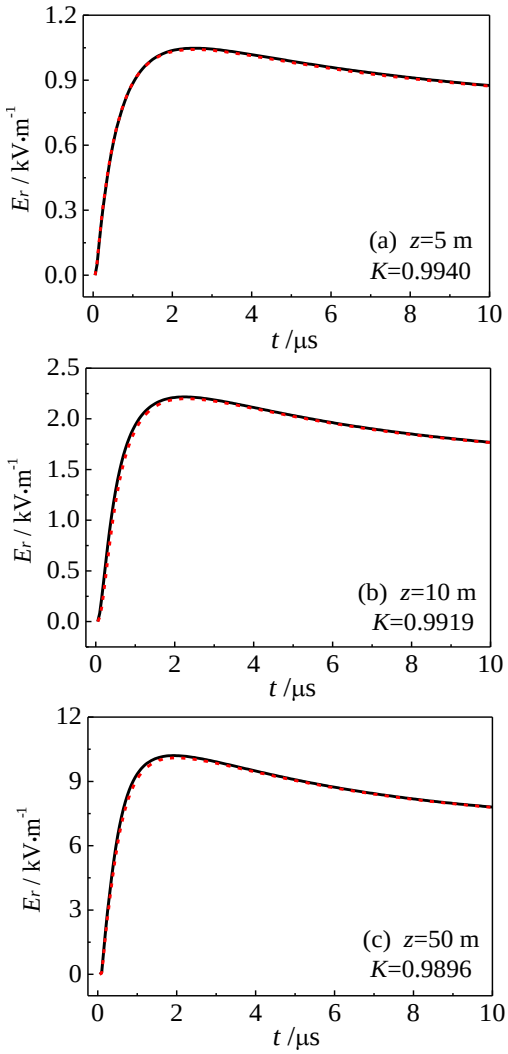

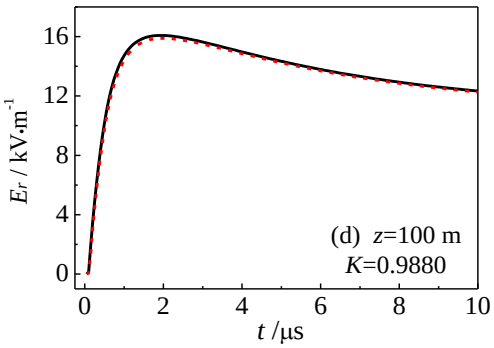

Fig. 8. Comparison of the horizontal field from the numerical solution of Sommerfeld's integrals (solid line) at a distance r=100m with that from the extended Cooray-Rubinstein formula (dotted line): (a) z=5m, (b) z=10m, (c) z=50m, and (d) z=100m. The ground conductivity is set to σ=0.001 S/m. The inclined angle of lightning channel $\alpha = \pi/6$, the azimuth angle $\varphi = \pi/2$, and $\varphi' = \pi/4$.

As follows from Fig. 8 and the calculation results about the peak value ratios K of the waveforms, it can be found that the horizontal electric field waveforms from the extended Cooray-Rubinstein formula are essentially coincident with those from the numerical solution of Sommerfeld's integrals at the height from z=5m to z=100m. According to the calculation results about the peak value ratios K, the deviation of the peak value increases slightly with the observation height increases. However, for the observation point with a height less than 100m, the deviation of the peak value is less than 1.2%, which is very small and can nearly be ignored. Thus, it can be concluded that the influence of the height on the extended Cooray-Rubinstein formula can be negligible while it is used for analyzing the interaction of lightning electromagnetic fields with power lines or electrical installations near the ground.

VII. CONCLUSION

In this paper, an extension of Cooray-Rubinstein formula was presented for the calculation the horizontal electric field from inclined lightning channel in frequency-domain. For this purpose, the Cooray formula was extended firstly for the calculation of horizontal electric field at ground level generated by the inclined channel. The influences of the ground conductivity, the observation distance, the inclined angle of lightning channel and the azimuth angle of observation point on the accuracy of the extended Cooray formula were also analyzed. It was found that the accuracy of the extended Cooray formula increases with the increasing ground conductivity and observation distance, but is not insensitive to the channel inclined angle and the observation azimuth angle. The extended Cooray formula can predict the horizontal field accurately at the distance beyond 100m.

Based on the extended Cooray formula, the Cooray-Rubinstein formula was extended for the calculation of horizontal electric field off the ground generated by the inclined channel. The accuracy of the extended Cooray-Rubinstein formula for inclined lightning channel was also validated by comparing the results with those from the numerical solution of Sommerfeld's integrals. The results showed that the accuracy of the extended Cooray-Rubinstein formula increases with the observation distance and the ground conductivity increase, but is not insensitive to the observation height. It was shown that the extended Cooray-Rubinstein formula could yield an acceptable approximation on the above-ground horizontal electric field with the exception of the observation point at close range under the ground conductivity less than 0.0001S/m.

It is worth noting that this extended Cooray-Rubinstein formula has no limitation regarding the channel shape so that it could be used for the calculation of horizontal electric field generated by any tortuous lightning channel.

ACKNOWLEDGMENT

The research is supported by National Natural Science Foundation Project of China under Grants No. 51707203 and 51377171.

REFERENCES

[1] M. J. Master and M. A. Uman, "Lightning induced voltages on power lines: Theory," *IEEE Trans. Power Appar. and Syst.*, vol. PAS-103, no. 9, pp. 2502-2518, 1984.

[2] E. M. Thomson, P. J. Medelius, M. Rubinstein, M. A. Uman, and J. Johnson, "Horizontal electric fields from lightning return strokes," *J. Geophys. Res.*, vol. 93, no. D3, pp. 2429-2441, 1988.

[3] V. Cooray, "Horizontal fields generated by return strokes," *Radio Sci.*, vol. 27, pp. 529-537, 1992.

[4] M. Rubinstein, "An approximate formula for the calculation of the horizontal electric field from lightning at close, intermediate and long ranges," *IEEE Trans. Electromagn. Compat.*, vol. 38, pp. 531-535, 1996.

[5] F. Rachidi, C. A. Nucci, M. Ianoz, and C. Mazzetti, "Influence of a lossy ground on lightning-induced voltages on overhead lines," *IEEE Trans. Electromagn. Compat.*, vol. 38, no. 3, pp. 250-264, Aug. 1996.

[6] F. Delfino, R. Procopio, M. Rossi, F. Rachidi, and C. A. Nucci, "Lightning return stroke current radiation in presence of a conducting ground: 2. Validity assessment of simplified approaches," *J. Geophys. Res.*, vol. 113, pp. D05111-1-D05111-11, 2008.

[7] J. R. Wait, "Concerning the horizontal electric field of lightning," *IEEE Trans. Electromagn. Compat.*,

vol. 39, no. 2, pp. 186, 1997.

[8] V. Cooray, "Some considerations on the "Cooray-Rubinstein" formulation used in deriving the horizontal electric field of lightning return strokes over finitely conducting ground," *IEEE Trans. Electromagn. Compat.*, vol. 44, no. 4, pp. 560-566, 2002.

[9] V. Cooray, "Horizontal electric field above-and underground produced by lightning flashes," *IEEE Trans. Electromagn. Compat.*, vol. 52, no. 4, pp. 936-943, 2010.

[10] G. Lupo, C. Petrarca, V. Tucci, and M. Vitelli, "EM fields generated by lightning channels with arbitrary location and slope," *IEEE Trans. Electromagn. Compat.*, vol 42, no. 1, pp. 39-53, Feb. 2000.

[11] Z. Jiang, B. Zhou, and S. Qiu, "Evaluation of electromagnetic fields due to inclined lightning channel on finitely conductive ground," *2014 Int. Conf. Lightning Protection (ICLP)*, Shanghai, pp. 255-259, 2014.

[12] X. Wang, Y. Chen, H. Wan, L. Wang, and Q. Yang, "Characteristics of lightning electromagnetic fields generated by tortuous channel," *IEICE Trans. Commu.*, vol. E99-B, no. 7, pp. 1558-1565, 2016.

[13] H. Wan, X. Wang, Y. Chen, X. Pan, and X. Lu, "Approximate calculation of the horizontal electric field at ground level from inclined lightning channel in frequency-domain," *2017 International Applied Computational Electromagnetics Society (ACES) Symposium in China (ACES-China 2017)*, Suzhou, China, Aug. 2017.

[14] V. Cooray, "On the accuracy of several approximate theories used in quantifying the propagation effects on lightning generated electromagnetic fields," *IEEE Trans. Antennas Propagat*., vol. 56, no. 7, pp. 1960-1967, 2008.

[15] X. Zhang and Y. Zhang, "An algorithm for calculating transient magnetic field and induced voltage inside wind turbine tower under lightning stroke," *ACES J.*, vol. 31, no. 1, pp. 72-78, 2016.

[16] P. R. Bannister, *Extension of Finitely Conducting Earth-Image-theory Results to Any Range*, Naval Underwater Systems Center, New London, 1984.

[17] V. Cooray, "Propagation effects due to finitely conducting ground on lightning-generated magnetic fields evaluated using Sommerfeld's integrals," *IEEE Trans. Electromagn. Compat.*, vol. 51, no. 3, pp. 526-531, 2009.

[18] V. A. Rakov and F. Rachidi, "Overview of recent progress in lightning research and lightning protection," *IEEE Trans. Electromagn. Compat.*, vol. 51, no. 3, pp. 428-442, 2009.

Haojiang Wan received the B.Eng., M.Eng. degrees from Nanjing Engineering Institute, Nanjing, China, in 2005, and 2008 and the Ph.D. degree from Shijiazhuang Mechanical Engineering College, Shijiazhuang, China, in 2011.

He is currently a Lecturer at Army Engineering University, Shijiazhuang Branch, Shijiazhuang, China. His research interests include lightning protection and electromagnetic compatibility.

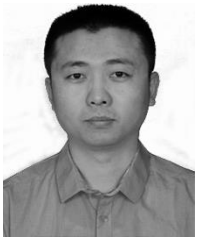

Xiaojia Wang received the B.Eng. degree from Hebei University of Technology, Tianjin, China, in 2010, and the M.Eng. degree from Shijiazhuang Mechanical Engineering College in 2013.

He is currently working toward the Ph.D. degree at National Key Laboratory on Electromagnetic Environment Effects, Army Engineering University, Shijiazhuang Branch, Shijiazhuang, China. His current research interests include lightning electromagnetic field modeling and electromagnetic compatibility.

Yazhou Chen received the B.Eng., M.Eng. and Ph.D. degrees from Shijiazhuang Mechanical Engineering College, Shijiazhuang, China, in 1996, 1999, and 2002, respectively.

He is currently a Professor at Army Engineering University, Shijiazhuang Branch, and a Member of IEEE. His research interests include computational technology of electromagnetic pulse, electromagnetic pulse protection and electromagnetic compatibility.

Drastic-Variation Condition of Electric Field and Its Applications in Microwave Heating

Zhengming Tang [1], Sanmei Zhang [1], Tao Hong [1], Fangyuan Chen [3], and Kama Huang [2]

[1] China West Normal University, Nanchong, 637002, China
zhengmtang@163.com, zhangsm@cwnu.edu.cn, scu_mandela@163.com

[2] College of Electronics and Information Engineering
Sichuan University, Chengdu, 610064, China
kmhuang@scu.edu.cn

[3] State Key Laboratory of Electromagnetic Environment
China Aerospace and Science Technology Corporation, Shanghai, 200090, China
fangyuanscu@outlook.com

Abstract ─ Microwave heating usually leads to non-uniform temperatures due to the existence of drastic-variation of electric field. In this paper, a numerical method combined with integral equation and spectrum analysis is proposed to find its critical condition. Results show that the electric field is generally unstable, and a tiny shift in microwave frequency, permittivity of dielectric object or cavity geometrical parameters will produce a drastic variation in electric field distribution, moreover, the smallest shift of parameter can be obtained by the reverse search. FEM method is used to verify the conclusions. Finally, some supplements for the interest regarding practical applications are presented and analyzed.

Index Terms ─ Drastic-variation condition, electric field, integral equation, microwave heating.

I. INTRODUCTION

Microwave heating has been widely used for domestic, scientific and industrial applications due to its convenience and high efficiency [1-3]. However, in a multimode cavity, microwave heating usually leads to non-uniform temperatures [4], which will restrict the quality of a product. Since heating uniformity is mainly dependent on and affected by the distribution of electric field [5], and in a multimode cavity the electric field is prone to be unstable, it is necessary to study the detailed characteristics of electric field.

The drastic-variation in electric field refers to the effects on either the distribution or amplitude, or both, because of the tiny shift in system parameters. The drastic-variation of electric field usually causes non-uniform heating and results in hot spots (huge temperature gradient in certain areas) and thermal runaway (uncontrollable temperature rise due to strong dielectric loss – temperature positive feedback of the heating object), which restrict heating efficiency and even lead to some serious safety issues [6]. The instability of the electric field, especially its critical condition, is of great importance to the prevention of hot spots, thermal runaway and enhancement of heating uniformity.

To determine the condition of a drastic-variation in electric field, it is important to find the relevant parameters. Several researches are published to investigate the characteristics of electric field, such as the study of improving electric field uniformity in reverberation chambers via mode stirs [7-8]. These might be considered as positive applications of the instability of electric field. Moreover, Hill studied the instability of electric field by examining the mode density in cavity [9]. He gave a relatively rough consideration, such as his research didn't involve the discussion of permittivity. Whereas, for microwave heating, permittivity is an important parameter that may affect the interaction between microwave and the heating object. More recently, Budko et al. investigated the electric field resonance by the spatial spectrum of electric field volume integral equation [10-11]. Although it can provide us with a useful guidance, it is not specifically aimed at the case of microwave heating.

This study presents a numerical method to determine the drastic-variation condition of electric field in multimode microwave heating system. Integral equation and spectrum analysis are used to find the electric field highly dependent parameters. On the bases of such analysis the relevant parameters are obtained, and then the critical condition for a drastic variation in electric field is analyzed. Results show that even if a tiny shift in microwave frequency, the permittivity of dielectric

Submitted On: September 2, 2017
Accepted On: April 10, 2018

object or cavity geometrical parameters may produce a drastic variation in electric field, and the smallest shift of parameter can be obtained by the reverse search. Because the critical condition plays an important role in preventing hot spots and improving heating uniformity, two examples are given in this paper, which provide some supplement for practical application.

II. METHODLOGY

The multimode microwave heating system analyzed is shown in Fig. 1. It consists of a rectangular metallic cavity connected to microwave source via a rectangular waveguide operating in the TE_{10} mode. The dimensions of the cavity and rectangular waveguide are $l_x \times l_y \times l_z$ and $a \times b \times c$, respectively. In addition, the area of access port is denoted as S_a. At the center of the bottom, there is a single cylindrical object, the radius, height and volume of which are r, h and V_{d}, respectively. Inside the cavity the permittivity can be shown as:

$$\varepsilon(r)=\begin{cases}\varepsilon_0\varepsilon_r(r)-i\dfrac{\sigma(r)}{\omega}, & r\in V_{\mathrm{d}}\\ \varepsilon_0, & r\notin V_{\mathrm{d}}.\end{cases} \tag{1}$$

where, $\varepsilon_r(r)$ is relative permittivity of dielectric object, ε_0 is permittivity of free space, and $\sigma(r)$ is conductivity.

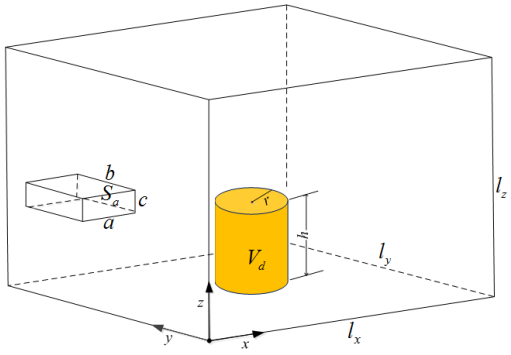

Fig. 1. Schematic of microwave heating.

The electromagnetic analysis of a microwave heating cavity containing dielectric objects and excited by a rectangular waveguide on the external surface can be performed using the Green's function of the empty structure. Moreover, the electric field can be represented by the sum of impress electric field on the external surface and the polarization electric field inside the dielectric object [12]. The impress electric field can be shown as [13]:

$$\mathbf{E}^{\mathrm{inc}}(\mathbf{r})=\iint_{S_a}\left[\mathbf{E}_{\mathbf{10t}}(\mathbf{r}')\cdot\nabla\times\overline{\overline{\mathbf{G}_{\mathbf{e}}}}(\mathbf{r},\mathbf{r}')\right]\mathrm{d}S_a, \tag{2}$$

where $\mathbf{r}'$ and $\mathbf{r}$ represent the source point and field point, respectively. $\mathbf{E}_{10\mathrm{t}}(\mathbf{r}')$ is a tangential impressed field over the cross area and $\overline{\overline{\mathbf{G}_{\mathbf{e}}}}(\mathbf{r},\mathbf{r}')$ is dyadic Green's function of the empty cavity [14-15]. When adding the polarization electric field, the total field can be expressed as:

$$\mathbf{E}(\mathbf{r})=\mathbf{E}^{\mathrm{inc}}(\mathbf{r})+j\omega\mu_0\int_{Vd}\bar{\bar{\mathbf{G}}}_{\mathbf{e}}(\mathbf{r},\mathbf{r}')\cdot\mathbf{J}\mathrm{d}r'. \tag{3}$$

Take into account the singularity arising when the field point coincides with the source point [16], Equation (2) becomes [17]:

$$\begin{aligned}\mathbf{E}^{\mathrm{inc}}(\mathbf{r})=&\left[\bar{\bar{\mathbf{I}}}+\frac{1}{3}\boldsymbol{\chi}(\mathbf{r})\right]\mathbf{E}(\mathbf{r})\\&-\lim_{\delta\to0}j\omega\mu_0\int_{V_d-V_\delta}\bar{\bar{\mathbf{G}}}_{\mathbf{e}}(\mathbf{r},\mathbf{r}')\cdot\mathbf{J}dr',\end{aligned} \tag{4}$$

where $\bar{\bar{\mathbf{I}}}$ is the 3×3 dyadic identity, $\boldsymbol{\chi}(\mathbf{r})$ is the relative electric contrast of the heating object with respect to free space, and

$$\boldsymbol{\chi}(\mathbf{r})=\frac{\sigma(\mathbf{r})-j\omega\varepsilon(\mathbf{r})}{-j\omega\varepsilon_0}-\bar{\bar{\mathbf{I}}}, \tag{5}$$

moreover, **J** is the induced polarized current density can be calculated as [18]:

$$\mathbf{J}=\left\{\sigma-j\omega\varepsilon_0\left[\varepsilon_r(r)-1\right]\right\}\mathbf{E}(\mathbf{r}). \tag{6}$$

Equation (3) is a typical volume scattering equation, the instability of which can be analyzed by its numerical characteristics. Since the eigenvalues of the electric field equation is linked to its resonant modes, the electromagnetic problem can be studied by the characteristics of this equation. By taking similar strategy in previous studies [10], the instability of electric field is characterized by its discrete eigenvalues, and the discrete eigenvalues are bounded by:

$$\sigma(r)-\sigma(r)\mathrm{Re}\lambda+\omega\left[\varepsilon(r)-\varepsilon_0\right]\mathrm{Im}\lambda\le0, r\in\mathrm{V_d}, \tag{7}$$

where, $\mathrm{R_e}\lambda$ and $\mathrm{I_m}\lambda$ are the real part and imaginary part, respectively. In Equation (7), when $\mathrm{R_e}\lambda\to0$, the following equation can be obtained:

$$\left|\mathrm{Im}\,\lambda\right|=\frac{\sigma(r)}{\omega\left[\varepsilon(r)-\varepsilon_0\right]}, r\in\mathrm{V_d}. \tag{8}$$

It is not difficult to see the distributions of eigenvalues are affected by microwave frequency, the relative permittivity, and the cavity geometrical parameters, hence, the instability of the electric field is affected by these parameters. Without loss of generality, the average rate of variation of electric field is defined to quantify the instability of electric field:

$$V_{av}=\frac{1}{n-1}\sum_{i=1}^{n}\left(E_i-E_{i0}\right)^2, \tag{9}$$

where n denotes the number of sampling points, E_{i0} and E_i denote the electric field amplitude of a single point before and after parameter shifting, respectively. Obviously, V_{av} can reflect the degree of electric field change of the whole system and the smallest shift of parameter, can be obtained by the reverse search of the critical value of V_{av}.

III. NUMERICAL RESULTS AND ANALYSIS

FEM method is used and performed by Comsol Multiphysics software 5.3b to calculate the electric field regarding the model shown in Fig. 1. The detailed parameters of the system are listed in Table1, moreover, the relative permittivity, the microwave frequency and microwave power are assumed as 10-j*0.1, 2.45 GHz, and 1w, respectively.

A. Dependent parameters

Figure 2 shows the detailed distribution of electric field for the case of 1% decrease in l_x and 1% increase in l_x, respectively. For simplicity, others are summarized in Table 2. Although the variation of electric field caused by the tiny shift of permittivity is relatively small, as can be seen, only a tiny shift of l_x or f can result in a drastic variation of electric field. The case of permittivity differs from the others mainly because it is also dependent on the volume ratio of dielectric body and cavity, as is demonstrated in [19]. A drastic variation of electric field will also be produced when the volume ratio of dielectric body and cavity big enough. With the increase in the dimension of dielectric body, the volume ratio of dielectric body and cavity becomes 0.04, the variation of electric field also turns out to be conspicuous, as can be seen in Fig. 3. In such a case, with only 1% decrease in ε_x or 1% increase in ε_x, the variation of electric field is 44.68% and 103.44%, respectively.

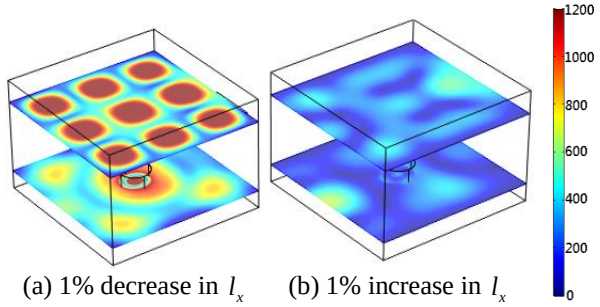

(a) 1% decrease in l_x (b) 1% increase in l_x

Fig. 2. Distribution of electric field after the shift of l_x.

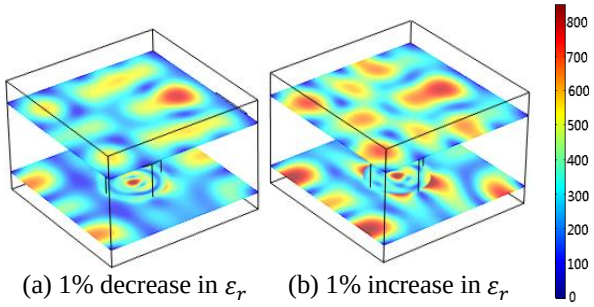

(a) 1% decrease in ε_r (b) 1% increase in ε_r

Fig. 3. Distribution of electric field after the shift of ε_r.

Table 1: Parameters of the microwave heating system

Parameter	Dimension and Value/(mm)	
	Dimension	Value
Cavity	$l_x \times l_y \times l_z$	267×270×188
Waveguide	$a \times b \times c$	50×78×18
Radius	r	25
Height	h	35

Table 2: Results of V_{av} because of only 1% shift of parameters

Parameter	Average Rate of Variation	
	V_{av-}	V_{av+}
f	58.16%	126.17%
ε_r	7.09%	5.46%
l_x	493.88%	34.65%

B. Critical values

The critical value of V_{av} is assumed as V_c, which means if the calculated V_{av} is larger than V_c, a drastic variation of electric field has been produced, and the reverse means the electric field hasn't made major change. Here, V_c =5% is assumed as a critical value, the reverse parameter search with a step of $\frac{1}{8000}$ is implemented. The smallest shift of parameters are then obtained as is shown in Table 3. For example, it shows that the electric field will have a drastic variation with a decrease of $\frac{1}{3200}$ or an increase of $\frac{3}{8000}$ in microwave frequency, respectively.

Table 3: The smallest shift of parameters

Parameter	Shift of Parameters/Average Rate	
	P_-/V_{av}	P_+/V_{av}
f	$-\frac{1}{3200}$ /5.42%	$+\frac{3}{8000}$ /5.42%
ε_r	$-\frac{3}{400}$ /5.12%	$+\frac{1}{100}$ /5.46%
l_x	$-\frac{19}{4000}$ /5.09%	$+\frac{9}{16000}$ /4.59%

IV. TYPICAL APPLICATION OF ELECTRIC FIELD CHARACTERISTICS

As is mentioned above, in a multimode microwave heating system, the electric field is sensitive to parameters such as microwave frequency, geometrical parameters, permittivity and so on. The information of the drastic-variation condition can help us in making better use of microwave energy.

A. System design

Usually, the price of a system component increases with its accuracy. Choosing the appropriate component

according to the requirements is both economical and effective for microwave heating. For example, magnetron, as the core part of the microwave oven, can be selected according to the critical conditions obtained. If for an ordinary microwave heating with low precision requirements, the magnetron with the frequency of 2450MHz±50MHz is enough, there is no need to spend more money on the one with the accuracy of ±10MHz. On the contrary, if a system requires high precision, such as in microwave chemistry, the high performance of the magnetron and the fine technics of the system should be ensured. Moreover, the influence of the attached material on the dielectric properties of the heated sample must be small enough. Therefore, in such a case, acquiring the drastic-variation condition of electric field is both important and necessary.

B. Improving heating uniformity

The instability of electric field has many possible uses in microwave engineering and has been investigated as an important factor to improve the reliability of EMC test. Similarly, new methods to improve the heating uniformity can be developed on the basis of mastering the characteristics of electric field, especially its drastic-variation condition.

One way to improve the heating uniformity is to imitate the method used in EMC test. For example, mode stirrer and turntable rotation were used to improve the uniformity of microwave heating [1]. Here is an example of the direct use of the instability of electric field to improve heating uniformity. In the system shown in Fig. 4, assume the length of l_x has a shift range of ±1cm, which means the wall of the cavity containing l_z and l_y is moveable. In addition, we assume the wall can move back and forth with a speed of 0.5cm/s within a range of 2 cm. Other parameters are assumed the same as those of the system shown in Table 1. As is demonstrated in [20], the variation of l_x we assumed is sufficient to cause large changes in the distribution of electric field in the system we designed. Therefore, the continuous movement of the wall will stimulate different standing waves with plenty of resonant modes. On account of the heating patterns associated with resonant modes begin to overlap, a time-averaged heating results and temperature rise in the heating object tends to be more uniform in the end. Since many heated objects contain large amounts of water, and the dielectric properties of which will vary with the temperature at different locations in the objects, it can be treated as the most common inhomogeneous load during the heating process. Hence, we calculate the temperature deviation of water due to small parameter changes.

Microwave heating is a process involves multiple physics, electromagnetic in the cavity and heated samples, as well as mass and heat transport [21]. The basic equations describing the electromagnetic field distribution inside the microwave cavity is the Maxwell equation. After this equation being solved, the power dissipated inside the heated object can then be obtained by the following equation:

$$P_{\mathrm{d}} = \frac{1}{2}\varepsilon_0 \omega \varepsilon''(\omega)\left|\mathbf{E}\right|^2, \tag{10}$$

where $\varepsilon''(\omega)$ is the imaginary part of the complex permittivity including the total loss. Finally, the temperature rise can be expressed as:

$$\rho C_{\mathrm{p}} \frac{\partial T}{\partial t} - \nabla \cdot (k_t \nabla T) = P_{\mathrm{d}}, \tag{11}$$

where ρ is density of the dielectric, C_{p} is the specific heat capacity, k_t is the thermal conductivity, and T is the real-time temperature.

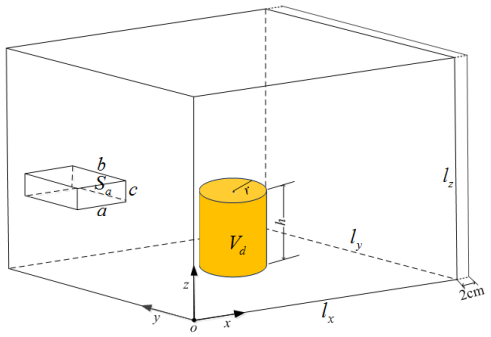

Fig. 4. Schematic of a moveable wall microwave heating.

Comsol Multiphysics software 5.3 is also used to perform the calculation of the temperature distribution of the dielectric object heated with the fixed wall cavity shown in Fig. 1 and the moveable wall cavity shown in Fig. 4. To solve the problem regarding the dynamics of the cavity wall we use this software's moving mesh function. In addition, we have assumed $\rho = 1000\mathrm{kg/m^3}$, $C_p = 4180\ \mathrm{J/(kg\cdot K)}$, and $k_t = 4180\mathrm{W/(m\cdot K)}$, respectively. Besides, the temperature-dependent permittivity of water is specified as [22- 23]:

$$\varepsilon_s = \frac{3\varepsilon_\infty T + A(\varepsilon_\infty + 2)^2 + \sqrt{\left[3\varepsilon_\infty T + A(\varepsilon_\infty + 2)^2\right]^2 + 72\varepsilon_\infty^2 T^2}}{12T},$$

with

$$A = 1186.78 \exp\left(\frac{2.88\times10^{-21}}{kT}\right), \tag{12}$$

where ε_∞ is the infinite frequency relative permittivity and assumed $\varepsilon_\infty = 5.5$, k is the Boltzmann's constant. After 10s of microwave heating, their temperature distribution, coefficient of variation (COV) and temperature rise histories [5] of the central cross section are compared in Fig. 5 and Fig. 6, respectively.

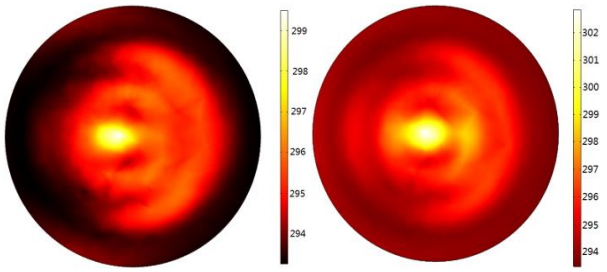

(a) (b)

Fig. 5. The temperature distribution of central cross section after 10s of microwave heating with: (a) fixed wall and (b) moveable wall.

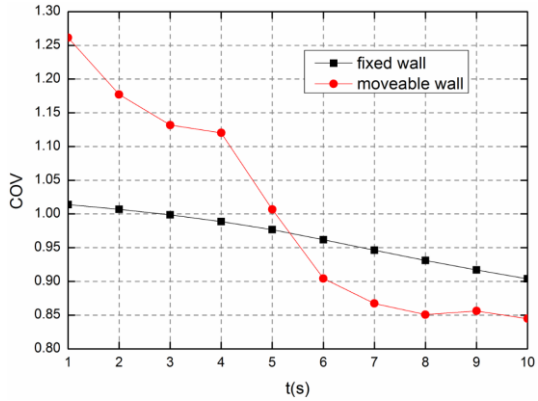

(a)

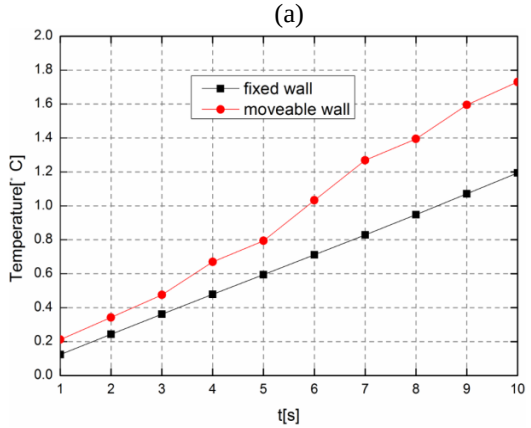

(b)

Fig. 6. Comparison of COV and temperature rise histories, with fixed wall and moveable wall: (a) COV, and (b) temperature rise histories.

The COV in Fig. 6 is defined as [5]:

$$COV = \frac{\sqrt{\sum_{i=1}^{n}\left(T_i - \overline{T}\right)^2}}{\Delta\overline{T}}, \quad (13)$$

where n are points considered in the ample, $\Delta\overline{T} = \overline{T} - 20^{\circ}\mathrm{C}$. It is well known that COV can effectively quantify the heating uniformity, and the smaller the COV is, the more uniform the heating sample is. As can be seen in Fig. 5, the temperature distribution of the object inside the moveable wall cavity is much more uniform than that of the fixed one. Due to the fact that the heating uniformity is highly dependent on the stability of electric field, Fig. 6 (a) also demonstrates that with the movement of the cavity wall, although it forms a more chaotic distribution at first, the heating uniformity can be significantly improved in the end. Moreover, Fig. 6 (b) shows that the temperature rise in the case of moveable wall is much faster than that in the case of fixed wall. This example also proves that it is feasible to make use of the instability of electric field to improve heating uniformity.

V. CONCLUSIONS

In this paper, we proposed a numerical method to study on the drastic-variation condition of electric field in a multimode microwave heating system. This method combined with integral equation and spectrum analysis. The characteristic of electric field and its dependent parameters were discussed. For microwave heating, the electric field is usually unstable, and a tiny shift in microwave frequency, permittivity of dielectric object or cavity geometrical parameters will produce a drastic variation in electric field distribution. Moreover, the smallest shift of parameter that results in a drastic variation of electric field can be obtained by the reverse search of the critical value. To make some supplements for the interest regarding practical applications, two examples of the drastic-variation condition in making better use of microwave energy were given.

ACKNOWLEDGMENT

This work was supported by the National Natural Science Foundation (No. 61731013), the Key Scientific Research Program of the Education Department of Sichuan Province (No.17AZ0377), Science Foundation of the Sichuan Province (No.2018FZ0008), and the Meritocracy Research Funds of China West Normal University (No. 17YC053)

REFERENCES

[1] M. Celuch, M. Soltysiak, and U. Erle, "Computer simulations of microwave heating with coupled electromagnetic, thermal, and kinetic phenomena," *Appl. Comput. Electrom.*, vol. 26, pp. 275-283, 2011.

[2] K. Pitchai, J. Chen, S. Birla, et al., "Modeling microwave heating of frozen mashed potato in a domestic oven incorporating electromagnetic frequency spectrum," *J. Food Eng.*, vol. 173, pp. 124-131, 2016.

[3] A. Tangy, I. N. Pulidindi, N. Perkas, et al., "Continuous flow through a microwave oven for the large-scale production of biodiesel from waste cooking oil," *Bioresource Technol.*, vol. 224, pp. 333-341, 2017.

[4] L. A. Campañone, J. A. Bava, and R. H. Mascheroni, "Modeling and process simulation of controlled microwave heating of foods by using of the resonance phenomenon," *Appl. Therm. Eng*., vol. 73, pp. 914-923, 2014.
[5] S. S. R. Geedipalli, V. Rakesh, and A. K. Datta, "Modeling the heating uniformity contributed by a rotating turntable in microwave ovens," *J. Food Eng.*, vol. 82, pp. 359-368, 2007.
[6] M. Chandran, V. B. Neculaes, D. Brisco, S. Katz, J. Schoonover, and L. Cretegny, "Experimental and numerical studies of microwave power re-distribution during thermal runaway," *J. Appl. Phys*., vol. 144, 204904, 2013.
[7] D. A. Hill, "Electronic mode stirring for reverberation chambers," *IEEE Transactions on Electromagnetic Compatibility*, vol. 36, pp. 294-299, 1994.
[8] R. Serra, A. C. Marvin, F. Moglie, et al., "Reverberation chambers à la carte: An overview of the different mode-stirring techniques," *IEEE Electromagnetic Compatibility Magazine*, vol. 6, pp. 63-78, 2016.
[9] D. A. Hill, *Electromagnetic Fields in Cavities: Deterministic and Statistical Theories*. John Wiley & Sons, New York, 2009.
[10] N. V. Budko and A. B. Samokhin, "Spectrum of the volume integral operator of electromagnetic scattering," *SIAM J. Sci. Comput*., vol. 28, pp. 682-700, 2006.
[11] N. V. Budko and A. B. Samokhin, "Classification of electromagnetic resonances in finite inhomogeneous three-dimensional structures," *Phys. Rev. Lett*., vol. 96, pp. 023904, 2006.
[12] F. Alessandri, M. Chiodetti, A. Giugliarelli, et al., "The electric-field integral-equation method for the analysis and design of a class of rectangular cavity filters loaded by dielectric and metallic cylindrical pucks," *IEEE Trans. Microw. Theory Tech.*, vol. 52, pp. 1790-1797, 2004.
[13] C. T. Tai, *Dyadic Green Functions in Electromagnetic Theory*. Institute of Electrical & Electronics Engineers (IEEE), 1994.
[14] C. T. Tai and P. Rozenfeld, "Different representations of dyadic Green's functions for a rectangular cavity," *IEEE Trans. Microw. Theory Tech.*, vol. 24, pp. 597-601, 1976.
[15] Y. Rahmat-Samii, "On the question of computation of the dyadic Green's function at the source region in waveguides and cavities," *IEEE Trans. Microw. Theory Tech.*, pp. 762-765, 1975.
[16] A. D. Yaghjian, "Electric dyadic Green's functions in the source region," *Proceedings of the IEEE*, vol. 68, pp. 248-263, 1980.
[17] W. C. Chew, "Some observations on the spatial and eigen function representations of dyadic Green's functions," *IEEE Trans. Antenna. Propag*., vol. 37, pp. 1322-1327, 1989.
[18] C. A. Balanis, *Advanced Engineering Electromagnetics*. John Wiley & Sons, New Jersey, 2012.
[19] Z. M. Tang, K. M. Huang, et al., "Study on stability of electric field in multimode microwave heating cavity," *Int. J. of App. Electrom*., vol. 50, pp. 321-330, 2016.
[20] Y. H. Liao, J. Lan, C. Zhang, T. Hong, Y. Yang, K. Huang, and H. C. Zhu, "A phase-shifting method for improving the heating uniformity of microwave processing materials," *Materials*, vol. 9, 2016.
[21] J. H. Ye, T. Hong, Y. Wu, et al., "Model stirrer based on a multi-material turntable for microwave processing materials," *Materials*, vol. 10, 2017.
[22] F. Torres and B. Jecko, "Complete FDTD analysis of microwave heating processes in frequency-dependent and temperature-dependent media," *IEEE Trans. Microw. Theory Tech.*, vol. 45, pp. 108-117, 1997.
[23] K. M. Huang and Y. H. Liao, "Transient power loss density of electromagnetic pulse in debye media," *IEEE Trans. Microw. Theory Tech*., vol. 63, pp. 135-140, 2015.

Zhengming Tang was born in Anyue, China, in 1981. He received his M.S. degree in Electrical Engineering from the Southwest Jiaotong University, and Ph.D. degree from Sichuan University, Chengdu, China, in 2012 and 2016, respectively. Currently, he is an Associate Professor of School of Electronic and Information Engineering of China West Normal University.

His research interests are in the areas of electromagnetic theory, microwave heating, and microwave chemistry.

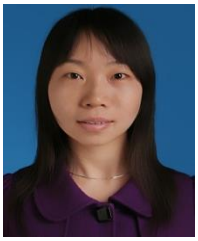

San-mei Zhang was born in Guangan, China, in 1982. She received her M.S. degree from Chengdu University of Technology in 2008, in Communication and Information System. She is currently a Lecturer of Education and Information Technology Center of China West Normal University.

Her research interests include numerical computation in electromagnetics, network virtualization, and communication network technologies.

Tao Hong was born in Hechuan, China, in 1989. He received his B.Sc. degree from Sichuan University in 2011, in Electronical and Information Engineering. From 2011, he has been working his Ph.D. and he received the Ph.D. degree in 2016. He is currently a Lecturer of School of Electronics and Information Engineering of China West Normal University.

His special fields of interest include electromagnetics, microwave engineering and microwave chemistry.

Fangyuan Chen was born in Zhumadian, China. He received the Ph.D. degree from Sichuan University in 2016, in Radio Physics. From 2013 to 2015, he was a Visiting Fellow, supported by China Scholarship Council, at the Department of Biological and Environmental Engineering, Cornell University, USA. From 2016, he was employed by China Aerospace Science and Technology Corporation.

His research interests are in numerical computation applied in electromagnetics, microwave heating, and antenna design.

Kama Huang (M'01–A'01–SM'04) was born in Chongqing, China, in 1964. He received the M.S. and Ph.D. degrees in Microwave Theory and Technology from the University of Electronic Science and Technology, Chengdu, China, in 1988 and 1991. He has been a Professor in the Department of Radio and Electronics of Sichuan University, Sichuan, China, from 1994, and has been the Director of the department since 1997.

In 1996, 1997, 1999, and 2001, he was a Visiting Scientist at the Scientific Research Center "Vidhuk" in Ukraine, Institute of Biophysics CNR in Italy, Technical University Vienna in Austria, and Clemson University in the U.S., respectively. At these institutions, he cooperated with the scientists to study the interaction between electromagnetic fields and complex media in biological structure and reaction systems. He has published over 100 papers. His research interests are in the areas of microwave chemistry and electromagnetic theory.

Huang is the Chief Scientist of the National Basic Research Program of China (973 Program), and he has received several research awards from the Chinese government.

Analysis and Suppression of EMI for Traction Control Unit Speed Sensors of CRH380BL Electric Multiple Unit

Yutao Tang [1], Feng Zhu [1], Hede Lu [2], and Xin Li [1]

[1] School of Electrical Engineering
Southwest Jiaotong University, Chengdu, 610031, China
835578907@qq.com, zhufeng@swjtu.edu.cn, lxwhere1000@my.swjtu.edu.cn

[2] School of Physical Science and Technology
Southwest Jiaotong University, Chengdu, 610031, China
luhede@qq.com;

Abstract ─ The doors of China railways high-speed 380BL-type (CRH380BL) electric multiple unit (EMU) at Changchun station in China could not be opened. It was analysed that the traction control unit (TCU) speed sensors were disturbed by the pantograph-catenary arc while lowering the pantograph. To solve this problem, firstly, the electromagnetic interference (EMI) for the second train body (02TB) of CRH380BL EMU where the pantograph-catenary is located at is tested. The results show that the intensity of EMI in space is increased significantly because of the pantograph-catenary arc. The distribution of spectrum of EMI is generally random, but the spectrum is mainly distributed in the range from 5MHz to 10MHz. Based on the test results, the coupling mechanism of EMI for the TCU speed sensor is analyzed in this paper. Then a method of nesting magnetic rings on the shielded cable is proposed for suppression of the interference. It can reduce the EMI about 8dB at the main frequency bandwidth mentioned above with 12 centimeters long Ni-Zn ferrite magnetic rings.

Index Terms ─ Electromagnetic interference (EMI), interference suppression, magnetic ring, pantograph-catenary arc, speed sensor.

I. INTRODUCTION

It becomes more and more difficult to ensure EMU in normal operation because of the complex electromagnetic environment [1]. A typical example about that issue is the doors of CRH380BL EMU at Changchun station in China cannot be opened while lowering the pantograph [2-3]. In order to ensure passengers safety, the train doors cannot be opened when the measured speed is beyond 5km/h for this EMU. It is analysed that the TCU speed sensors are disturbed by EMI from the pantograph-catenary arc in above case. Therefore, the further study of EMI for the TCU speed sensors is necessary to ensure reliable operation of EMU.

There are few studies for this issue and most of them mainly focus on speed sensors of China railways high-speed 2-type (CRH2) EMU, such as [4]-[11]. For example, some researchers were concerned about the over voltage caused by conduction interference. However, there were little analysis of the coupling mechanism of interference [4]-[9]. Combined with some experimental investigations, Yang concluded that the damage of sensor under pantograph-catenary detachment was caused by transient train body voltage fluctuation [10]. Zhao said that the surge pulse group would cause faulty speed sensors when the insulation performance of speed sensor became worse [11].

As an extension of previous works, firstly, based on the above description, this paper analyses the working principle of the door control unit (DCU) and the logical relation between TCU speed sensors and DCU of this EMU. Secondly, the EMI of the TCU speed sensor on the second train body (02TB) is tested. The results show that the intensity of EMI in space is increased significantly because of the pantograph-catenary arc. Then the jamming mechanism of the speed sensor is analyzed. Researches show that the common-mode current from the pantograph-catenary arc on the surface of the shield cable causes the instability of the ground potential and lead to above malfunction. A method of nesting magnetic-ring on shield cable of TCU speed sensor to suppress the EMI of common-mode is proposed in this paper. Although there are many researches about using the magnetic-ring to suppress EMI at present [12]-[14], most of them are referring to the simulation model. Few people apply this method to EMI suppression under the above conditions. Experiment is used to verify the effectiveness of suppression in this situation at the end of this paper. It indicates that it can reduce the EMI about 8dB at the main frequency bandwidth mentioned above by using 12 centimeters long Ni-Zn ferrite magnetic rings. The

Submitted On: September 25, 2017
Accepted On: April 16, 2018

method is also effective for discrete interference in 10MHz~30MHz.

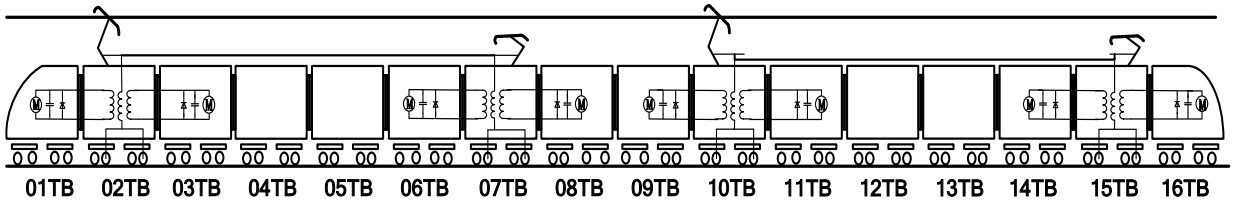

Fig. 1. Structure for the TBs of CRH380BL EMU.

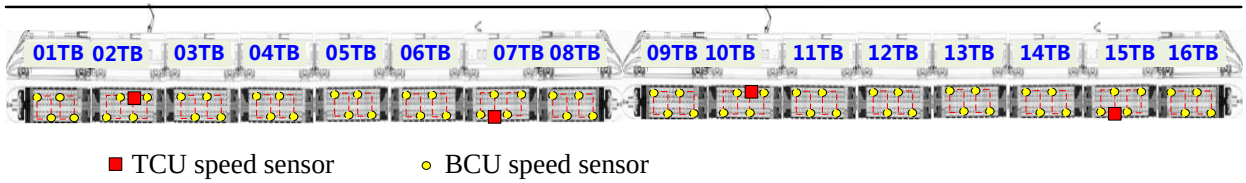

Fig. 2. Diagram of speed sensors position distribution in CRH380BL EMU.

II. ANALYSIS OF LOGICAL RELATIONSHIP FOR TRAIN DOORS

As for the TBs of CRH380BL EMU, the Fig. 1 shows its structure, consisting of 16 marshaling TBs. Their serial numbers are from 01 to 16. The motors are 01TB, 03TB, 06TB, 08TB, 09TB, 011TB, 14TB and 16TB, and all the remaining of TBs are trailers. Besides, there are four pantographs on the train roofs of 02TB, 07TB, 10TB and 15TB respectively. The rest of two pantographs are in standby when the pantographs on the train roofs of 02TB and 07TB being used and vice versa.

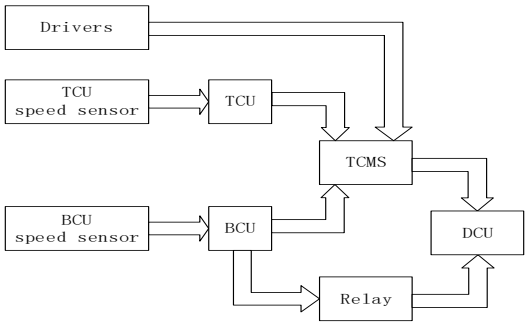

Fig. 3. The logic diagram of DCU.

There are two types of speed sensors on the CRH380BL EMU: TCU speed sensors and brake control unit (BCU) speed sensors. The installation position of those sensors is shown in Fig. 2. According to the CRH380BL EMU, the closure of door is controlled by the DCU. As described in Fig. 3, there are three ways to close the train doors. First of all, the driver can send message to DCU directly to close all the doors by train control and management system (TCMS). Secondly, the two kinds of speed sensors send the speed signal into TCU and BCU respectively, and the signal will be compared with 5km/h. As long as the speed is measured by one of TCU speed sensors is more than 5km/h, all the doors will be closed. As for the BCU speed sensors, it can only give the control to the corresponding train doors. For example, if the speed is detected by one of BCU speed sensors on 02TB exceeds the limit, then just the train door of 02TB won't be opened. Thirdly, when a speed signal which is detected by the BCU speed sensors is far greater than 5km/h, the signal will be sent to DCU by the relay instead of TCMS to close the door quickly.

III. EMI TEST

A. The magnetic field test

The pantograph-catenary arc will be formed between the catenary and the pantograph when the EMU is lowering the pantograph. Its main frequency component is about 5MHz [15], and it can generate the powerful magnetic field. A CRH380BL EMU which had above fault was selected as a test object at Changchun station in China. The strength of the magnetic field in the space was tested by using the EMI receiver (ESCI-3; 9KHz~3GHz; -40dBμV~+137dBμV) and the loop antenna (HFH2-Z2; 9KHz~30MHz). The situation of field test is shown in Fig. 4.

Taking 02TB as the object of study, the magnetic field intensity was measured several times when the pantograph of 02TB being lowered. The loop antenna was erected at a horizontal distance of 3m from the center of the orbit. The maximum magnetic field intensity could be close to 54dBμA/m (The antenna coefficient of the loop antenna is 20dB/m within the frequency range of this test). Some electromagnetic sensitive devices can be disturbed by such high frequency and large amplitude magnetic field. However, the magnetic field intensity

will be reduced significantly when it is far away from the pantograph. Because the CRH380BL EMU is about 400 meters, the speed sensors which is far away from 02TB won't be influenced when the pantograph of 02TB being lowered.

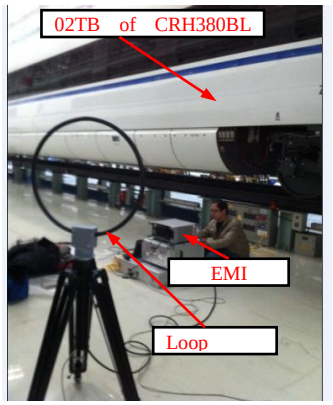

Fig. 4. The field test of magnetic field intensity.

According to the working principles of speed sensors and the DCU, the BCU speed sensors just affect the corresponding doors and the TCU speed sensors can influence all the doors of this EMU. All the doors instead of the single door could not be opened normally in this fault. We believe that TCU speed sensor was disturbed and led to this breakdown.

B. The EMI test of TCU speed sensor

The EMI of TCU speed sensor on 02TB was tested by using the spectrum analyzer (Agilent 9340B; 9KHz~3GHz; -40dBμV~+137dBμV) and current clamp (BK-CP-02; 10Hz~100MHz) when the pantograph of 02TB being lowered. The situation of physical connections is shown in Fig. 5. The Fig. 6 shows the test results without lowering the pantograph. It comes from the electromagnetic waves that already exist in the environment. The two typical results of test are displayed in Fig. 7.

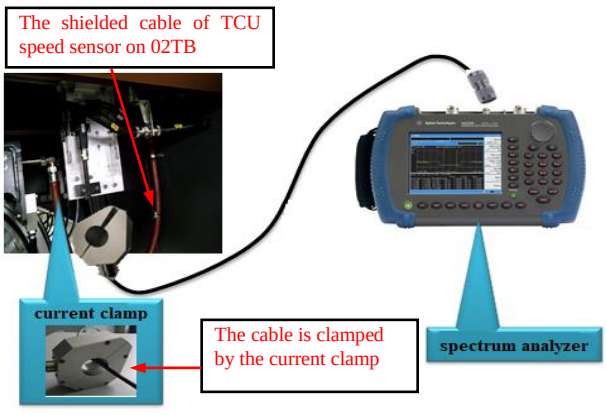

Fig. 5. The diagram of physical connections.

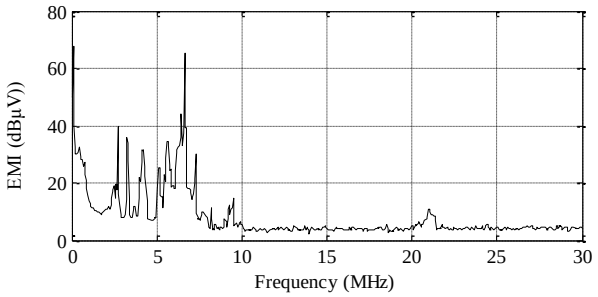

Fig. 6. The test results without lowering the pantograph.

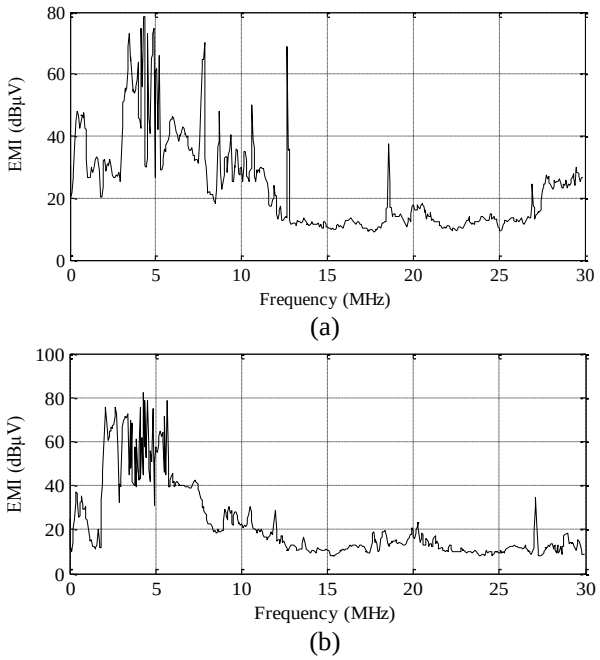

Fig. 7. The waveform of EMI for TCU speed sensor.

The results show that the pantograph-catenary arc will cause EMI on the cable of the speed sensor. The distribution of spectrum of EMI is generally random, but the spectrum is mainly distributed in the range from 5MHz to 10MHz. A small amount of discrete interference occur in the range of 10MHz~30MHz.

IV. ANALYSIS OF THE MECHANISM OF EMI

There is a high frequency component in the pulse wave which is emitted by the pantograph-catenary arc. It can cause the disturbance on the shield cable of speed sensors. The outer conductor of the cable braid shield of TCU speed sensor is made of metal wire. As described in Fig. 8, the cable braid shield is not shielded completely because of the many tiny holes on it. The induced electric field *E* will be formed on the surface of the cable because of the EMI. A portion of the interference will be coupled to the core wire inside the cable through

tiny holes. It can form the induced electric field E' on the core wire as depicted in Fig. 9. Because the E>E', it will form a potential difference U between the cable braid shield and core wire. The value of interference can be expressed by the value of U [16]:

$$U = I \times Z_t \times L_m, \quad (1)$$

where I is the induced current, Z_t is the transfer impedance of each meter cable, L_m is the effective length of the cable. Based on document [17], Z_t is given by:

$$Z_t = Z_d + j\omega(M_h \pm M_b), \quad (2)$$

where Z_d is the diffusion impedance, its value decreases as the increase of frequency [18]:

$$Z_d \approx \frac{4}{\pi d^2 nC\sigma\cos\alpha} \cdot \frac{(1+j)d/\delta}{\sinh[(1+j)d/\delta]}, \quad (3)$$

M_h is the hole inductance and M_b is the braid inductance [19]:

$$M_h = \frac{2\mu_0 C}{\pi\cos\alpha}\left[\frac{b}{\pi(d_0+2d+h)}\right]^2 \exp(-\frac{\pi d}{b}-2\alpha), \quad (4)$$

$$M_b = \frac{\mu_0[ndh+(b-\frac{bh}{d})\frac{h+d}{2}+B]A}{2\pi C(d_0+2d+h)\cos\alpha}, \quad (5)$$

where d is the wire diameter, C is the number of carriers in the braid, n is the number of wires in each carrier, δ is the skin depth, σ is the conductivity of shield and b is the distance between the adjacent carriers. The value of the pitch angle of the weave α and the distance between the braid layers h can be calculated accurately by using the picks p (number of carrier crossings per unit length) and the diameter under the braid d_0 [20],
and

$$A = (\sqrt{v}+1)^2\cos(2\alpha), \quad (6)$$

$$B = n(d^2 - \frac{\pi d^2}{4}). \quad (7)$$

Where v is the number of holes in the braid.

The type of braided coaxial cables which are used on TCU speed sensors of the CRH380BL EMU are determined by the following primary parameters: d=0.12mm, C=24, n=6, d_0=5.54mm, p=45mm, σ=5.8×107S/m, μ_0=4π×10-7H/m. As shown in Fig. 10, the calculated values Z_t by the formula (2)~(7) are higher than the test values generally, especially at the high frequency band. Therefore, it is necessary to revise the formula for the calculation of Z_t.

Because the response of the high frequency transient electromagnetic field on the woven mesh is more complex. The extra attenuation of vortex current caused by the magnetic field between the inner and outer layers of the braid network cannot be ignored. Therefore, the extra fluctuating effects M_e [21] is added into the calculation of Z_t:

$$M_e = -\frac{1.16}{Cnd}\arctan\frac{n}{3}\sin(\frac{\pi}{2}-2\alpha)\sqrt{\frac{\mu_0}{\sigma}}\sqrt{\omega}e^{j\frac{\pi}{4}}. \quad (8)$$

At the same time, the attenuation of transmitted electromagnetic waves at high frequency will not be ignored when the woven mesh with curvature. Therefore, the curvature coefficient K of woven mesh is proposed to revise the M_h in this study, and the values of K are from 0 to 1. The Fig. 11 shows the variation of the transfer impedance (M_e has been added) of the above cable with several typical values of K.

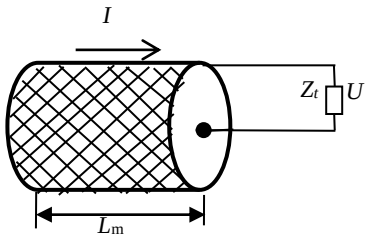

Fig. 8. The diagram of braided coaxial cable.

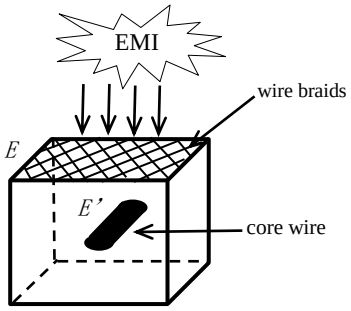

Fig. 9. The section of braided coaxial cable.

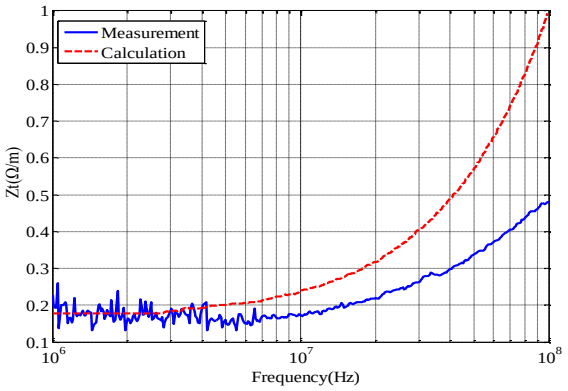

Fig. 10. The comparative diagram of the calculated values and the test values of Z_t.

The results of calculation and measurement of transfer impedance with different K are compared in large quantities. The calculated values of Z_t for this cable is the closest to the test values when the K is 0.85

within the frequency range of 30MHz. So formula (4) has been amended:

$$M_h^* = 0.85 M_h . \quad (9)$$

The formula (2) has been modified:

$$Z_t^* = Z_d + j\omega(M_h^* \pm M_b) + M_e . \quad (10)$$

The comparison of the calculated values of Z_t^* and the test results is shown in Fig. 12.

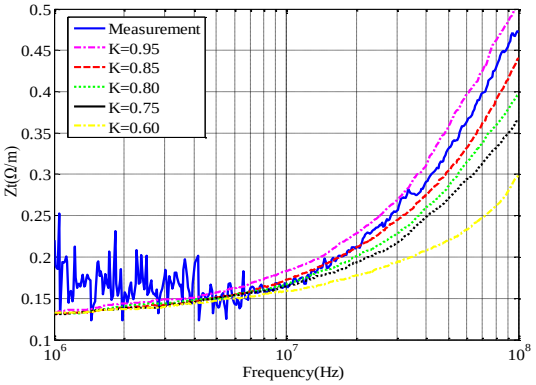

Fig. 11. The curve of the values of the transfer impedance with different *K*.

The values of I and L_m are got by field test. The maximum value of I on the shield cable is 95mA. The L_m of TCU speed sensor on 02TB is 1m. The rest of shield cable is inside the metal housing, and it will not be disturbed. The Fig. 7 shows that the EMI is mainly concentrated in the frequency range of 5MHz~10MHz. Z_t^*=150mΩ/m can be calculated when f=5MHz (The EMI of the pantograph-catenary arc is random. But the frequency of the strongest interference is about 5MHz by field test). The U can be calculated: U≈14mV.

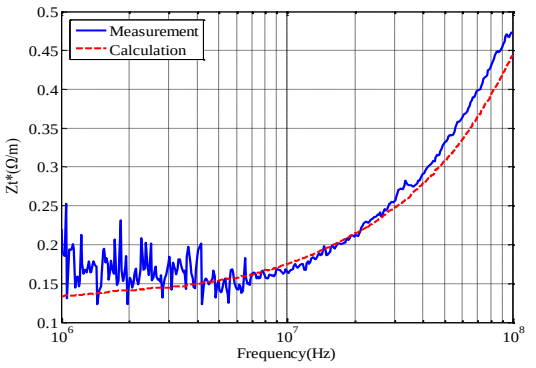

Fig. 12. The comparative diagram of the calculated values and the test values of Z_t^*.

According to the test results shown in Fig. 7, the maximum interference of TCU speed sensor on 02TB is about 80dBμV. The voltage value can be converted to 10mV, which is consistent with the theoretical analysis.

The above voltage is calculated at single frequency point. The actual interference voltage will reach up to about 4kV because of the superposition of power energy spectrum [22]. It was the instantaneous high voltage that led to the fault of speed sensors.

V. TEST RESULTS OF INTERFERENCE SUPPRESSION

The method of nesting Ni-Zn ferrite magnetic rings on shield cable of TCU speed sensor is used to suppress EMI in this paper. Ni-Zn ferrite magnetic rings are often used to suppress 1MHz or more high-frequency EMI because of its low permeability and high resistivity [23].

The interference suppression characteristics of four different Ni-Zn ferrite magnetic rings are compared in Table 1. Their sizes are suitable for the cables of the TCU speed sensors and the impedance-frequency curve are shown in Fig. 13. It can be seen that the interference suppression capability of type 1 is the strongest in the main frequency mentioned above (5MHz~10MHz) of EMI. As a result, type 1 (E04SR401938) is chose in this study.

In order to study the suppression of the EMI by magnetic rings, a simulation experiment has been done in the laboratory. The sinusoidal signal generated by the signal generator (Agilent N9310A; 9KHz~3GHz; -127dBm~+13dBm) was radiated by the transmitting antenna (HK116; 30MHz~1GHz) onto the cable (Length is 1m) of the TCU speed sensor. The spectrum analyzer, current clamp and loop antenna mentioned above were used to receive interference on the cable. The suppression effect of EMI after nesting the Ni-Zn ferrite magnetic rings (type 1) with different numbers on cable was tested, and the results were shown in Fig. 14.

Table 1: The main parameters of four different types of magnetic rings

Type	Part No.	Internal Diameter	External Diameter	Height
1	E04SR40 1938	19mm	38mm	40mm
2	E04ST25 1512D	15mm	28mm	12mm
3	E04ST28 1613D	16mm	31mm	13mm
4	E04ST40 2715D	27mm	42mm	15mm

Because the height of magnetic ring (type1) is 40mm and the length of cable is 1m, it results that the maximum number of that rings is 25. As shown in Fig. 14, the suppression effect is not increased obviously when the number of magnetic rings is increased to more than 5. According to the results of the experiment, the different numbers of magnetic rings (type1) are nested on the cable of TCU speed sensor on 02TB of this EMU.

When the number of the magnetic rings is greater than three, that is, when the suppression effect is more than 8dB, the malfunction of the abnormal locking for the train doors can be solved.

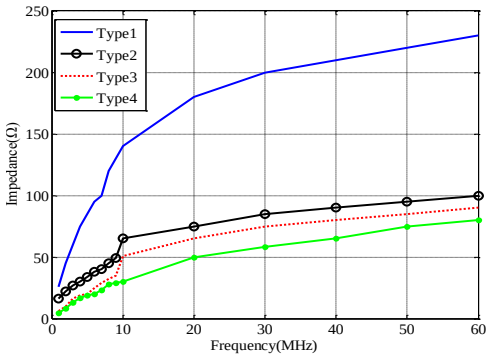

Fig. 13. The impedance-frequency curve of four Ni-Zn ferrite magnetic rings.

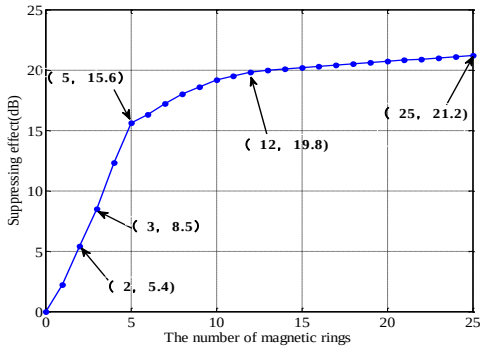

Fig. 14. The suppression effect of EMI after nesting different numbers of magnetic rings on cable.

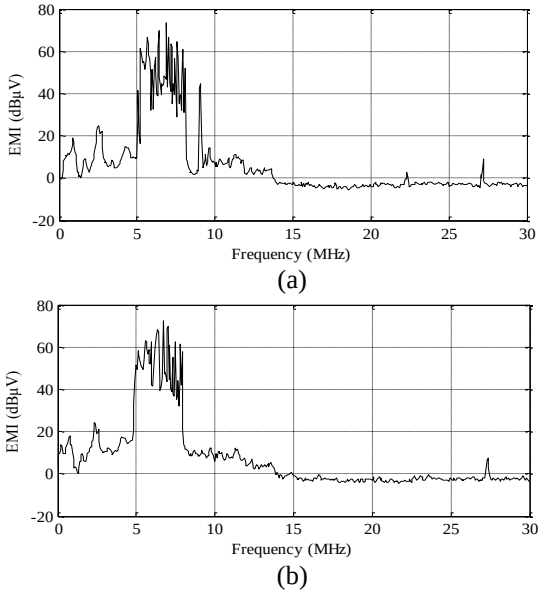

Fig. 15. The waveform after EMI is suppressed.

When the pantograph of 02TB being lowered, the EMI was tested after nesting three Ni-Zn ferrite magnetic rings on the shield cable of TCU speed sensor on 02TB. The results are shown in Fig. 15.

As shown in Fig. 15, the peak of EMI is decreased by about 8dB after using the magnetic ring when the frequency is below 10MHz. When the frequency is 10MHz~30MHz, the discrete interference is reduced obviously. Basically, the magnetic rings can absorb the electromagnetic radiation energy and reduce Z_t of cable. So as to achieve the purpose of interference suppression. In this way, the train doors can be opened normally.

VI. CONCLUSION

In this paper, a method of suppressing the EMI from the pantograph-catenary arc for the TCU speed sensor of CRH380BL EMU was proposed. Based on the malfunction of this EMU at Changchun station in China, the mechanism of EMI was analyzed systematically. It indicated that the TCU speed sensors were disturbed and led to the fault of DCU. According to the test results, the abnormal locking of the train doors was solved effectively after nesting three (12cm) Ni-Zn ferrite magnetic rings on the shield cable of TCU speed sensor.

ACKNOWLEDGMENT

We would like to thank the anonymous reviewers for their insightful comments. This paper is supported by the National Natural Science Foundation of China (U1434203).

REFERENCES

[1] F. Zhu, D. P. Niu, and C. W. Xu, "Measurement and analysis on ambient magnetic field inside the bodywork of CRH1," *Journal of Electric Science and Technology*, vol. 27, no. 2, pp. 42-46, June 2012.

[2] K. Huang, Z. G. Liu, F. Zhu, Z. S. Zheng, and Y. Cheng, "Evaluation scheme for EMI of train body voltage fluctuation on the BCU speed sensor measurement," *IEEE Transactions on Instrumentation and Measurement*, vol. 66, no. 5, pp. 1046-1057, May 2017.

[3] J. B. Yang, F. Zhu, J. Li, M. Sha, and D. Q. Yuan, "Electromagnetic interference measurement and analysis of high-speed electric multiple units speed sensor," *Journal of Electronic Measurement and Instrumentation*, vol. 29, no. 3, pp. 433-438, Mar. 2015.

[4] G. Gao, B. Yuan, Y. Feng, and G. Wu, "Over-voltage analyzing for high speed railway phase-separation switch," *in Proc. International Conference on Electric Power Equipment - Switching Technology IEEE*, pp. 207-209, 2012.

[5] H. Wu, "Research on Vehicle Body Over-Voltage Surge," Department of Electrical Engineering,

Southwest Jiaotong University, M.S., 2013.
[6] S. Hatsukade, "Reduction method of surge voltage on AC railcar's body," *Foreign Rolling Stock*, vol. 50, no. 2, pp. 70-75, 2010.
[7] S. Hatsukade and M. Nagata, "Reduction of EMI from traction circuits using shielded cable," *Qr of Rtri*, vol. 49, no. 1, pp. 20-25, Feb. 2008.
[8] S. Hatsukade and T. Maeda, "Experiment and basic analysis of the surge on a rolling stock's body," *IEEE Trans. P&E*, vol. 125, no. 8, pp. 754-758, 2005.
[9] W. F. Han, X. Y. Hu, S. Xiao, G. N. Wu, G. Q. Gao, D. L. Liu, and K. S. Yang, "Analysis of railcar's body over-voltage for electric multiple unit in the case of lightning contact," *Journal of Railway Science & Engineering*, vol. 10, no. 4, pp. 117-123, Aug. 2013.
[10] J. Yang, "EMC experiment and protection method on control vehicle speed and distance measuring equipment of CRH2 HST," *Railway Signaling Commun. Eng.*, vol. 7, no. 5, pp. 21-24, Oct. 2010.
[11] J. P. Zhao and J. J. Gong, "Fault analysis and treatment of CRH2037A EMU's LKJ system," *Science & Technology Information*, no. 22, pp. 743-745, 2011.
[12] Y Guan, G Yue, W Chen, Z Li, and W Liu, "Experimental research on suppressing VFTO in GIS by magnetic rings," *IEEE Transactions on Power Delivery*, vol. 28, no. 4, pp. 2558-2565, Oct. 2013.
[13] M. Szewczyk, J. Pawlowski, K. Kutorasinski, and W. Piasecki, "High frequency model of magnetic rings for simulation of VFTO damping in gas-insulated switchgear with full-scale validation," *IEEE Transactions on Power Delivery*, vol. 30, no. 5, pp. 2331-2338, Oct. 2015.
[14] Z. T. Xiang, W. D. Liu, J. L. Qian, Y. L. Zhang, Y. Z. Shen, and S. P. Wang, "Simulation test and computation of suppressing very fast transient over-voltage in GIS by magnetic rings," *Proceedings of the Chinese Society for Electrical Engineering*, vol. 25, no. 19, pp. 101-105, Oct. 2005.
[15] Z. J. Shen. "Electromagnetic Interference Caused by Arc in Pantograph-Catenary System," *Department of Electrical Engineering, Beijing Jiaotong University, M.S.*, 2013.
[16] R. Tiedemann, "Current flow in coaxial braided cable shields," *IEEE Transactions on Electromagnetic Compatibility*, vol. 45, no. 3, pp. 531-537, Aug. 2003.
[17] P. M. Yang, T. B. Lu, L. Qi, and X. S. Gu, "Calculation of transfer impedance of braided shielded cable," *in Proceedings of The Symposium on Electrical Theory and New Technology*, Xi'an, China, pp. 318-321, Aug. 2005.
[18] R. Otin, J. Verpoorte, and H. Schippers, "Finite element model for the computation of the transfer impedance of cable shields," *IEEE Trans. On EMC*, vol. 54, no. 4, pp. 950-958, Nov. 2011.
[19] A. Morriello, T. M. Benson, A. P. Duffy, and C. F. Cheng, "Surface transfer impedance measurement: a comparison between current probe and pull-on braid methods for coaxial cables," *IEEE Trans. On EMC*, vol. 40, no. 1, pp. 69-76, Feb. 1998.
[20] S. Sali, "An improved model for the transfer impedance calculations of braided coaxial cables," *IEEE Trans. On EMC*, vol. 33, no. 2, pp. 139-143, May 1991.
[21] A. K. Bhattacharyya, *EMC Analysis Methods and Computational Models*, [M]. Wiley, 1997.
[22] Z. G. Yu, M. S. Liu, T. T. Zhang, W. F. Wei, G. Q. Gao, G. G. Wu, and B. C. Jia, "Test research on arcing during pantograph rising and lowering process for electric multiple units," *Electrical & Energy Management Technology*, no. 17, pp. 15-20, Sept. 2017.
[23] H. Zhang, Z. B. Zhao, and L. Liu, "Test research on the suppressing radio interference of DC transmission lines by ferrite cores," *Transactions of China Electrotechnical Society*, vol. 28, sup. 2, pp. 180-184, Dec. 2013.

Yutao Tang was born in Sichuan Province, China, in 1991. She received the B.S. degree in Automation from Southwest Science and Technology University, Mianyang, China, in 2013, and is currently working toward the Ph.D. degree in Electrical Engineering at Southwest Jiaotong University, Chengdu, China.

She has participated in the 2017 International Applied Computational Electromagnetics Society Symposium in China (ACES-China 2017) and made a presentation.

Her research interests include electromagnetic environment test and evaluation, and electromagnetic compatibility analysis and design.

Feng Zhu was born in Anhui Province, China, in 1963. He received the B.S. degree in Physics from Huaibei Normal University, Huaibei, China, in 1984, the M.S. degree in Physics from Sichuan University, Chengdu, China, in 1987, and the Ph.D. degree in Electro-

magnetic Theory and Microwave Techniques from Southwest Jiaotong University, Chengdu, in 1997.

He is currently a Professor in the Department of Electrical Engineering, Southwest Jiaotong University. His research interests include electromagnetic environment test and evaluation, electromagnetic compatibility, and numerical electromagnetic methods.

Hede Lu was born in Shandong Province, China, on October 4, 1988. He received the B.S. degree in Electronic Information Science and Technology from Southwest Jiaotong University, Chengdu, China, in 2012, and is currently working toward the Ph.D. degree.

His research interests include electromagnetic compatibility, electromagnetic environment test and evaluation, and transmission line analysis.

Xin Li received the B.S. degree in Electronic Information Science and Technology from Southwest Jiaotong University, Chengdu, China, in 2013. He is currently pursuing the Ph.D. degree in Electrical Engineering from Southwest Jiaotong University, Chengdu, China. His current research interests include analysis on the electromagnetic compatibility of electric locomotive.